UNIVERSITY OF EAST ANGLIA

SCHOOL OF CHEMISTRY

Unravelling Vibrational and Electronic Coherences via Two-Dimensional Electronic Spectroscopy of Zinc-Porphyrins*

Franco Valduga de Almeida Camargo

This copy of the thesis has been supplied on condition that anyone who consults it is understood to recognise that its copyright rests with the author and that use of any information derived therefrom must be in accordance with current UK Copyright Law. In addition, any quotation or extract must include full attribution.

Norwich, February of 2017.

*Research funded by Coordenação de Aperfeiçoamento de Pessoal de Nível Superior (CAPES).

Acknowledgments

This thesis is the result of three intense years of studies and research, and I was lucky find a large number of people who have helped me overcome them in different ways. Acknowledging everyone here would result in too large a section, so I will mostly restrict it to people who impacted this thesis very directly.

First and foremost I thank Ismael Heisler. He has helped me in every step of the PhD, from inviting me to apply at UEA, to helping write the proposal for funding, giving support whilst I was settling in Norwich, teaching me the basics of two-dimensional electronic spectroscopy, developing the Labview code used in this thesis and discussing results.

Another major strike of luck was having Professor Steve Meech as a supervisor. His guidance was priceless, and I have the utmost admiration for his scientific skills and for the way he manages the group. I am very grateful for his careful help proof reading this thesis and making suggestions that resulted in substantial improvements.

I am specially grateful to Chris Hall for his patience and teaching skills when we were performing transient absorption experiments, as well as for his friendship and willingness to discuss ideas, papers and experiments.

Lena Grimmelsmann arrived in our group to spend three months of her PhD learning about 2D spectroscopy. In this short period she found ways to help perform experiments, prepare samples and analyze data in the final stages of the material which now comprises Chapter 5. Working with her was a real delight and she also became a great friend.

Other people in the group and at UEA who were not directly involved in this project also had considerable impact along the way. Garth Jones accepted to be my co-supervisor and was always a positive presence. I am grateful to Sergey Laptenok, Jamie Conyard, James Frost and Roberta Moca for their help on many occasions in the lab and for helpful discussions.

I thank Maria Marin Altaba and Paula Garcia Calavia for their patience in giving

basic advice to a physicist in a chemistry lab. I also thank Professor David Russell for giving us permission to use their equipment many times.

A group of technicians and staff from the School of Chemistry have also made a positive impact in this PhD by helping make big and small things possible along the way. Matthew Myles' help with cuvettes was invaluable, and so was the help of Roy Carter with IT issues, Pete, Tim and Matthew with liquid nitrogen and Gareth, who built many bits and pieces essential to perform the experimental work. Lisa, Laura and Matthew at the teaching lab have been very helpful with the vacuum line, making arrangements to suit challenging experimental schedule requirements. I am deeply grateful for their support.

Stephen Ashworth, Richard Stephenson, Yohan Chan, Alexander Romanov, Theresa Quirós, Robin Blagg and Lucca Rocchigiani have all been helpful on different occasions. The same can be sair of the administrative staff from the School of Chemistry, and I thank Joanne Burd, John Pullinger, Sharron Haines, Katharine Millard and Liz Jesse for their help with multiple issues over the years.

All experiments described in this thesis were performed in samples synthesized in the group of Professor Harry Anderson in the University of Oxford. I am indebted to Dr Rene M. Oetterli and Dr Dmitri Kondratuk for synthesizing some of the samples, and to Professor Anderson and Dr Martin Peeks, who shared some of their time for helpful discussions throughout my studies.

Unrelated to the research work itself, I have to thank Susana Ramalhete, Serena Monaco, Valeria Gabrielli, Karol Nartowski and Fabiana Diuk for their continuous friendship. I also thank my parents and my brother for their long distance support throughout the PhD.

Last, all of this was made possible by the Brazilian funding agency CAPES, which provided the money for my studentship, travel to Norwich and for the rather unreasonable tuition fees that UEA charges of PhD students from outside the European Union. I am extremely grateful for their support. I tried my best through this PhD to make the very most of the opportunity and I hope the skills I acquired can be of value in Brazil in the future. I also thank EPSRC for funding our lab.

Abstract

Two-dimensional electronic spectroscopy (2D-ES) is a cutting edge experimental method to probe ultrafast phenomena such as energy transfer, chemical reactions, coherent wavepacket motion, etc. It is an extension of transient absorption methods which recovers the signal as a function of the excitation frequency, resolving signals that are overlapped in traditional techniques, and allowing simultaneous high spectral resolution in excitation frequency and high temporal resolution of the dynamics. 2D-ES studies of light-harvesting systems from photosynthetic organisms reported coherent wavepacket motion, attributed to electronic coherences between different exciton states. Vibrational and vibronic coherences can also be observed with 2D-ES, and it is thus important to study the specific signatures of each. In this thesis, we present an experimental setup that is well suited to recover coherent wavepacket motion and employ it to study vibrational coherences in a zinc-porphyrin monomer. A first experiment is analyzed with the traditional convention of using only the real part of the complex-valued 2D-ES signal, and interference between neighboring oscillatory features is revealed, explained and modeled. We also find that when the full complex-valued signal is analyzed, the most pronounced interference features disappear, and in this case an analysis based on double-sided Feynman diagrams suffices to describe all observations. We then report an experiment with a blue-shifted laser spectrum, which matches the molecular absorption in a way that is more commonly found in 2D-ES studies, and observe signatures that closely resemble the features expected for a purely electronic coherence, which we explain considering the laser spectrum for all three field-matter interactions. Finally, we demonstrate a 2D-ES experiment with a red-shifted spectrum which exclusively probes coherences in the ground state, complementing experiments with the blue-shifted spectrum. We argue that a combination of the two suffices for unambiguous interpretation of coherences in 2D-ES, lifting the need for an ultrabroadband laser.

Contents

Chapter 1

Introduction

In time resolved spectroscopy non-linear optical signals are used in order to obtain information about dynamical properties of matter in real time. The advent of ultrashort laser pulses in the 1980s enabled phenomena in the range of femtoseconds to be studied [1, 2], and significant effort is currently being devoted to the development of attosecond pulses and techniques to further improve time resolution [3, 4]. Time-resolved spectroscopies have been widely used to study many different phenomena such as energy transfer [5, 6], coherent wavepacket motion [7], the dynamics of solvation [8, 9], relaxation [10], chemical reaction [11] and conformation dynamics [12].

Broadly speaking, non-linear optical techniques can be divided between resonant and non-resonant, and among the resonant we have fluorescence and absorption based methods, the latter corresponding all time-resolved experiments reported in this thesis. To directly access temporal dynamics in absorption techniques, the time delay between at least a pair of pulses has to be experimentally controlled, and a signal originating from two different pulses is at least of second-order in the field of the pulses. Because the second order nonlinear susceptibility vanishes for isotropic media, third-order techniques are generally used, with the most common being broadband transient absorption (also referred to as pump probe) [2].

In pump probe experiments, the sample is initially illuminated with a pulse, referred to as the pump, and after a controlled time interval it is illuminated again with a second pulse, called the probe, and the spectrum of the probe is acquired after the sample (see Figure 1.1a). A chopper is placed in the beam path of the pump, so that some probe pulses will be detected when the chopper blocked the pump, and the remaining probe

shots will be detected when the pump beam was not blocked by the chopper, and thus illuminated the sample. This configuration permits the calculation of a differential probe spectrum of the probe between the pump on and pump off cases for any desired value of the temporal delay between pump and probe. This differential spectrum contains the effect of the pump on the probe's absorption measured at a known time interval between the pulses; variation of the time delay yields dynamical information.

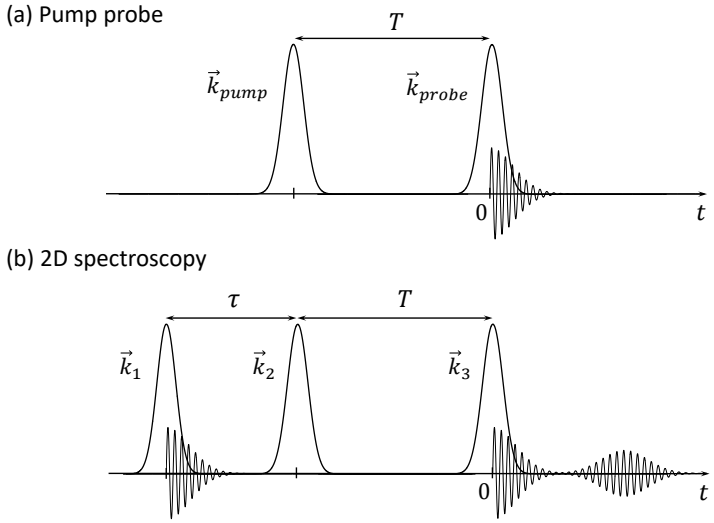

Figure 1.1: **(a)** Pulse sequence in a transient absorption experiment. **(b)** Pulse sequence in two-dimensional spectroscopy, where a pair of phase-locked pump pulses is used, to recover the excitation frequency. See text for details.

Because pump-probe experiments are absorption methods, dynamics both in the ground and in electronically excited states can be probed, whereas time resolved fluorescence experiments are sensitive to excited state dynamics only [13]. Overlapping signals due to many different phenomena can pose a challenge in the interpretation of pump-probe experiments, especially when ultrafast temporal resolution is desired. That happens because ultrashort pulses are intrinsically broadband in frequency. Hence, a transient absorption experiment with ultrashort pump and probe pulses can give sub 10 femtosecond temporal resolution, but the changes in the probe absorption at a given frequency ω_3 might be due to original absorption at any ω_1 frequency in the broadband pump spectrum. If high spectral resolution is desired it is possible to use a narrowband pump pulse. Such a pulse will necessarily be longer in time however, thus creating a trade-off between the ability to access ultrafast dynamics and the ability to clearly assign the absorption frequency responsible for it.

Two dimensional electronic spectroscopy extends transient absorption techniques in

a way that overcomes this problem [14, 15]. In essence, the concept is the following. As mentioned before, transient absorption experiments are third-order nonlinear optical measurements, with the system interacting twice with the pump pulse and once with the probe pulse, with the time interval between pump and probe being experimentally controlled. The time versus frequency resolution trade-off described above concerns the time resolution after the pump interaction and the frequency of pump excitation. We now note that this excitation frequency can in principle be recovered by performing the experiment with two pump pulses, scanning the time delay between them for each fixed waiting time relative to the probe (see Figure 1.1b). This time delay between the two pump pulses is called the coherence time (τ), and the third-order signal as a function of τ will be modulated by the frequency of the excited transitions. Therefore, if such a delay is added to a pump probe experiment with broadband pulses, the original excitation frequency may be retrieved through a Fourier transform of the data over the τ interval. The resulting data is a collection of correlation maps between excitation and emission frequency, one for each value of the delay between pump and probe: $S(\omega_1, T, \omega_3)$. In Section 2.6 we show that this is the convolution of the system's response function with the excitation fields, corresponding therefore to the most information that can be extracted from a third-order technique.

Multidimensional experiments are commonplace in NMR spectroscopy, having been first demonstrated in the 1970s [16] and flourishing to the extent that Richard Robert Ernst was awarded the Nobel Prize in Chemistry in 1991 [17]. NMR spectroscopy relies on radio frequency pulses with typical frequencies between 60 and 1000 MHz to excite and probe nuclear spin transitions. These frequencies correspond to optical cycles between 16.67 and 1 nanosecond (wavelengths of 0.3 and 5 meters respectively), which implies that the excitation frequencies to be recovered are in this range as well. In order to recover them in the time domain with the principle described above, it is essential that the data acquisition recovers the temporal oscillation during τ accurately, which presents different challenges in the visible and infrared spectral regions than in the radio frequency region.

The critical difference is that the wavelength of visible light lies in the region of 400 to 700 nm, with the corresponding optical cycles in the order of a few femtoseconds. Consequently, proper acquisition of the excitation frequency requires control of the time delay between the two pump pulses with an accuracy that is a fraction of this cycle. The

challenge is that typical vibrations and air currents found in the environment can generate mechanical displacements of the sub micrometer magnitude in optical components mounted on a table. Such mechanical fluctuations will affect the beam paths and compromise our ability to accurately retrieve the excitation frequency. This problem is referred to as phase stability and will be discussed in detail in Section 3.5.

In the face of these challenges, it was only in the late 1990s that two-dimensional spectroscopy was first demonstrated in the visible (2D-ES) [18] and infrared (2D-IR) [19] spectral regions. Because the phase stability requirement is less stringent in the infrared, the development of 2D spectroscopy in this region flourished faster than in the visible. Also, most applications in the visible require acquisition of maps for many different population time (T) delays, as in a pump-probe experiment, whereas in the infrared acquisition of a few population times can be sufficient to reveal important structural information about proteins, DNA, etc [20]. Thus, the long data acquisition times which follow from the fine scanning between the pump pulses becomes more of a problem in the visible.

Over time 2D-ES has become a much more accessible technique, thanks technical developments by multiple groups [21], but it remains much more challenging than traditional pump-probe experiments, posing the question of whether implementing it is worthwhile given real world constraints. In order to address that question we discuss below the information that can be recovered from 2D-ES experiments.

1.1 What information does two-dimensional spectroscopy recover?

Up to now we have described the development of 2D spectroscopy as a means to overcome the intrinsic ambiguity in terms of excitation frequency in transient absorption experiments when ultrafast time resolution is desired. However, from our pulse sequence discussion and Figure 1.1 we concluded that 2D spectroscopy comprises the most complete third-order nonlinear optical technique. That is because a third-order signal results from three field-matter interactions, and in 2D spectroscopy we use broadband pulses for all of these interactions and experimentally control the time delay between them, finally acquiring the spectrally resolved signal, and that is the maximum level of sophistication

possible. Actually, it can be shown that the signal from other third-order techniques such as photon echo, transient absorption and hole burning are all two-dimensional cuts or integrals of parts of the three-dimensional 2D-ES maps [14]. We also argued that 2D maps are correlation plots between excitation and emission frequencies for a given population time, which means that overlapping peaks in the emission frequency axis can be separated if they have different excitation frequencies. This section gives a few concrete examples of how 2D-ES can be more useful than long established techniques, when applied to real problems.

Line-broadening mechanisms and spectral diffusion

In lineshape theory it is usual to make a distinction between homogeneous and inhomogeneous line broadening, according to the sort of microscopic mechanism that causes it. 2D spectroscopy is the only experimental technique which allows a simultaneous and direct measurement of both contributions [22].

Homogeneous line broadening originates from a statistical loss of coherence that is equally experienced by all molecules in the ensemble, such as the line broadening due to the finite lifetime duration of the excited states, or collisions with the surrounding bath. Inhomogeneous broadening, on the other hand, is related to differences in the local environment for different molecules within the ensemble, causing slightly different frequencies of absorption for each. In linear absorption, inhomogeneous broadening is characterized by Gaussian lineshapes, while a Lorentzian lineshape is an indication of homogeneous broadening [23].

Because both contributions are often present, the distinction between the two mechanisms in linear absorption is not trivial, whereas absorptive 2D spectra (with T close to zero to avoid dynamical effects) possess different lineshapes in each case [24, 25]. In 2D spectroscopy, homogeneous broadening corresponds to a 2D Lorentzian star-shaped signal, with cuts along both the diagonal and anti-diagonal yielding Lorentzian lineshapes of the same width [26]. In the inhomogeneous case, the peak will broaden along the diagonal, but the photon echo nature of the 2D measurement removes the inhomogeneous broadening along the anti-diagonal, resulting in an overall elliptical lineshape stretched along the diagonal [27]. Moreover, the inhomogeneous broadening is given by the diagonal cut of the 2D map, while the homogeneous broadening is given by the anti-diagonal cut,

so both are simultaneously recovered [28].

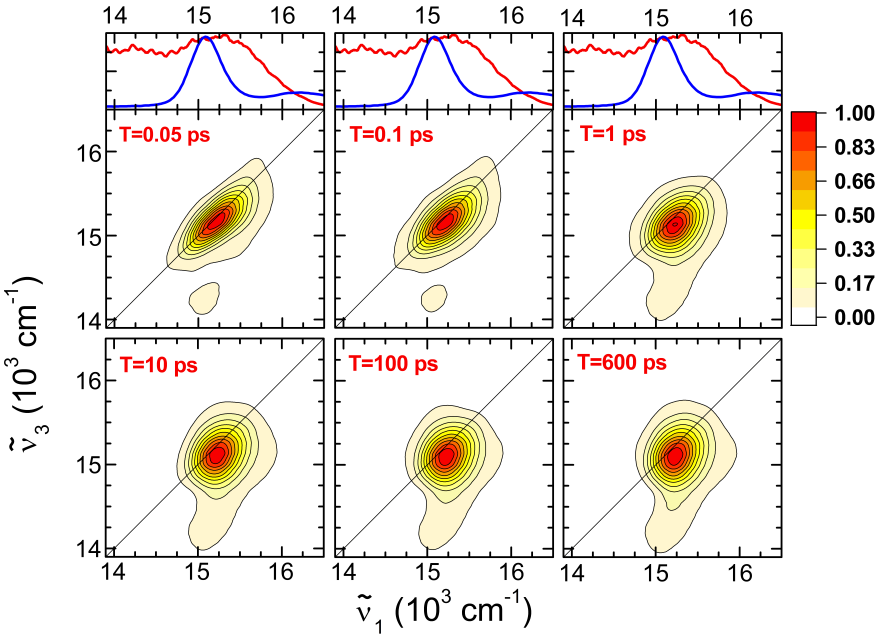

Figure 1.2: Series of absorptive 2D-ES maps of chlorophyll a monomers in acetone. The graphs on top show the linear absorption (blue) and the laser (red) spectra. The map at $T = 0.05$ ps has amplitude stretched along the diagonal, marking an inhomogeneously broadened transition. As T increases, the amplitude gradually becomes rounded, indicating spectral diffusion. Adapted from reference [29] with permission.

Still within the lineshape discussion one might realize that some part of the inhomogeneous line-broadening observed at early times might be lost for longer waiting times, as each molecule in the ensemble has the chance to probe different local environments and lose the initial correlation of transition frequencies [30]. This dynamical phenomenon is called spectral diffusion and its effect on absorptive 2D lineshapes is a gradual change from an elliptical shape at early times to a circular one at later times, as exemplified in Figure 1.2 for Chlorophyll a in acetone [29]. The dynamics of 2D lineshapes has been widely used to study spectral diffusion in the infrared region [27], but has also found applications in the visible [29, 31–33].

Chemical exchange and chemical reactions

2D spectroscopy can also be used to investigate chemical exchange and reactions if different species are associated with an unique spectral signature. In the case of chemical exchange, we are discussing a system of multiple inter-converting species in thermodynamic equilibrium [34]. At early population times a 2D spectrum will have diagonal

peaks corresponding to each individual species, but as interconversion takes place cross-peaks between them form on the exchange rate timescale [35], allowing thermodynamic information to be recovered [36, 37].

Furthermore, if a chemical reaction takes place in the excited state and reactants and products have distinct spectral signatures, time evolution of the cross-peaks between these frequencies will follow the reaction dynamics. For instance, during this PhD I have studied a butadiyne-linked zinc-porphyrin dimer for which all angles between the two porphyrin units are allowed in solution. The lowest electronic transition is a function of this angle, with planar conformers absorbing at low energies, and perpendicular conformers absorbing at high energies. This can be seen in the two peaks in the linear absorption spectra on the top graphs in Figure 1.3 (blue line), where the peak at low wavenumber (13500 cm^{-1}) corresponds to planar and that at high wavenumber (14950 cm^{-1}) corresponds to twisted conformers [38].

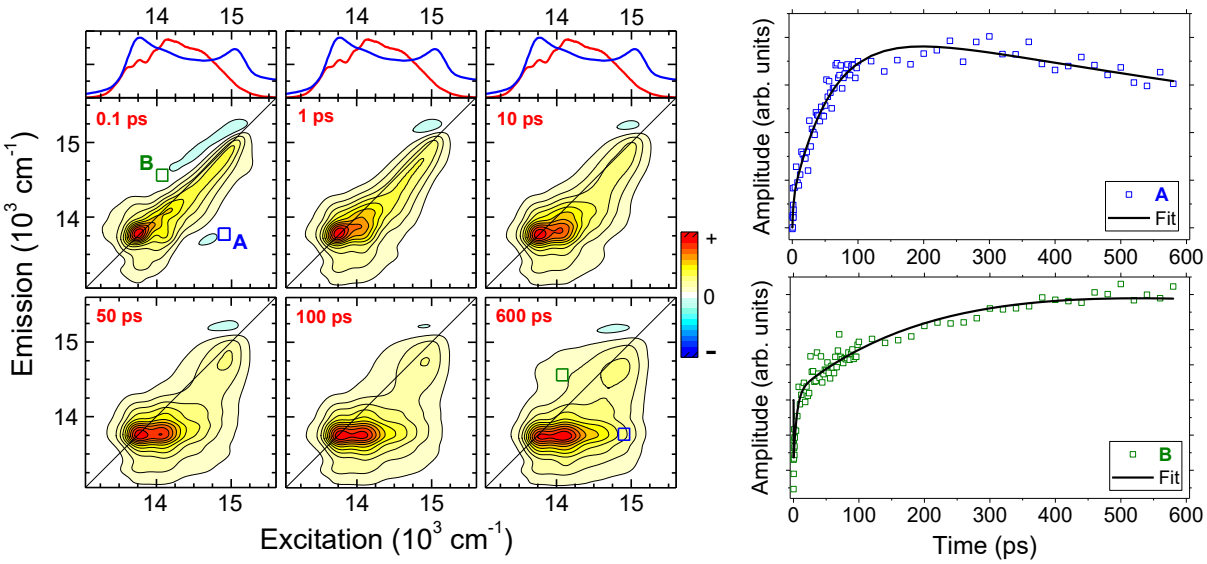

Figure 1.3: Series of absorptive maps for a butadiyne-linked zinc-porphyrin dimer in n-pentane with 1% of pyridine by volume. The top graphs show the linear absorption (blue) and the laser (red) spectra. See text for details. Adapted from reference [39] with permission.

The ground state is therefore an equilibrium between different conformers that absorb light at different energies, which implies in an inhomogeneously broadened transition. Accordingly, the absorptive 2D-ES spectrum at the early time of $T = 0.1$ ps has amplitude stretched along the diagonal, as discussed in the previous Section. However, the electronic excited state of this molecule strongly favors the planar conformers, with the perpendicular ones being more than 6 kT higher in energy [38]. Consequently, once a pop-

ulation of twisted conformers in the excited state is formed (marked by excitation at high wavenumber in the 2D maps), this energy gradient will drive them towards planarity, and this planar conformers will emit at low wavenumber. Indeed, the series of 2D-ES maps in Figure 1.3 shows gradual amplitude growth in the region of high excitation and low emission wavenumbers (below the diagonal), unambiguously resolving the conformational planarization reaction in the excited state. The time trace of point A, shown on the right, shows an increase of amplitude in a 60 ps timescale.

Moreover, in the ground state chemical exchange between both species takes place as well, forming cross peaks both above and below the diagonal. While below the diagonal most of the amplitude is due to the planarization reaction in the excited state, the region above the diagonal corresponds to signal emission by twisted conformers which were planar during the initial excitation, which is only allowed to happen in the ground state (where the energy barrier is within kT). Therefore, the chemical exchange can be observed background-free in this region, and the time trace B on the lower right hand side of Figure 1.3 shows that an increase in amplitude is indeed observed in a timescale of 250 ps. Analyzing the 2D-ES maps with a global fit tool we identified the different timescales of the different processes in this molecule [39].

In this particular case, due to the slow timescales, a series of narrowband pump and broadband probe transient absorption measurements could be used instead of 2D-ES, and we have replicated the study in this way, including solvent viscosity and temperature studies [40]. 2D-ES still has the advantage of simultaneously giving in one experiment the result of all different narrowband pump experiments possible within the spectral range used in the 2D-ES broadband pump. The work on the porphyrin dimer has been left out of this thesis for purposes of cohesion, but the interested reader is referred to references [39, 40]. Other examples of 2D-ES being used to study reaction dynamics can be found in references [41–45].

Energy transfer mechanisms

Another phenomenon that can be probed by 2D-ES in a particularly convenient way is energy transfer between different excited states. Much like chemical exchange and reactions, energy transfer is observed through the dynamics of cross-peaks connecting the states between which energy is flowing. This problem is directly relevant to natural

photosynthetic systems [46–53] as well as synthetic ones [54–56], and has thus attracted much attention. In Figure 1.4c (adapted from reference [52]) signatures of energy transfer in the Fenna-Mathews-Olson complex (the structure and linear absorption of which are shown in Figures 1.4a,b) can be observed as time elapses from 100 fs to 1 ns.

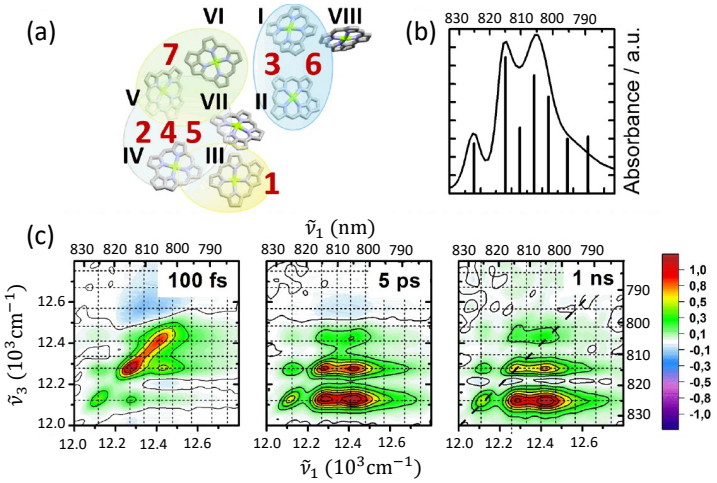

Figure 1.4: Adapted with permission from reference [52]. Copyright 2016 American Chemical Society. **(a)** Arrangement of bacteriochlorophyll a molecules within the FMO units. **(b)** Linear absorption spectrum of the Fenna-Mathews-Olson complex at 77 K with excitonic transitions represented by vertical bars. **(c)** Absorptive 2D-ES spectra with dashed lines indicating excitonic transition energies. All spectra are normalized to their maximum value were recorded in 1:2 aqueous buffer:glycerol mixture at 77 K.

Intramolecular couplings and coherences

The possibility of uncovering electronic couplings was one of the main features that brought 2D-ES to prominence. Electronic couplings are an intrinsic part of many important systems and play essential roles in the processes that make these systems relevant in the first place. In 2D spectroscopy coupled transitions are distinctively marked through the presence of cross-peaks corresponding to their energies already at zero waiting time. For instance, molecular aggregates [54], semiconductor quantum wells [57–60], photosynthetic complexes [46] and polymers [61] all have electronic couplings in their excited state structures. 2D-ES studies helped shed light on their properties, and this type of signals can be used to unravel the energy level structure of complex systems [62]. Such signatures reveal coupling in general, and are observed also from electronic transitions coupled to vibrational modes [63], and intricate analysis can be used to assign the specific nature of coupled states [64].

Besides the presence of cross-peaks at zero waiting time, if two states are coupled,

a coherent superposition between them during the waiting time can be prepared by a broadband laser pulses [27,65,66]. The fact that the system is in a coherent superposition of states instead of in a population during T implies that the corresponding signals will be modulated by the frequency of this coherence. As a consequence, signals that oscillate as a function of T will be found in different positions of the 2D maps. For instance, studies of coherent superposition of states in semiconductor quantum wells in the liquid helium temperature range provided insight into quantum mechanics and many body effects [58–60, 67].

1.2 This thesis

The main theme of this thesis is coherent superpositions in molecular systems, and in this Section we briefly review the state of affairs in late 2013 (the start of this PhD) with regard to molecular and biological systems. We begin by emphasizing two points. First, capturing coherent oscillations as a function of T requires fine experimental scanning of this time interval, which is challenging for a technique that is already scanning the τ interval with interferometric precision. Second, the oscillations are expected to dephase with a lifetime similar to that of the states involved. So, coupled excitonic states are expected to dephase in the sub-100 femtosecond timescale (at room temperature), while vibrationally coupled electronic transitions may give rise to coherences that live for a few picoseconds [66].

Nonetheless, one early study on the Fenna-Mathews-Olson light-harvesting complex at 77 K observed such oscillations in cross-peaks connecting different excitonic levels, and attributed them to electronic coherences between the corresponding excitons [68]. The paper suggested such long lived coherences could be part of the energy transfer mechanism, with the consequence that natural photosynthesis would be at least partially quantum mechanical in its function following light absorption. Although the dephasing time seemed too slow for electronic coherences, evidence was also presented suggesting that the protein scaffold protected the coherence generated from dephasing [69].

Further pioneering studies observed the presence of oscillatory signals at room temperatures. First, Collini *et al.* reported them for conjugated polymers [70] in 2009 and later for light-harvesting proteins of marine algae [71], while Panitchayangkoon *et al.* observed

oscillations in a study of the FMO complex [72] in 2010. As more evidence of oscillatory signals in photosynthetic systems was gathered [73–76], some studies highlighted that while the presence of oscillations meant that some coherent superposition was prepared during T, further evidence was required to differentiate between vibrational and electronic coherences [63, 64, 77–79].

In 2011 Turner *et al.* emphasized the possibility of distinguishing electronic from vibrational coherences using 2D-ES alone, but lacked theoretical support [80]. In the same year, Panitchayangkoon *et al.* argued that the relative phase of the oscillation of different excitation-emission coordinates could be used to establish the underlying nature of a coherence, although conclusive theoretical arguments were not presented [81]. Other studies mentioned the possibility of using relative phases to infer information [77, 82, 83], but no comprehensive experimental study supporting them was presented. In 2012 phase variations of vibrational coherences in a dye were presented, but the data was not explained and remains unpublished [84].

In 2008 Cheng and Fleming demonstrated theoretically that vibrational and electronic coherences result in distinct oscillations if rephasing and non-rephasing signals are considered separately [85]. In 2012, when studies of vibrational coherences in simpler molecular systems where only vibrational coupling was expected, were published only the absorptive [86] or the absolute valued [87] 2D-ES spectra were analyzed. In fact, as late as 2013 an article assigned electronic coherences to oscillations of a single coordinate of absolute valued 2D-ES maps in a molecular dimer [88], although spectra necessary to rule out vibrational coherences were not presented, and the paper was criticized in a comment by Halpin *et al.* [89]. This series of papers indicates the challenges of studying coherences in 2D-ES.

In the meantime, theoretical work by multiple groups described the impact of long-lived coherences on the functionality of light-harvesting systems, deepening interest in the matter [90–94]. Also, other theoretical studies, recognizing the ubiquity of vibrational coupling, began to address the problem of mixed vibrational and electronic coupling (labeled vibronic) [95–99], and Tiwari *et al.* pointed out that from such mixing a different coherence pathway results [100]. In 2014 and 2015 two 2D-ES studies on a molecular dimer were published addressing this issue [101, 102], but the data analysis focused on the oscillation of a single cross-peak, so much information present in the data was not

assessed. Eventually, in 2015 the Hauer group used multiple polarization schemes in 2D-ES to expand a previous study [103] in a spatially oriented artificial light harvester to rigorously demonstrate the presence of the oscillatory pathway forecast by Tiwari *et al.* [104].

Within this context, a comprehensive study of purely vibrational coherences in 2D-ES was lacking, and the main focus of this thesis is to provide such a study. The first critical point necessary is an understanding of the features expected in 2D-ES measurements of vibrationally coupled electronic transitions. In Chapter 2 we provide a review of third-order perturbative theory which establishes the theoretical framework employed throughout the thesis.

A second outstanding requirement in performing a comprehensive study of vibrational coherences in 2D-ES is to build an experimental setup capable of acquiring 2D-ES spectra for many values of T with very good signal-to-noise. In Chapter 3 we describe our 2D-ES setup in detail, discussing the challenging factors of the technique, different approaches to overcome then and our own approach. The data acquisition and data processing steps leading to complex-valued 2D-ES spectra are discussed in detail.

The third outstanding matter is to find a molecular system with all the requirements to test the different aspects of the theory with a minimum of other phenomena that might create overlapping signals. In Chapter 4 we present such system, a zinc-porphyrin monomer, and report basic 2D-ES results on it. We then discuss the challenges in data analysis to study oscillatory signals at multiple coordinates of the 2D-ES maps, eventually establishing a suitable method for our purposes. We discover in our data an interference phenomenon between different overlapping third-order coherence pathways, which we are able to model with standard third-order response function theory.

In Chapter 5 we further refine our analysis by considering the complex-valued 2D-ES maps, observing that the interference observed in Chapter 4 becomes much less pronounced and that the results closely match theoretical predictions. We use this to gain further insight into the interference phenomenon discovered in Chapter 4. We then note that our experiments were performed with laser spectrum profiles that compared to the sample absorption in a way that is often unattainable in practice, leading us to perform new 2D-ES experiments with a blue-shifted spectrum which better represents usual experimental conditions for samples with broader absorption spectra than ours. Surprisingly,

the results with the blue-shifted spectrum drastically deviate from the previous ones, with key coherence signatures being completely suppressed. Further, the observed results match the expected signatures for pure electronic coherences.

We then show that these results are explained through careful consideration of the laser spectrum simultaneously with the contributing pathways. Consequently, under common excitation conditions, electronic and vibrational coherences can show signatures more similar than previously thought. Finally, this newly gained insight about the laser spectrum effect is explored further to propose a 2D-ES experiment that can be performed to complement experiments in which vibrational and electronic coherences result in the same signatures. This newly proposed experiment is sensitive only to vibrational coherences in a background-free region of the excitation-emission plane, and we conclude Chapter 5 demonstrating it. In Chapter 6 we discuss the future work for which this thesis paved the way.

Chapter 2

Theoretical Framework

This thesis is focused on experimental two-dimensional electronic spectroscopy (2D-ES) studies of electronic transitions coupled to vibrational modes. In some respects 2D-ES is the analogue of 2D-NMR in the visible spectral range. The relevant theory behind this technique is large and well developed, ranging from basic quantum mechanics [105, 106], electromagnetism [107] and statistical mechanics [108] to more advanced topics within these fields such as density matrices [109], nonlinear optics [23, 110] and lineshape theory [23, 66], going through to optics [111] and the physics of ultrashort laser pulses [112]. Clearly this Chapter will not be able to include all of this material.

Instead, this Chapter aims to present the aspects of the theory which proved most important for the interpretation of the experiments performed, which were the double-sided Feynman diagrams (also known as Liouville-space pathways) cast within the framework of semi-classical perturbation theory. The experience of the author was that learning about the double-sided Feynman diagrams was made difficult because different sources present them in different contexts, with different notation and degrees of rigor. However, once a clear understanding of the diagrammatic picture is achieved, designing and interpreting 2D-ES experiments becomes much simpler. The objective of this Chapter is to provide future students who will work with 2D-ES with a unified reference that presents the diagrammatic theory that we perceive as the most convenient for 2D-ES.

The approach chosen is the following. In Section 2.1 we present the basics of quantum mechanics using the density matrix formalism, which allows us to include statistical ensembles in the description of a quantum system. We derive the equations for the expectation values of operators in terms of the density matrix only, as well as the Liouville-von

Neumann equation, which describes the time evolution of the density matrix, thus showing that quantum mechanics can be fully discussed using the density matrix to represent the system instead of the wavefunction. During the derivation of the Liouville-von Neumann equation we carefully include the presence of a statistical ensemble for the density matrix, which is tedious but demonstrates that thermodynamic effects can be modeled, via the addition of a phenomenological term in the equation for pure states.

In Section 2.2 we use the results from Section 2.1 to develop a perturbative expansion of the density matrix to approach the general problem of calculating the dynamics of a system under a time dependent Hamiltonian that can be written as a time independent part plus a time dependent perturbation of much smaller energies. In Section 2.3 we proceed to specify that the perturbation to the Hamiltonian consists of a time dependent electric field, and treat the light-matter interaction semi-classically within the point-dipole approximation. As a result, we obtain an expression which compares directly with the non-linear optical polarization, which allows us to write the n^{th}-order response function of a quantum system in terms of the transition dipole moment operators in the interaction picture and the density matrix.

In Section 2.4 we apply this result step by step to obtain the first-order (linear) response function for a two level system. We then proceed to compute the first order polarization which results from the interaction with a laser pulse within the semi-impulsive limit. During this process the basic concepts of the double-sided Feynman diagrams are elucidated one by one, including their relation to the rotating wave approximation. Following this, we use these new insights to discuss the third-order response function and polarization in Section 2.5, with the aim of establishing that the diagrammatic approach is much more convenient than working out all the terms in the equations step by step.

Section 2.6 is then dedicated to making the connection between the third-order double-sided Feynman diagrams and the signals and parameters from 2D-ES, including a discussion of the phase matching of different third-order signals and the essential differences between rephasing and non-rephasing pathways. In Section 2.7 we extend the diagrammatic approach to include systems more complex than a two level system. In particular we analyse the case of an electronic transition coupled to a nuclear vibrational mode, and that of a three level system in which two electronic excited states have similar energies. In this context, we discuss the possibility of observing coherent wavepacket motion in

2D-ES due to the existence of pathways which include a coherent superposition of states during the population time, which is one of the main focuses of this thesis, and we make predictions regarding the the specific signatures of these pathways in 2D-ES experiments. In Chapter 5 we will experimentally explore the possibility of distinguishing between such systems.

Finally, we note that the diagrammatic analysis of the third-order signals intrinsically assumes that all transitions are infinitely sharp, which is never the case in nature. We then follow the approach by Butkus *et al.* [78] to include the effect of broad transitions, especially on coherence pathways, and obtain some predictions about the consequences, which we test experimentally in Chapter 4.

A description of 2D lineshapes is not included in this Chapter, being placed in the Appendix instead. This is because the theory by Butkus *et al.* combined with the diagrammatic theory suffice to understand the core findings of this thesis. Therefore, we considered more convenient to describe traditional 2D lineshape theory directly where it is used, as part of the calculations of 2D-ES spectra for an electronic transition coupled to a vibrational mode.

2.1 Density matrix

In this work we use two-dimensional electronic spectroscopy (2DES) to study different molecular systems. As with any form of spectroscopy, we must choose a theoretical framework to discuss the experiment and its results in a systematic way and, in principle, a few different approaches would be possible. Quantum electrodynamics, treating the electromagnetic radiation quantum-mechanically would clearly be the most rigorous and consistent option [113]. However, most of the research that is done in the field of nonlinear optics is discussed within the semi-classical framework established by Mukamel [23], Boyd [110], Bloembergen [114], Shen [115] and others, which unified the description of most nonlinear optical experiments and basically consists of treating the electromagnetic field with Maxwell's equations and the rest of the system quantum-mechanically via a perturbative approach [23].

Treating the system quantum-mechanically means that its physical state is described

by a wavefunction $|\psi(t)\rangle$, the evolution of which is given by the Schrödinger equation [106]

$$\frac{\partial}{\partial t}|\psi(t)\rangle = -\frac{i}{\hbar}\hat{H}(t)|\psi(t)\rangle . \tag{2.1}$$

To set the stage for the discussion, we first stress that the experimental measurements will always be performed over an ensemble of molecules. The problem which arises is that this description does not allow for the inclusion of thermal distributions: the statistical weighting has already been used to account for the fact that a pure quantum state can be any normalized linear combination of the system's eigenstates. So, to treat the system quantum-mechanically and also add a simultaneous thermodynamical description we use the density matrix formalism [105]. The density matrix of a system described by the wavefunction $|\psi(t)\rangle$ is defined as:

$$\hat{\rho}(t) \equiv |\psi(t)\rangle \langle\psi(t)| . \tag{2.2}$$

If we assume the existence of a complete orthonormal set of eigenstates $|n\rangle$, then we can write the expansion:

$$|\psi(t)\rangle = \sum_n c_n(t)|n\rangle . \tag{2.3}$$

Equivalently, we have for the bra:

$$\langle\psi(t)| = \sum_n c_n^*(t)\langle n| . \tag{2.4}$$

Using the last couple of equations we can write the density matrix as:

$$\hat{\rho}(t) \equiv \sum_{n,m} c_n c_m^*(t)|n\rangle\langle m| . \tag{2.5}$$

Looking at the last equation we recognize that if we want to represent the density operator as a matrix, its elements are given by:

$$\rho_{nm}(t) = c_n(t)c_m^*(t). \tag{2.6}$$

At this point we can define the density matrix of a statistical average of pure quantum states. By 'pure quantum state' we mean any normalized linear combination of eigenkets

from a complete set. So for instance, in a $1/2$ spin system, the states $|+\rangle$, $|-\rangle$ and $1/2\,|+\rangle + \sqrt{3}/2\,|-\rangle$ are all pure states. If we want to conceive a description of a statistical ensemble composed by 30% of the first, 20% of the second and 50% of the third then the wavefunction:

$$\frac{3}{10}\,|+\rangle + \frac{2}{10}\,|-\rangle + \frac{5}{10}\left(\frac{1}{2}\,|+\rangle + \frac{\sqrt{3}}{2}\,|-\rangle\right) = \frac{11}{20}\,|+\rangle + \frac{5\sqrt{3}+4}{20}\,|-\rangle \tag{2.7}$$

is clearly not adequate to describe the system, for it is not normalized and even if we were to normalize it, it would correspond to a pure state. The same occurs with any linear combination we could try. It is the density matrix approach that allows us to write the state of a statistical mixture in an intuitive way, as we will soon prove. So first we define the density operator of a system composed by a statistical average of N different pure states $|\psi^j\rangle$, each corresponding to a probability p^j, in such an intuitive way:

$$\hat{\rho} = \sum_{j=1}^{N} p^j\,|\psi^j\rangle\,\langle\psi^j|\,. \tag{2.8}$$

Our goal now is to derive formulas to correctly compute both the expectation value of any given operator and the time evolution of the system. The expectation value of an operator $\hat{A}$ for a statistical mixture of pure states can be computed by first working out the expectation value for each component of the mixture and then weighting the results by the probability of each pure state. For any given component $|\psi^j\rangle$ of the system, we have:

$$\left\langle \hat{A} \right\rangle^j = \langle\psi^j|\,\hat{A}\,|\psi^j\rangle = \sum_n \sum_m (\rho^j)_{nm} A_{mn}, \tag{2.9}$$

where $(\rho^j)_{nm}$ is the nm element of the density matrix of the pure state j. We also stopped explicitly writing the time dependence for the sake of simplicity: from now on, we will only write it when emphasis is required. The index j is being used as a superscript to emphasize that it arises for a different physical reason than the indexes n and m: the former is related to how many different statistical components form the system, while the latter are related to the different eigenkets that are being used as a basis for the Hilbert space. Looking at the last equation we note that the sum over m is merely the matrix

product of $\hat{\rho}^j$ and $\hat{A}$:

$$\sum_m (\rho^j)_{nm} A_{mn} = (\rho^j A)_{nn}. \tag{2.10}$$

Thus, equation 2.9 becomes:

$$\left\langle \hat{A} \right\rangle^j = \sum_n (\rho^j A)_{nn}. \tag{2.11}$$

But this expectation value accounts only for the system's j component. To have the full expectation value, we must sum over all possible values of j weighting each by its probability p^j:

$$\left\langle \hat{A} \right\rangle = \sum_{j=1}^{N} p^j \sum_n (\rho^j A)_{nn} = \sum_n \left(\left(\sum_{j=1}^{N} p^j \rho^j \right) A \right)_{nn} = \sum_n (\rho A)_{nn} = \mathrm{Tr}(\rho A). \tag{2.12}$$

This last formula allows us to compute the expectation value of any given operator without refering to the wavefunction, but only to the density matrix and the operator itself.

The other requirement for a full quantum description of a system is a treatment of its time evolution. In the wavefunction formalism, this is fulfilled using Schrödinger's equation (2.1). It is necessary to derive an equivalent equation for the density operator. For this, we use the matrix representation of the density operator, whose elements are given by

$$\rho_{nm} = \sum_{j=1}^{N} p^j c_m^{j*} c_n^j, \tag{2.13}$$

as can be seen from equations 2.6 and 2.8. To proceed with the derivation of an equation for the time evolution of the density operator, we note that using the product rule for derivatives, we know the time derivative of the density operator is given by:

$$\frac{\partial \rho_{nm}}{\partial t} = \sum_{j=1}^{N} \frac{\mathrm{d}p^j}{\mathrm{d}t} c_m^{j*} c_n + \sum_{j=1}^{N} p^j \left(c_m^{j*} \frac{\partial c_n^j}{\partial t} + c_n^j \frac{\partial c_m^{j*}}{\partial t} \right). \tag{2.14}$$

As previously mentioned, the first term in this equation arises from the fact that we are dealing with a statistical mixture of pure quantum states. To advance with a rigorous treatment of this term, statistical mechanical considerations would have to be made and phenomena such as dephasing and population relaxation would be described. The usual approach in the nonlinear optics community is to treat this term phenomenologically [27], and this is what we will do here. As far as the latter terms in equation 2.14 are concerned,

we can use Schrödinger's equation to obtain relations for the time derivatives. First, we note that the n^{th} component of the vector created by applying the Hamiltonian operator on the wavefunction is:

$$\left(\hat{H}\left|\psi\right\rangle\right)_n = \sum_m H_{nm} c_m. \tag{2.15}$$

Using this last formula to write the n^{th} component of Schödinger's equation we have:

$$\frac{\partial c_n^j}{\partial t} = -\frac{i}{\hbar}\sum_l H_{nl} c_l^j, \tag{2.16}$$

and for its adjoint:

$$\frac{\partial c_n^{j*}}{\partial t} = \frac{i}{\hbar}\sum_l H_{ln} c_l^{j*}. \tag{2.17}$$

Thus substituting in equation 2.14 we have:

$$\begin{aligned}
\frac{\partial \rho_{nm}}{\partial t} &= \sum_{j=1}^{N} \frac{\mathrm{d}p^j}{\mathrm{d}t} c_m^{j*} c_n - \frac{i}{\hbar}\sum_{j=1}^{N} p^j \sum_l \left(c_m^{j*} H_{nl} c_l^j - c_n^j H_{ln} c_l^{j*}\right) \\
&= \sum_{j=1}^{N} \frac{\mathrm{d}p^j}{\mathrm{d}t} c_m^{j*} c_n - \frac{i}{\hbar}\sum_l \left(H_{nl}\sum_{j=1}^{N} p^j c_m^{j*} c_l^j - H_{ln}\sum_{j=1}^{N} p^j c_n^j c_l^{j*}\right) \\
&= \sum_{j=1}^{N} \frac{\mathrm{d}p^j}{\mathrm{d}t} c_m^{j*} c_n - \frac{i}{\hbar}\sum_l \left(H_{nl}\rho_{lm} - \rho_{nl} H_{ln}\right).
\end{aligned} \tag{2.18}$$

Now we note that the term inside the parenthesis corresponds to the matrix elements of the commutator of $\hat{H}$ with $\hat{\rho}$. Therefore we have:

$$\frac{\partial \rho_{nm}}{\partial t} = \sum_{j=1}^{N} \frac{\mathrm{d}p^j}{\mathrm{d}t} c_m^{j*} c_n - \frac{i}{\hbar}\left[\hat{H}, \hat{\rho}\right]_{nm}, \tag{2.19}$$

which is the quantum mechanical equivalent of the Liouville-von Neumann equation from classical statistical mechanics and describes the time evolution of a quantum system in the density matrix formalism.

As previously mentioned, the first term in the right-hand side of equation 2.19 is related with the thermodynamics of the system, while the quantum mechanical description is given by the second term. In fact, by performing the same derivation we performed assuming a pure quantum system (as opposed to a statistical ensemble) one would arrive at equation 2.19 without the first term in the right-hand side. This can easily be seen by

noting that for a pure system $p = 1$ at all times and thus its derivative equals to zero. So, for a pure system we have:

$$\frac{\partial \hat{\rho}}{\partial t} = -\frac{i}{\hbar}\left[\hat{H}, \hat{\rho}\right]. \tag{2.20}$$

Equation 2.20 is the one most commonly called the Liouville-von Neumann equation and in this work we shall adopt this convention. Equation 2.20 is more useful than equation 2.19 in the sense that a rigorous treatment of the statistics in equation 2.19 is not readily accessible and also quite difficult. There are two reasons why we opted to present the more complicated derivation. The first is consistency: if we argue in favor of the density matrix approach because it allows us to include statistical ensembles, we ought to derive equations for statistical ensembles. The second is that by deriving equation 2.19 we showed that all effects arising from statistical dynamics are contained in the first term (the second is independent of p^j). Thus, even if rigorous treatment of the first term is not accessible, we know that we can model the thermodynamic phenomena via the addition of a phenomenological term to equation 2.20, which is the most commonly adopted approach.

2.2 Semi-classical perturbation theory

Being in possession of the equations 2.12 and 2.19 to compute expectation values and the time dependence of the density matrix respectively, now our focus shifts to describing nonlinear optical experiments with this formalism. For that, we first need to incorporate the light-matter interaction in the Hamiltonian, for which we write:

$$\hat{H}(t) = \hat{H}_0 + \hat{W}(t), \tag{2.21}$$

where we are making the assumption that $\hat{H}_0$ is time independent and that the time dependent interaction with the optical field can be modeled with the addition of $\hat{W}(t)$. Generally speaking the molecular Hamiltonian is very complex, but it is assumed that a set of eigenfunctions exists and is known, satisfying the time independent Schrödinger equation $\hat{H}_0 |n\rangle = E_n |n\rangle$, and all physically meaningful wavefunctions of this system can be written as linear combinations of these eigenfunctions. The essential idea behind perturbation theory is the assumption that the laser intensity is sufficiently weak such that the eigenstates $|n\rangle$ from the molecular Hamiltonian $\hat{H}_0$ can still be used as a basis

to describe the wavefunction even when the laser is on. In other words, the time dependent part of the Hamiltonian $\hat{W}(t)$ can change the coefficients of the eigenstates in the expansion of the wavefunction as a linear combination of $|n\rangle$, but not the eigenstates themselves.

To proceed, it is convenient to define the wavefunction in what is referred to as the interaction picture [27, 105, 106]. So far we have presented the density matrix starting from the Schrödinger picture, where the operators are taken to be time independent and the wavefunction has its dynamics given by Schrödinger's equation. The other option commonly used is the Heisenberg picture, where the wavefunctions are time independent and it is the operators which are a function of time, with the time evolution given by the Heisenberg equation of motion. The Heisenberg picture is more analogous to classical mechanics because the momentum, position and other observables are a function of time – nonetheless both pictures are equivalent [105, 106]. We note that the Hamiltonian in equation 2.21 has one term dependent and one independent of time, and we are concerned with the regime in which the eigenfunctions of the time independent part $\hat{H}_0$ can still be used as a basis. Hence, if the initial condition is:

$$|\psi(0)\rangle = \sum_n c_n(0)\,|n\rangle\,, \tag{2.22}$$

then we would like to obtain $c_n(t)$ such that:

$$|\psi(t)\rangle = \sum_n c_n(t) e^{-\frac{iE_n t}{\hbar}}\,|n\rangle\,, \tag{2.23}$$

for $t > 0$. Equation 2.23 is just the wavefunction in the Schrödinger picture, but by writing the $e^{-\frac{iE_n t}{\hbar}}$ factor explicitly we have effectively decoupled the trivial time evolution under the time independent part of the Hamiltonian – this factor remains present even when $\hat{W}(t)$ is absent, and the time dependence of $c_n(t)$ results solely from the presence of the time dependent part of the Hamiltonian. To see this, we can note that whenever $\hat{W}(t) = 0$, then $c_n(t) = c_n(0)\ \forall\ t$, and hence time independent. Therefore we see that it makes sense to define the wavefunction in the interaction picture through:

$$|\psi(t)\rangle \equiv e^{-\frac{i}{\hbar}\hat{H}_0 t}\,|\psi_I(t)\rangle\,, \tag{2.24}$$

where the exponential of an operator is defined by its Taylor series expansion (see Chapter 2 of reference [23]) and is merely the time evolution operator for a system with Hamiltonian $\hat{H}_0$. It can be shown (see, for example, Section 5.5 of [106]) that $|\psi_I(t)\rangle$ satisfies the equation:

$$\frac{\mathrm{d}}{\mathrm{d}t}|\psi_I(t)\rangle = -\frac{i}{\hbar}\hat{W}_I(t)|\psi_I(t)\rangle\,, \tag{2.25}$$

where we have used the fact that observables (such as $\hat{W}_I(t)$) in the interaction picture are defined as:

$$\hat{W}_I(t) = e^{\frac{i}{\hbar}\hat{H}_0 t}\hat{W}(t)e^{-\frac{i}{\hbar}\hat{H}_0 t}. \tag{2.26}$$

It is clear from equation 2.25 that the evolution of the wavefunction in the interaction picture is determined only by the time-dependent perturbation in the Hamiltonian, whereas from equation 2.26 we can see that observables in the interaction picture have their time evolution determined by $\hat{H}_0$ (and it can be shown that they satisfy a Heisenberg-like equation – see reference [23]). As for the time evolution of the density matrix, it can be shown that it satisfies:

$$\frac{\mathrm{d}}{\mathrm{d}t}\hat{\rho}_I(t) = -\frac{i}{\hbar}\left[\hat{W}_I(t), \hat{\rho}_I(t)\right]. \tag{2.27}$$

We can formally integrate this equation from t_0 to t to obtain:

$$\hat{\rho}_I(t) = \hat{\rho}_I(t_0) - \frac{i}{\hbar}\int_{t_0}^{t}\left[\hat{W}_I(\tau), \hat{\rho}_I(\tau)\right]\mathrm{d}\tau, \tag{2.28}$$

which we can iteratively solve by substituting it into itself, resulting in (see reference [27]):

$$\hat{\rho}_I(t) = \hat{\rho}_I(t_0) + \sum_{n=1}^{\infty}\left(-\frac{i}{\hbar}\right)^n \int_{t_0}^{t}\mathrm{d}\tau_n \int_{t_0}^{\tau_n}\mathrm{d}\tau_{n-1}... \int_{t_0}^{\tau_2}\mathrm{d}\tau_1 \left[\hat{W}_I(\tau_n), \left[\hat{W}_I(\tau_{n-1}), ... \left[\hat{W}_I(\tau_1), \hat{\rho}_I(t_0)\right]...\right]\right]. \tag{2.29}$$

Finally, to return to the Schrödinger picture we see from equation 2.24 that we can apply the time evolution operator of the unperturbed Hamiltonian $\hat{U}_0(t, t_0)$ on the left and

$\hat{U}_0^\dagger(t,t_0)$ on the right of both sides of the previous equation, resulting in [27]:

$$\hat{\rho}(t) = \hat{\rho}^{(0)}(t) + \sum_{n=1}^{\infty}\left(-\frac{i}{\hbar}\right)^n \int_{t_0}^{t} \mathrm{d}\tau_n \int_{t_0}^{\tau_n} \mathrm{d}\tau_{n-1} ... \int_{t_0}^{\tau_2} \mathrm{d}\tau_1 \\ \hat{U}_0(t,t_0)\left[\hat{W}_I(\tau_n), \left[\hat{W}_I(\tau_{n-1}), ... \left[\hat{W}_I(\tau_1), \hat{\rho}_I(t_0)\right] ...\right]\right] \hat{U}_0^\dagger(t,t_0). \quad (2.30)$$

We emphasise that in this equation the perturbation of the Hamiltonian remains in the interaction picture and therefore contains time evolution operators implicit wherever it appears. We have also used the notation $\hat{\rho}^{(0)}(t)$ to represent the density matrix of the system if the perturbation $\hat{W}_I(t)$ is not present, as it is the first term of a series expansion. Applying this notation to all other terms we can write for equation 2.30:

$$\hat{\rho}(t) = \hat{\rho}^{(0)}(t) + \sum_{n=1}^{\infty} \hat{\rho}^{(n)}(t), \quad (2.31)$$

where $\hat{\rho}^{(n)}(t)$ is the n^{th}-order density matrix and it contains n interactions with the perturbation $\hat{W}_I(t)$.

2.3 Connection to non-linear optics

Our discussion so far was quite general in the sense that no assumptions were made about the time-dependent perturbation – the only one was that it is weak enough so that the eigenstates of the non-perturbed Hamiltonian can still be used as a basis set. Now we want to consider the case in which the time dependent perturbation is an electromagnetic wave. If the wavelength is much larger than the size of the quantum system we are describing and if the intensity is sufficiently low (but not to the point that quantum treatment of the field becomes necessary), we can apply the dipole approximation, in which the quantum system is considered a point dipole insofar as its interaction with the electromagnetic radiation is concerned. Then, if the quantum system's electric dipole moment operator is $\hat{\mu}$ and the electric field of the electromagnetic wave is $E(t)$, we have:

$$\hat{W}(t) = -\hat{\mu}E(t), \quad (2.32)$$

where we are ignoring the vectorial character of both the electric field and dipole moment to simplify the equations, as careful treatment of the spatial components would divert the attention from the key concepts we want to discuss. Here we remind the reader that the matrix representation of the dipole operator μ_{ij} is such that the diagonal elements have the contribution of each eigenstate to the system's permanent dipole moment, whereas the off-diagonal elements ($i \neq j$) are related to the light-induced transition from eigenstate i to eigenstate j, with $|\mu_{ij}|^2$ being proportional to the oscillator strength of this transition [27]. Substituting equation 2.32 into equation 2.30 we get:

$$\hat{\rho}(t) = \hat{\rho}^{(0)}(t) - \sum_{n=1}^{\infty} \left(-\frac{i}{\hbar}\right)^n \int_{t_0}^{t} \mathrm{d}\tau_n \int_{t_0}^{\tau_n} \mathrm{d}\tau_{n-1} ... \int_{t_0}^{\tau_2} \mathrm{d}\tau_1 E(\tau_n)E(\tau_{n-1})...E(\tau_1) \\ \hat{U}_0(t,t_0)\left[\hat{\mu}_I(\tau_n), [\hat{\mu}_I(\tau_{n-1}), ... [\hat{\mu}_I(\tau_1), \hat{\rho}_I(t_0)] ...]\right] \hat{U}_0^{\dagger}(t,t_0). \quad (2.33)$$

In this equation we see that the n^{th} term of the expansion contains the electric field n times, which is very similar to the way in which the macroscopic polarization P induced in a material system by an applied electric field is described in non-linear optics [107]:

$$P = \epsilon_0 \left(\chi^{(1)}E + \chi^{(2)}EE + \chi^{(3)}EEE + ...\right). \quad (2.34)$$

In order to make a connection between equations 2.33 and 2.34 we can use the fact that the macroscopic polarization is an observable given by the expectation value of the dipole operator, which we can write by substituting the density matrix from equation 2.33 into equation 2.9, which gives:

$$\begin{aligned} P(t) &= \mathrm{Tr}(\hat{\mu}\hat{\rho}(t)) \\ &= \left\langle \hat{\mu}\hat{\rho}^{(0)}(t) \right\rangle - \sum_{n=1}^{\infty} \left(-\frac{i}{\hbar}\right)^n \int_{t_0}^{t} \mathrm{d}\tau_n \int_{t_0}^{\tau_n} \mathrm{d}\tau_{n-1} ... \int_{t_0}^{\tau_2} \mathrm{d}\tau_1 E(\tau_n)E(\tau_{n-1})...E(\tau_1) \\ &\quad \left\langle \hat{\mu}\hat{U}_0(t,t_0)\left[\hat{\mu}_I(\tau_n), [\hat{\mu}_I(\tau_{n-1}), ... [\hat{\mu}_I(\tau_1), \hat{\rho}_I(t_0)] ...]\right] \hat{U}_0^{\dagger}(t,t_0) \right\rangle. \quad (2.35) \end{aligned}$$

If we assume that $\hat{\rho}_I(t_0)$ is an equilibrium density matrix which does not evolve under $\hat{H}_0$, we can make $t_0 \longrightarrow -\infty$, and note that in this case the interaction picture is the same as the Schrödinger picture, allowing us to drop the 'I' subscript. We can also use the invariance of the trace under cyclic permutations and note that $\hat{U}_0^{\dagger}(t,t_0)\hat{\mu}\hat{U}_0(t,t_0) = \hat{\mu}_I(t)$.

Consequentially we can write the n^{th} term of the sum (which corresponds to the n^{th}-order polarization) as:

$$P^{(n)}(t) = -\left(-\frac{i}{\hbar}\right)^n \int_{-\infty}^{t} \mathrm{d}\tau_n \int_{-\infty}^{\tau_n} \mathrm{d}\tau_{n-1} ... \int_{-\infty}^{\tau_2} \mathrm{d}\tau_1 E(\tau_n)E(\tau_{n-1})...E(\tau_1) \\ \langle \hat{\mu}_I(t) \left[\hat{\mu}_I(\tau_n), \left[\hat{\mu}_I(\tau_{n-1}), ... \left[\hat{\mu}_I(\tau_1), \hat{\rho}(-\infty)\right] ...\right]\right]\rangle \,. \quad (2.36)$$

Further, because we want to consider spectroscopic techniques with multiple pulses (perturbations), it is convenient to make a change of variables from absolute time to time intervals:

$$\begin{aligned} \tau_1 &= 0 \\ t_1 &= \tau_2 - \tau_1 \\ t_2 &= \tau_3 - \tau_2 \\ &\vdots \\ t_n &= t - \tau_n, \end{aligned} \quad (2.37)$$

as these time intervals are quantities we can experimentally control in multiple pulse spectroscopic techniques. To convert equation 2.36 to time intervals we merely substitute each variable, making sure to calculate the integral extremes and the differentials. For instance, for the integral in $\mathrm{d}\tau_n$ we compute the new extremes by noting that when $\tau_n = t$, then $t_n = 0$; similarly, when $\tau_n \longrightarrow -\infty$, then $t_n \longrightarrow +\infty$. Finally, $\mathrm{d}\tau_n = -\mathrm{d}t_n$, because t is not a function of τ_n. We note that the negative sign acquired when converting the differential is canceled by the minus sign which arises from the change between upper and lower integration limits. Applying this procedure to all new variables we obtain:

$$P^{(n)}(t) = -\left(-\frac{i}{\hbar}\right)^n \int_{0}^{\infty} \mathrm{d}t_n \int_{0}^{\infty} \mathrm{d}t_{n-1} ... \int_{0}^{\infty} \mathrm{d}t_1 \\ E(t - t_n)E(t - t_n - t_{n-1})...E(t - t_n - t_{n-1} - ... - t_1) \\ \langle \hat{\mu}_I(t_n + t_{n-1} + ... + t_1) \left[\hat{\mu}_I(t_{n-1} + ... + t_1), ... \left[\hat{\mu}_I(0), \hat{\rho}(-\infty)\right] ...\right]\rangle \,. \quad (2.38)$$

In equation 2.38 it can be seen that the macroscopic n^{th}-order polarization is just a convolution of n electric fields (which are the only terms in the integrals that are a function of t) with the term inside the brackets containing the nested commutators,

which is function of the n time intervals. This is very similar to equation 2.34, which shows the expansion of the polarization in terms of the susceptibilities. Susceptibilities are defined in the frequency domain however, and clearly what we have in equation 2.38 are their time domain equivalents, which are called the response functions $R^{(n)}(t_n, ..., t_1)$. We can thus write:

$$P^{(n)}(t) = \int_0^\infty \mathrm{d}t_n \int_0^\infty \mathrm{d}t_{n-1} ... \int_0^\infty \mathrm{d}t_1 \\ E(t-t_n)E(t-t_n-t_{n-1})...E(t-t_n-t_{n-1}-...-t_1)R^{(n)}(t_n, ..., t_1), \quad (2.39)$$

where:

$$R^{(n)}(t_n, ..., t_1) = \\ -\left(-\frac{i}{\hbar}\right)^n \langle \hat{\mu}_I(t_n + t_{n-1} + ... + t_1) \left[\hat{\mu}_I(t_{n-1} + ... + t_1), ... \left[\hat{\mu}_I(0), \hat{\rho}(-\infty)\right] ...\right]\rangle , \quad (2.40)$$

which is the n^{th}-order nonlinear response function. We note in equations 2.39 and 2.40 that the n^{th}-order macroscopic signal emitted by the system results from n interactions between the density matrix and the fields. The transitions induced by the electric fields are taken into account in the nested commutators, while the temporal information of the electric field used is accounted for through the convolution integrals. We emphasize that the dipole operator outside the nested commutators plays a different role than the others, as t_n is the time interval between the n^{th} perturbation and t, which means that no perturbation takes place during this interval. Thus, $\hat{\mu}(t_n + t_{n-1} + ... + t_1)$ represents the field emission from the non-equilibrium density matrix which resulted from n previous interactions with the perturbation. We also point out that causality requires that $R^{(n)}(t_n, ..., t_1) \neq 0$ only if $t_i \geq 0 \ \forall \ i \in \{1, ..., n\}$, and that all even-order response functions are zero for isotropic media as a result of symmetry [110].

2.4 Linear response function

Having made the connection between the quantum-mechanical description of a system and macroscopic observables from non-linear optics using perturbation theory to write the n^{th}-order response function, we now aim to develop a physical picture for these results.

To that end, we will discuss the first-order (linear) response function in this Section, before proceeding to the non-linear third-order response function, which is the basis for the 2D-ES experiments. To write the linear response we make $n = 1$ in equation 2.40, resulting in:

$$R^{(1)}(t_1) = -\frac{i}{\hbar} \langle \hat{\mu}_I(t_1) \, [\hat{\mu}_I(0), \hat{\rho}(-\infty)] \rangle \, . \tag{2.41}$$

The macroscopic first-order polarization is:

$$P^{(1)}(t) = \int_0^\infty \mathrm{d}t_1 E(t - t_1) R^{(1)}(t_1). \tag{2.42}$$

Going back to equation 2.41 and expanding the commutator, we obtain:

$$R^{(1)}(t_1) = -\frac{i}{\hbar} \left(\langle \hat{\mu}_I(t_1) \hat{\mu}_I(0) \hat{\rho}(-\infty) \rangle - \langle \hat{\mu}_I(t_1) \hat{\rho}(-\infty) \hat{\mu}_I(0) \rangle \right) . \tag{2.43}$$

As an example, we want to calculate the linear response for a two level system interacting with an optical excitation starting from equation 2.43. The eigenstates of $\hat{H}_0$ are $\langle g| = (1 \; 0)$ and $\langle e| = (0 \; 1)$, with eigenvalues E_g and E_e respectively. We also assume the system starts in the ground state, that is:

$$\hat{\rho}(-\infty) = |g\rangle\langle g| = \begin{pmatrix} 1 \\ 0 \end{pmatrix} \begin{pmatrix} 1 & 0 \end{pmatrix} = \begin{pmatrix} 1 & 0 \\ 0 & 0 \end{pmatrix} . \tag{2.44}$$

We also need to write the transition dipole operator in the interaction picture. First, we remember that in the Schrödinger picture:

$$\hat{\mu} = \begin{pmatrix} 0 & \mu_{eg} \\ \mu_{eg} & 0 \end{pmatrix} . \tag{2.45}$$

To convert it to the interaction picture we can use equation 2.26. That requires evaluating $e^{\pm \frac{i}{\hbar} \hat{H}_0 t}$ for the two level system, which we can compute using [23, 106]:

$$e^{\pm \frac{i}{\hbar} \hat{H}_0 t} = |g\rangle \, e^{\pm \frac{i}{\hbar} E_g t} \, \langle g| + |e\rangle \, e^{\pm \frac{i}{\hbar} E_e t} \, \langle e| \, . \tag{2.46}$$

Carrying out these operations, we obtain:

$$\hat{\mu}_I(t) = \begin{pmatrix} 0 & \mu_{eg} e^{-\frac{i}{\hbar}(E_e - E_g)t} \\ \mu_{eg} e^{\frac{i}{\hbar}(E_e - E_g)t} & 0 \end{pmatrix}. \tag{2.47}$$

From this expression we can obtain both $\hat{\mu}_I(t_1)$ and $\hat{\mu}_I(0)$, which we need for equation 2.43. At this point we have the matrix representation of all the operators on the right-hand side of equation 2.43, and we start by computing $\hat{\mu}_I(0)\hat{\rho}(-\infty)$:

$$\hat{\mu}_I(0)\hat{\rho}(-\infty) = \hat{\mu}_I(0)\left|g\right\rangle\left\langle g\right| = \mu_{eg}\left|e\right\rangle\left\langle g\right| = \begin{pmatrix} 0 & 0 \\ \mu_{eg} & 0 \end{pmatrix}. \tag{2.48}$$

We can interpret this term in the following way: at time $t = 0$ the external electric field perturbs the equilibrium density matrix $\hat{\rho}(-\infty)$. We remind the reader that the density matrix is the sum of the unperturbed matrix $\hat{\rho}^{(0)}$ (the zero order term) with the perturbed density matrices which we can compute order by order (see equation 2.31), and now we are in the process of computing the polarization generated by the perturbation up to first order. Equation 2.48 shows that the first order effect of the external electric field is to generate an off-diagonal element in the density matrix (a coherent superposition between excited and ground states). We now can complete the calculation of the first term inside the trace in equation 2.43:

$$\langle \hat{\mu}_I(t_1)\hat{\mu}_I(0)\hat{\rho}(-\infty)\rangle = \langle \hat{\mu}_I(t_1)\mu_{eg}\left|e\right\rangle\left\langle g\right|\rangle = \mathrm{Tr}\begin{pmatrix} \mu_{eg}^2 e^{-\frac{i}{\hbar}(E_e - E_g)t_1} & 0 \\ 0 & 0 \end{pmatrix}, \tag{2.49}$$

where we have used equation 2.47 to obtain $\hat{\mu}_I$. The interaction between the density matrix and the second dipole operator in equation 2.49 includes two parts of the light-matter interaction sequence: the first is the propagation of the non-equilibrium density matrix generated by the external electric field at $t = 0$, which takes place during t_1 – the time interval after the interaction between the system and the perturbation. During this time interval the perturbation no longer interacts with the system, so its propagation in time is determined by the undisturbed Hamiltonian. The second step arises from the transition dipole operator itself, which takes the coherence generated by the perturbation in equation 2.48 back to a ground state population, and corresponds to the signal emission.

In equation 2.43 we need the trace of equation 2.49, which is simply $\mu_{eg}^2 e^{-\frac{i}{\hbar}(E_e-E_g)t_1}$.

To finalize the calculation of the linear response we need to compute the second term inside the brackets in equation 2.43:

$$\begin{aligned}\langle\hat{\mu}_I(t_1)\hat{\rho}(-\infty)\hat{\mu}_I(0)\rangle &= \langle\hat{\rho}(-\infty)\hat{\mu}_I(0)\hat{\mu}_I(t_1)\rangle \\ &= \langle|g\rangle\langle e|\,\mu_{eg}\hat{\mu}_I(t_1)\rangle = \mathrm{Tr}\begin{pmatrix}\mu_{eg}^2 e^{\frac{i}{\hbar}(E_e-E_g)t_1} & 0\\ 0 & 0\end{pmatrix}. \quad (2.50)\end{aligned}$$

At this point, it is interesting to note that the physical interpretation of this term is the same as that from equations 2.48 and 2.49, with the sole difference being that the dipole operators are acting on the bra of the density matrix instead of the ket. To clarify, the term $\langle\hat{\mu}_I(t_1)\hat{\mu}_I(0)\hat{\rho}(-\infty)\rangle$ describes processes in which the density matrix follows the pathway $|g\rangle\langle g| \longrightarrow |e\rangle\langle g| \longrightarrow |g\rangle\langle g|$, while the term $\langle\hat{\rho}(-\infty)\hat{\mu}_I(0)\hat{\mu}_I(t_1)\rangle$ corresponds to the pathway $|g\rangle\langle g| \longrightarrow |g\rangle\langle e| \longrightarrow |g\rangle\langle g|$.

Indeed, both terms in equation 2.43 corresponded to the same process for the following reasoning. Because both the transition dipole moment and the density matrix are Hermitian, $\hat{\rho}(-\infty)\hat{\mu}_I(0) = \hat{\mu}_I^\dagger(0)\hat{\rho}^\dagger(-\infty) = (\hat{\mu}_I(0)\hat{\rho}(-\infty))^\dagger$, so these terms are just the Hermitian adjoint of one another, and thus the underlying physical processes must be the same. The dipole operator representing the signal emission appears inside the trace, so due to the trace's invariance under cyclical permutations it can also be pictured as acting on the bra (see second equality in equation 2.50), and hence the symmetry between the two terms in equation 2.43 is complete.

Finally, to conclude the calculation of the linear response we substitute equations 2.50 and 2.49 into equation 2.43:

$$\begin{aligned}R^{(1)}(t_1) &= -\frac{i}{\hbar}\mathrm{Tr}\begin{pmatrix}\mu_{eg}^2\left[e^{-\frac{i}{\hbar}(E_e-E_g)t_1} - e^{\frac{i}{\hbar}(E_e-E_g)t_1}\right] & 0\\ 0 & 0\end{pmatrix} \\ &= \frac{i}{\hbar}\mu_{eg}^2\left(e^{\frac{i}{\hbar}(E_e-E_g)t_1} - e^{-\frac{i}{\hbar}(E_e-E_g)t_1}\right) = \frac{2i}{\hbar}\mu_{eg}^2\sin(\omega_{eg}t_1), \quad (2.51)\end{aligned}$$

where $\omega_{eg} = \frac{E_e-E_g}{\hbar}$. Here it is worth noticing that the term $e^{-\omega_{eg}t_1}$ corresponds to the interactions with the ket, while the term $e^{\omega_{eg}t_1}$ corresponds to the interactions with the bra. The linear response is a macroscopic property of the system and although it has been defined under the framework of semi-classical perturbation theory, it is independent of the

actual perturbation. It is only when we compute the macroscopic first order polarization through equation 2.42 that we need to take the actual form of the electric field into account, which is done via the convolution with the linear response function. In order to describe the oscillatory external electric field, if ω is the field's angular frequency, we can write:

$$2E'(t)\cos(\omega t) = E'(t)(e^{-i\omega t} + e^{i\omega t}) = E(t) + E^*(t). \tag{2.52}$$

In equation 2.52, $E'(t)$ is the envelope of the electric field, which determines its temporal duration, while the cosine gives the temporal oscillation. We are following the convention that the time-domain electric field is a real function, but it is useful to separate it into its positive and negative complex exponential components. Also, we have defined $E(t) \equiv E'(t)e^{-i\omega t}$ because a forward propagating wave is usually written as $\cos(\mathbf{k}\cdot\mathbf{x} - \omega t)$ (we note that $\cos(-\mathbf{k}\cdot\mathbf{x} + \omega t)$ also propagates in the direction of $\mathbf{x}$; a counter propagating wave has both the spatial and temporal terms with the same sign). Substituting equations 2.52 and 2.51 in equation 2.42 we get:

$$\begin{aligned} P^{(1)}(t) &= \frac{i\mu_{eg}^2}{\hbar}\left[\int_0^\infty E'(t-t_1)e^{-i\omega(t-t_1)}(-e^{-i\omega_{eg}t_1} + e^{i\omega_{eg}t_1})\mathrm{d}t_1 + ... \right. \\ &\qquad \left. ... + \int_0^\infty E'(t-t_1)e^{i\omega(t-t_1)}(-e^{-i\omega_{eg}t_1} + e^{i\omega_{eg}t_1})\mathrm{d}t_1\right] \\ &= \frac{i\mu_{eg}^2}{\hbar}\left[e^{-i\omega t}\int_0^\infty E'(t-t_1)(-e^{-i(\omega_{eg}-\omega)t_1} + e^{i(\omega_{eg}+\omega)t_1})\mathrm{d}t_1 + ... \right. \\ &\qquad \left. ... + e^{i\omega t}\int_0^\infty E'(t-t_1)(-e^{-i(\omega_{eg}+\omega)t_1} + e^{i(\omega_{eg}-\omega)t_1})\mathrm{d}t_1\right]. \end{aligned} \tag{2.53}$$

At resonance, $\omega = \omega_{eg}$ and we have:

$$\begin{aligned} P^{(1)}(t;\omega_{eg}) &= \frac{i\mu_{eg}^2}{\hbar}\left[e^{-i\omega_{eg}t}\int_0^\infty E'(t-t_1)(-1 + e^{2i\omega_{eg}t_1})\mathrm{d}t_1 + ... \right. \\ &\qquad \left. ... + e^{i\omega_{eg}t}\int_0^\infty E'(t-t_1)(-e^{-2i\omega_{eg}t_1} + 1)\mathrm{d}t_1\right]. \end{aligned} \tag{2.54}$$

We note that we wrote equations 2.53 and 2.54 keeping the term corresponding to the interaction with the ket on the left and the one corresponding to the interaction with the bra on the right hand side of the square brackets in all integrals. Also, the first integral corresponds to an interaction between the system and $E(t)$, while the second integral corresponds to an interaction between the system and $E^*(t)$. Looking at the first

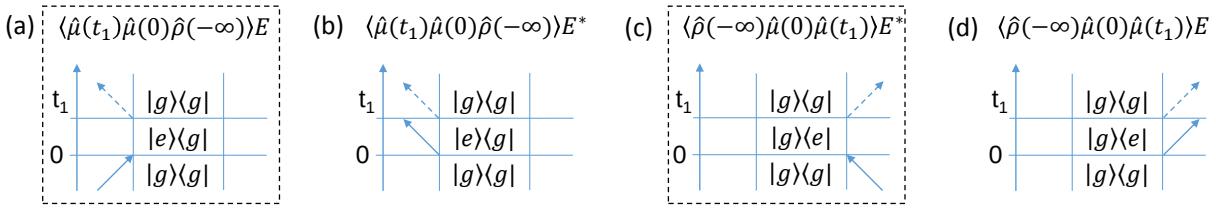

Figure 2.1: Liouville-space pathways for the linear response of a two-level system of ground state $|g\rangle$ and excited state $|e\rangle$. The vertical arrow represents time, and each horizontal line marks a time in which an interaction between the field and the systems takes place. The density matrix at each stage is written between two vertical lines, and the electric field of each interaction is represented by an arrow connecting to the density matrix. Arrows corresponding to $E(t) = E'(t)e^{i(\mathbf{k}\cdot\mathbf{x}-\omega t)}$ point to the right, while those corresponding to $E^*(t)$ point to the left. On the top of each pathway its corresponding term in the first order polarization is written. The pathways that survive the rotating wave approximation are enclosed in dashed boxes.

integral, we note that the the term $e^{2i\omega_{eg}t_1}$ inside the square brackets oscillates rapidly between positive and negative values as a function of t_1, and therefore the contribution from this term to the total integral is much smaller than the contribution from the -1 term. Exactly the same reasoning applies for the second integral, and neglecting the rapidly oscillating terms results in adopting the so called rotating wave approximation. Interestingly, we also see that the first integral results in a $e^{-i\omega_{eg}t}$ polarization and has its amplitude arising from the term of the response function that interacted with the ket, while the second integral results in a $e^{+i\omega_{eg}t}$ polarization and has its amplitude arising from the interaction between $\hat{\mu}(0)$ and the bra.

So far, we have seen that during the calculation of the first order polarization we managed to physically interpret the terms in the equation based on specific field-matter interaction sequences, although doing so is cumbersome with all the explicit equations. There is a more convenient diagrammatic way to account for these interactions, which is very useful when we want to assess which field-matter interaction processes generate signals in spectroscopic experiments, which is shown in Figure 2.1 and described next.

We have seen that from the linear response function alone the processes involved in the first-order interactions of a two level system with an external oscillatory electric field are $|g\rangle\langle g| \longrightarrow |e\rangle\langle g| \longrightarrow |g\rangle\langle g|$, and $|g\rangle\langle g| \longrightarrow |g\rangle\langle e| \longrightarrow |g\rangle\langle g|$. Therefore, if we draw a vertical axis to represent time, we can draw this sequence of density matrices from bottom to top. To finalize representing the macroscopic signals generated from this we just need to incorporate the external field. Regarding this, we have learned that for a density matrix starting in $|g\rangle\langle g|$ an electric field $E(t) = E'(t)e^{i(\mathbf{k}\cdot\mathbf{x}-\omega t)}$ resonant with the

transition interacts with the ket, while its complex-conjugate E^* interacts with the bra, in both cases generating an excitation. Thus, we can represent $E(t)$ with an arrow pointing to the right and $E^*(t)$ with an arrow pointing to the left.

The resulting diagrams shown in Figure 2.1 are called Liouville-space pathways or double-sided Feynman diagrams (and sometimes, informally, Feynman diagrams) and as an example we will interpret the diagram (a) from Figure 2.1. At time $t = 0$ the system, which was initially in equilibrium in the ground state $|g\rangle\langle g|$, interacts with the perturbation $E(t) = E'(t)e^{i(\mathbf{k}\cdot\mathbf{x}-\omega t)}$ which is represented by an arrow pointing to the right and connecting to the density matrix at the $t = 0$ horizontal line. Because the arrow is pointing towards the density matrix, it corresponds to an excitation, and in the case of the two level system we are considering, it has to be from $|g\rangle$ to $|e\rangle$, and it is implicitly assumed that the external field is resonant with this transition. Because we are looking at the first-order polarization, all signals will arise from a single interaction between the system and the external field, and after the specific interaction we described the density matrix is left in a $|e\rangle\langle g|$ coherence. The time interval t_1 is defined as the interval between the first and the second interactions, so because in a first order process there is a single interaction, it extends to infinity in our case. Therefore, the density matrix will emit the signal from the $|e\rangle\langle g|$ coherence it was left in after the interaction, returning to $|g\rangle\langle g|$, and this is represented by a dashed arrow.

The pathway (b) from Figure 2.1 arises from the same term in the response function, but the interaction is with $E^*(t)$, and we showed in equation 2.54 that the term corresponding to this interaction is negligible in the rotating wave approximation, and in the diagrammatic picture we just developed this can be observed in an intuitive way. This double-sided Feynman diagram corresponds to $\langle\hat{\mu}(t_1)\hat{\mu}(0)\hat{\rho}(-\infty)\rangle\, E^*$, so the transition dipole operator at $t = 0$ interacts with the ket of the density matrix (as it is acting on the left). For the two level system, the only possibility would be to take the density matrix to $|e\rangle\langle g|$, but the conjugate field E^* excites bras and de-excites kets. Therefore, because the initial ket is in the ground state and it cannot be de-excited, no signal is expected from this diagram, matching with our discussion following equation 2.54 and the rotating wave approximation.

The pathways (c) and (d) are exactly analogous, with the difference being that they are the adjoints of (a) and (b) respectively, representing exactly the same field-matter

interactions. Therefore, there is no need to represent pathways (b) and (d), as they correspond to negligible macroscopic signals, and we only need to represent one of pathways (a) and (c). The convention is that we only draw double-sided Feynman diagrams for which the signal emission is from the ket, which correspond to transition dipole operator, and the existence of a complex conjugate is implicit, as both reflect the same physical processes.

Now that we have related the equations to the diagrammatic representation of the Liouville-space pathways, we note that the could have written the diagram (a) from Figure 2.1 in a more intuitive way. We start with the following constraints: $\hat{\rho}(-\infty) = |g\rangle\langle g|$, we will consider only resonant pathways (that is, the ones which fulfill the requirements of the rotating wave approximation), the signal emission must happen from the ket and leave the system in a population state, and we are considering first-order processes (that is, a single field will interact with the system). Bearing this in mind, we can draw all combinations of arrows for the electric field and the density matrix which results from that interaction, which will finally lead to all possible pathways. For the first interaction, we see that if it happens from the ket, it requires that it is an arrow pointing to the right (which excites kets or de-excites bras and has a phase of $e^{i(\mathbf{k}\cdot\mathbf{x}-\omega t)}$). Excitation of the ket takes the density matrix to $|e\rangle\langle g|$, and the signal emission happens from this state, accumulating the phase and wavevector from all previous interactions (which is a single one in this case). This is the pathway (a) in Figure 2.1.

Using these rules it is intuitive not to include the pathways (b) and (d), because it makes no sense to de-excite the ground state, so the rotating wave approximation is easily included by only drawing resonant interactions. And finally, we can start drawing a diagram with the first field interacting with the bra and taking it to the excited state, as in (c), but then the signal emission happens from the bra, indicating that this is the complex conjugate of another pathway, and thus needs not be drawn. Although this picture might not seem particularly useful for the linear response, we note that it brought a concise representation of the physical process taking place, from which we know the phase and wavevector of the exciting field and of the emitted signal, and we will see in the next Section and throughout this thesis how this can be very helpful when considering higher order experiments.

2.5 Third-order nonlinear response

Having computed the linear response function for a two level system, we now proceed to consider the non-linear response functions. For isotropic media, all even-ordered response functions vanish due to symmetry requirements (if the orientation of the field is reversed, then the orientation of the induced polarization must also reverse, which does not happen if the field is multiplied an even number of times) [110]. Therefore, the lowest order non-linear response function in the electric dipole approximation for isotropic media is $R^{(3)}$, which we will discuss in this Section. We start by substituting $n = 3$ in equation 2.40:

$$\begin{aligned} R^{(3)}(t_3, t_2, t_1) &= -\left(\frac{-i}{\hbar}\right)^3 \langle \hat{\mu}_I(t_3 + t_2 + t_1) \left[\hat{\mu}_I(t_2 + t_1), [\hat{\mu}_I(t_1), [\hat{\mu}_I(0), \hat{\rho}(-\infty)]]\right]\rangle \\ &= \frac{i}{\hbar^3} \langle \hat{\mu}_{I3} \left[\hat{\mu}_{I2}, [\hat{\mu}_{I1}, [\hat{\mu}_{I0}, \hat{\rho}(-\infty)]]\right]\rangle \,, \end{aligned} \tag{2.55}$$

where in the second line we use a shorthand notation, dropping the temporal variables and displaying the functional dependence of the dipole operators with an index corresponding to the last time interval present. Expanding the commutators and rearranging the terms, we get:

$$\begin{aligned} \langle \hat{\mu}_{I3} \left[\hat{\mu}_{I2}, [\hat{\mu}_{I1}, [\hat{\mu}_{I0}, \hat{\rho}(-\infty)]]\right]\rangle = & \\ & \langle \hat{\mu}_{I3}\hat{\mu}_{I1}\hat{\rho}(-\infty)\hat{\mu}_{I0}\hat{\mu}_{I2}\rangle - \langle \hat{\mu}_{I2}\hat{\mu}_{I0}\hat{\rho}(-\infty)\hat{\mu}_{I1}\hat{\mu}_{I3}\rangle + ... \\ & + \langle \hat{\mu}_{I3}\hat{\mu}_{I2}\hat{\rho}(-\infty)\hat{\mu}_{I0}\hat{\mu}_{I1}\rangle - \langle \hat{\mu}_{I1}\hat{\mu}_{I0}\hat{\rho}(-\infty)\hat{\mu}_{I2}\hat{\mu}_{I3}\rangle + ... \\ & + \langle \hat{\mu}_{I3}\hat{\mu}_{I0}\hat{\rho}(-\infty)\hat{\mu}_{I1}\hat{\mu}_{I2}\rangle - \langle \hat{\mu}_{I2}\hat{\mu}_{I1}\hat{\rho}(-\infty)\hat{\mu}_{I0}\hat{\mu}_{I3}\rangle + ... \\ & + \langle \hat{\mu}_{I3}\hat{\mu}_{I2}\hat{\mu}_{I1}\hat{\mu}_{I0}\hat{\rho}(-\infty)\rangle - \langle \hat{\rho}(-\infty)\hat{\mu}_{I0}\hat{\mu}_{I1}\hat{\mu}_{I2}\hat{\mu}_{I3}\rangle \,, \end{aligned} \tag{2.56}$$

where we have written the term corresponding to signal emission from the ket on the left and those with emission from the bra on the right, so that each line contains one term and its complex conjugate. We have also used the invariance of the trace under cyclical permutations to write $\hat{\mu}_{I3}$ on the right for the terms emitting from the bra. In the literature the different terms of this equation are frequently labeled R_α, but some authors use $\alpha \in \{1, 2, 3, 4\}$ [23, 116], while others use $\alpha \in \{1, 2, 3, 4, 5, 6\}$ [27] – the latter being more commonly used in the infrared community to include three level systems, where excited state absorption pathways are possible. These notations are inconsistent

with each other – for instance, R_3 corresponds to an excited state absorption pathway in the infrared notation and to a ground state bleach pathway in the visible. Moreover, although we have so far ignored spatial components, in reality the third-order response function is a fourth-rank tensor (so that its product with three electric field vectors is a vector), and therefore a representation of its components would require 4 indexes. Hence it is confusing to introduce subscripts to refer to parts of the response function, each of which is still a fourth-ranked tensor, the components of which we are not treating explicitly. Nonetheless, as we saw in Section 2.4, each term in equation 2.56 corresponds to a different pathway, so we will introduce the notation in spite of the above mentioned caveats, hoping this paragraph is enough to clarify potential sources of confusion to the reader. We follow the convention from references [23, 116] to define the terms on the left of equation 2.56 as:

$$R_1 = \langle \hat{\mu}_{I3}\hat{\mu}_{I0}\hat{\rho}(-\infty)\hat{\mu}_{I1}\hat{\mu}_{I2}\rangle \tag{2.57}$$

$$R_2 = \langle \hat{\mu}_{I3}\hat{\mu}_{I1}\hat{\rho}(-\infty)\hat{\mu}_{I0}\hat{\mu}_{I2}\rangle \tag{2.58}$$

$$R_3 = \langle \hat{\mu}_{I3}\hat{\mu}_{I2}\hat{\rho}(-\infty)\hat{\mu}_{I0}\hat{\mu}_{I1}\rangle \tag{2.59}$$

$$R_4 = \langle \hat{\mu}_{I3}\hat{\mu}_{I2}\hat{\mu}_{I1}\hat{\mu}_{I0}\hat{\rho}(-\infty)\rangle\,. \tag{2.60}$$

Similarly to the linear response function described in Section 2.4, each of these terms describes a pathway of the system's density matrix, which we can read from the order in which the transition dipole moments act on the density matrix. However, the effect of the transition dipole operator acting on the density matrix depends only on the eigenstates of the Hamiltonian and allowed transitions, but the spectroscopic signals we measure depend on the electric field actually being resonant to these transitions, which is taken into account in the convolution integral between the response function and the electric field. From equation 2.39, we have for the third-order polarization:

$$P^{(3)}(t) = \int_0^\infty \mathrm{d}t_3 \int_0^\infty \mathrm{d}t_2 \int_0^\infty \mathrm{d}t_1 E(t-t_3)E(t-t_3-t_2)E(t-t_3-t_2-t_1)R^{(3)}(t_3,t_2,t_1). \tag{2.61}$$

If we assume that the total electric field consists of three laser pulses (the case in the 2D-ES experiments we describe throughout this thesis), we can write:

$$E(t) = E_1(t)(e^{i\omega_1 t} + e^{-i\omega_1 t}) + E_2(t)(e^{i\omega_2 t} + e^{-i\omega_2 t}) + E_3(t)(e^{i\omega_3 t} + e^{-i\omega_3 t}), \tag{2.62}$$

and we see that the product between the electric fields and the third-order response function contains $6 \times 6 \times 6 \times 4 = 864$ terms contributing to the third-order macroscopic polarization. Recalling that in Section 2.4 explicitly calculating the linear response function became cumbersome, and only four terms contributed, we conclude that computing the third-order response function on those same general terms is not an option. In practice, we know that we need to consider only the terms that satisfy the rotating wave approximation, and in real life experiments with ultrashort laser pulses we shall see that the well-defined time order between them and their phase matching conditions will determine which contributions are ultimately relevant.

If the external electric field consists of three laser pulses in the semi-impulsive limit, we can write:

$$E_1(t) = |E_1|\delta(t)\left(e^{i(\mathbf{k_1}\cdot\mathbf{x}-\omega_1 t+\phi_1)} + e^{i(-\mathbf{k_1}\cdot\mathbf{x}+\omega_1 t-\phi_1)}\right) \tag{2.63}$$

$$E_2(t) = |E_2|\delta(t-t_1)\left(e^{i(\mathbf{k_2}\cdot\mathbf{x}-\omega_2 t+\phi_2)} + e^{i(-\mathbf{k_2}\cdot\mathbf{x}+\omega_2 t-\phi_2)}\right) \tag{2.64}$$

$$E_3(t) = |E_3|\delta(t-t_1-t_2)\left(e^{i(\mathbf{k_3}\cdot\mathbf{x}-\omega_3 t+\phi_3)} + e^{i(-\mathbf{k_3}\cdot\mathbf{x}+\omega_3 t-\phi_3)}\right). \tag{2.65}$$

In this case we have a definite time order (E_1 is followed by E_2 and then E_3) so we know that the first interaction $\hat{\mu}_I(0)$ happened with E_1, the second ($\hat{\mu}_I(t_1)$) with E_2, and the third ($\hat{\mu}_I(t_2-t_1)$) with E_3. Therefore, time ordering generates a drop from the $6 \times 6 \times 6 \times 4 = 864$ terms to $2 \times 2 \times 2 \times 4 = 32$ in equation 2.61.

The rotating wave approximation further reduces the number of terms. To see how that is, we consider R_2, for example, for which we see in equation 2.58 that $\hat{\mu}_{I0}$ acts on the equilibrium density matrix from the right (that is, acts on the bra). We take $\hat{\rho}(-\infty) = |g\rangle\langle g|$, so the only resonant option is for the transition dipole operator to excite the bra, corresponding to an arrow pointing to the left and leading to $|g\rangle\langle e|$. We saw in Section 2.4 that it is the conjugate field that excites the bra, so in this step we are intuitively including the term $e^{i(-\mathbf{k_1}\cdot\mathbf{x}+\omega_1 t-\phi_1)}$ from equation 2.63 and neglecting its conjugate.

We proceed to the next transition dipole operator $\hat{\mu}_{I1}$, which acts from the left in equation 2.58 (therefore, on the ket), interacts with E_2 and finds the system in $|g\rangle\langle e|$. Thus, the only resonant option is that the ket is excited and the resulting density matrix is $|e\rangle\langle e|$, an excited state population. We saw in Section 2.4 that the non-conjugated

field excites the ket, so we are selecting for the second pulse the term $e^{i(\mathbf{k_2}\cdot\mathbf{x}-\omega_2 t+\phi_2)}$ from equation 2.64.

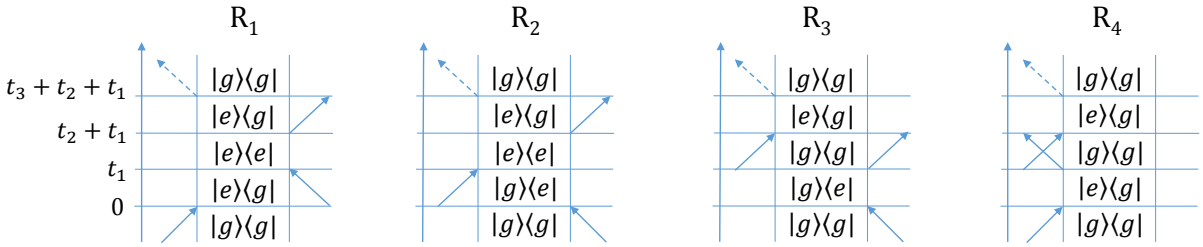

Figure 2.2: Liouville-space pathways that survive the rotating wave approximation and generate significant third-order polarization.

Finally, the third time interval starts when $\hat{\mu}_{I2}$ interacts with the bra, as it is acting on the right in equation 2.58. The bra is in the excited state, and because we are considering a two level system, the only resonant option is to de-excite it back to the ground state taking the density matrix to $|e\rangle\langle g|$. Once more, from Section 2.4 we know that it is the non-conjugated field that de-excites the bra, so we have selected the term $e^{i(\mathbf{k_3}\cdot\mathbf{x}-\omega_3 t+\phi_3)}$ from equation 2.65. At this point, all three interactions with the external field have taken place and the density matrix was left in a state for which the signal emission happens from the ket, returning the system to a $|g\rangle\langle g|$ ground state population. Hence, through this process we have seen that one single Liouville-space pathway results from the term R_2 in the third-order nonlinear response function (equation 2.58), and its diagrammatic representation can be seen in Figure 2.2. If we apply this same systematic procedure to the other terms in the response function (equations 2.57, 2.59 and 2.60), we find that for each a single resonant pathway survives, and they are all shown in Figure 2.2.

Having established the Liouville-space pathways that generate significant third-order polarization contributions, we will now move on to present the principles of two-dimensional spectroscopy, which is the focus of this thesis, and later return to the Liouville-space pathways in this specific context.

2.6 Principles of 2D spectroscopy

In this section we shall briefly present the basic theory of 2D spectroscopy, which has already been detailed in the literature [14, 116, 117]. As briefly discussed in Chapter 1, 2D-ES is a third-order nonlinear optical technique that employs three distinct pulses in

order to generate a correlation map between excitation and detection frequencies, in much the same way as multidimensional nuclear magnetic resonance techniques. In the context of the third-order response function theory laid out in Section 2.5, this means that within the limits of experimental pulse duration the time intervals are well defined and each field-matter interaction happens with a different pulse.

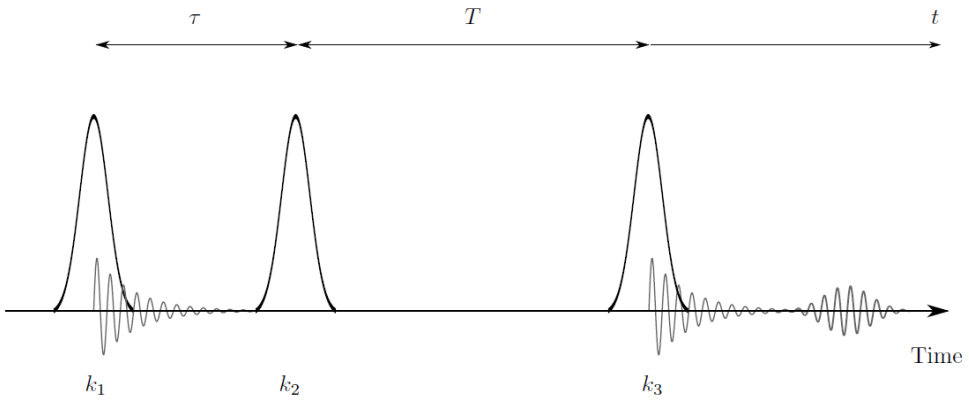

Figure 2.3: Pulse sequence of a two-dimensional spectroscopy experiment in the semi-impulsive limit. The time interval between the first and second pulses is labeled τ and called the coherence time, while the one between the second and third pulses is labelled T and referred to as the population time. The time interval following the third pulse corresponds to the signal emission, thus being called emission or detection time, and is represented by t.

The pulse sequence employed in a bidimensional measurement is shown in Figure 2.3, which we will now discuss in terms of the four double-sided Feynman diagrams from Figure 2.2. As usual, the representation in Figure 2.3 has time running from left to right, so that the more to the left a pulse is drawn the earliest it arrived at the sample. In all of them, the system starts from an equilibrium density matrix in the ground state $|g\rangle\langle g|$, and the interaction with the first pulse takes the system to a coherence, marking the beginning of the first experimental time interval. We name the time interval between the first and second pulses the coherence time (traditionally labeled τ instead of t_1) because the system is in a coherence (either $|e\rangle\langle g|$ or $|g\rangle\langle e|$). The fact that the system is in a coherence during τ implies that a macroscopic polarization is created as the system is propagated under the undisturbed Hamiltonian, and it is called the free induction decay.

The arrival of the second pulse now brings the density matrix to a population (either $|e\rangle\langle e|$ or $|g\rangle\langle g|$), so the time evolution during this period corresponds to the population relaxation, which is usually modeled with one or more exponential decays. Formally speaking under this level of treatment both $|g\rangle\langle g|$ and $|e\rangle\langle e|$ are stationary states and

the theory predicts no relaxation, so we will ignore it for now. The system will remain in the population state until the arrival of the third pulse disturbs it again, so the time interval between the second and third pulses is called the population time, and is labelled T, instead of $t_1 + t_2$. Finally, for all four pathways in Figure 2.2, the third pulse takes the system back to a coherence state $|e\rangle\langle g|$, from where the density matrix will once again propagate under the unperturbed Hamiltonian.

The third-order nonlinear response of a system is a complex-valued function of three time variables and contains all the information a third-order technique can recover from the system, and the ultimate aim of two-dimensional spectroscopy is to measure it experimentally. That requires scanning all time variables τ, T and t, although in practice it is often more convenient to use a prism to disperse the emitted signal and detect the frequency resolved signal in terms of the detection wavenumber $\tilde{\nu}_3$. As for the coherence time, it is usually scanned by experimentally controlling the temporal delay between the first two pulses, which must be done with phase stability within a fraction of the cycle of the excitation pulses, which is the main challenge in the experimental development of 2D-ES.

The main advantage of achieving this stability is that the data acquired for each T as a function of τ and $\tilde{\nu}_3$ can be Fourier transformed over the first time period, resulting in a correlation map between $\tilde{\nu}_1$ and $\tilde{\nu}_3$. Here $\tilde{\nu}_1$ is the wavenumber corresponding to the coherence induced in the system during the first time interval, that is the wavenumber of the first arrow in the double-sided Feynman diagrams, which is the excitation wavenumber. This is of crucial importance, because in traditional one dimensional broadband transient absorption techniques there is complete ambiguity about the excitation frequency of any given signal measured at $\tilde{\nu}_3$, as explained in Chapter 1. In terms of double-sided Feynman diagrams, the same four diagrams from Figure 2.2 all contribute to the signal (for a two level system), but there is no well defined time-ordering between the first and second interactions, which happen with the same pump pulse. Therefore, the ability to recover the excitation wavenumber in 2D-ES represents invaluable progress over the typical transient absorption experiments.

Phase matching

The technical details regarding the experimental recovery of the complex-valued third-order polarization will be laid out in Chapter 3, but the discussion from the previous paragraph raises a question we have not yet considered: in which direction will the third order polarization signal be emitted? The answer depends on the spatial geometry of the excitation pulses, and it can be read from the double-sided Feynman diagrams. Initially we notice that from equation 2.61 we have that the electric fields are all multiplied together, so considering they are given by equations 2.63, 2.64 and 2.65 in the semi-impulsive limit, we can see that the overall phase acquired by the third-order polarization will be $e^{i((\pm\mathbf{k}_1\pm\mathbf{k}_2\pm\mathbf{k}_3)\cdot\mathbf{x}\pm\phi_1\pm\phi_2\pm\phi_3)}$. Therefore, all contributions from equation 2.61 will have a specific propagation direction among the $\pm\mathbf{k}_1 \pm \mathbf{k}_2 \pm \mathbf{k}_3$ possibilities.

To know the direction corresponding to a given Liouville-space pathway all we need to consider is whether the conjugated or non-conjugated field contributed to each interaction, remembering that the conjugated field is $E_j^*(t) = |E_j|e^{-i\mathbf{k}\cdot\mathbf{x}+i\omega t-i\phi}$ and points to the left in the diagrammatic representation. Thus, looking at Figure 2.2 we see that the diagrams for R_1 and R_4 have the second interaction with the conjugated field, while the other two take place with the non-conjugated field, meaning that for them $\mathbf{k}_{sig} = \mathbf{k}_1 - \mathbf{k}_2 + \mathbf{k}_3$. On the other hand, the terms R_2 and R_3 interact first with the conjugated field and then twice with the non-conjugated field, so the propagation direction of their signal is $\mathbf{k}_{sig} = -\mathbf{k}_1 + \mathbf{k}_2 + \mathbf{k}_3$.

In practice, a 2D-ES experiment can be designed with many different incoming pulse geometries, and care must be taken regarding which third order signals will reach the detector in each case. One of the common geometries is the pump-probe geometry, in which beams 1 and 2 are collinear, while beam 3 has an angle, which has the advantage that $\mathbf{k}_1 = \mathbf{k}_2$, from which it follows that the signal propagates in the $\mathbf{k}_3$ direction for all pathways from Figure 2.2. Another common geometry is the boxcar geometry, in which the beams focus on the sample starting from different corners of a square, which is the geometry we use, and the phase matching will be described in detail in Chapter 3.

Rephasing and non-rephasing

For now we have noticed that the diagrams R_2 and R_3 always share a common propagation direction, which is also true for diagrams R_1 and R_4, which raises the question of

whether something else differs between them. In order to address this question, we will follow the density matrix along the pathways R_1 and R_3 writing the response at each step. Starting with R_1, we refer to equation A.3 and step by step apply the transition dipole moment operators, propagate the density matrix and finally take the trace. We note that there is no propagation during T because the density matrix is in a population during this time interval. We have:

$$\begin{pmatrix} 1 & 0 \\ 0 & 0 \end{pmatrix} \xrightarrow{i\hat{\mu}_{I0}\hat{\rho}} \begin{pmatrix} 0 & 0 \\ i & 0 \end{pmatrix} \xrightarrow{\tau} \begin{pmatrix} 0 & 0 \\ ie^{-i\omega_{eg}\tau} & 0 \end{pmatrix} \xrightarrow{i\hat{\mu}_{I0}\hat{\rho}\hat{\mu}_{I1}} \begin{pmatrix} 0 & 0 \\ 0 & ie^{-i\omega_{eg}\tau} \end{pmatrix} \xrightarrow{i\hat{\mu}_{I0}\hat{\rho}\hat{\mu}_{I1}\hat{\mu}_{I2}}$$

$$\begin{pmatrix} 0 & 0 \\ ie^{-i\omega_{eg}\tau} & 0 \end{pmatrix} \xrightarrow{t} \begin{pmatrix} 0 & 0 \\ ie^{-i\omega_{eg}(t+\tau)} & 0 \end{pmatrix} \xrightarrow{i\langle\hat{\mu}_{I3}\hat{\mu}_{I0}\hat{\rho}\hat{\mu}_{I1}\hat{\mu}_{I2}\rangle} ie^{-i\omega_{eg}(t+\tau)}. \quad (2.66)$$

Conversely, for R_3 we have:

$$\begin{pmatrix} 1 & 0 \\ 0 & 0 \end{pmatrix} \xrightarrow{i\hat{\rho}\hat{\mu}_{I0}} \begin{pmatrix} 0 & i \\ 0 & 0 \end{pmatrix} \xrightarrow{\tau} \begin{pmatrix} 0 & ie^{+i\omega_{eg}\tau} \\ 0 & 0 \end{pmatrix} \xrightarrow{i\hat{\mu}_{I1}\hat{\rho}\hat{\mu}_{I0}} \begin{pmatrix} 0 & 0 \\ 0 & ie^{+i\omega_{eg}\tau} \end{pmatrix} \xrightarrow{i\hat{\mu}_{I1}\hat{\rho}\hat{\mu}_{I0}\hat{\mu}_{I2}}$$

$$\begin{pmatrix} 0 & 0 \\ ie^{+i\omega_{eg}\tau} & 0 \end{pmatrix} \xrightarrow{t} \begin{pmatrix} 0 & 0 \\ ie^{-i\omega_{eg}(t-\tau)} & 0 \end{pmatrix} \xrightarrow{i\langle\hat{\mu}_{I3}\hat{\mu}_{I1}\hat{\rho}\hat{\mu}_{I0}\hat{\mu}_{I2}\rangle} ie^{-i\omega_{eg}(t-\tau)}. \quad (2.67)$$

Comparing equations 2.66 and 2.67 we note that the former has a functional dependence on $t+\tau$, while the latter has a functional dependence on $t-\tau$. This is a consequence of the fact that in equation 2.66 the initial excitation happens on the ket, and thus the time propagation during the following time interval is $e^{-i\omega_{eg}\tau}$, while in equation 2.67 the initial excitation is on the bra, for which the time propagation is $e^{+i\omega_{eg}\tau}$. To assess the consequences of this, let us consider that the ensemble of molecules generating the macroscopic signal presents inhomogeneous broadening, i.e., different molecules in the ensemble absorb light at slightly different wavelengths, reflecting the fact that they are experiencing different environments. If the distribution of transition frequencies due to the inhomogeneous broadening can be described by a Gaussian, then the response functions for the broadened system will be the convolution of this Gaussian with the results from equations

2.66 and 2.67:

$$R_1 \longrightarrow i \int \mathrm{d}\omega_{eg} e^{\frac{-(\omega_{eg}-\overline{\omega_{eg}})^2}{2\Delta\omega^2}} e^{-i\omega_{eg}(t+\tau)} \tag{2.68}$$

$$R_3 \longrightarrow i \int \mathrm{d}\omega_{eg} e^{\frac{-(\omega_{eg}-\overline{\omega_{eg}})^2}{2\Delta\omega^2}} e^{-i\omega_{eg}(t-\tau)}, \tag{2.69}$$

where $\Delta\omega^2$ is the width of the Gaussian distribution of frequencies and $\overline{\omega_{eg}}$ is its average. Using the convolution theorem, we obtain:

$$R_1 \propto i e^{-i\omega_{eg}(t+\tau)} e^{\frac{-\Delta\omega^2(t+\tau)^2}{2}} \tag{2.70}$$

$$R_3 \propto i e^{-i\omega_{eg}(t-\tau)} e^{\frac{-\Delta\omega^2(t-\tau)^2}{2}}. \tag{2.71}$$

Here we see that a major difference arises due to the presence of the second exponential, the argument of which is real. In equation 2.70, as t increases from zero to infinity, the second exponential monotonically decreases towards zero. However, in equation 2.71, the argument of the second exponential starts from $\frac{-\Delta\omega^2\tau^2}{2}$ at $t = 0$, and increases to 0 at $t = \tau$, where it has a maximum, and then decreases as $t > \tau$. Therefore, the macroscopic polarization has a maximum for $t = \tau$, which is known as a photon echo.

The interpretation of the photon echo is that the first pulse creates a macroscopic alignment of many individual dipoles forming a $|g\rangle\langle e|$ coherence. These individual dipoles are experiencing different environments, so they rapidly dephase following the initial pulse. The third pulse then interacts with the system to create a $|e\rangle\langle g|$ coherence, which is the adjoint of the one present in the first time interval, and therefore has the opposite temporal evolution to the first. This means that the dephasing of the $|e\rangle\langle g|$ coherence during t exactly cancels that of the $|g\rangle\langle e|$ during τ, such that at $t = \tau$ the individual dipoles are in phase again, a process which is called rephasing. Therefore, the pathways R_2 and R_3 are called rephasing pathways, while the pathways R_1 and R_4 are called non-rephasing pathways, as the signal they generate is analogous to a free-induction decay. In experimental implementations of 2D-ES they can be measured separately either by using the different phase matching or the different phase between them, which we will discuss in Chapter 3. For now, we simply emphasize that complex-valued rephasing and non-rephasing signals can be experimentally recovered separately.

Up to this point we have laid out the basics of semi-classical perturbation theory

using the density matrix, developed a diagrammatic approach to systematically obtain the pathways that generate significant signals in non-linear experiments of any order, presented the concept of two-dimensional spectroscopy along with some of its advantages and discussed the difference between rephasing and non-rephasing signals in the third-order case. The focus of this thesis is on 2D-ES of coupled electronic transitions, and we study the case of vibrational coupling in detail. Therefore, the remainder of this Chapter is devoted to discuss 2D-ES of coupled systems using the formalism of the double-sided Feynman diagrams as described above.

2.7 Coupled systems

In molecular systems it is usually the case that electronic transitions are coupled to nuclear vibrational modes. As a result, the energy-level structure of a two level system becomes more complex, as a ladder of vibrationally excited states is coupled to both the ground and electronic excited states, which are represented in what is known as the displaced harmonic oscillator model. In that model, the electronic excited state is pictured as being displaced relative to the ground state as a function of the vibrational coordinate q, and optical excitation is considered to take place preserving the value of q (see Figure 2.4a). The presence of these extra energy levels adds many more third-order pathways than the four found in a two level system, and in this section we will describe them. In Figure 2.4b we also show the energy level structure of a three level system where the two electronic excited states have similar energies, which is similar to what arises when excitonic coupling is present between two chromophores [118], a case of wide interest [46, 95, 119]. In this Section we will extend the third-order Liouville-space pathways from Section 2.5 to both cases in Figure 2.4 and discuss the implications in 2D-ES measurements.

2.7.1 Vibrational coupling

In this Section we will use the Liouville-space pathway approach to discuss the most important third-order signals which arise from broadband laser excitation of an energy level structure such as that from Figure 2.4a. The energy shift between any two different neighbouring sub-levels is equal in energy if the nuclear potential is harmonic, and we

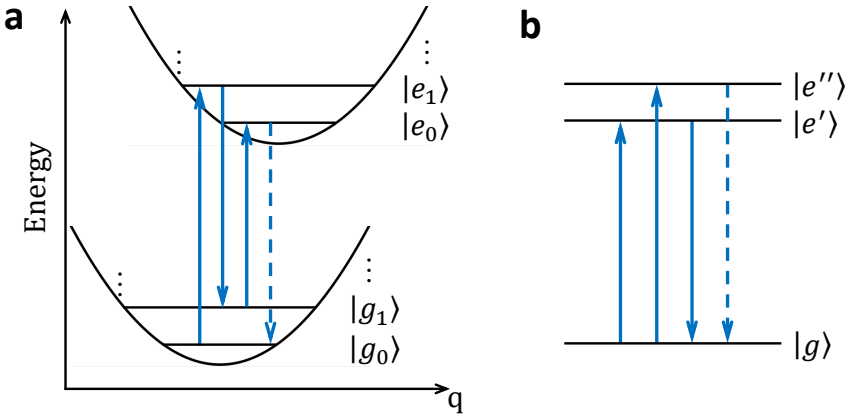

Figure 2.4: **(a)** Scheme of the energy levels for an electronic transition coupled to a vibrational mode, along with one possible third-order pathway. **(b)** Energy level scheme for a three level system, with two electronic excited states of similar energy, along with one possible third-order pathway. In this representation of the pathways time runs from left to right, the signal emission is represented by a dashed arrow and we are not including notation to indicate whether each interaction happens with the bra or the ket.

will assume that electronic transitions between any two sub-levels are allowed. For different molecules different transitions between sublevels are favored, but for the examples studied in this thesis 0-1 transitions dominate. If we assume that the vibration's energy is significantly larger than k_BT, then most of the population will start from the ground state $|g_0\rangle\langle g_0|$. Thus, it is reasonable to draw the double-sided Feynman diagrams for a 4-level system (consisting of the two lowest sub-levels in the ground state and the two lowest in the electronic excited state) and use them as a guide regarding what features can be expected in 2D signals from this system.

In order to draw all resonant double-sided Feynman diagrams, we first notice that the starting point still is equation 2.56, with the main difference being that the transition dipole operators have more transitions available in the four level displaced harmonic oscillator system than in the two level system from Section 2.5. In this problem of higher dimensionality, it is more convenient to write the double-sided Feynman diagrams than to carry out all operations such as in Section 2.4 with 4×4 matrices. We will assume that the laser spectrum is such that transitions between the ground and electronic excited states are covered among any pair of the lowest sublevels of each, but that the transition between different sublevels on the same electronic state is not covered. We consider that the system starts in the ground state $|g_0\rangle\langle g_0|$ and follow the transition dipole operators in each term of equation 2.56, considering all possible resonant transitions. It helps to realize that all resonant transitions are still going to be between the two electronic states,

so effectively all new pathways are going to be similar to the ones from Figure 2.2, but involving different combinations of sublevels.

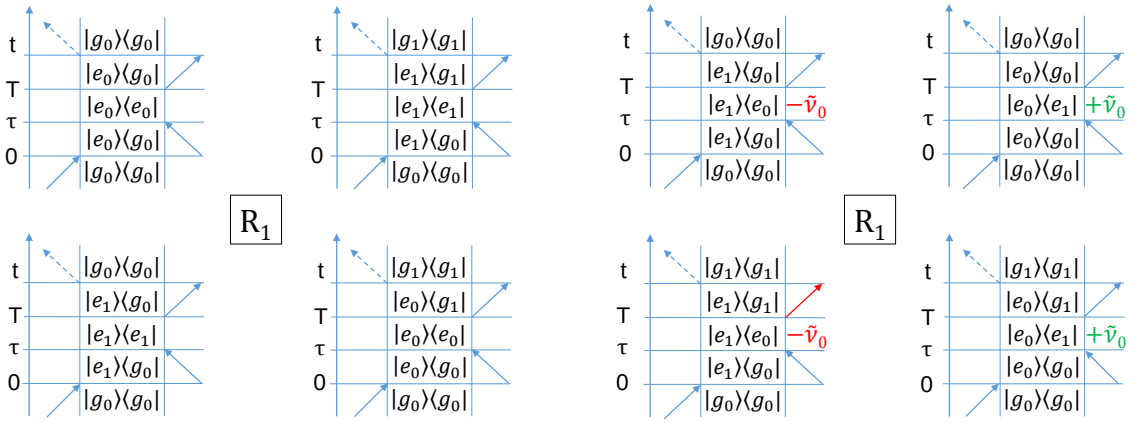

Figure 2.5: Non-rephasing R_1 pathways for the displaced harmonic oscillator model. During T the four pathways on the left are in an excited electronic state population, while the four pathways on the right are in a vibrational coherence in the electronic excited state.

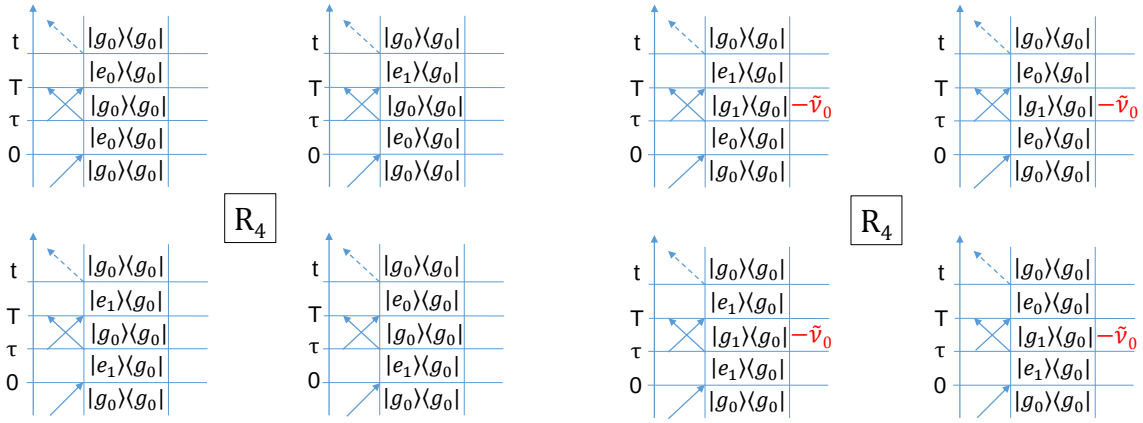

Figure 2.6: Non-rephasing R_4 pathways for the displaced harmonic oscillator model. During T the four pathways on the left are in an electronic ground state population, while the four pathways on the right are in a vibrational coherence in the ground state.

We can count how many pathways are expected considering R_1 from Figure 2.2, for instance. We note that now the first interaction can correspond to an excitation of the ket to either $|e_0\rangle$ or to $|e_1\rangle$, so there are two possibilities. The second interaction happens with the bra and can take it either to $\langle e_0|$ or to $\langle e_1|$, resulting in two more possibilities, while the third interaction will then de-excite the bra to either $\langle g_0|$ or to $\langle g_1|$ regardless of the state in which it is in, giving another pair of possibilities. Finally the signal emission must happen so that the final density matrix is a population, so only one option exists. Therefore, we have $2^3 = 8$ pathways corresponding to R_1. This logic applies in the same way for R_2, R_3 and R_4, so in total we have $2^3 \times 4 = 32$ pathways. By systematically accounting for all combinations we can draw all pathways, and the results are shown for

the non-rephasing case in Figures 2.5 (R_1) and 2.6 (R_4), and for the rephasing case in Figures 2.7 (R_2) and 2.8 (R_3).

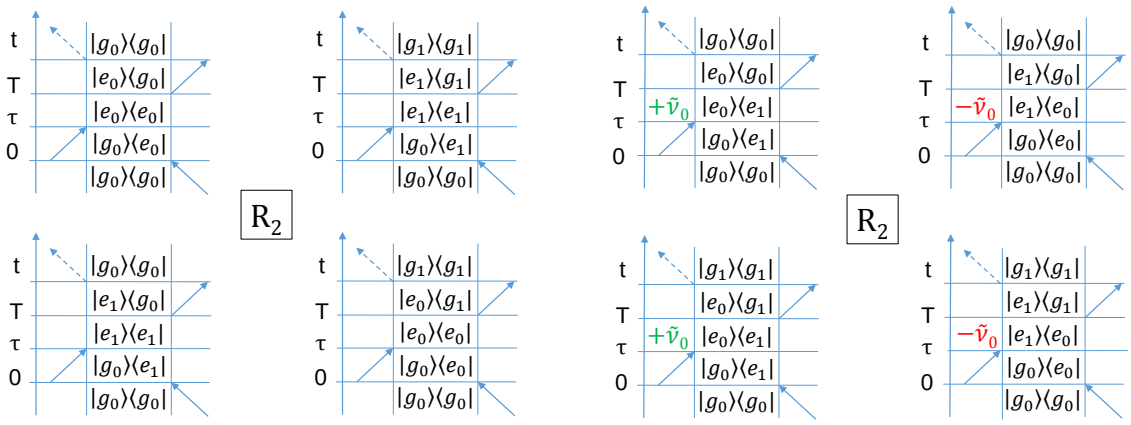

Figure 2.7: Rephasing R_2 pathways for the displaced harmonic oscillator model. During T the four pathways on the left are in an excited electronic state population, while the four pathways on the right are in a vibrational coherence in the electronic excited state.

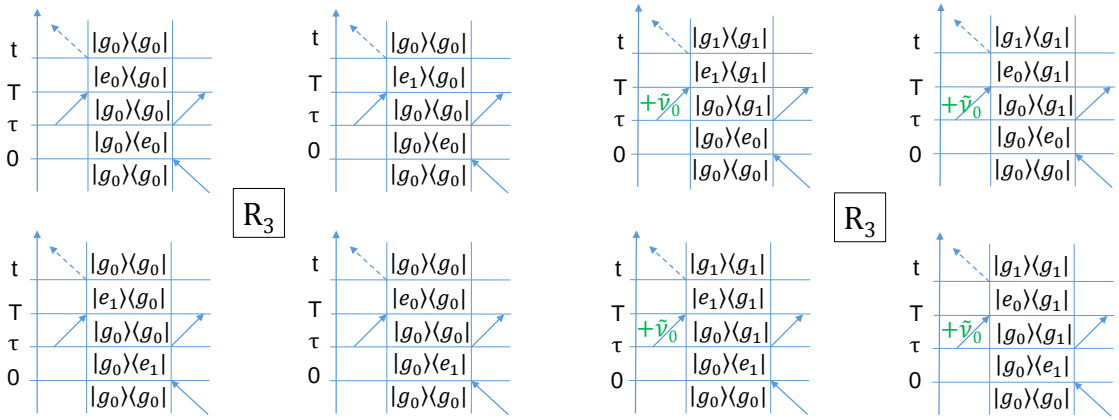

Figure 2.8: Rephasing R_3 pathways for the displaced harmonic oscillator model. During T the four pathways on the left are in an electronic ground state population, while the four pathways on the right are in a vibrational coherence in the ground state.

Now that we have all the third-order pathways which will generate the macroscopic signals drawn, we can analyze how their signatures on 2D-ES spectra will appear. To do that, we start by making a connection between the double-sided Feynman diagrams and the information we recover experimentally in 2D-ES. The excitation wavenumber $\tilde{\nu}_1$ recovered in 2D-ES is the wavenumber corresponding to the first arrow in the double-sided Feynman diagrams. Hence, for each diagram in Figures 2.5-2.8, the excitation wavenumber is determined by the energy gap between the initial and final states related to this interaction. The detection or emission wavenumber is similarly determined by the signal emission dashed arrow in the diagrams. And finally the other experimentally controlled parameter is the population time T, and we are able to measure the third-order

signal as a function of this delay, which will reflect the dynamics of the density matrix during that period. The wavenumbers corresponding to the second and third arrows are not directly accessible from the experiment.

In a displaced harmonic oscillator energy level structure for a vibrational mode of wavenumber $\tilde{\nu}_0$, there are three different wavenumbers which can induce transitions between the ground and electronic excited states of the system. These are $\tilde{\nu}_{eg}$, which corresponds to the transitions $|g_0\rangle \longleftrightarrow |e_0\rangle$ and $|g_1\rangle \longleftrightarrow |e_1\rangle$; $\tilde{\nu}_{eg} + \tilde{\nu}_0$, which corresponds to the transitions $|g_0\rangle \longleftrightarrow |e_1\rangle$; and finally $\tilde{\nu}_{eg} - \tilde{\nu}_0$, which corresponds to the transitions $|g_1\rangle \longleftrightarrow |e_0\rangle$. This allows us to go through all of the diagrams and label them according to the excitation and emission wavenumbers, hence locating where in the excitation-emission plane $(\tilde{\nu}_1, \tilde{\nu}_3)$ that particular signal will be located.

Now that we know how to read the excitation and emission wavenumbers from the double-sided Feynman diagrams, the final consideration concerns the last experimental parameter, the population time T. In Section 2.5 we saw that during this time period the density matrix of a two level system is always in a population state, and thus the evolution observed during this period is population relaxation. For the displaced harmonic oscillator energy level structure however, the possibility arises that the first and second interactions with the laser pulses take place at different wavenumbers, hence leaving the density matrix in a vibrational coherence during T. In Figures 2.5-2.8 we have displayed the pathways so that the ones for which the density matrix is in a population during T (referred to as population pathways from now on) are shown on the left, while those for which the density matrix is in a coherence during T (referred to as coherence pathways from now on) are shown on the right.

At this point, we need to address the question of how the presence of a coherence during T affects the signal emitted. If the system is in a coherence during T, it will propagate in time under the unperturbed Hamiltonian $\hat{H}_0$, which will result in an oscillation of frequency corresponding to the energy separation between the two coherent states. Therefore, as the delay T is experimentally scanned, the macroscopic polarization generated by these diagrams will oscillate in amplitude, thus creating beatings in 2D-ES signals at the $(\tilde{\nu}_1, \tilde{\nu}_3)$ coordinate defined by the first and last arrows.

Moreover, we notice that there are four coherences to be found in the diagrams from Figures 2.5-2.8: $|g_0\rangle\langle g_1|$, $|g_1\rangle\langle g_0|$, $|e_0\rangle\langle e_1|$ and $|e_1\rangle\langle e_0|$. Because the density matrix is

Hermitian, $|g_0\rangle\langle g_1| = |g_1\rangle\langle g_0|^*$, and so on. Therefore, if the coherence $|g_0\rangle\langle g_1|$ modulates the third-order signal as $e^{+i\nu_0 T}$, then $|g_1\rangle\langle g_0|$ will modulate the signal as $e^{-i\nu_0 T}$: one oscillation will take place with a positive and the other with a negative frequency (which we are representing in wavenumber units).

The difference between a positive and a negative frequency is the phase shift between real and imaginary parts of the signal, as well as their relative amplitudes. A positive frequency corresponds to an oscillation of the form $e^{+i\nu_0 T} = \cos(\nu_0 T) + i\sin(\nu_0 T)$, while a negative frequency corresponds to an oscillation of the form $e^{-i\nu_0 T} = \cos(\nu_0 T) - i\sin(\nu_0 T)$. Moreover, a signal for which the imaginary part is zero contains an equal mix of positive and negative frequencies (if $f(t) \in \mathbb{R}$, then $\mathrm{FT}[f(t)](\omega) = \mathrm{FT}[f(t)]^*(-\omega)$). Because we can measure both the real and imaginary parts of the third-order signal (see Chapter 3), if we preserve the complex-valued 2D-ES maps we can differentiate between the coherence pathways of frequencies with opposite signs, which we explore in Chapter 5.

For now, we will summarize the information from the diagrams in schematic $(\tilde{\nu}_1, \tilde{\nu}_3)$ maps, which we will build in the following way. First, we will draw rephasing and non-rephasing maps individually, as we can separate them in the experiment. Every Liouville-space pathway from Figures 2.5-2.8 will be represented as a geometric symbol, with squares being used to indicate that the electronic population during T is in the excited state, and triangles representing pathways for which the electronic population is in the ground state during T. Black solid symbols represent population pathways, while open symbols correspond to coherence pathways, with green marking pathways that generate beatings of positive frequency and red marking pathways that generate beatings of negative frequency.

These geometric symbols are sorted in the $(\tilde{\nu}_1, \tilde{\nu}_3)$ plane according to their excitation and emission wavenumbers, as determined by the first and last arrows in the diagrammatic representation. Because sometimes multiple diagrams are found at the same $(\tilde{\nu}_1, \tilde{\nu}_3)$ coordinate, the symbols are drawn around this coordinate and inside a black circle, the centre of which corresponds to the coordinate of all diagrams it encircles. As a result, we have Figure 2.9.

Before we proceed, we emphasize two aspects from Figure 2.9. The first is the presence of pathways in what is usually called the stimulated emission region (detection wavenumber at $\tilde{\nu}_{eg} - \tilde{\nu}_0$), which serves as a reminder that when a vibration is coupled to an electronic transition, the emission can be red-shifted, leaving the system in a hot ground

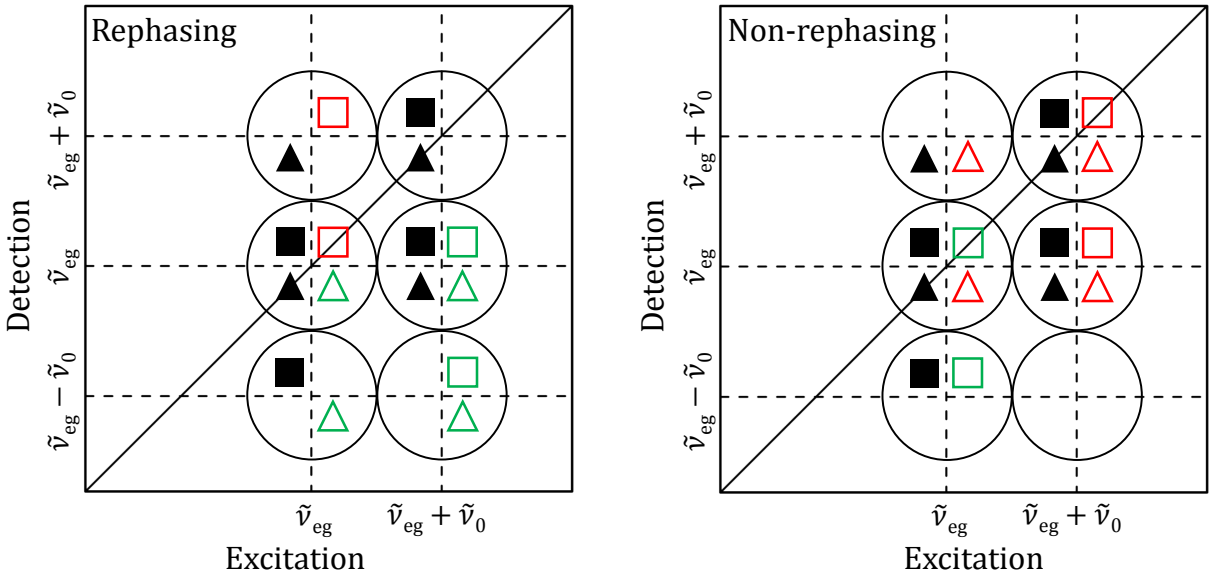

Figure 2.9: Scheme of Liouville-space pathways in rephasing (left) and non-rephasing (right) 2D-ES maps. Each geometric figure marks a pathway, with squares representing an excited state and triangles representing a ground state population during T. Black geometric figures correspond to non-oscillatory pathways, whereas oscillatory ones are marked with open diagrams, which are red if the corresponding frequency is negative and green if it is positive. The signal corresponding to each geometric figure is centred in the black circle within which the figure is contained.

state. Therefore, although signals can be detected at $\tilde{\nu}_3 = \tilde{\nu}_{eg} - \tilde{\nu}_0$, no electronic state exists at that energy. Instead, a sublevel associated with the ground state creates the energy gap at that wavenumber. Thus, care must be taken when inferring the existence of a state due to the presence of a 2D-ES signal.

The second aspect is that out of the three oscillatory pathways observed at the stimulated emission region $\tilde{\nu}_3 = \tilde{\nu}_{eg} - \tilde{\nu}_0$ in rephasing maps, two of them correspond to vibrational coherences in the ground state during T. So although a tempting hand waving argument can be made that if a signal is detected in the stimulated emission region, its population time dynamics must have taken place in the electronic excited state, we have just shown that coherent beatings in the ground state also generate contributions in this spectral region. We do note however that the both population pathways with $\tilde{\nu}_3 = \tilde{\nu}_{eg} - \tilde{\nu}_0$ have an excited state population during T, so it is only for coherent pathways that the argument breaks down.

Figure 2.9 will be discussed many more times throughout this thesis as the basis of our experimental results, but for now we move on to discuss another relevant case of coupling which shows similar signatures in 2D-ES to the ones we just described: the case

of electronic coupling.

2.7.2 Purely electronic coherences

In this Section we show all Liouville-space pathways for the energy level scheme displayed in Figure 2.4b, which is a three level system with two distinct electronic excited states $|e'\rangle$ and $|e''\rangle$ of similar energy. We are considering this as an abstraction from the case of molecular aggregates, where dipole-dipole coupling between two chromophores can lead to excitonic splitting of the excited state into two delocalized exciton states, and the energetic separation between them depends on the strength of the coupling [118]. This coupling is typically in the same range of frequencies corresponding to nuclear vibrational modes [78]. In this specific case of dipole-dipole coupling giving rise to excitonic splitting of the excited state, a double-exciton state is also formed at twice the energy of the excited state of a single chromophore, thus differing slightly from the energy level scheme from Figure 2.4b [95, 98, 118].

However, the focus of this thesis is on vibrational signatures observed in 2D-ES, and the essential reason we are including the three level system is because we want to discuss pathways in which an electronic coherence can be formed during T, and all that is required for that is the existence of two different excited states which can be accessed through the interaction of the same ground state with light. Therefore, it is not relevant here whether these excited states arose due to dipole-dipole coupling or merely because a molecule happened to have such an energy level structure in the first place. Thus so we will stick to this model and note that the extension to the aggregate with dipole-dipole coupling has been described in the literature [78].

We can draw all double-sided Feynman diagrams for this energy level structure in the same way as we have done in Section 2.7.1, and the results are shown in Figures 2.10 (rephasing) and 2.11 (non-rephasing). We note that the absence of a sublevel associated with the ground state substantially reduces the number of pathways (from 32 to 16). That is because of the three excitation fields, one of them has to cause a de-excitation (with the second de-excitation being caused by the signal emission), and therefore at this step of the pathways only one option is possible instead of two, thus halving the total number of diagrams.

The scheme for the energy level structure analogous to Figure 2.9 is shown in Figure

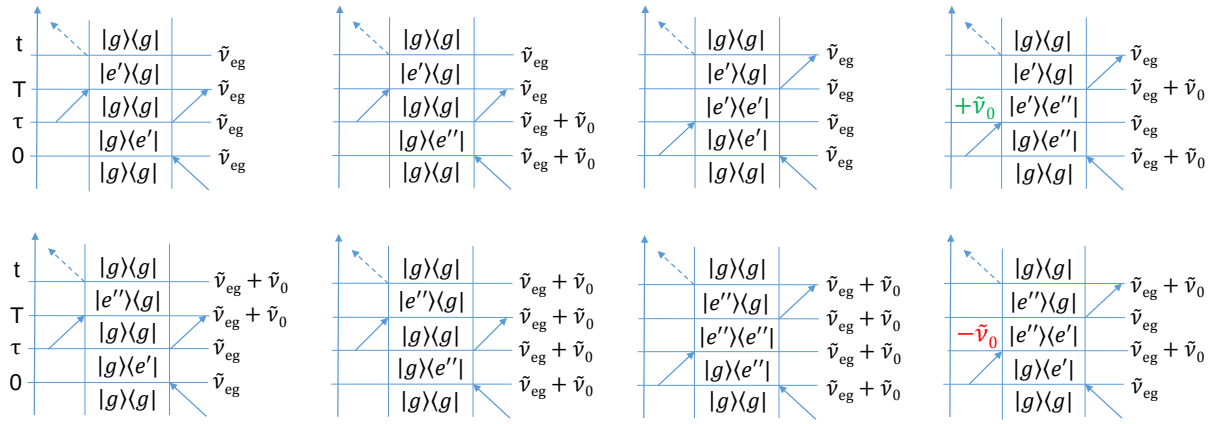

Figure 2.10: Rephasing Liouville-space pathways for the energy level scheme in Figure 2.4b.

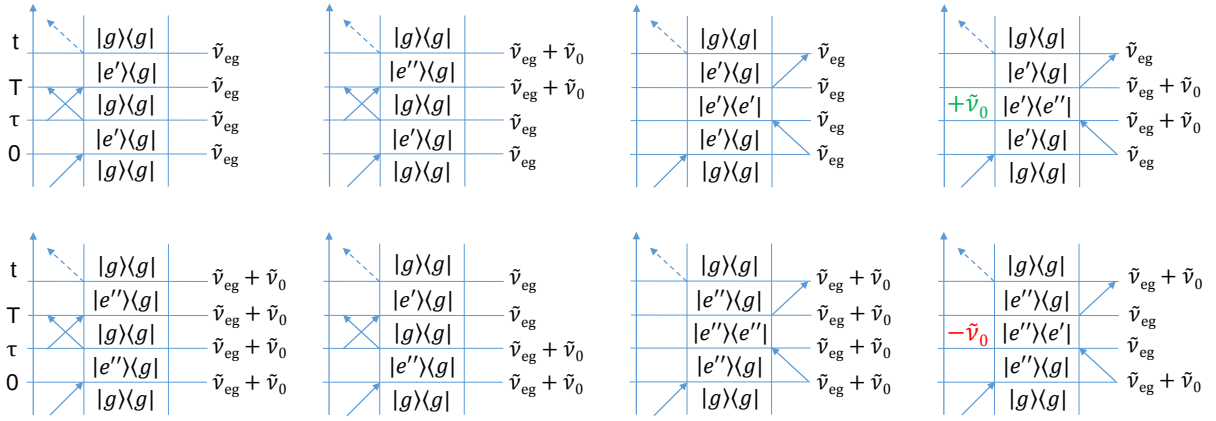

Figure 2.11: Non-rephasing Liouville-space pathways for the energy level scheme in Figure 2.4b.

2.12 and there are a few important differences between them. First, it is clear that the 2D signal contributions in the stimulated emission region disappear completely, as would be expected intuitively.

The most important difference between Figures 2.9 and 2.12 regards the signatures of coherent superpositions during T. In the case of vibrational coupling, rephasing and non-rephasing maps had 8 coherence pathways each, distributed around 5 different $(\tilde{\nu}_1, \tilde{\nu}_3)$ coordinates. When there are no sublevels associated with the ground state, however, only four oscillatory pathways in total are forecast, with diagonal oscillations being expected from non-rephasing maps and cross-peak oscillations being expected from rephasing maps.

This observation shows that the presence of oscillatory features in the stimulated emission region of a sample marks the presence of sublevels associated with the ground state, therefore indicating a vibrational origin for the coherences. In conclusion their absence combined with oscillatory diagonal peaks in the non-rephasing maps and oscillatory cross-peaks in the rephasing maps strongly points towards an electronic origin for the

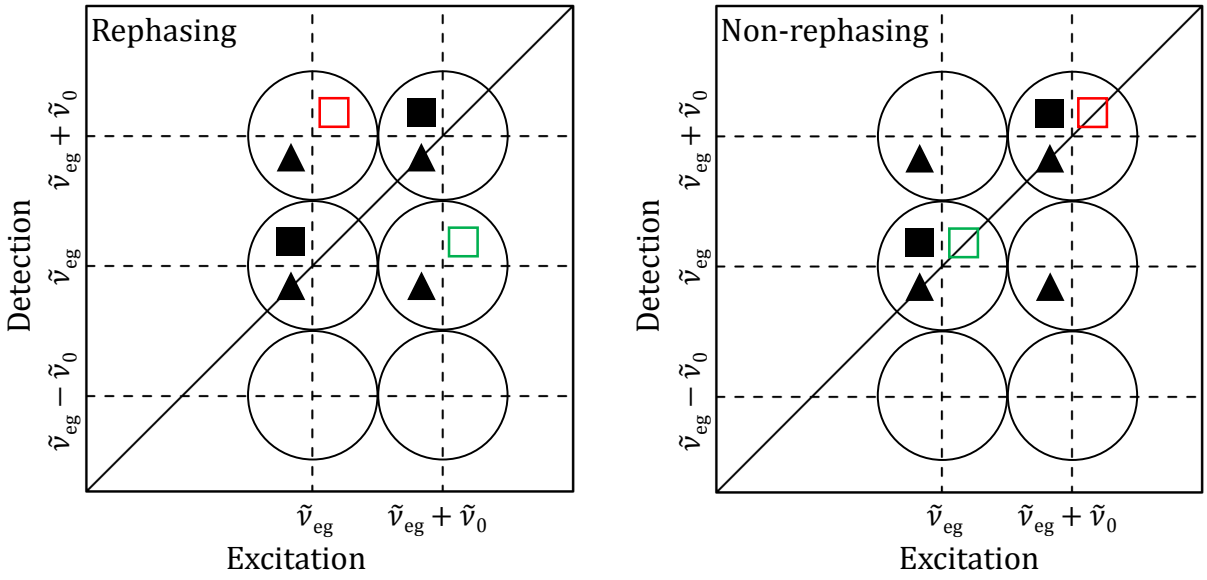

Figure 2.12: Scheme of Liouville-space pathways in a rephasing (left) and non-rephasing (right) 2D maps for the energy level structure shown in Figure 2.4b. See caption of Figure 2.9 for details.

coherences generating those beatings. This result was first established in reference [85] and used in reference [120].

2.8 Beyond the diagrammatic analysis

In real experiments each transition has a linewidth associated with it, so features in real 2D-ES maps rarely look as sharp as the schemes above suggest. This has important consequences. Amid the debate on how to distinguish between electronic and vibrational coherences, some papers have reported that the phase of the oscillations in 2D-ES maps as a function of excitation and detection could be used as a criterion [77, 82]. For instance, it was argued that a phase shift of $\frac{\pi}{2}$ between diagonal and cross peak oscillations in the FMO complex were evidence of coherent quantum transport effects (and therefore, electronic coherence) [81]. Other studies on much simpler molecular systems have observed interesting relationships between the relative phase of oscillations on 2D-ES maps. The Scholes group has reported in a Thesis [84] what looked like a systematic phase variation in the 2D-ES response of Cresyl Violet, which has its lowest electronic transition coupled to a vibration; however no explanation or thorough description of the observations was shown. Reference [86] also has studied both experimentally and theoretically phase shifts between different oscillatory signals in the 2D spectra of a phtalocyanine monomer, but

only shifts of 0 or π were forecast or observed. The main limitation of the approach in reference [86] is the assumption that the absorption maxima related to the $0-0$ and $0-1$ transitions are clearly determined and sharp, which is very rarely the case in practice.

Our analysis of the third-order response functions and how they appear on 2D-ES data up to this point has also relied on the assumption of well-defined energy. This was convenient because it allowed us to develop the diagrammatic approach as a way in which to systematically obtain the most important third-order signals for a given energy-level structure, from where we can read the excitation and detection wavenumbers, as well as see which state the density matrix is in during T, which determines the dynamics of the signal as a function of that time.

The theory of 2D-ES lineshapes has been widely discussed in the literature [27,66]. The main focus of this thesis is on coherence pathways and the oscillatory features as a function of T they generate in 2D-ES measurements, so we will not discuss 2D lineshape theory in depth, but only note some key results. Rephasing and non-rephasing third-order signals present what is called a 'phase-twisted' lineshape, which is a mix between absorptive and dispersive, and arises from the Fourier transform of the coherence time variable of either a rephasing or a non-rephasing signal, which was first noticed in 2D-NMR [17]. Because rephasing and non-rephasing signals have the density matrix in coherent superpositions which are the adjoint of one another, the phase-twist acquired by them is the same with opposite signals, meaning that the real part of an equally weighted sum of rephasing and non-rephasing signals $R_1 + R_2 + R_3 + R_4$ has a purely absorptive character, while the imaginary part is purely dispersive [121, 122].

For our work, on the coherent oscillations in 2D-ES, our main concern is only to extend the view from the double-sided Feynman diagrams, which predict oscillations at specific coordinates, to a view which considers the broadening which inevitably takes place in real systems. This problem has only been approached in a convenient way by Butkus *et al.* in 2012 [78], quite a few years after the pioneering experimental studies which observed persistent coherent oscillations in light-harvesting systems, and we will follow their argument below.

The main idea is that if we neglect environment induced relaxation, the third-order nonlinear response function $R(\tilde{\nu}_1, T, \tilde{\nu}_3)$ can be approximated by the sum of all resonant

Liouville-space pathways experimentally detected:

$$R(\tilde{\nu}_1, T, \tilde{\nu}_3) \approx \sum_n R_n(\tilde{\nu}_1, T, \tilde{\nu}_3), \tag{2.72}$$

where each value of n corresponds to a different resonant pathway. Then, for each pathway, as given by equations A.3–A.6 we apply the same procedure used for the linear response function in Section 2.4. If the result for the j^{th} time interval is labeled G_j and called the propagator for the density matrix, and the signal of each pathway can be written as:

$$R_n(\tilde{\nu}_1, T, \tilde{\nu}_3) = A_n \iint \mathrm{d}\tau \ \mathrm{d}t \ e^{i2\pi c(\tilde{\nu}_3 t + \tilde{\nu}_1 \tau)} \left[\pm G_3(t) G_2(T) G_1(\tau)\right]_{(n)}, \tag{2.73}$$

where the two integrals correspond to the Fourier transforms to represent the response function in excitation and emission wavenumbers instead of time and A_n is a complex prefactor determined by the transition dipoles. To proceed, we make the ansatz that:

$$G_j(t_j) = \theta(t_j) e^{-i\epsilon_j t_j - \gamma_j t_j}, \tag{2.74}$$

where $t_j \in \{\tau, T, t\}$, $\theta(t)$ is the Heaviside step-function, γ_j is a phenomenological dephasing constants and ϵ_j is the energy difference between the ket and the bra from the density matrix for the pathway considered during the first, second or third time intervals (which can be positive, negative or zero if the density matrix is in a population). In reference [78] it was noticed that for $\gamma_1 \approx \gamma_2 \approx \gamma_3$ equation 2.73 can be analytically integrated, giving a mathematical expression for the contribution of a single double-sided Feynman diagram as a function of $(\tilde{\nu}_1, T, \tilde{\nu}_3)$. Introducing the notation $\tilde{\nu}_1 + \frac{\epsilon_1}{2\pi c\hbar} = s_1$, $\tilde{\nu}_3 + \frac{\epsilon_3}{2\pi c\hbar} = s_3$ (i.e., s_j are just wavenumber displacements from the center of that particular peak), the peak amplitude profile obtained was:

$$R_n(s_3, T, s_1) = A_n L(s_1, s_3) e^{-\gamma T} \cos\left(\frac{|\epsilon_2| T}{\hbar} + \phi(s_1, s_3)\right), \tag{2.75}$$

where $L(s_1, s_3)$ is the lineshape and $\phi(s_1, s_3)$ is the phase, which for the rephasing (upper sign) and non-rephasing(lower sign) signals are given by:

$$L(s_1, s_3) = \frac{\sqrt{|\gamma^2 \pm s_1 s_3|^2 + \gamma^2 (s_3 \mp s_1)^2}}{(s_1^2 + \gamma^2)(s_3^2 + \gamma^2)}, \tag{2.76}$$

$$\phi(s_1, s_3) = \mathrm{sgn}(\epsilon_2) \arctan\left(\frac{\gamma(s_3 \mp s_1)}{\mp s_1 s_3 - \gamma^2}\right). \tag{2.77}$$

The most interesting feature about this result is that it predicts that each and every oscillatory Feynman diagram contributing to the 2D-ES signal of a sample will oscillate with varying phases as one moves away from the center of its contribution in the $(\tilde{\nu}_1, \tilde{\nu}_3)$ plane. The implication is clear: whenever the electronic transitions overlap with one another in the linear absorption spectrum (which is a very common case), then overlapping oscillatory contributions from different Feynman diagrams will have different phases and amplitudes at different $(\tilde{\nu}_1, \tilde{\nu}_3)$ coordinates, and interference patterns can be formed in the oscillatory amplitude of the total signal. A corollary of this observation is that the maxima of the oscillation amplitude for a given sample may not coincide to what follows by merely looking at the schematic 2D maps that are built based on the double-sided Feynman diagrams alone, such as figures 2.9 and 2.12.

In principle this may seem rather discouraging, as every different molecule will have different levels of overlap between transitions and the oscillatory signatures may be found at unpredictable points in the 2D maps, with equally an unpredictable phase. On the other hand, careful analysis of equation 2.77 leads one to realize that the phase of the oscillations is constant along the diagonal for rephasing signals and constant along the anti-diagonal for non-rephasing ones (because the arctangent is an odd function). Thus it can be expected that the 2D-ES oscillations of a sample for which the linear absorption spectrum shows a vibronic progression with significant overlap between peaks will form interference maxima and minima aligned with the diagonal for rephasing signals and aligned with the anti-diagonal for non-rephasing ones. These ideas have been experimentally tested and will be thoroughly discussed in Chapter 4, with the results being published in reference [123].

2.9 Summary

In this chapter we presented selected points of the vast theoretical framework that is important to understand 2D-ES, focusing especially on the most relevant points for the work described later in this thesis. We started from the formulation of quantum mechanics representing the system using its density matrix instead of its wavefunction, highlighting how this allows us to treat incoherent statistical ensembles, which is not feasible with

the wavefunction approach. We then considered how to treat the time evolution of the density matrix of a system interacting with a perturbation field, making a connection with nonlinear optics when the perturbation is an electric field treated classically. In order to develop the concept of double-sided Feynman diagrams, we calculated in detail the linear response function of a two level system, showing how the rules for drawing double-sided Feynman diagrams follow from the equations. This was used to discuss the third-order response function and the principles of 2D-ES, including the difference between rephasing and non-rephasing signals. This discussion was then extended to coupled-systems, where more complex energy level structures are found. We used the diagrammatic approach to make predictions of 2D-ES signals for the cases of vibrational coupling and for a three-level system that resembles the case of electronic dipole-dipole coupling. Finally, we discussed limitations of the diagrammatic approach and presented and extension of it as treated by Butkus *et al.* [78], which is extensively used later in this thesis.

Chapter 3

Two-Dimensional Electronic Spectroscopy

3.1 Historical context

Two-dimensional electronic spectroscopy (2D-ES) was first implemented by the Jonas group [18] at about the same time as it was first implemented in the infrared (IR) region [19]; the latter flourished at a faster rate than the former [27]. One of the reasons for the different rates of scientific development of the technique in the visible and infrared spectral regions is that the experimental challenges for building a setup that is stable enough to recover good quality data increases as one employs shorter wavelengths. This is because a shorter optical cycle duration (1.67 fs at 500 nm, for instance) makes maintenance of the phase stability more challenging [14]. Over the years a number of different optical configurations were proposed and proven to be adequate [21], with the current efforts of some groups leading to setups that operate in the ultraviolet (UV) [124–126] and terahertz [127–130] spectral regions (although phase stability is not the main challenge in the latter case). Reviewing the full historical development of 2D-ES is outside the scope of this thesis, so the present discussion will be restrained to the development of the setup assembled for this work and its comparison to others [131].

As mentioned above, the biggest experimental challenge for 2D-ES is maintaining phase stability, but as is also the case with any other spectroscopic method, avoiding

or removing scattering contributions is another critical point. Light scattering in the same direction of the signal compromises the signal to noise ratio and can even create "ghost"peaks in 2D maps [27]. These problems have been addressed in a number of different ways over the years [55, 132–135], but no implementation has so far been proved to possess an overwhelming number of advantages [21].

One of the most common setups for two-dimensional spectroscopy employs the boxcar geometry, where four parallel propagating beams are focused on the sample with each starting from a different corner of a square. In this case, the third-order signal arising from one interaction with each of three of the beams is emitted in the direction of the fourth beam, which can then be used as a local oscillator for heterodyne detection [132]. Another common way to implement a 2D-ES spectrometer, initially in the IR but now also in the visible and UV, is based on the pump-probe geometry [124, 134]. These schemes have two major advantages. The first is their intrinsic phase stability, which is achieved by using a pulse shaper (or birefringent wedges [136]) to generate phase stable collinear pump pulses, whose relative phase is then known and adjustable. Also, in the pump-probe geometry the signal's phase matching direction is the same as the probe, which means that absorptive spectra can be obtained automatically, without the need to recover the phase without the need to perform separate measurements or extra signal processing. The third advantage is that the probe beam can easily be a white light continuum as is usual in pump probe experiments, whereas in other setups the probe is usually an attenuated replica of the pump beams, limiting the detection spectral region [137].

On the other hand, exactly because the signal and the probe beam are automatically phased, this also means that the rephasing and non-rephasing contributions cannot be easily separated from each other, requiring phase-cycling [138]. Further, there is no simple way to manipulate each beams' polarization independently. A fully collinear geometry can also be employed [139], in which case a strong background and contributions from other nonlinear optical signals generated in the same direction needs to be subtracted through phase-cycling, reducing the sensitivity of the apparatus. Nonetheless, experimental development is ongoing and new ideas are still being proposed to improve 2D-ES setups in all geometries [21, 27, 134, 136].

In the following paragraphs we will present the laser system used and the setup built for the present work.

3.2 Laser system

The 2D spectrometer assembled for this work is based on a commercial amplified laser system and a commercial noncollinear parametric amplifier (NOPA). The amplifier consisted of a regenerative Ti:Saphire system (Spectra Physics Spitfire ACE pumped by an Evolution laser and seeded by MAITAI oscillator) generating 120 fs pulses centered at 800 nm with energy of 500 μJ at a rate of 10 kHz. About 90% of the power was used to pump the NOPA system (TOPAS White, Light Conversion). After the NOPA the laser pulses typically have 15 fs pulsewidth and their central wavelength can be tuned from 490 nm to 750 nm. Besides the internal compressor in the NOPA, a second prism compressor had to be assembled to remove chirp from the pulses. The NOPA output varies with the wavelength, but a typical power at 550 nm was 350 mW (35 μJ per pulse at 10 kHz). To avoid nonlinear effects in the sample, a neutral density filter was used to reduce the power entering the 2D setup to around 4 mW. The pulse to pulse fluctuation of the NOPA system was typically below 0.5% rms for the central wavelength of the spectrum.

3.3 Two-dimensional spectrometer

In the present work the setup assembled employs the boxcar geometry and is based on an earlier development which uses only conventional optics reported by Selig *et al.* [140]. The boxcars geometry consists of having four mutually parallel beams geometrically disposed in the corners of a square before being focused onto the sample. This arrangement allows the detection of the rephasing and nonrephasing signals separately by selecting the phase matching (see Section 2.6).

The main difference between the approach based on conventional optics and others is that two beamsplitters are used to generate the four phase coherent beams, which are then delayed from one another via the synchronous movement of two mechanical delay stages, as shown in Figure 3.1. An alternative option is to use a diffractive optics element to generate the four beams [142]. The option of using a noncollinear geometry also creates further challenges in terms of phase stability, for any vibration on the optical table that alters the pathlength of one of the beams and not of the others will correspond to a shift in phase. One of the solutions to achieve phase-locking in this geometry is to add pulse delays in a pairwise fashion, which effectivelly makes pathlength fluctuations anti-

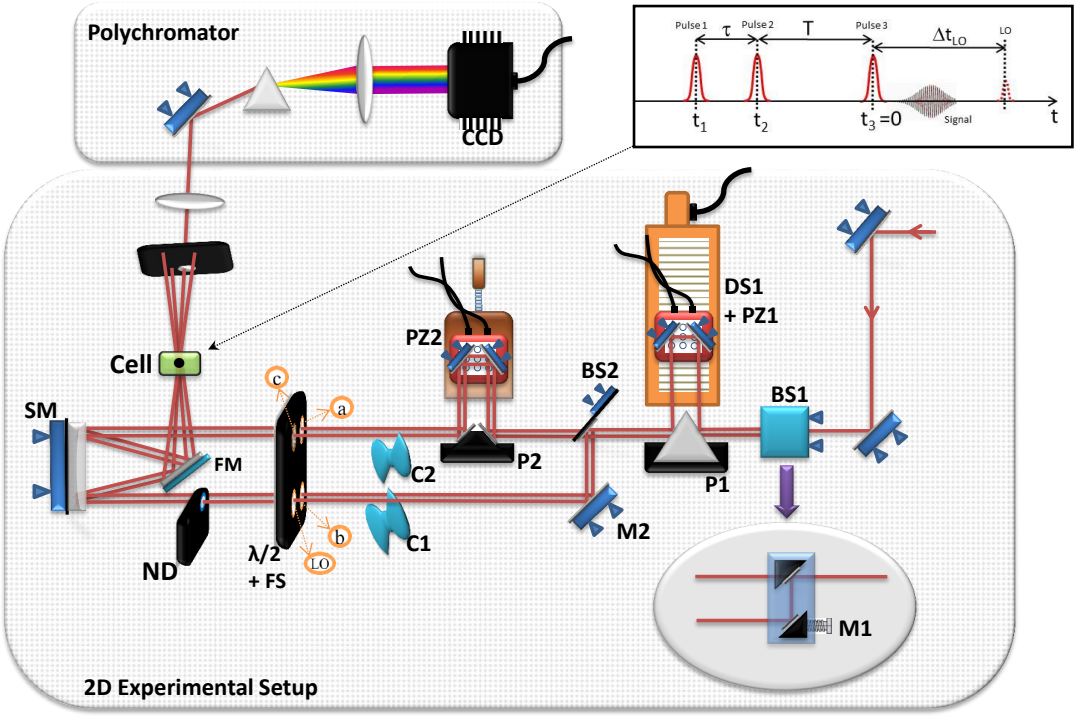

Figure 3.1: Sketch of the experimental setup assembled where: BS1,2 are beamsplitters; P1,2 are aluminium coated knife-edge right angle prisms; DS1 and PZ1,2 are mechanical and piezoelectric delay stages respectively; C1,2 are optical choppers; $\lambda/2 + FS$ are half wave plates plus fused silica windows; ND is a neutral density filter; SM is a spherical mirror; FM is a folding mirror. The upper right corner illustrates the pulse arrival sequence on the sample as well as the signal emission and LO position in time relative to pulse c. In the upper left the homemade polychromator is shown, composed of a mirror, a highly dispersive prism, a lens and the CCD camera [141].

correlated with one another and lead to compensation of phase jitter [142]. This will be explained in more detail later.

Figure 3.1 shows a sketch of the experimental apparatus. First the 4 mW input beam is directed to the setup with two mirrors. Two irises in the entrance of the setup and further irises along the way are present to support the alignment's day to day reproducibility. Both beamsplitters were tailor made through thin film deposition on a 500 μm thick fused silica window (Vortex Optical Coatings) and have approximately 50% transmission-reflection from 350 to 950 nm. The first beamsplitter (BS1) creates two phase coherent beams at different heights separated from one another by about 2.5 cm and the lowest of them propagating 7 cm above the plane of the table. Here the intention was to keep all beams as close as possible to the table to reduce the impact of eventual angular oscillations of the optical mounts on the actual pathlength.

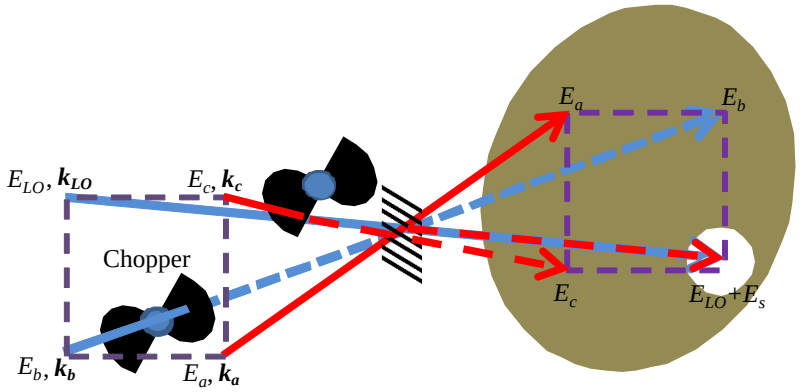

Figure 3.2: The beam geometry employed in the setup (boxcar) and the choppers.

Further along, the upper beam will be split into what we shall call beams c and LO (see labels in Figures 3.1 and 3.2), while the lower beam will be split into beams a and b. Before that, the upper beam is steered towards a pair of delay stages mounted on top of each other. The lower of them (Newport, UTS100CC), DS1, can move over 100 mm (∼600 ps) and has a bidirectional precision of 2 fs, while the upper one (Physik Instrumente, P-622.ZCD), PZ1, is a piezo mover and can travel over a 250 μm range (∼1.5 ps) with precision of about 0.5 fs. The initial alignment here is such that the position of the delay stage compensates the extra 2.5 cm travelled by the lower beam after the beamsplitter.

Next both the upper and lower beams will each encounter a beamsplitter (BS2), so that afterwards 4 phase coherent beams are propagating collinearly and are geometrically disposed at the corners of a 2.5 cm sided square (Figure 3.2). Beams a and c now go through a second delay stage (PZ2) similar to PZ1, and its alignment is such that it makes up for the extra distance travelled by beams b and LO after the beamsplitters BS2. All beams then pass through an achromatic half wave plate, to allow for separate control of each beam's polarization. Finally, all 4 beams hit a spherical mirror (SM) with focal length of 15 cm, which focuses all of them to a single spatial position. The folding mirror (FM) in the setup has the single purpose of steering the beams sideways. The two choppers in the setup represent the biggest novelty in this apparatus and they allow for a better removal of scattering contributions than earlier setups, so their functioning will be explained in more detail later.

The sample is positioned at the spherical mirror's focal point and the transmitted beams a, b and c are blocked, while the LO is collimated and directed to the homemade polychromator [141]. The polychromator spatially disperses the LO and signal spectra

using a highly dispersive flint glass prism. The spectra are then imaged with a 20 cm focal length lens onto a CCD camera with a single line of pixels, where each laser shot is independently acquired. Finally, to avoid the LO beam of generating competing signals as it moves through the sample in the same focal position, it is attenuated by a neutral density filter and delayed by around 400 fs relative to the other beams by propagating through a fused silica plate.

The CCD camera employed in this experiment is a line scan camera consisting of 1x1024 pixels (e2v AVIIVA EM1) whose acquisition rate can be adjusted up to 77 kHz. The camera is trigged by the laser TTL signal at 10 kHz and then sends a TTL signal to a voltage acquisition board, which allows the acquisition of the TTL signal of each chopper. Therefore for each camera acquisition the state of both choppers is also recorded, which allows the acquisition software to determine whether beams b and c were blocked or not when each LO pulse was acquired, so that each configuration can be used to recover different signals, as described in the next Section (3.4).

3.4 Pump-probe measurement and removal of light scattering

Even though the camera employed allows for shot to shot acquisition at 10 kHz, the fastest chopper rate was chosen to be 1 kHz instead of the more obvious 5 kHz. This is for two reasons, the most important being the air turbulence induced within the setup by a chopper rotating at such a high rate, which perturbs phase stability. The second reason is that with the sizes of the chopper's slits and beams which we had, the beams would only be partially blocked with such a high rotation frequency. Actually, even with the fastest chopper working at 1 kHz, in which case one bundle of 5 shots should go through and the next 5 shot bundle should be blocked, it so happens that the initial and final shots of each bundle have to be discarded due to partial blocking. Therefore once the camera is triggered to start acquisition, a delay is explicitly added to ignore the first laser shot. After this delay the camera integrates the signal over the next 300 μs so that the middle 3 shots of each 5 shot bundle are acquired, with the integration stopping to avoid the final partially blocked shot. Careful choice of the choppers slit sizes can avoid the partial blocking at higher chopping rates, but a way of dealing with the resulting turbulence

would still be necessary. In our case, covering the choppers would have required major changes in the setup design, so we opted to keep the lower rate.

Before addressing how the present chopper sequence allows better scattering removal and fast data acquisition let us briefly discuss the previous approaches to dealing with scattered light in the boxcar geometry. As previously mentioned, scattering contributions along the same direction as the LO and signal beams are the major experimental concern. Scattered light arising from the pump beams is phase coherent with the LO and signal, thus generating interferometric signals at the detector [132]. Further, the fact that the LO propagates through the sample with a 400 fs delay relative to the pump beams means that it too can be contaminated with pump-probe signals, for it acts as a probe for transient grating signals induced by any of the other beams [138].

While the pump-probe contamination of the LO is entirely avoided in some setups by having the LO propagate around the sample, that has its own limitations, for the heterodyne detection works best if the LO beam has been through the sample. That happens because the transmission of the LO through the sample ensures its envelope and phase suffer the same distortions as the signal's, such that in the heterodyne detection these distortions are not seen as part of the signal [143], which allows samples with much higher optical densities than the usual 0.3 to be studied.

Some of the procedures proposed to handle the scattering include the use of double modulation with lock-in detection [135] or shutters [132]. The downside of the lock-in detection scheme is that it requires lasers with very high repetition rates, and the shutters scheme significantly slows down the measurements. The design proposed by our group is an intermediate of those, in the sense that choppers and shutters act similarly, but choppers can be synchronized with laser pulses and detection electronics, allowing us to acquire signals from the camera for bundles of 5 laser shots when different beams are unblocked [131].

The chopper sequence we employed essentially blocks and unblocks beams b ($\mathbf{k}_b$) and c ($\mathbf{k}_c$) creating the configuration shown in Figure 3.3, where the temporal width of the laser shots was exaggerated to emphasize the temporal structure of the pulses. Chopper 1 (C1) is synchronized with the laser at 1/10 of its repetition rate (one cycle for every 1 ms) and acts on beam b, while chopper 2 (C2) acts on beam c and has a frequency of 1/20 of the laser repetition rate (one cycle for every 2 ms). This creates 4 different configurations

of laser incidence in the sample (labeled A, B, C and D in Figure 3.3) that are repeated over time: for every pair of blocked/unblocked events of beam b, beam c will be once blocked (A and B) and once unblocked (C and D).

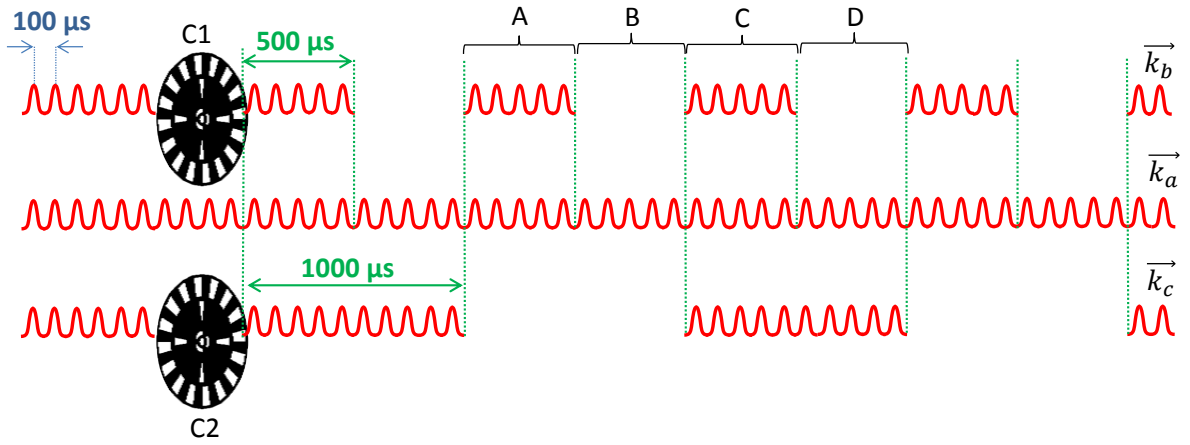

Figure 3.3: Scheme showing the different sample illuminations that arise from the chopper sequence used. Chopper C1 acts on beam b with a frequency of 1 kHz and chopper C2 acts on beam c with a frequency of 500 Hz.

The CCD camera is synchronized with the laser frequency, which allows us to set its operation to acquire separately each bundle of laser shots created by the choppers, from A to D, as shown in Figure 3.3. This allowed us to include in the detection software a routine to manipulate these contributions. If S_n represents the scattering contributions and pump-probe signals resulting from beam $n \in \{a, b, c\}$, and E_{LO} and E_S are the LO and signal electric fields respectively, the detection software performs the following computations:

$$\begin{aligned}
\alpha = A - B &= |S_a + S_b + E_{LO}|^2 - |S_a + E_{LO}|^2 \\
&= |S_b|^2 + 2\mathrm{Re}\{S_a S_b^*\} + 2\mathrm{Re}\{S_b E_{LO}^*\}, \qquad (3.1)\\
\beta = C - D &= |S_a + S_b + S_c + E_S + E_{LO}|^2 - |S_a + S_c + E_{LO}|^2 \\
&= |E_S|^2 + |S_b|^2 + 2\mathrm{Re}\{S_a S_b^*\} + 2\mathrm{Re}\{S_b E_{LO}^*\} + 2\mathrm{Re}\{S_a E_S^*\} + \ldots \qquad (3.2)\\
&\ldots + \ 2\mathrm{Re}\{S_b E_S^*\} + 2\mathrm{Re}\{S_c E_S^*\} + 2\mathrm{Re}\{S_b S_c^*\} + 2\mathrm{Re}\{E_S E_{LO}^*\}, \\
\beta - \alpha &= |E_S|^2 + 2\mathrm{Re}\{S_a E_S^*\} + 2\mathrm{Re}\{S_b E_S^*\} + 2\mathrm{Re}\{S_c E_S^*\} + \ldots \qquad (3.3)\\
&\ldots + \ 2\mathrm{Re}\{S_b S_c^*\} + 2\mathrm{Re}\{E_S E_{LO}^*\}.
\end{aligned}$$

Ideally our system would actually detect only the last term in equation 3.3, for it corresponds to the signal being heterodyned by the local oscillator. However the first

five terms in equation 3.3 are also phase coherent with the LO and will interfere in the detector. Nonetheless, they bring negligible contributions to the measured signal for the following reasons.

First, the 3 terms $2\mathrm{Re}\{S_n E_S^*\}$ result from the interference between the signal field and the part of Rayleigh scattering from beam n that happens to propagate in the signal direction. Because the signal field is small, this term is also usually small – however, it can become significant for highly scattering samples. Second, the term $2\mathrm{Re}\{S_b S_c^*\}$ has no pump probe contribution in the direction of detection: any such contribution would have the same direction of propagation of either beam b or beam c, while we detect in the direction of the LO beam. Therefore its actual contribution on the CCD is merely the interference of the Rayleigh scattering contributions of beams b and c in the direction of the signal, which is also small.

As for the remaining term, it is the homodyne signal, which is usually large enough to be clearly detected. What has to be mentioned now is that the spectral interferometry procedure involves applying a Fourier window to the signal's inverse Fourier transform over the detection frequency, so that the signal is resolved as a function of the detection time [132]. After this, the signal will be separated in different contributions according to the relative time delays between the beams that interfered to generate each. So the homodyne signal, that interferes with no other beam will appear centered at $t = 0$ (see Figure 3.8 in Section 3.6). The heterodyne signal, which is the interference between the homodyne and the LO beam will appear centered at t_{LO}, for it is the interference of the signal (generated at time zero) and the LO (delayed by t_{LO} from time zero).

Beyond allowing the selection of the heterodyne signal from the homodyne, this Fourier windowing process also contributes to the removal of any light scattering contributions that are not centered at the relevant delay time. It should be noted though that some of the small contributions left over in equation 3.3 can have amplitude around t_{LO} for some combinations of population and coherence times, so that the windowing procedure is not the main determinant in removing them: they actually are so small that their presence is insignificant.

Looking at equation 3.3 it still seems that many scattering contributions are present and all we did was state they are small. So it is actually important to stress that what the second chopper allowed us to do was to remove the term $2\mathrm{Re}\{S_b E_{LO}^*\}$ from equation

3.2. This term contains the pump probe contribution that arises from the interaction of beams b and LO with the sample, which is not systematically discarded by the windowing procedure and can be significant for samples with strong transient absorption signals [131].

The other major advantage of the present scheme is that the pump probe and the LO spectra can be recorded for each population time, along with the 2D spectra, therefore at the same time and under very similar experimental conditions. To explain how that is possible, we will repeatedly refer to Figure 3.3 and detail the measurement process for one given population time. First, the camera acquires the signal corresponding to case B in the chopper sequence of Figure 3.3. In this case beams b and c are blocked and the sample is illuminated only with beams a and LO. There may be some pump probe contamination of the LO arising from beam a, but this is generally be much smaller than the LO amplitude, so the signal acquired by the camera at this chopper configuration is essentially the LO spectrum.

After acquiring the LO spectrum, the pump-probe signal is acquired for the given population time by computing equation 3.1, which subtracts the acquisition when only beams a and LO are present from the acquisition when beam b is unblocked too. In order to get the correct population time delay, the stage DS1 needs to be moved in order to make up for the relative delay between beam c and the LO (which is measured before the experiment starts). This brings the LO beam to time zero (see inset of Figure 3.1) and therefore creates a pump-probe signal with beam b as the pump (whose position in time is the corresponding population time) and the LO as the probe, as can be seen in Figure 3.3.

Once the LO and pump-probe spectra have been recorded, DS1 returns to its previous position and the 2D data acquisition is performed by scanning the coherence times (Figure 3.4). A typical measurement of one population time consists of scanning 60 coherence times and averaging over 300 laser shots for each delay, which takes about 1 minutes, including the collection of the LO and pump-probe spectra.

3.4.1 Delay stages movement sequence

The last section showed that a 2D-ES measurement requires a very intricate set of motions by the delay stages. The purpose of this section is to explain how that is correctly accomplished in our experimental design. First, we note that the final result of

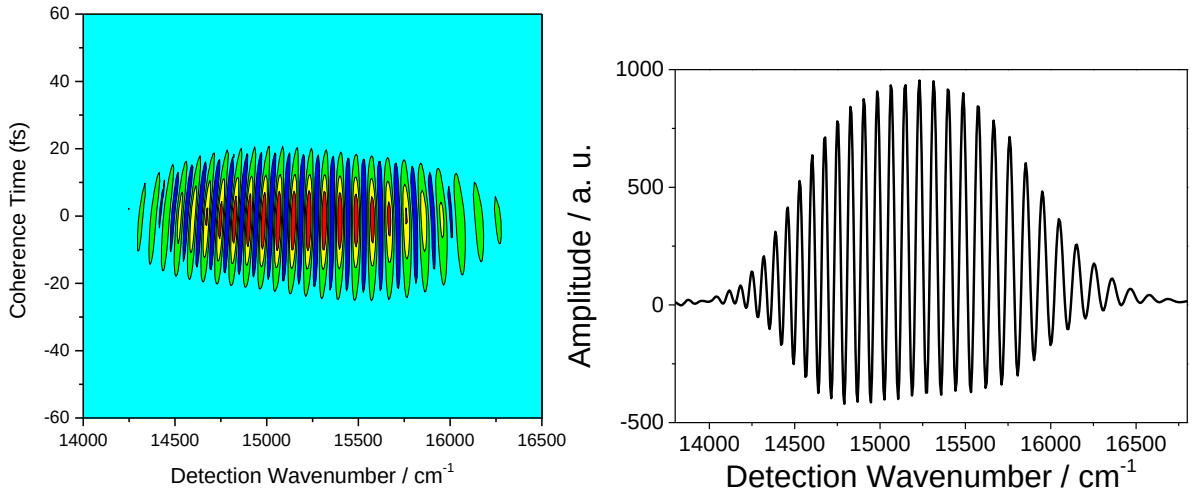

Figure 3.4: Left: typical interferogram measured with the 2DES setup. Right: a horizontal cut from the interferogram, accounting for the signal acquired in a single coherence time ($\tau = 0$ in this case).

our measurement is a complex function $S^{(3)}(\omega_t, T, \omega_\tau)$ which contains both absorptive – $\mathrm{Re}\{S^{(3)}(\omega_t, T, \omega_\tau)\}$ – and dispersive – $\mathrm{Im}\{S^{(3)}(\omega_t, T, \omega_\tau)\}$ – information regarding the material's third-order response.

As it turns out though, $S^{(3)}(\omega_t, T, \omega_\tau)$ is not directly recovered from 2D measurements with the boxcars geometry. To understand this it is important to note that the pulse arrival order has an effect on the direction of the different nonlinear signals generated. Bearing in mind the third order response function considerations from Section 2.5, we recall that the absorptive 2D lineshape is given by the sum of equally weighted rephasing and the non-rephasing signals [122]. Therefore, it is important to record both. The third-order nonlinear response which arises from perturbing the sample with pulses a, b and c (neglecting the weaker LO) will consist of many contributions – 864 to be exact, see Section 2.5 – and they will propagate in one of the $\pm\mathbf{k}_a \pm \mathbf{k}_b \pm \mathbf{k}_c$ directions.

The main advantage of using the boxcar geometry is that the third-order signals which follow a first interaction with pulse a, a second with pulse b and a third with pulse c propagate in spacial directions where no other signals are present, which is why it is sometimes referred to as being 'background-free'. In Section 2.5 we saw that a consequence of requiring that each interaction happens with a different pulse, assuming the semi-impulsive limit and the rotating wave approximation, is that the number of contributions to the third-order polarization was reduced from 864 to 4. Two are rephasing, and propagate in the $\mathbf{k}_s = -\mathbf{k}_1 + \mathbf{k}_2 + \mathbf{k}_3$ direction, while the other two are non-rephasing and propagate

in the $\mathbf{k}_s = \mathbf{k}_1 - \mathbf{k}_2 + \mathbf{k}_3$ direction. We emphasize that in these equations the numeric indexes refer to the time arrival order of the beams in the sample. So here 2 refers to the second pulse to arrive, regardless whether it is pulse a, b or c.

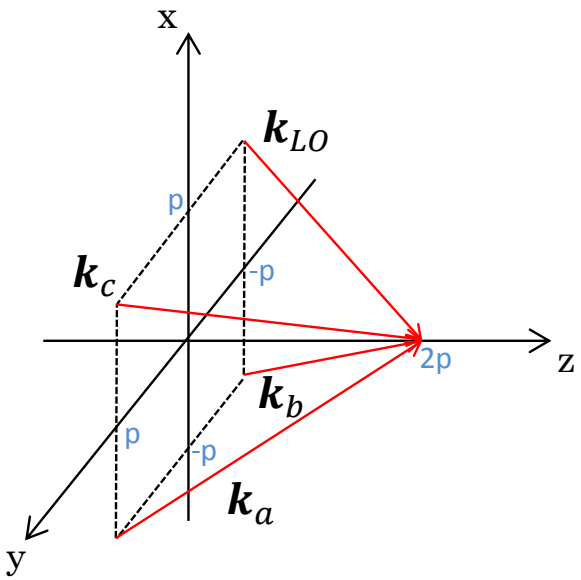

Figure 3.5: Representation of the wave vectors in the boxcars geometry with a coordinate system. The z component is equal for all beams, while the x and y components are equal in module to each other for all beams. In this scheme the modulus of the x and y components is called p and the z component was arbitrarily chosen to be $2p$.

Our detector is positioned so that it captures only signals travelling in the LO direction and now we will discuss which contributions are measured, for which we will repeatedly refer to Figures 3.5, where we sketch the boxcar geometry using a coordinate system, and 3.6, where we show the time ordering of the pulses. From Figure 3.5 we notice that we can write the wave vector of each pulse as:

$$\begin{aligned} \mathbf{k}_a &= (p, -p, 2p) \\ \mathbf{k}_b &= (p, p, 2p) \\ \mathbf{k}_c &= (-p, -p, 2p) \\ \mathbf{k}_{LO} &= (-p, p, 2p). \end{aligned} \tag{3.4}$$

Now we are in position to discuss the pulse arrival sequence and which signals are detected in each case. If the pulse a is the first to arrive followed by b and then c (which is seen in the right-hand side of Figure 3.6 for the extreme case when pulses b and c overlap, *i.e.*,

for population time zero), then $\mathbf{k}_1 = \mathbf{k}_a$, $\mathbf{k}_2 = \mathbf{k}_b$ and $\mathbf{k}_3 = \mathbf{k}_c$. In this case, by inspection we can see that there is only one combination of signs in $\mathbf{k}_s = \pm\mathbf{k}_1 \pm \mathbf{k}_2 \pm \mathbf{k}_3$ that is equal to $\mathbf{k}_{LO}$ (which is our direction of detection):

$$-\mathbf{k}_1 + \mathbf{k}_2 + \mathbf{k}_3 = -\mathbf{k}_a + \mathbf{k}_b + \mathbf{k}_c = \mathbf{k}_{LO}, \tag{3.5}$$

which is just the rephasing contribution we discussed in the previous chapter. Therefore, our experimental setup acquires the rephasing contribution by having the pulse a being the first to arrive, followed by b and then c.

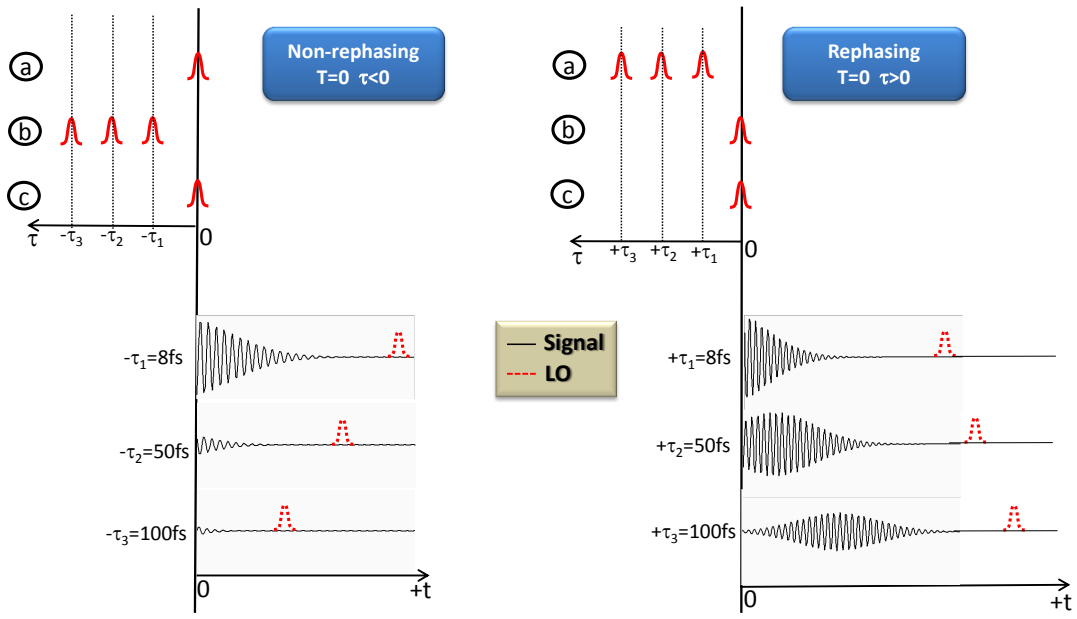

Figure 3.6: Pulse arrival time ordering scheme for rephasing and non-rephasing cases.

In this pulse sequence, the non-rephasing signal propagates in the $\mathbf{k}_a - \mathbf{k}_b + \mathbf{k}_c = (-p, -3p, 2p)$ direction which does not correspond to any of the incoming beams. One option to detect it would be to place a second detector and local oscillator beam in this direction. However that adds the difficult task of adding an extra local oscillator and guaranteeing the detectors of the rephasing and non-rephasing signals are equally calibrated, for an equally weighed sum is required for absorptive signals. Another option that overcomes this difficulty relies on the time ordering impact on phase matching [121]: we note that if pulse b is the first to arrive, followed by a and then c, then $\mathbf{k}_1 = \mathbf{k}_b$,

$\mathbf{k}_2 = \mathbf{k}_a$ and $\mathbf{k}_3 = \mathbf{k}_c$ and the non-rephasing signal will propagate in the direction:

$$\mathbf{k}_1 - \mathbf{k}_2 + \mathbf{k}_3 = \mathbf{k}_b - \mathbf{k}_a + \mathbf{k}_c = \mathbf{k}_{LO}. \tag{3.6}$$

Therefore, instead of using a second detector in another direction, we can actually also have the non-rephasing signal being generated in the same direction as the LO merely by having pulse b being the first to arrive, followed by a and then c.

Now that it is clear how the rephasing and non-rephasing signals can be acquired, we can finally address the movement sequence of the delay stages. We take the starting temporal position of the beams as that where a, b and c are overlapped and the LO arrives about 350 fs later in the sample, due to the extra material it has traveled through. In Figure 3.6 both the rephasing (right-hand side) and the non-rephasing (left-hand side) acquisitions are illustrated, with the LO pulse shown as a dashed Gaussian.

The population time (T) zero is determined by the condition that beam a or b is overlapped with c. This is also taken as the origin for both coherence and detection timescales (labeled τ and t respectively). The population time is defined as $T = t_c - t_n$, where n is the second to arrive between a and b.

The coherence time is defined as $\tau = t_b - t_a$, which is physically intuitive for this is the variable we would like to scan over, but it can create some confusion for graphical representations. According to this definition, if $t_b > t_a$ then τ is positive, the pulse order is a, b, c (c is always the last of the pulses) and the rephasing signal is being generated in the LO direction (Figure 3.6, right).

On the other hand, if $t_b < t_a$ then τ is negative, the pulse order is b, a, c and the non-rephasing signal is being generated in the LO direction. Thus in the coherence timescale the convention of "more negative means earlier"no longer applies. However it does still apply for the detection timescale t, so in Figure 3.6 the coherence timescales were drawn as a support, but to evaluate early or late arrival the position on the t scale must be considered. The result is that left means earlier and right means later.

The first step to start a measurement is setting the population time delay to the desired value, which is accomplished by moving DS1 and thus altering the relative delay between the pairs of beams (a, b) and (c, LO). Once that is set, the scan over coherence times can be performed by moving the delay stage PZ2, which changes the relative delays between the pairs of pulses (a, c) and (b, LO). As a consequence of this movement, the coherence

time (delay between a and b) can be scanned, but there is a side effect: the delay between c and LO is also altered. This could be relevant because the Fourier windowing procedure that was mentioned above assumes a constant delay between the signal and the LO, and the third-order signal can only start to be generated after the third pulse (c) hits the sample. As it turns out though, the signal emission maximum has its position in time determined by the coherence time, which can be seen in Figure 3.6, more strikingly for the rephasing case (see Equations 2.70 and 2.71). For the non-rephasing one has to imagine a continuation of the signal for negative detection times to figure out where the maximum amplitude would be. Therefore, by delaying the LO against c we are effectively ensuring that delay between signal maximum and the LO remains the same over the scan [131].

Consequentially, to obtain the non-rephasing signal (negative coherence times) PZ2 has to be scanned forwards. Pulse b is the first to arrive and the movement changes the time delay of pulses a and c relative to it. For positive coherence times things get slightly more complicated. In this case PZ2 is moved backwards, for now we need the time order to be (a, b, c). The problem is that by moving PZ2 backwards pulse c will follow pulse a and both will arrive at the sample before pulse b, which would alter the desired phase-matching. Thus, to move pulse b so that it is the second to arrive and correct for the population time, the delay stage PZ1 has to be moved forwards by the same amount that PZ2 was moved backwards [140].

It is also interesting to note that this movement sequence of the delay stages naturally corresponds to a measurement in the rotating frame (see Sections 2.4 and 2.5) [27, 134]. That is because of the constant phase shift between the signal and LO (see Figure 3.6) which is applied simultaneously with the phase shift corresponding to the coherence time scan. To clarify what we mean by that we have to consider the phase of the signal being measured. If $\Delta\varphi_{ab} = \varphi_a - \varphi_b$ and $\Delta\varphi_{cLO} = \varphi_c - \varphi_{LO}$, then the signal is proportional to:

$$I_s \propto \mathrm{Re}\left(e^{-i(\Delta\varphi_{ab}-\Delta\varphi_{cLO})}e^{-i\omega(\tau-t)}R'(\tau,T,t)\right) = \mathrm{Re}\left(e^{-i(\Delta\varphi_{ab}-\omega t)}e^{i(\Delta\varphi_{cLO}-\omega\tau)}R'(\tau,T,t)\right), \tag{3.7}$$

where $R'(\tau,T,t)$ is the envelope of the response function. From the discussion above we saw that by changing the coherence time by $\tau' = \tau+\Delta\tau$, this also moves the local oscillator in the opposing direction: $t'_{LO} = t_{LO} - \Delta\tau$. Then it follows directly from equation 3.7 that the signal's phase variation due to the coherence time change is exactly cancelled

by the corresponding LO delay. This means that in our measurement the signal will not oscillate close to the optical frequency as a function of the coherence time, because the phase which is continuously added to LO as we scan τ cancels that and brings the overall frequency to zero (thus the rotating wave frame nomenclature), meaning that we only acquire the envelope of the response function as we scan the coherence time.

There are two major advantages that follow from measuring in the full rotating wave frame. The first is data acquisition time: if a direct measurement of the response function is desired, it is necessary to acquire data for at least two coherence time steps for each cycle of the highest frequency present in the signal. At 600 nm, for instance, the optical cycle is approximately of 2 fs, thus requiring coherence time steps shorter than 1 fs to properly recover the signal. In our typical measurements, coherence time steps of 4 or 5 fs were enough, representing a large reduction in data acquisition time. The second advantage is that acquiring only the envelope of the response function relieves the phase stability requirement for the setup: instead of keeping the phase stable to a fraction of the optical cycle one has only to keep it stable to a fraction of the pulse duration ($\sim$15 fs).

3.5 Phase stability of the setup

First, let us recall that the signal field's phase is determined by its corresponding phase matching, as given by equation 3.7. For instance the rephasing signal in our setup corresponds to $\mathbf{k}_s = -\mathbf{k}_a + \mathbf{k}_b + \mathbf{k}_c$ and the heterodyne detected 2DES signal has the phase:

$$\Delta\varphi_s = -\varphi_a + \varphi_b + \varphi_c - \varphi_{LO} + \varphi_{sig}, \tag{3.8}$$

where the heterodyned detected signal has the subscript "s"and the homodyne signal has its own phase φ_{sig} arising from the interaction between the laser pulses and the sample [144]. The overall phase fluctuation can be written as:

$$\delta(\Delta\varphi_s) = (\delta\varphi_b - \delta\varphi_a) + (\delta\varphi_c - \delta\varphi_{LO}). \tag{3.9}$$

And now, to get a full analysis of the total phase fluctuation it is possible to go through the experimental setup for each beam (Figure 3.1) and keep track of all possible phase

fluctuations in each optical element in its path. For instance, doing that for beam a we can write the equation:

$$\delta\varphi_a = \delta\varphi_{BS1} + \delta\varphi_{M1} + \delta\varphi_{BS2L} + \delta\varphi_{PZ2+P2} + \delta\varphi_{SM} + \delta\varphi_{FM}. \tag{3.10}$$

Doing that for all other beams one can compute the two terms on the right-hand side of equation 3.9:

$$\delta\varphi_b - \delta\varphi_a = \delta\varphi_{M2} - \delta\varphi_{PZ2+P2} \tag{3.11}$$

$$\delta\varphi_c - \delta\varphi_{LO} = -\delta\varphi_{M2} + \delta\varphi_{PZ2+P2} \tag{3.12}$$

from where it can be seen that the contributions are anti-correlated and the net result is that $\delta(\Delta\varphi_s) = 0$. So even though the phase of different beam pairs fluctuates significantly during even short time intervals, this experimental configuration is such that they cancel out almost perfectly, allowing the measured signal to have a much more stable phase [142].

It must be stressed that this analysis focused on phase fluctuations induced by optical elements on the setup, disregarding single beam fluctuations that can be created by strong air currents in the setup for instance. To minimize this problem the setup is enclosed by a box to minimize air currents and the optical components are assembled within as small an area as possible on the bench (30 cm x 50 cm).

3.6 Data processing

In this Section we will describe the multiple steps necessary to generate complex-valued 2D-ES spectra from our experimental setup. For each given value of the population time T, the raw data we collect consists of three files. The first corresponds to the transient grating signal of the sample interfering with the local oscillator as a function of the coherence time τ, which is spectrally resolved in the emission axis $\tilde{\nu}_3$, and thus contains the main 2D-ES signal (Figure 3.4 is an example). We shall refer to this type of data as a spectral interferogram. The other files are used to recover the phase, with the second containing the pump probe spectrum for the same T, acquired with beam b acting as the pump and the LO acting as the probe; and the third file contains the LO spectrum after it propagated through the sample (both files are obtained as described in Section 3.4).

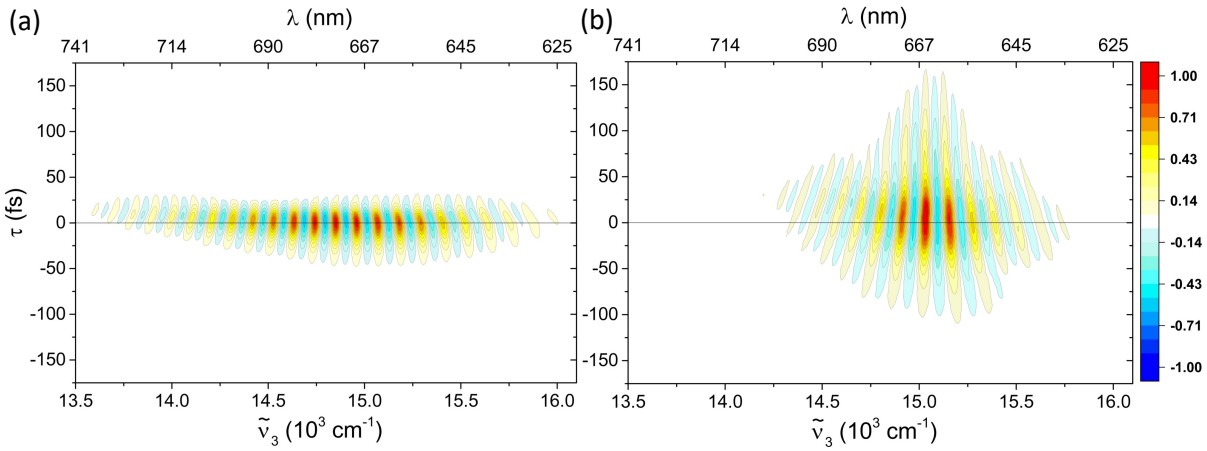

Figure 3.7: **(a)** Transient grating signal from a fused silica window at $T = 0$ fs interfering with the LO beam, as a function of τ. The LO beam arrived 321.2 fs later than the others on this day (see text). **(b)** Same as (a), but for a porphyrin monomer sample at $T = 70$ fs. This is part of the set of experiments discussed in Section 5.1.

Before starting the measurement, the following two steps are always performed. First we obtain the relative delay between the local oscillator and the other beams by performing a transient grating FROG scan of a fused silica window with beam c blocked. Here we use the delay stages DS1 + PZ1 (see Figure 3.1), which delays beams c and LO against a and b, and the signal is emitted along the direction of beam c. In order to direct this signal to the detection system, a flip mirror is introduced into the setup in this step, and the LO beam is blocked after the window. Secondly, these changes are then reversed and with the setup back to what was described in Section 3.3 we perform a 2D-ES scan of the fused silica window at $T = 0$ fs, obtaining the three files described in the previous paragraph. Figure 3.7a shows the window transient grating signal interfering with the LO beam as a function of τ for the data presented in Section 5.1, which we will use as a reference here.

In Figure 3.7b we show the spectral interferogram of a zinc-porphyrin monomer sample at $T = 70$ fs recorded after the fused silica data in Figure 3.7a. The details of the sample are given in Section 4.1 and the local oscillator and linear absorption spectra for this measurement are shown in Figure 5.1, but they are not essential for the data processing discussion. The objective is to use the spectral interferograms from Figures 3.7a,b to obtain complex-valued 2D-ES spectra as a function of excitation and emission wavenumbers $(\tilde{\nu}_1, \tilde{\nu}_3)$. We begin by noting that the spectral interferogram $I_{SI}(\tau, T =$

70 fs, $\tilde{\nu}_3$) from Figure 3.7b is computed from equation 3.3 and can be written as:

$$\begin{aligned} I_{SI}(\tau, T = 70, \tilde{\nu}_3) =& |E_s(\tau, T = 70, \tilde{\nu}_3)|^2 \\ &+ E_s(\tau, T = 70, \tilde{\nu}_3) E^*_{\mathrm{LO}}(\tilde{\nu}_3) e^{i2\pi c\tilde{\nu}_3(t_s - t_{\mathrm{LO}})} \\ &+ E^*_s(\tau, T = 70, \tilde{\nu}_3) E_{\mathrm{LO}}(\tilde{\nu}_3) e^{-i2\pi c\tilde{\nu}_3(t_s - t_{\mathrm{LO}})}, \end{aligned} \tag{3.13}$$

where we have neglected the scattering contributions written in equation 3.3. We recall that due to the chopping sequence used the intensity of the LO beam has already been removed from this expression. We now note that each of the terms in equation 3.13 is centered at a different point along the detection time axis (t, which is the Fourier pair of $2\pi c\tilde{\nu}_3$): the first term is centered at $t = 0$, while the second and third terms are centered at t_{LO} and $-t_{\mathrm{LO}}$ respectively. We are interested in recovering $E_s(\tau, T, \tilde{\nu}_3)$, and in order to isolate this term we can perform a Fourier transform of the data over the $\tilde{\nu}_3$ axis. Figure 3.8 shows the absolute value of this Fourier transform for $\tau = 0$ fs of both the window and the sample signal at $T = 70$ fs (from Figure 3.7a,b) and all three terms from equation 3.13 can be identified. This is the same windowing procedure mentioned when we discussed the removal of light-scattering contributions in Section 3.4.

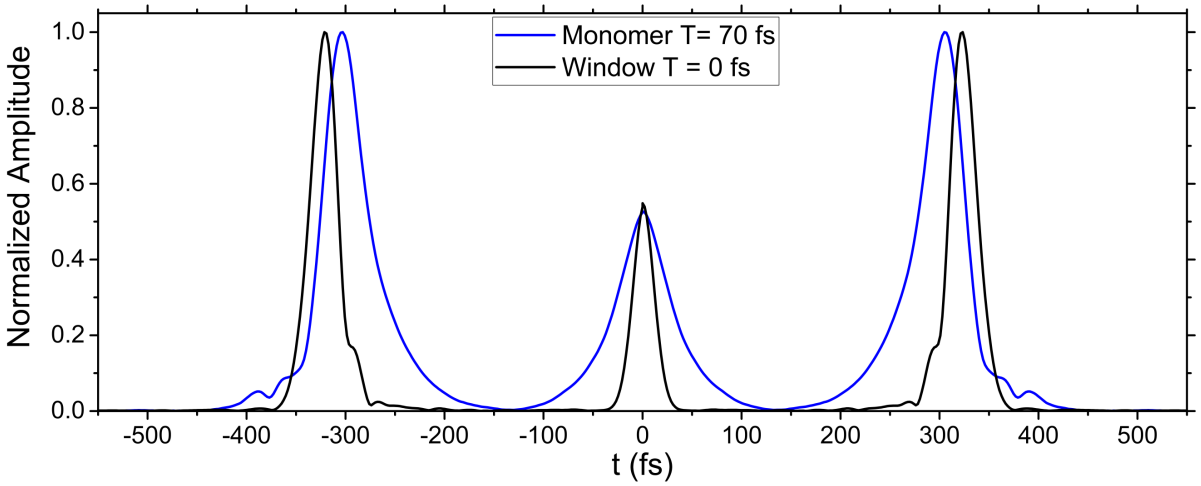

Figure 3.8: Fourier transform of the interferograms from Figures 3.7a (black) and 3.7b (blue) at $\tau = 0$ fs. The desired signal $E_s(\tau, T, \tilde{\nu}_3)$ can be recovered from the peak at positive detection times (see text).

In order to isolate the 2D-ES signal we apply this Fourier transform along $\tilde{\nu}_3$ for each coherence time point, and then apply a rectangular filter in the time domain that selects

only the the term which contains the desired signal:

$$E_s(\tau, T, \tilde{\nu}_3)E^*_{\mathrm{LO}}(\tilde{\nu}_3)e^{i2\pi c\tilde{\nu}_3(t_s-t_{\mathrm{LO}})} = |E_s(\tau, T, \tilde{\nu}_3)||E_{\mathrm{LO}}(\tilde{\nu}_3)|e^{i2\pi c\tilde{\nu}_3(t_s-t_{\mathrm{LO}})}e^{i(\phi_s-\phi_{\mathrm{LO}})}, \quad (3.14)$$

where we have rewritten the signal and conjugated LO fields as a product between their absolute value and phase. For each value of T we acquire the intensity of the LO beam traveling through the sample $|E_{\mathrm{LO}}(\tilde{\nu}_3)|$, and from our reference window measurement (Figure 3.7a and black line in Figure 3.8) we can recover the phase $e^{i2\pi c\tilde{\nu}_3(t_s-t_{\mathrm{LO}})}e^{i(\phi_s-\phi_{\mathrm{LO}})}$, as the delay between the LO beam and the transient grating signal is known [145]. This still does not perfectly recover the phase for the 2D-ES spectra, because ϕ_s for the non-resonant transient grating signal of the window measured in the $-\boldsymbol{k}_a + \boldsymbol{k}_b + \boldsymbol{k}_c$ direction is different than ϕ_s from the sample, which includes rephasing and non-rephasing resonant signals. Therefore, a direct reference to the sample is required, which is made using the pump-probe measurement and the projection-slice theorem [146].

In order to prepare the data for that, we first recall that so far we have isolated the absolute value of the signal $|E_s(\tau, T, t)|$ and recovered the $\tilde{\nu}_3$ dependence of the phase for each coherence time. Next, we proceed to perform a Fourier transform back from t to $\tilde{\nu}_3$, yielding $E_s(\tau, T, \tilde{\nu}_3)$. This signal is a slowly varying function of τ, because the delay stage movement sequence employed is in the full rotating wave frame (see Section 3.4.1). Thus, to recover the oscillatory signal as a function of τ, we can multiply the measured signal by $e^{i2\pi c\tilde{\nu}_0\tau}$, where $\tilde{\nu}_0$ is the central wavenumber of our laser spectrum. Figure 3.9 shows the real part of the signal obtained from this procedure for the data in Figures 3.7 and 3.8 for $\tilde{\nu}_3 = 15435$ cm^{-1}. Figure 3.9 makes clear why measuring in the rotating wave frame is so useful: in our data acquisition we scanned τ in time steps of 5 fs, but from this Figure it is clear that when not measuring in the rotating frame sub-femtosecond time steps would be necessary, requiring greater phase stability and longer acquisition times.

At this stage we have $E_s(\tau, T, \tilde{\nu}_3)$ with the correct oscillatory behavior as a function of τ, so in order to obtain the desired 2D-ES spectrum, we merely apply a Fourier transform over τ, yielding $\tilde{E}_s(\tilde{\nu}_1, T, \tilde{\nu}_3)$, with rephasing and non-rephasing spectra being obtained by applying the Fourier transform to the positive and negative coherence time axes respectively. As mentioned above, the phase of these spectra is not yet correct, and to correct it we employ a phasing algorithm [14, 140, 146].

The phasing algorithm is based on the projection-slice theorem from Fourier analysis,

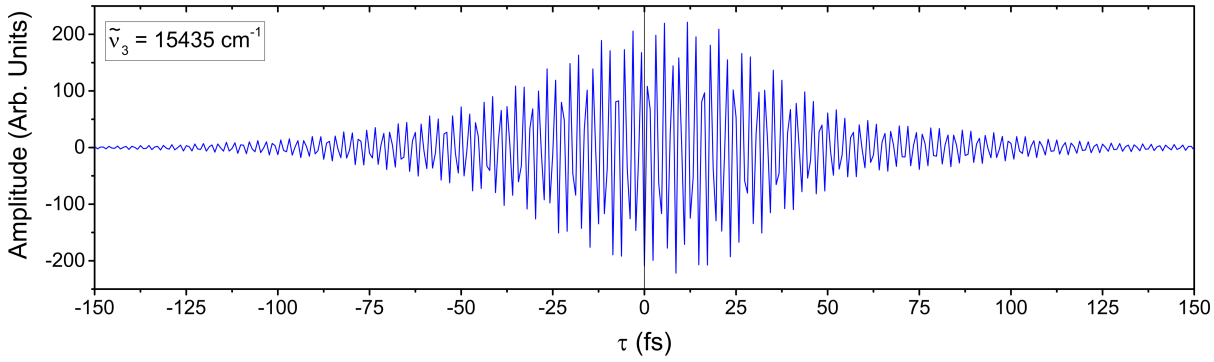

Figure 3.9: Real part of the signal field as a function of τ for $\tilde{\nu}_3 = 15435$ cm^{-1} extracted from Figure 3.8 as described in the text. Positive (negative) values of τ correspond to the rephasing (non-rephasing) signal.

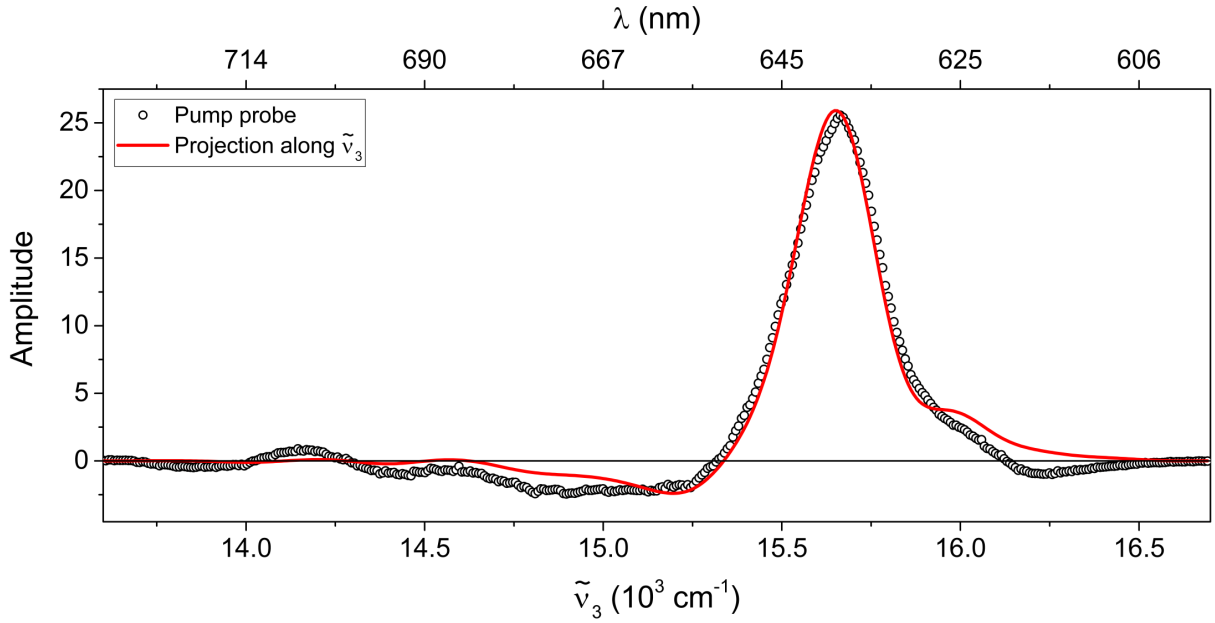

Figure 3.10: Comparison between the integral of the real part of sum of rephasing and non-rephasing 2D-ES spectra to the pump probe spectrum. The phase of the 2D-ES spectra has been adjusted to give the best match between them (see text).

which when applied to 2D-ES states that the integral of a properly phased absorptive 2D-ES spectrum over the excitation axis ($\tilde{\nu}_1$) is equal to the broadband transient absorption spectrum (commonly referred to as the pump probe spectrum) [14]. Pump probe spectra automatically include both rephasing and non-rephasing pathways, and an absorptive 2D-ES lineshape corresponds to an equally weighed sum of rephasing and non-rephasing spectra [121, 122]. Therefore, in order to recover the correct phase of our spectra we sum rephasing and non-rephasing contributions and multiply them by an overall phase $e^{i((\tilde{\nu}_3-\tilde{\nu}_0)2\pi c t_c+\varphi_c)}$, where t_c and φ_c are parameters which can be adjusted by a genetic fitting algorithm which find the values which correspond to the best match between the pump

probe and the 2D-ES integral over $\tilde{\nu}_1$ [132]. An amplitude scaling factor is also used to properly scale the 2D-ES amplitude to the pump probe. As a result, we finally obtain the desired complex-valued 2D-ES maps, which are shown in Figure 3.11a (absorptive, the real part) and 3.11b (dispersive, imaginary part). Now that the correct phase has been recovered, the complex-valued rephasing and non-rephasing maps can also be plotted (these are shown in Figures 5.2 and 5.3 in Chapter 5, where they are used).

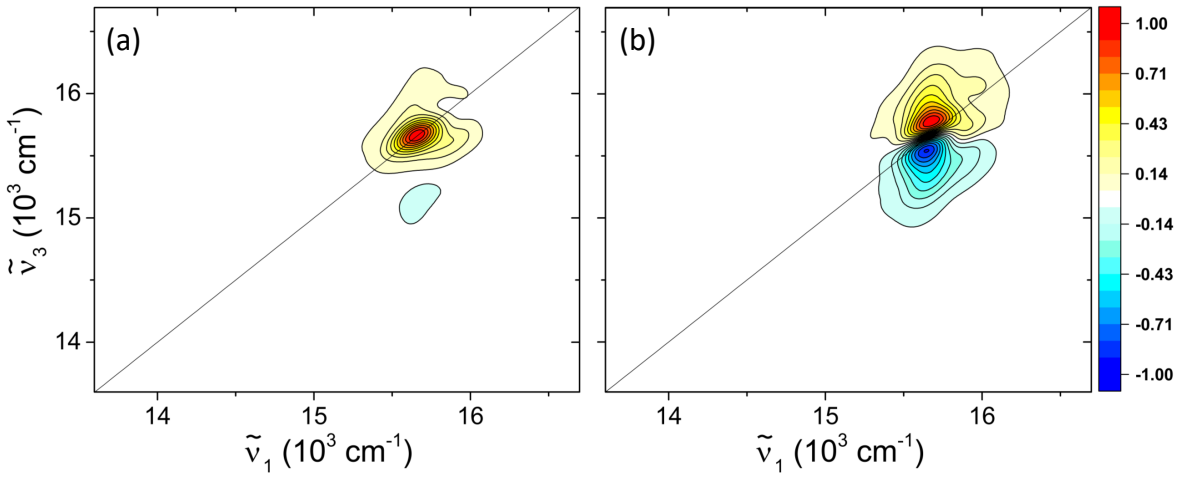

Figure 3.11: **(a)** Absorptive and **(b)** dispersive 2D-ES maps at $T = 70$ fs after the phasing process is complete. Each map is individually normalized. The sample has negligible signal below 15000 cm^{-1}, which can be observed here and in Figure 3.7b. The pulse has bandwidth in this region however, as Figure 3.7a shows, so the $(\tilde{\nu}_1, \tilde{\nu}_3)$ scales were chosen to match those from Figure 3.7a.

3.7 Summary

In conclusion, the experimental setup described in this Chapter combines many advantages for the measurement of 2D-ES spectra. The boxcar geometry ensures minimal background and allows us to independently recover rephasing and non-rephasing spectra. The optical design ensures phase stability and places the measurement in the rotating wave frame, which significantly reduces data acquisition times (also helped by the near shot-to-shot acquisition rate), allowing us to scan many more values of T in a reasonable time span. Finally, the two choppers enable us to both better remove scattering contributions and to acquire the local oscillator and the pump probe spectra quasi simultaneously with the 2D-ES signal, which helps ensure that the data processing required to recover the final maps is performed comparing datasets acquired under almost identical conditions. In the next Chapters we use this setup to perform detailed experiments on vibrational

wavepacket motion on a porphyrin monomer with very good signal to noise, which allows us to establish results on coherence pathway signatures in 2D-ES.

Chapter 4

Vibrational Signatures in 2D-ES

This and the following Chapter focus on investigating signatures of vibrational coherences in 2D-ES, which are observed in the form of oscillatory signals at some $(\tilde{\nu}_1, \tilde{\nu}_3)$ points as a function of T, as we described in Section 2.7. Vibrations coupled to electronic transitions are ubiquitous [147, 148] and it is thus important that control studies benchmarking vibrational signatures in 2D-ES are performed. To this end, we study a zinc-porphyrin monomer which has its lowest singlet electronic transition strongly coupled to a vibrational mode at 375 cm^{-1}. Because excitonic effects can be ruled out, a monomer molecule consists in an ideal sample to test the predictions based on the double-sided Feynman diagrams made in Chapter 2. While the zinc-porphyrin monomer is a simple molecule when compared to systems that have typically been studied with 2D-ES [15, 49, 55, 77, 116, 149–151], the studies of comparably simple systems reported in the literature [80, 86, 150] were performed before fast data acquisition with good signal over noise was available. Besides that, some theoretical developments only arose after those studies were published, i.e., significant advances in data analysis tools have been developed since the pioneering experiments, and newer theory – such as that of Section 2.8 –remained untested.

Historically, oscillations in 2D-ES signals have been the subject of a lot of attention since measurements on the Fenna-Matthews-Olson (FMO) complex showed oscillatory behaviour with picosecond dephasing times [68]. These were assigned as electronic in origin (in spite of the expectation that electronic coherences should dephase in much faster timescales [69]) and interpreted as possibly playing a role in a coherent energy transfer mechanism in the FMO complex and other light harvesting systems [68,72]. However, later

experimental and theoretical work questioned the assignment of the beating signatures as arising from a pure electronic coherence [100, 152, 153].

These developments highlight the importance of understanding oscillatory signals in 2D-ES. Essentially, the main reason why interpreting beating signatures in 2D-ES is difficult is the technique's great sensitivity to capture different molecular phenomena, often via oscillations as a function of population time. For instance, the three pulse sequence used in 2D-ES can create coherences between all allowed transitions that are resonant with the excitation field, all of which can generate their own oscillatory signals. This will generally include electronic coherences between different energy levels and – if the electronic transition is coupled to one or more vibrational modes – also coherences between the different vibrational sublevels [18]. On top of that, Raman modes of the solvent may also generate oscillations in 2D-ES maps through non-resonant pathways if the excitation laser has broader bandwidth than the Raman frequency [154].

In this chapter we report 2D-ES studies of the porphyrin monomer and start discussing the results on the basis of absorptive spectra. We proceed to analyse coherent oscillations, for which we focus on rephasing and non-rephasing maps separately. We find that the results do not match the forecast from the Feynman diagrams alone. However, we note that previous work by Butkus *et al.* showed that the phase of coherent oscillations due to a single Feynman diagram is a function of $(\tilde{\nu}_1, \tilde{\nu}_3)$, and when interference between oscillations from neighboring color peaks is taken into account, experiment and calculations are shown to match well. We conclude the Chapter by discussing the consequences of these results; an earlier description of this data was published in reference [123].

4.1 Steady state spectroscopy of the zinc-porphyrin monomer

The zinc-porphyrin monomer samples were synthesized by the group of Professor Harry L. Anderson at the University of Oxford as reported in reference [155]. Figure 4.1 shows the UV-visible linear absorption spectrum of the porphyrin chromophore in toluene with 1% of pyridine to suppress aggregation. As it is typical of porphyrins, it is characterized by the presence of two distinct bands in the visible: the so called Q and B-bands [156]. The Q-band corresponds lowest energy transitions which are quasi-forbidden, the maximum

absorption of which in toluene with 1% of pyridine is observed at 15550 cm^{-1} (643 nm). The B band (also called Soret band) is strongly allowed, having an extinction coefficient more than 6 times larger than the Q band, and here it consists of two peaks in the blue region of the spectrum. The split observed both in the Q and B bands can be attributed to the asymmetric substituents (see Figure 4.1), which lower the symmetry from D_{4h} to D_{2h}, creating a distinction between the x and y axes [157, 158]. Besides these two bands, a third one can also be seen, a very broad (albeit not very intense) absorption ranging from around 28000 cm^{-1} to 34000 cm^{-1}, which is sometimes called the N band.

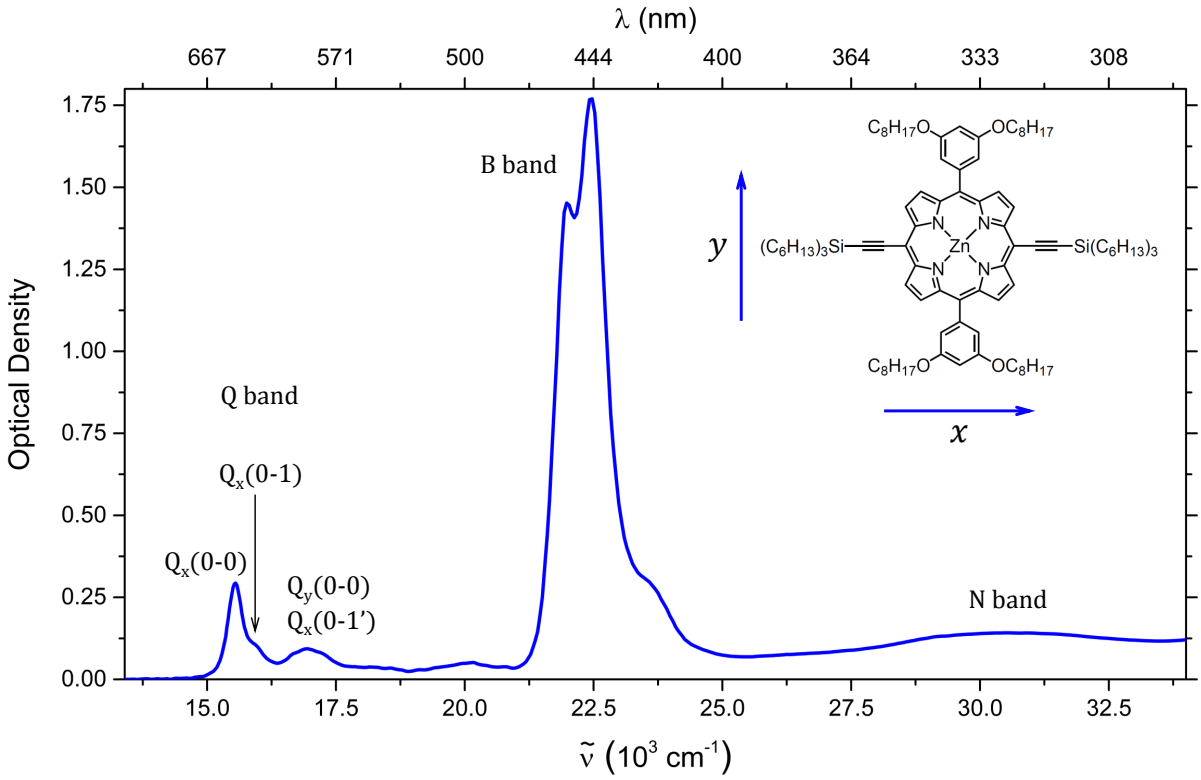

Figure 4.1: Linear absorption of the porphyrin monomer in the visible and near UV. Inset: structure of the porphyrin monomer and transition dipole moment orientation in the molecular frame.

There are absolute assignments of the dipole transition directions based on quantum mechanical calculations [158], polarized absorption experiments in stretched polymer film [159] and excitation dependence of the fluorescence anisotropy [160]. The least energetic peak in the B band, here observed at 21980 cm^{-1} (455 nm), has been assigned to the B_x transition, whereas the peak at 22450 cm^{-1} (445 nm) has been assigned mostly to the B_y transition, although vibronic contributions from B_x are overlapping [160].

Our work in this thesis focuses on the Q band, so in Figure 4.2 we show the normalized linear absorption spectrum of this band alone (blue line), as well as the fluorescence

spectrum with excitation at 625 nm (16000 cm^{-1} – red line). The main absorption peak at 15550 cm^{-1} corresponds solely to the Q_x transition and is accompanied by a vibronic shoulder which is blue-shifted from the main transition by around 375 cm^{-1} [161]. The vibrational mode at 375 cm^{-1} corresponds to a zinc-pyrrole breathing motion (ν_8 in the usual nomenclature) and strongly couples to the electronic transition in metalloporphyrins [162].

Previous work mistakenly assigned the transition dipole moments of this lower energy band ($\tilde{\nu} < 16350$ cm^{-1}) as being parallel to the y axis in the molecular reference frame [160], but a more recent study has reassigned these as being parallel to the x axis [161], which is consistent with the intuitive picture that π-conjugation between the butadiyne links along the x axis and the porphyrin extends the spatial localization and lowers the energy of this transition (see Figure 4.1), as also observed in butadiyne-linked porphyrin oligomers [157]. This electronic transition at $\tilde{\nu} = 15550$ cm^{-1} will thus be referred to as $Q_x(0-0)$, while the vibronic shoulder at 15925 cm^{-1} will be labelled $Q_x(0-1)$, consistent with reference [160]. That study has shown that the other absorption peak in the Q-band, centred at around 17000 cm^{-1} (588 nm), has contributions from transition dipole moments in both x and y directions in the molecular frame, so within that band there are contributions from $Q_y(0-0)$, as well as vibronic peaks from the Q_x transition coupled to higher energetic vibrational modes.

Focusing in the Q band, in Figure 4.2 we see that the emission maximum is observed at 15480 cm^{-1}, corresponding to a Stokes shift of only 70 cm^{-1} (3 nm in this spectral region). The monomer is thus a very convenient sample in order to benchmark vibrational coherences in 2D-ES, as a large Stokes shift would have to be taken into account when addressing coherence pathways, whereas here it seems safe to assume that the minor shift observed will not significantly affect coherent wavepacket dynamics in the excited state. The fluorescence spectrum also shows there are further vibrational modes coupled to the Q_x transition, as indicated by the broad emission band around 14200 cm^{-1} (704 nm), corresponding approximately to a 1350 cm^{-1} red-shift from the main absorption peak. It is established that zinc-porphyrins have their main electronic transition coupled to a vibrational mode in this region [162, 163], and a blue-shift of 1350 cm^{-1} from $Q_x(0-0)$ results in $\tilde{\nu} = 16900$ cm^{-1}, which is roughly the centre of the higher energetic absorption band, where reference [160] found contribution from both x and y polarizations. Therefore,

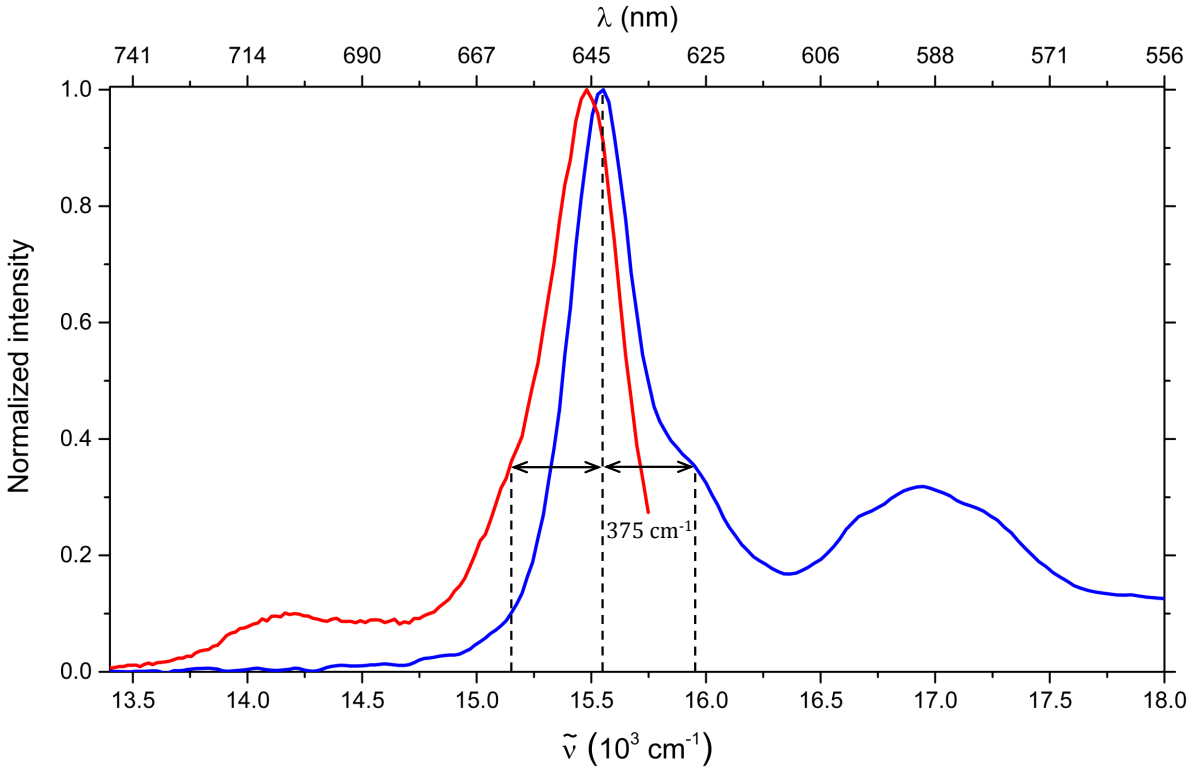

Figure 4.2: Linear absorption (blue) and fluorescence (red) of the porphyrin monomer. The excitation wavelength was 625 nm (16000 cm^{-1}).

besides consisting of the $Q_y(0-0)$ transition, that band also includes the vibronic peak from the 1350 cm^{-1} mode coupled to Q_x, and this will be referred to as $Q_x(0-1')$, where the prime indicates a different vibrational mode.

For the 2D-ES measurements the samples were diluted in different solvents with 1% by volume of pyridine (toluene in this Chapter and *n*-pentane in the next) to achieve a maximum optical density of around 0.3 in the spectral region excited by the laser (the Q band in this work), corresponding to a concentration of approximately 80 μM in 1 mm pathlength cells, and 400 μM in 200 μm pathlength cells. The 200 μm pathlength cells have the advantage that at 5 times higher solute concentration the Raman contributions from the solvent are minimized, compared to the signals from the sample. Moreover, the fact that there are 5 times as many molecules in the same focal spot also means that higher signals can be obtained for the same incident power and sample optical density, which allowed us to perform the measurements at lower power (usually a factor of 2) when the short pathlength cells were used. Generally 1 mm pathlength cells were used for the experiments in this Chapter (performed in 2014) and 200 μm cells were used for the experiments in the next Chapter (performed in 2015 and 2016), although repeat

experiments included both pathlengths throughout. The only pathlength dependent result was the relative importance of Raman modes of the solvent compared to vibrational modes of the samples described above.

The reason to add 1% by volume of pyridine to all samples is to prevent aggregation, as pyridine coordinates the central zinc of the porphyrin. To confirm that 1% was enough to suppress aggregation, comparisons to the linear absorption at lower solute concentrations as well as with more pyridine were made, and no signs of aggregation were observed in the samples used. Some of the 2D-ES experiments were performed flowing the sample and the results obtained were usually the same of those in static cells. The exception was when the solvent was dichloromethane (either with 1% of pyridine or in a 10:10:1 mixture of dichloromethane, tetrahydrofuran and pyridine), for which the transient grating signal was observed to drop nearly to zero within one second of illuminating the sample at a 10 kHz repetition rate. This drop in signal was avoided by flowing the sample, in which case the 2D-ES experiments yielded the same results as for other solvents. Still, none of the experiments in dichloromethane are further discussed in this thesis, as the origin of this bleaching and its effect in the data were not established.

4.2 2D-ES experiments on the zinc-porphyrin monomer

In order to study vibrational coherences from the 375 cm^{-1} mode with 2D-ES, we used the laser spectrum shown in Figure 4.3a, which covers both the $Q_x(0-0)$ and the $Q_x(0-1)$ transitions. The choice of leaving significant bandwidth on the red side of the absorption is important because 2D-ES peaks redshifted from the main transition in the detection axis are expected for this system (see Section 2.7.1). Figure 4.3b shows the TG-FROG of the corresponding pulses obtained using a fused silica window, which shows the pulses were close to the Fourier Transform limit. The vertical dashed line in Figure 4.3b corresponds to the maximum frequency as obtained by a fit of the profile to a single Gaussian for each time step, and shows that the central frequency stays approximately constant.

In order to recover the real and imaginary parts of our 2D-ES spectra (ultimately allowing us to obtain absorptive lineshapes) we need to phase the data by comparing the integral of the 2D-ES signals along the excitation axis to a broadband transient

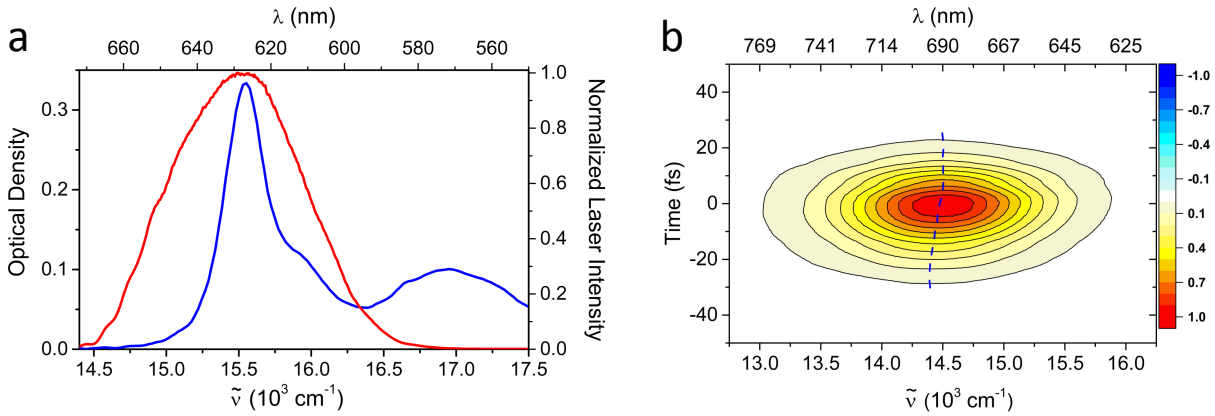

Figure 4.3: **(a)** Linear absorption of the zinc-porphyrin monomer sample (blue line) and normalized laser spectrum used for the 2D-ES measurements described in this chapter. **(b)** Transient grating FROG of the pulses used in the experiment obtained using a fused silica window.

absorption measurement recorded under the same conditions, as described in Section 3.6. For completeness, in Figure 4.4a we show the broadband transient absorption spectrum obtained using pulse b as the pump and pulse LO as the probe at $T = 120$ fs, while Figure 4.4b shows the typical quality of the phasing procedure for this experiment. We note that on both sides of the main peak there are signs of excited state absorption, which will be discussed later, along with the 2D-ES data.

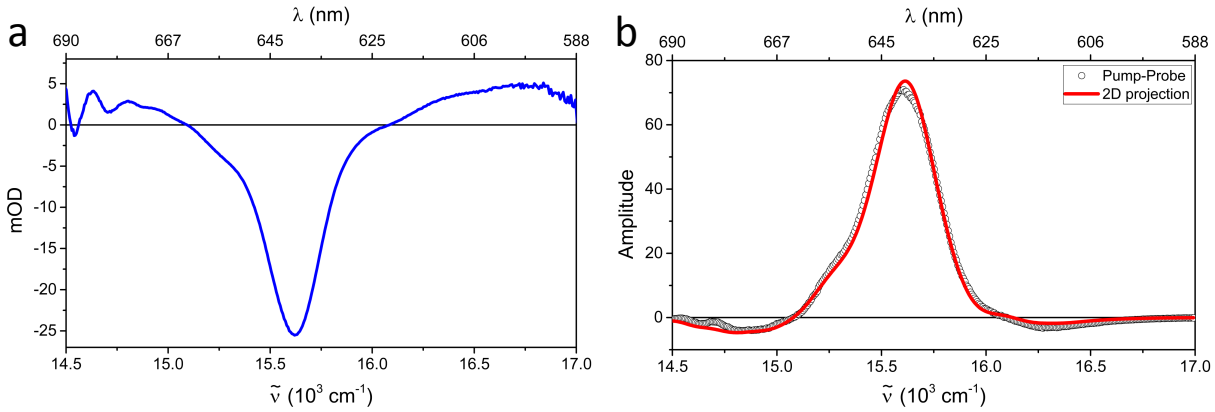

Figure 4.4: **(a)** Broadband transient absorption at $T = 120$ fs. **(b)** Comparison between the broadband transient absorption spectrum and the integral along $\tilde{\nu}_1$ of the real part of the rephasing plus non-rephasing spectra after the phasing process.

The absorptive 2D-ES spectrum at $T = 120$ fs is shown in Figure 4.5a. At this relatively early time, the expected absorptive 2D-ES map for one electronic transition coupled to a single vibration is made up of a six-peak structure, as sketched in Figure 2.9 for rephasing and non-rephasing signals – the absorptive consists of overlaying these contributions. The expected peak positions in the 2D map form a rectangular lattice where neighboring points are displaced by $\tilde{\nu}_0 = 375$ cm^{-1} along $\tilde{\nu}_1$ or $\tilde{\nu}_3$, so for this sample

significant overlap between neighbouring contributions is present, as the corresponding peak in the linear absorption has a width of around 400 cm^{-1}. To ease comparison with theory, the central positions of the expected peaks were marked with circles and labelled from A to F in Figure 4.5a. Considering the displaced harmonic oscillator model, the peak marked as F consists only of oscillatory contributions, and we chose to display the map at $T = 120$ fs because the off-diagonal oscillations are more pronounced at this time.

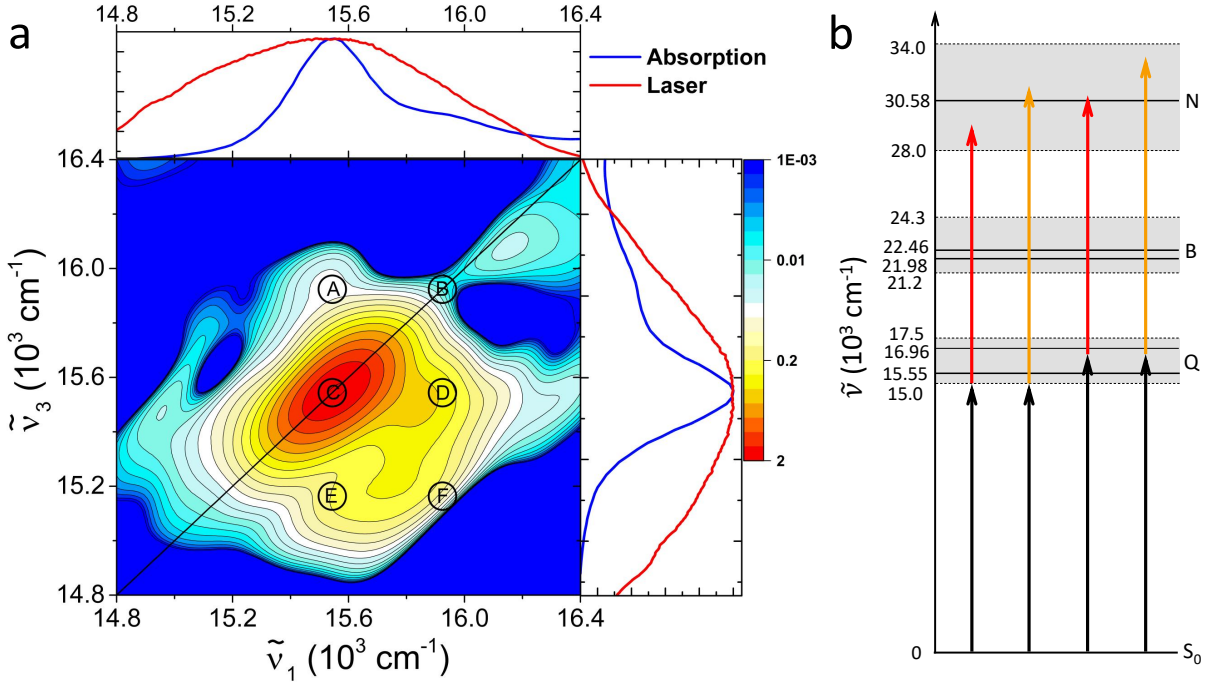

Figure 4.5: **(a)** Absorptive 2D-ES spectrum of the zinc-porphyrin chromophore in toluene at population time $T = 120$ fs. The sample's linear absorption (blue) and the laser spectrum (red) are shown in the top and right-side graphs. The signal's amplitude is shown in colors, divided in 21 evenly spaced contour lines on a $\log_{10}$ scale. The center of different Feynman diagram contributions are marked with circles and labelled with letters. **(b)** Energy level scheme for the excited state absorption contributions. The black arrows represent the lowest and highest possible excitation energies in the Q band in this experiment. The orange and red arrows correspond to the high and low energy edges of the laser spectrum. See text for details.

Comparing the signals from Figure 4.5a and the marked Feynman diagram positions, we see that there is some agreement (for instance, points A, D and E), but also significant deviation between the experimental results and the predictions of the displaced harmonic oscillator model, especially in point B. We point out that color scale plots suffer in their ability to display contributions of vastly different amplitudes, so in order to avoid the intense diagonal contribution obscuring smaller contributions, we spaced the colors in Figure 4.5a using a $\log_{10}$ scale.

The experimental signal is dominated by an intense diagonal peak (C) at $\tilde{\nu}_1 = \tilde{\nu}_3 =$

15550 cm^{-1}, the lineshape of which is elongated along the diagonal, showing this is an inhomogeneously broadened transition. In Figure 4.5a one can also see the presence of the cross-peaks labelled A, D and E, whereas another local maximum of amplitude is found between the points E and F. Some structure can also be seen elsewhere, but it is in the blue shades of the color scale, thus being a factor of 50 smaller than the main amplitude.

However, the most striking disagreement between the predicted peaks and measured signal is the nearly absent signal amplitude at point B, which should be the center of a peak with a lineshape similar to that of the diagonal peak at C. From the transient absorption measurement in Figure 4.4a it can be readily observed that on both sides of the main peak the signal does not go to zero, but goes through a change of sign, which can be attributed to excited state absorption (ESA), as no other contribution gives rise to signatures with opposite sign. The ESA features are broad and are seen on both sides of the main peak, suggesting that a background of ESA may be overlapping with the signal throughout the spectral region studied. In absorptive 2D-ES maps we observe the sum of ground state bleach (GSB), stimulated emission (SE) and excited state absorption at any given $(\tilde{\nu}_1, \tilde{\nu}_3)$ position, so unless the ESA contribution outweighs the others, the resulting signal will be positive. This means that the possibility that the observed signal is lying on top of an eventual ESA background is difficult to assess.

In Figure 4.5a the logarithmic color scale used implies that only positive features can be displayed, while zero and negative amplitudes are all represented in the same darkest shade of blue. The transient absorption data from Figure 4.4 shows that the signal amplitude at $\tilde{\nu}_3 = 15925$ cm^{-1} is still positive, at around 11% of the maximum value, but it changes sign at $\tilde{\nu}_3 = 16100$ cm^{-1}, suggesting that partial cancellation between ESA and GSB/SE may be hiding the presence of peak B in figure 4.5. In our considerations of the displaced harmonic oscillator model in Section 2.7.1 we have only included one electronically excited state, so all signals predicted were of positive sign. That was because each molecular system has its own higher energy excited states, and the transition dipoles for the transitions between them and lower lying excited states can vary widely, so that no useful predictions can be made from generic Liouville-space pathways such as those in Section 2.7.1. For the particular zinc-porphyrin monomer we are studying here however, the energetic separation between the very broad N band and the Q band we are studying happens to be partially resonant with the laser spectrum, thus making ESA from the Q

to the N band possible, and it is established that this absorption is strong [160].

In order to discuss the ESA in more detail, in Figure 4.6 we show a series of absorptive 2D-ES spectra from $T = 110$ fs to $T = 160$ fs using a symmetric z scale common for all plots with the minimum value observed corresponding to the darkest shade of blue (-0.14 at $T = 160$ fs). We observe a spread of negative signals across the $(\tilde{\nu}_1, \tilde{\nu}_3)$ plane around the positive contributions, consistent with the hypothesis of a negative background being present throughout. Moreover, the negative contributions are more intense in the region defined by $15500 \leq \tilde{\nu}_1 \leq 16250$ cm^{-1}. We also note that there are oscillations in the negative signals as a function of population time, which is expected because of the vibrational coherences arising from the 375 cm^{-1} mode, which generate oscillatory contributions centered in all six positions highlighted in Figure 4.5a. For instance, it can be seen that at position B ($\tilde{\nu}_1 = \tilde{\nu}_3 = 15925$ cm^{-1}) the signal amplitude is around zero at 110 fs, but increases to a positive value after 140 fs, indicating that a positive signal consisting of both oscillatory and non-oscillatory contributions can be there, as forecast in Figure 2.9.

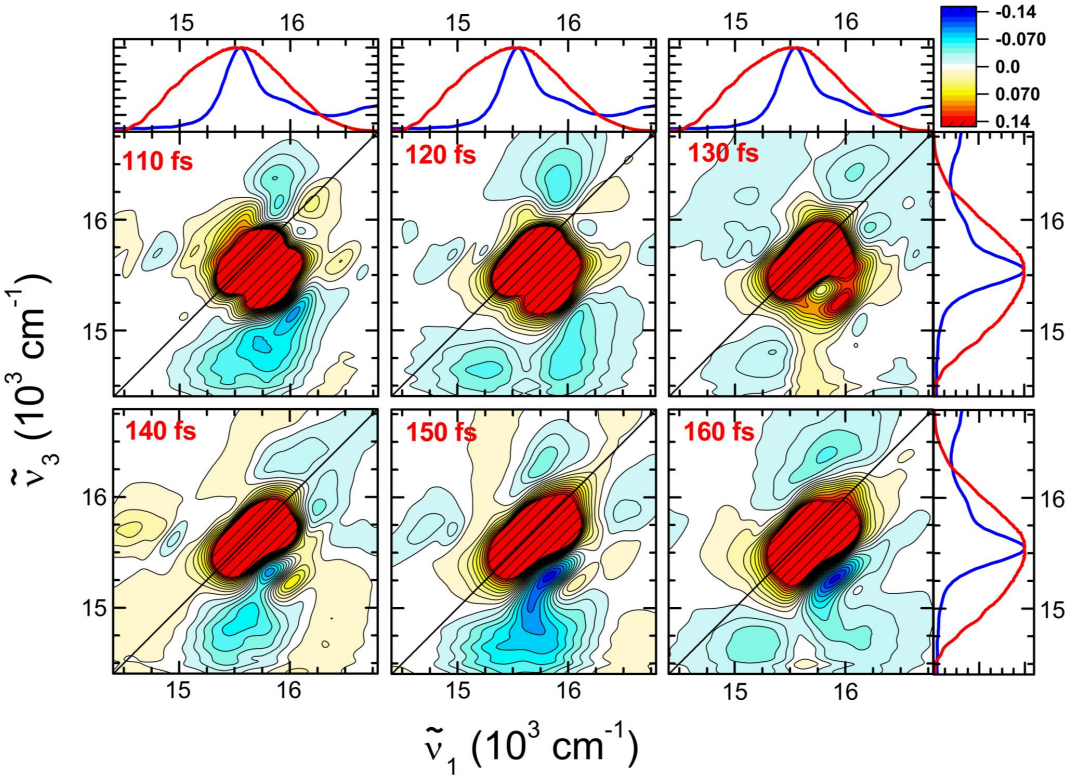

Figure 4.6: Series of absorptive 2D-ES spectra of the zinc-porphyrin chromophore in toluene from $T = 110$ fs to $T = 160$ fs. In order to highlight the negative features, the color scale range has been chosen between 0.14 and -0.14, which was the minimum observed value in this population time range.

ESA pathways have the first two interactions generating a population in the first electronically excited state, and then the third field induces a coherence between this and a higher excited state, from where the signal is emitted (Figure 4.5b shows the energies involved compared to the laser spectrum). Therefore, we can make the following considerations regarding where ESA signals are expected for this measurement. Along the excitation axis $\tilde{\nu}_1$ there can only be ESA signatures at wavenumbers absorbed by the molecule, so $\tilde{\nu}_1 > 15000$ cm^{-1}. For the detection axis $\tilde{\nu}_3$, as the only requirements are that the emission be allowed and lie within the detection range given by the laser spectrum, there are no general restrictions. Thus, in order to discuss the experimental observations we need to consider the Q and N bands and the laser spectrum, as indicated in Figure 4.5b. In this Figure the Q, B and N bands in the linear absorption are represented, with dashed lines indicating the approximate beginning and end wavenumber of each, while the band within is highlighted with a grey background and the main transitions are shown with black lines. The black arrows on the left indicate an excitation at $\tilde{\nu}_1 = 15000$ cm^{-1}, corresponding to the lowest end of the Q band absorption, and the arrows on top of them have lengths corresponding to 14500 cm^{-1} (red) and 16650 cm^{-1} (orange), corresponding to the wavenumbers in which the laser spectrum used had 2% of maximum intensity. Because both extremes of the spectrum lie within the N band after starting from the lowest Q band absorption, we expect that for $\tilde{\nu}_1 = 15000$ cm^{-1} negative contributions will be present throughout the entire $\tilde{\nu}_3$ range. Indeed in Figure 4.6 we observe that for $\tilde{\nu}_1 < 15000$ cm^{-1} the amplitude is very close to zero.

The black arrows on the right of Figure 4.5b represent $\tilde{\nu}_1 = 16650$ cm^{-1}, the blue edge of our laser spectrum, and can be used to apply the same reasoning above to the highest wavenumber region accessed by our experiments. On top of these arrows the red and orange arrows again represent the edges of the laser spectrum, showing that for initial absorption at the highest excitation present in our experiment, the third interaction can also lead to the N band. Thus, if for both extremes of absorption excitation from the Q to the N band is possible for the whole spectral range, we can expect that a background of negative signals be present throughout the 2D-ES maps for $\tilde{\nu}_1 \geq 15000$ cm^{-1}. Finally, we note that it is for the intermediate value of $\tilde{\nu}_1 \sim 15900$ cm^{-1} that the maximum amplitude of the laser spectrum leads to the maximum absorption in the N band, corroborating the hypothesis that peak B in Figure 4.5a is not present due to almost perfect cancellation

with ESA signals.

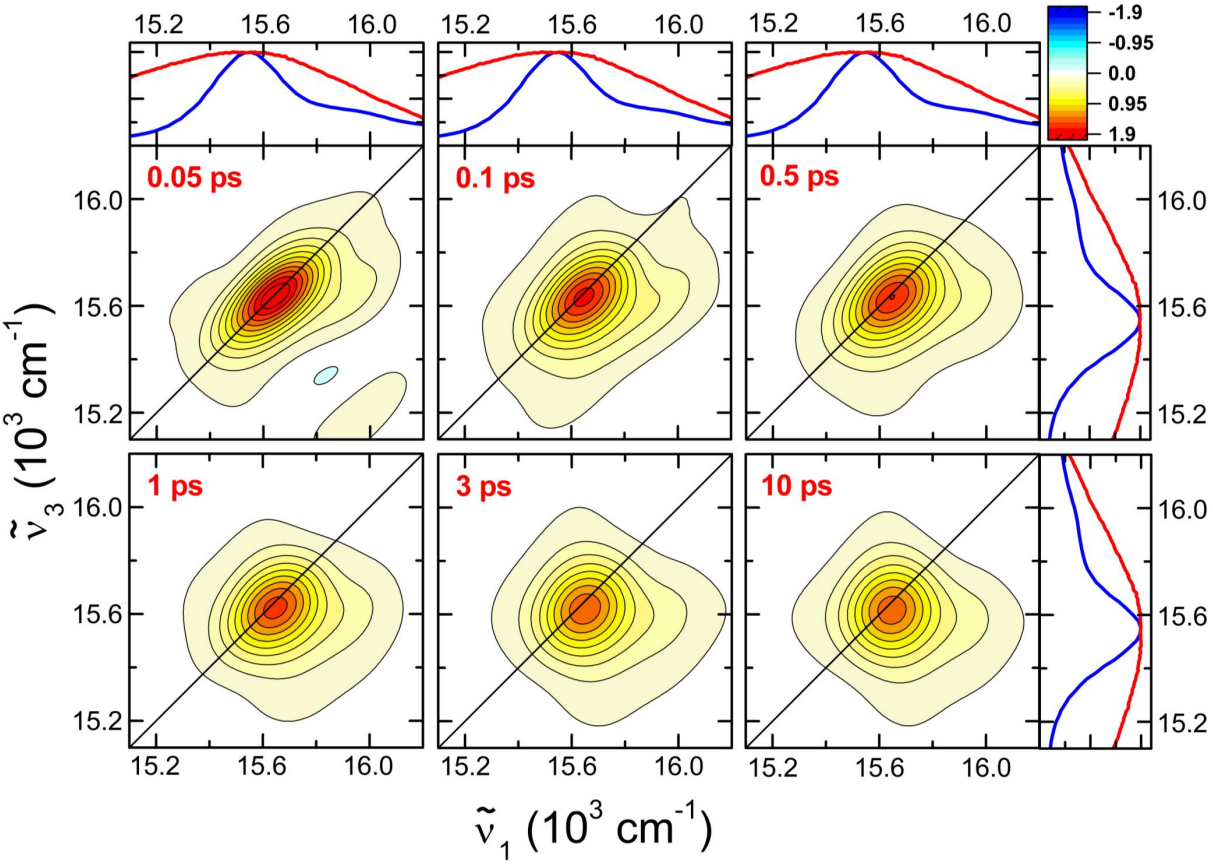

Figure 4.7: Series of absorptive 2D-ES spectra of the zinc-porphyrin chromophore in toluene at selected values of T. The color scale is symmetric and normalized to the maximum signal at $T = 0.05$ ps.

Finally, we would like to briefly discuss the spectral evolution observed for the porphyrin monomer in toluene. To that end, in Figure 4.7 we show a series of absorptive 2D-ES maps at values of T selected to highlight the changes observed in the spectrum (the main differences between Figures 4.7 and 4.6 are the color scale and values of T shown). At $T = 50$ fs the lineshape is elongated around the diagonal, indicating an inhomogeneously broadened transition. We observe that as T increases, the lineshape gradually becomes round, which we assign to solvent-induced spectral diffusion. Although performing a careful analysis of the spectral diffusion process for this molecule is outside the scope of this thesis, we note that the timescale of the lineshape change is around 3 picoseconds, consistent with solvent dynamics timescales of toluene [164]. Furthermore, we observe that at $T = 0.05$ ps the maximum signal lies very close to the diagonal, and it gradually shifts below the diagonal along $\tilde{\nu}_3$. This shift of the maximum signal towards lower detection wavenumbers happens within 1 picosecond and is consistent with the Stokes-shift

observed in the steady-sate fluorescence. Coherent oscillations due to vibrational coupling are also present and will be discussed in detail in the next Section.

4.3 Interference between oscillatory signatures

Now we move on to study the coherent oscillations over T observed in the 2D-ES spectra of the zinc-porphyrin monomer. As discussed in Section 2.7.1, it is more convenient to analyse coherent oscillations in rephasing and non-rephasing maps individually, as each contain only half of the total double-sided Feynman diagrams, resulting in less overlap and simpler interpretation. That Section culminated with Figure 2.9, which is a scheme of where the most important pathways are displayed at their corresponding coordinates in rephasing and non-rephasing 2D-ES maps. Because we will refer to it repeatedly, a copy of that Figure is shown here for convenience (Figure 4.8). The schemes in Figure 4.8 show that a vibrationally coupled electronic transition results in 2D-ES rephasing spectra with six peaks (although the one labelled F in Figure 4.5 above is of purely oscillatory character), while the non-rephasing spectra have only five peaks (with the one missing being at the position labelled F).

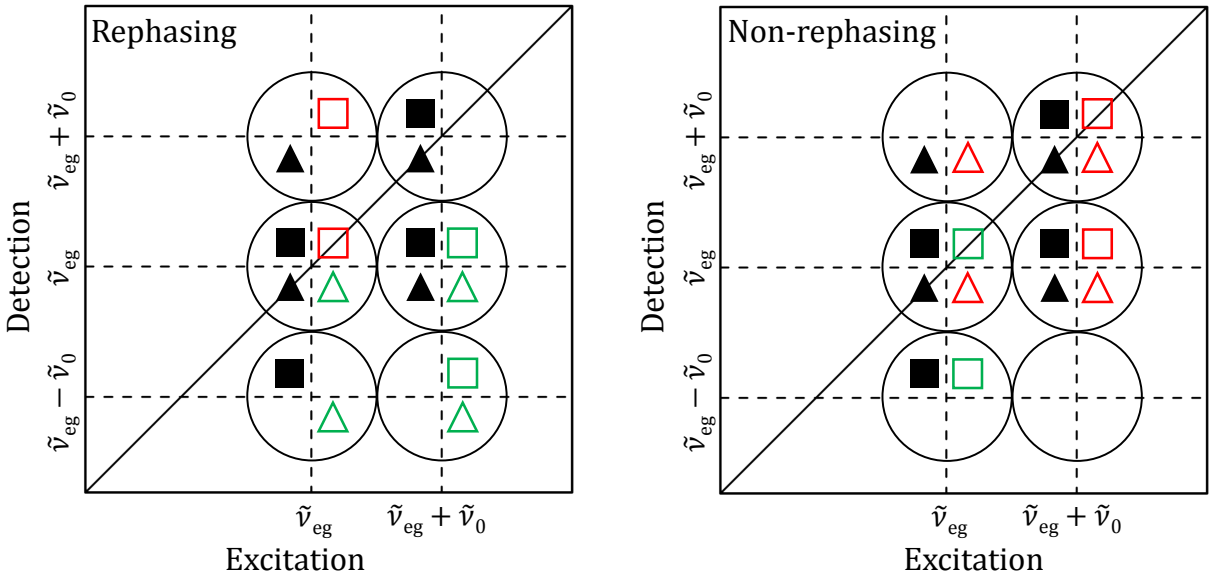

Figure 4.8: Copy of Figure 2.9. Scheme of Liouville-space pathways in a rephasing (left) and non-rephasing (right) 2D maps for the energy level structure shown in Figure 2.4b. See caption of Figure 2.9 for details.

Systematically studying coherent oscillations in 2D-ES spectra can be a difficult task, not only because of the experimental challenge of acquiring a large number of 2D-ES maps

for different values of T with good signal to noise, but also because the sheer amount of data makes the analysis challenging – the datasets discussed in the next Chapter typically consist of over 5 Gb of data after the phasing procedure. Some groups have focused their analysis in single points (or small regions around a point) in the $(\tilde{\nu}_1, \tilde{\nu}_3)$ plane [70, 71, 87, 88, 101, 165], but that can be deceptive in many ways. One reason is that, as discussed in Chapter 2, vibrationally and electronically coupled systems are spectroscopically similar and both give rise to oscillatory contributions, so the presence of an oscillation in a single $(\tilde{\nu}_1, \tilde{\nu}_3)$ pair bears no information regarding the physical nature of the coherence generating it, with even a Raman mode of the solvent being a potential source of oscillations. Although complementary experiments can be used to assess potential contributions from vibrational coherences, this is hardly reasonable justification to ignore the information present in the whole $(\tilde{\nu}_1, \tilde{\nu}_3)$ plane and focus only at a single point. Coherent oscillations appear in patterns, and the presence of a pattern (or lack thereof) helps establish how reliable the data and conclusions are. Here we shall start the discussion with series plots of 2D-ES maps and gradually refine our approach towards a comprehensive analysis, presenting the limitations of different methods.

Our first approach towards analysing the coherent oscillations can be making a series of plots of both rephasing and non-rephasing contributions for different values of T. Because we know the electronic transition we are studying is coupled to a 375 cm^{-1} vibrational mode, we expect coherent oscillations with a period of 89 fs, so in the top of Figure 4.9 we plot a series of 6 rephasing maps with a 30 fs population time interval. In this Figure the peak positions predicted from the displaced harmonic oscillator for the 375 cm^{-1} vibrational coupling are marked by the intersections of the dashed lines. Similarly to what was observed for the absorptive case (Figure 4.5a), the cross-peaks are not completely resolved. This happens for the reasons discussed in Section 4.2, with the aggravating factor of the phase-twisted lineshapes, which extend further in the $(\tilde{\nu}_1, \tilde{\nu}_3)$ plane (see Appendix A). Therefore, the tails of the strongest peak will help obscure smaller oscillatory features.

Careful analysis of the rephasing maps in Figure 4.9 shows that different parts of the signal are oscillating as a function of T. Perhaps the clearest is the main diagonal peak C ($\tilde{\nu}_1 = \tilde{\nu}_3 = 15550$ cm^{-1}), which increases until it reaches a maximum at $T = 150$ fs, after which it decreases and rises again at 240 fs. We note that the value at $T = 240$ fs is smaller than that at $T = 150$ fs, which is expected as population relaxation and dephasing

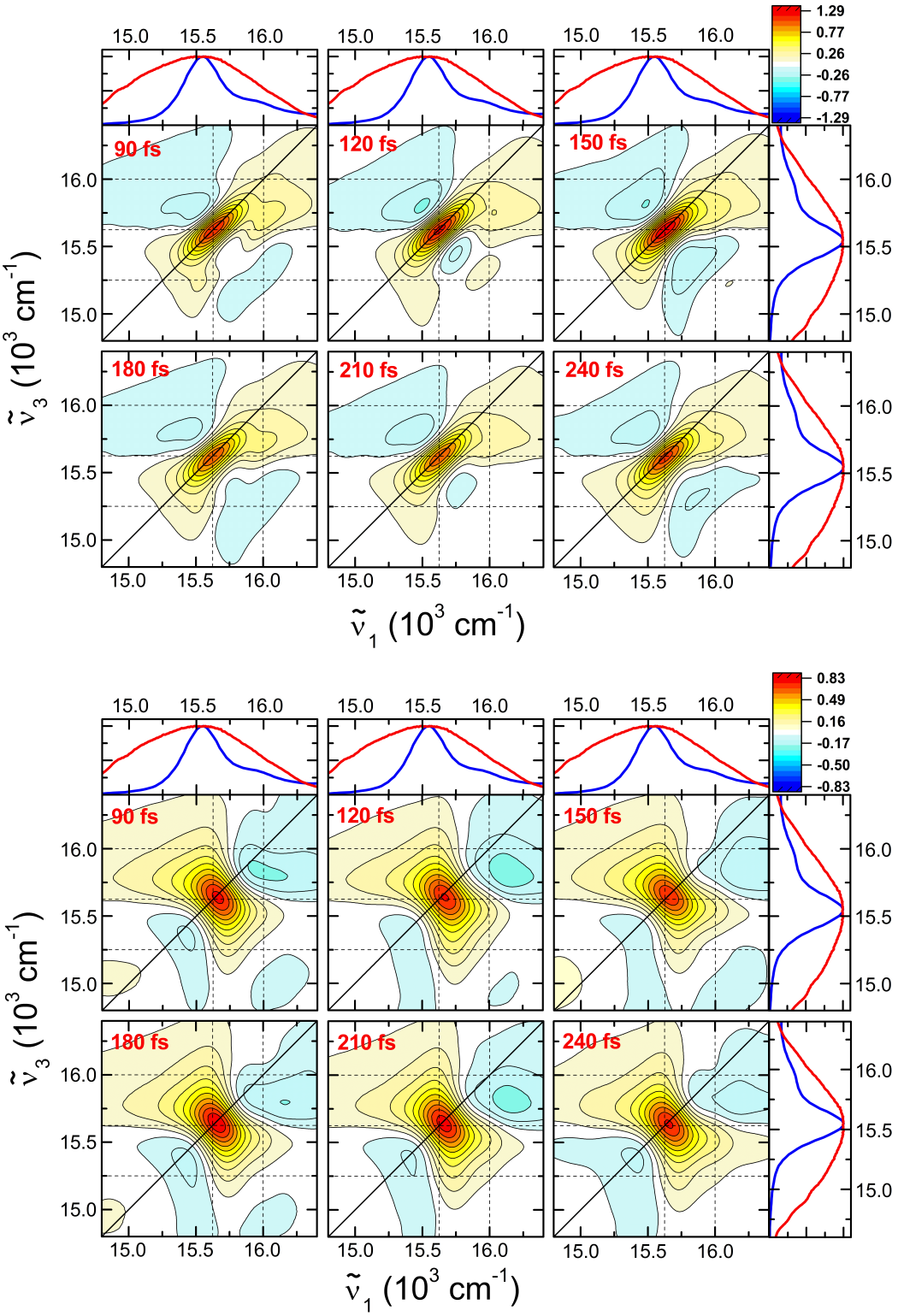

Figure 4.9: Rephasing (top) and non-rephasing (bottom) 2D-ES maps from 90 to 240 fs. The color scale is normalized by the maximum signal: 1.29 at 150 fs (top) and 0.825 at 180 fs (bottom). The points where the dashed lines cross mark the six expected peak positions.

are both contributing to signal amplitude decay. Therefore, it is clear that even a movie of color plots is not an effective way to assess the coherent oscillations, because it is hard to follow the simultaneous relaxation and oscillation of many different coordinates. Nonetheless, it is interesting to note that the observed lineshape comes closest to that of a single electronic transition at $T = 150$ fs, while at $T = 90$ fs significant amplitude from the oscillatory cross-peaks below the diagonal obscures the negative part of the lineshape in this region. This result shows that these oscillations at different $(\tilde{\nu}_1, \tilde{\nu}_3)$ points are not in phase.

For completeness, we show the corresponding series of non-rephasing 2D-ES maps at the bottom of Figure 4.9. The non-rephasing lineshapes are intrinsically broader (as they are derived from a free induction decay signal, whereas the rephasing correspond to a photon-echo signal), so identification of cross-peaks is more difficult in this case, and the result we observe resembles the non-rephasing lineshape of a single electronic transition even more closely [66, 166]. As for the oscillatory contributions, most of them are expected at the corners of the square which is cut by the diagonal line (points A-D), so that they lie on top the most intense non-oscillatory contributions, contrary to the rephasing case, where most oscillatory amplitude is found below the diagonal, on top of smaller backgrounds.

In Figure 4.9 we see that the amplitude is dominated by non-oscillatory signals – the oscillatory features are small compared to the main amplitude, which dominates all color plots. Because we are specifically interested in the signatures from vibrational coherences, we need different ways to visualize the data. The questions we want to address regard which regions of the $(\tilde{\nu}_1, \tilde{\nu}_3)$ plane present oscillatory behavior and what the phase relationships between them are. In order to address that, we begin by looking at amplitude traces over T of individual $(\tilde{\nu}_1, \tilde{\nu}_3)$ points where oscillations are expected. In Figure 4.10 we show the rephasing (a) and non-rephasing (b) maps at $T = 120$ fs, and (below) the time traces for three selected $(\tilde{\nu}_1, \tilde{\nu}_3)$ points. Point 1 corresponds to the cross-peak labelled F ($\tilde{\nu}_1 = 15925$ cm^{-1}, $\tilde{\nu}_3 = 15175$ cm^{-1}) in Figure 4.5, where two coherence Feynman diagrams and no population ones are centred for rephasing signals. We find that the corresponding trace, displayed in blue in Figure 4.10c, shows an oscillation with period of around 89 fs.

Still in Figure 4.10c, we consider points 2 and 3 – point 2 corresponds to the lower

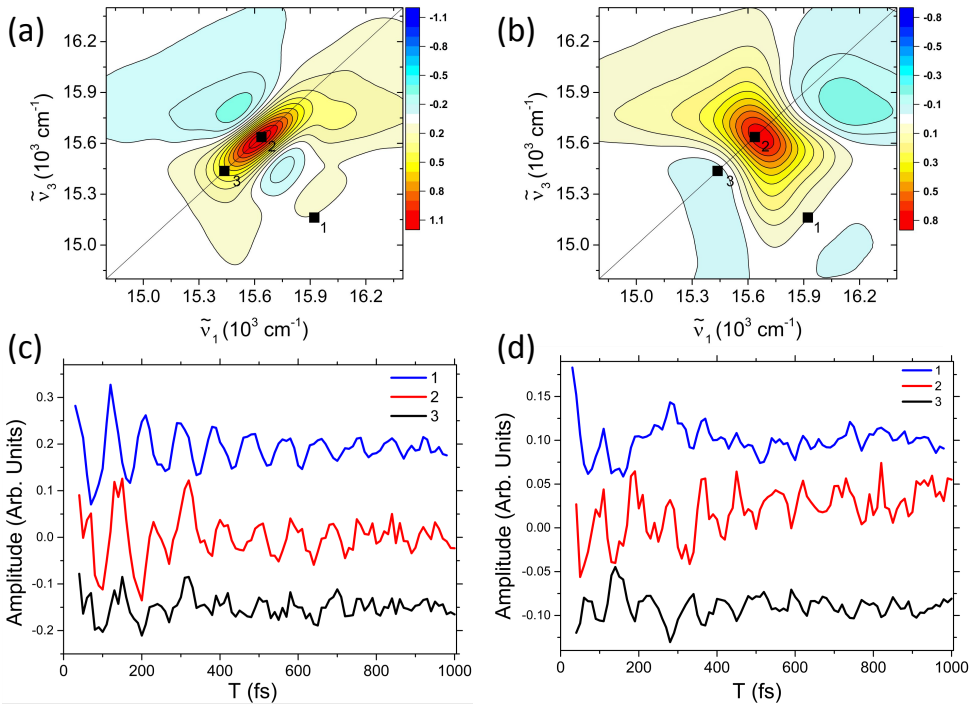

Figure 4.10: Real rephasing **(a)** and non-rephasing **(b)** 2D-ES spectra at population time $T = 120$ fs. The squares labelled 1, 2 and 3 mark positions for which the traces over T are shown in **(c)** – rephasing – and in **(d)** – non-rephasing. The curves are vertically offset to facilitate visualization.

diagonal peak at $\tilde{\nu}_1 = \tilde{\nu}_3 = 15650$ cm^{-1}, where two rephasing oscillatory pathways are centered; and point 3 is at $\tilde{\nu}_1 = \tilde{\nu}_3 = 15450$ cm^{-1}, where no pathways are centered, and thus any oscillations arise from the broadened lineshapes from nearby pathways. Accordingly, the trace of point 3 (black line in Figure 4.10c) shows an oscillation of smaller amplitude than that of 1. The trace of point 2 on the other hand (red line in Figure 4.10c) shows comparable oscillatory amplitude as that of point 1. It is also interesting to note that points 2 and 3, both along the diagonal, oscillate in phase, whereas point 1 (which is connected to point 2 by a line perpendicular to the diagonal) oscillates out of phase with the previous two. This is in agreement with the prediction from Section 2.8 that rephasing oscillation lineshapes have constant phase along the diagonal.

In Figure 4.10d we plot the non-rephasing amplitude traces over T for the same points. There are no non-rephasing oscillatory pathways centered at point 1, so the minor oscillatory amplitude can be understood as resulting from the lineshape tails from pathways centered elsewhere. The same applies to point 3, but this is closer to the main diagonal peak, where two oscillatory pathways are centered. That the oscillatory amplitude at 3 is clearer than in 1 reflects this overlap. Finally, point 2 is the center of two non-rephasing

oscillatory pathways, and accordingly we observe an oscillation of larger amplitude. We also note that the phase-shift observed among these 3 traces follows the description of Section 2.8, where the phase of non-rephasing oscillatory lineshapes was predicted to be constant along the anti-diagonal direction, matching the fact that points 1 and 2 oscillate in phase with each other, but not in phase with point 3.

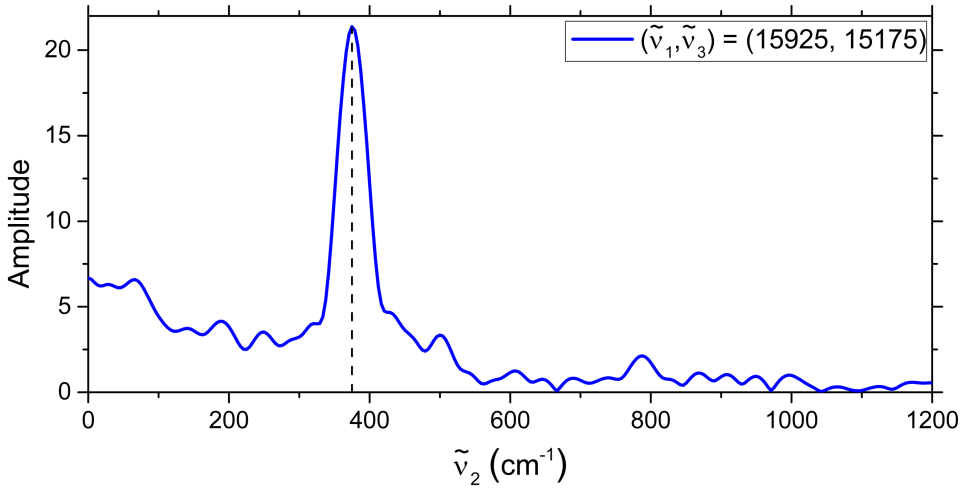

Figure 4.11: Power spectrum of the rephasing trace at ($\tilde{\nu}_1 = 15925$ cm^{-1}, $\tilde{\nu}_3 = 15175$ cm^{-1}). The maximum amplitude is found at $\tilde{\nu}_2 = 375$ cm^{-1} and is marked with a dashed vertical line.

However, the overall picture of the coherent oscillations remains incomplete. We have analyzed only three coordinates, while we have forecast pathways contributing at six coordinates, and even when some of those coordinates were not at the central position of any pathway (points 1 and 3 for the non-rephasing) we still observed oscillations. Therefore, it is important to find means to assess oscillatory behavior across the entire excitation-detection plane. To that end we have developed a program in Labview which allows us to scan ($\tilde{\nu}_1, \tilde{\nu}_3$) while the corresponding amplitude trace over T is displayed in real time on the screen, and inspecting the data shows that oscillatory time traces at 375 cm^{-1} can be found in many regions. Scanning the rephasing maps with the software, for instance, we observe that maximum oscillatory amplitude occurs in the region around that of cross-peak F ($\tilde{\nu}_1 = 15925$ cm^{-1}, $\tilde{\nu}_3 = 15175$ cm^{-1}). Performing a Fourier Transform of this trace we obtain the power spectrum shown in Figure 4.11. In this Figure, amplitude at 375 cm^{-1} is found to dominate the oscillation at this coordinate, but no information is available about the oscillatory amplitude around this coordinate.

In order to fully investigate the amplitude and phase of the oscillations resulting from the 375 cm^{-1} mode, we can perform a Fourier transform of all population time traces in

the 3D matrix formed by stacking all different population times measured (in our case, 97 2D spectra with population times ranging from 30 fs to 1 ps with time steps of 10 fs), as originally introduced in references [103, 167, 168]. This means that the resulting data will be a function of $(\tilde{\nu}_1, \tilde{\nu}_2, \tilde{\nu}_3)$, where $\tilde{\nu}_1$ is the wavenumber corresponding to the Fourier pair of T. Performing the Fourier Transform of the pure signal, as done in Figure 4.11, results in large baselines around $\tilde{\nu}_2 = 0$ because of the non-oscillatory parts of the 2D-ES signal. To avoid such artefacts, we initially perform a global multi-exponential fit to the 2D maps, and then Fourier transform only the residuals of the fit [169], which contain the background-free coherent oscillations. The resulting Fourier transformed 3D matrix will have an amplitude and a phase for every set of excitation, population and detection wavenumbers $(\tilde{\nu}_1, \tilde{\nu}_2, \tilde{\nu}_3)$. This allowed us to build a Labview software in which it is possible to scan the different population wavenumbers $(\tilde{\nu}_2)$ and observe in real time the corresponding oscillatory amplitude in the usual excitation-detection plane. We can also scan the excitation-detection plane and see the corresponding power spectrum (oscillation amplitude as a function of $\tilde{\nu}_2$ for the selected $(\tilde{\nu}_1, \tilde{\nu}_3)$ pair), thus creating a practical way to systematically assess different oscillation frequencies present in the data.

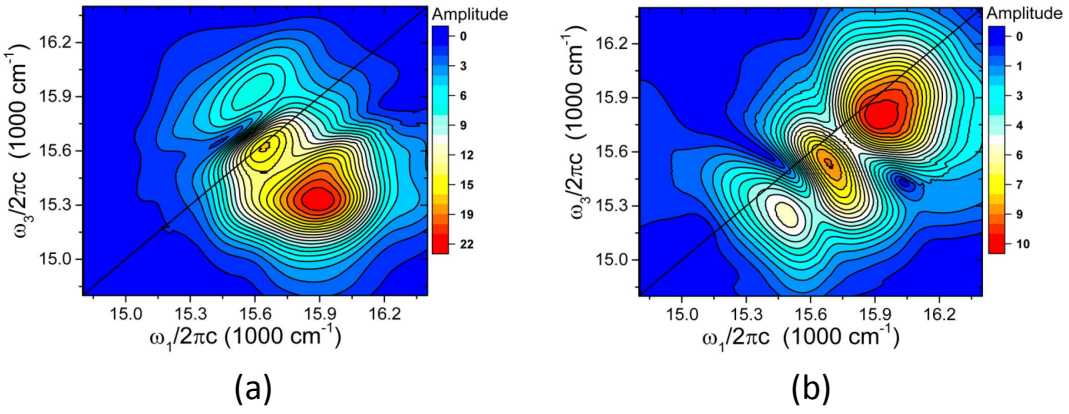

Figure 4.12: Amplitude of the 375 cm^{-1} oscillation in the real rephasing **(a)** and non-rephasing **(b)** 2D-ES maps.

For this particular experiment, the frequencies that stand out in the Fourier transformed 3D matrix were the 375 cm^{-1} corresponding to the expected vibrational coupling revealed in the linear absorption spectrum and, at much smaller intensity, the 787 cm^{-1} Raman mode of toluene, which is the only strong toluene mode within our spectral bandwidth and can be seen in Figure 4.11. By fixing $\tilde{\nu}_2 = 375$ cm^{-1} and plotting the amplitude distribution of the Fourier transformed 3D matrix as a function of $(\tilde{\nu}_1, \tilde{\nu}_3)$ we obtain

Figures 4.12 (a) and (b) for the rephasing and non-rephasing spectra respectively. Significantly in both cases the amplitude of the 375 cm^{-1} oscillation is distributed along the $(\tilde{\nu}_1, \tilde{\nu}_3)$ in a pattern that does not resemble the 5 oscillatory peaks forecast in Figure 4.8. However, we do find that most of the rephasing oscillatory amplitude is found around the region of peaks C, D, E and F (see Figure 4.5 for coordinate labels), while non-rephasing amplitude lies mostly around the region of peaks A, B, C and D. Both of these observations are expected from the diagrammatic analysis, suggesting that the unexpected peak pattern formed might be caused by interference between neighbouring peaks which partially overlap.

We expect the lineshapes from oscillatory pathways to partially overlap because the vibronic shoulder overlaps with the main electronic transition in the linear absorption spectrum (Figure 4.2). To assess the expected effects from this overlap we refer back to equation 2.77, an expression for the phase of the oscillation corresponding to a single Feynman diagram originally obtained by Butkus *et al.* [78]. As discussed previously, it follows from this equation that the phase of a single rephasing oscillatory pathway is constant along the diagonal. Therefore, as contributions centred in different $(\tilde{\nu}_1, \tilde{\nu}_3)$ with phases varying along $(\tilde{\nu}_1, \tilde{\nu}_3)$ overlap, we expect maxima and minima of oscillatory amplitude to form parallel to the diagonal, exactly as observed in Figure 4.12a. The argument for the non-rephasing case is the same, but it applies to the anti-diagonal, and once more is in agreement with the observations from Figure 4.12b.

To further confirm the interference hypothesis we have plotted the phase of the 375 cm^{-1} oscillation in figure 4.13 (a) and (b), where the amplitude of the oscillation is indicated with contour lines and the phase at each excitation-detection pair is shown with a color scale. The expected relationship is found: the rephasing oscillation has its overall phase constant along the diagonal, with variations of up to 2π found along the anti-diagonal, while the opposite is observed in the non-rephasing. So even though the oscillation amplitude in the excitation-detection plane for rephasing and non-rephasing contributions does not resemble what would be expected from a simplistic Feynman diagram picture including only 0-0 and 0-1 transitions, there is a clear explanation for the deviations.

In spite of the qualitative agreement, we note that Equation 2.77 was derived analytically under a set of assumption, and it gives the phase of one single Liouville-space

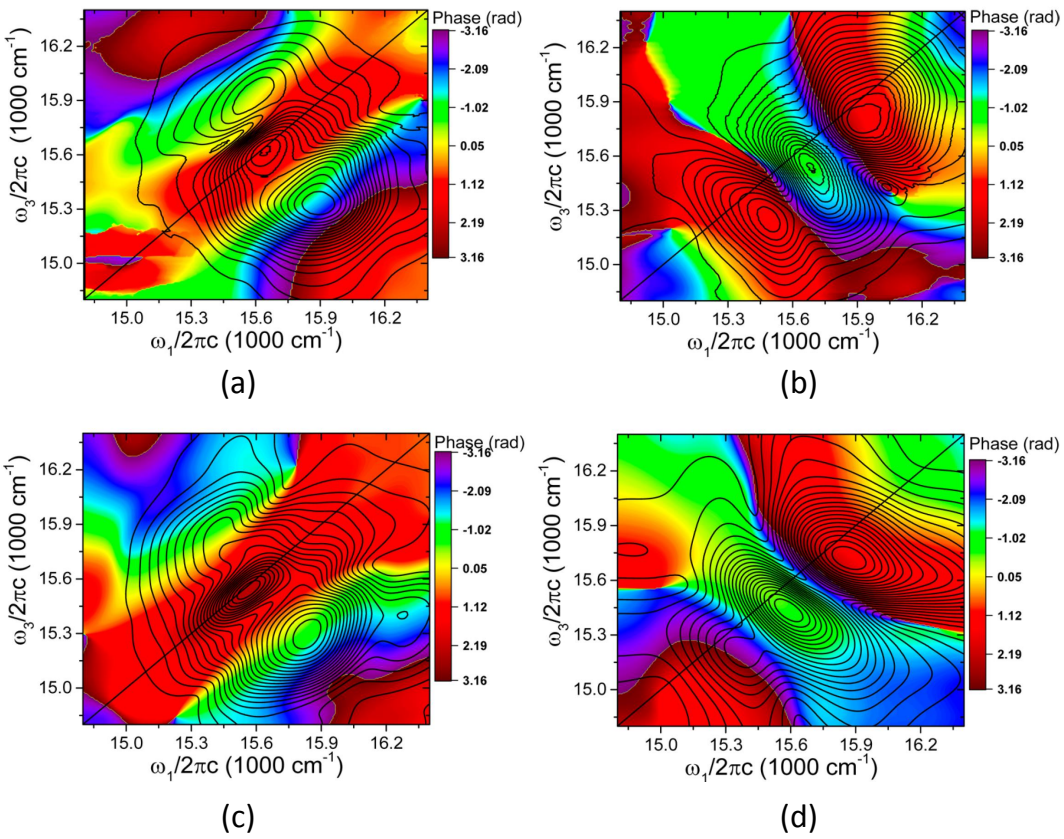

Figure 4.13: Amplitude (contour lines) and phase (color scale) of the 375 cm^{-1} oscillation present in the real rephasing **(a)** and non-rephasing **(b)** experimental 2D-ES spectra of the zinc-porphyrin monomer. Graphs **(c)** and **(d)** are the same but for calculated 2D-ES data (see text for details).

pathway. Our experiment detects many and we are making considerations regarding the overlap effect. To further support that the amplitude and phase of the 375 cm^{-1} oscillation can indeed be reliably recovered from our measurements and that their profiles differ from the Feynman diagrams forecast due to interference between different pathways, we have implemented simulations of 2D-ES spectra based on a traditional response function theory, which includes the whole vibrational ladder, is completely independent from the assumptions used to derive Equation 2.77, has no effects due to finite pulse duration and pulse overlap and should automatically account for interferences. The approach used to simulate the 2D-ES signal from the porphyrin monomer is discussed in detail in Appendix 1.

In order to confirm the oscillatory behavior found in the experiment for the 375 cm^{-1} oscillation, we calculated rephasing and non-rephasing spectra from $T = 0$ to $T = 1000$ fs in time steps of 10 fs and then applied the same analysis used for the experimental data described above. The calculated results for both amplitude and phase of the 375 cm^{-1}

oscillation for rephasing and non-rephasing signals are shown in Figures 4.13c,d. Good agreement is found with the experimentally recovered maps (Figures 4.13a,b), thus validating the previous discussion.

4.4 Summary

To summarize, we have experimentally investigated coherence signatures in 2D-ES arising from the coupling of a 375 cm^{-1} vibrational mode to the lowest singlet electronic transition of a zinc-porphyrin monomer. Comparison of the results with the predictions from the diagrammatic analysis alone proved unsatisfactory. However, the work of Butkus *et al.* [78] led us to both to predict that interference effects take place among overlapping neighboring oscillatory contributions, and to qualitatively describe the rephasing and non-rephasing interference patterns in the $(\tilde{\nu}_1, \tilde{\nu}_3)$ plane. Calculations of 2D-ES spectra based on a traditional response function theory of a two-level system with a spectral density based on a multi-mode Brownian oscillator model that automatically takes overlapping lineshapes into account were performed, and the results matched well with the experiment, further confirming the interference hypothesis.

It follows that although considerations on Feynman diagrams are useful, at least for low frequency coherent oscillations in molecular systems there will always be overlap between neighboring peaks. Thus, the oscillations observed are a sum of signals arising from different Feynman diagrams, with the phase of individual contributions being given by equation 2.77. When there is such overlap between neighboring pathways, the phase and amplitude of the coherent oscillations will deviate from predictions from diagrammatic analysis that assumes infinitely sharp transitions. Therefore neither the phase nor the amplitude of an oscillation are reliable sources of assignment of a particular coupling and its nature unless more sophisticated analysis is employed which accounts for these effects.

Chapter 5

Laser Spectrum Effects in Coherence Pathways

In the previous Chapter we discussed the basic 2D-ES results for the zinc-porphyrin monomer, addressing the issue of analyzing large datasets in order to have a global picture of coherent oscillations in what are effectively 3D spectra (obtained by finely scanning T and performing a Fourier transform to obtain the results as a functions of $\tilde{\nu}_2$). On the basis of these results and those from Section 2.8 we predicted and detected the presence of interference between neighbouring oscillatory pathways in 2D-ES. Nonetheless, the whole analysis was based only on the real part of rephasing and non-rephasing spectra, following the usual approach in the 2D-ES literature for molecular systems in that period. However, in 2013 Seibt and Pullerits [167] showed that by analysing the complex-valued 2D-ES spectra information on the frequency sign of any coherent oscillations during T can be recovered and used to isolate ground from excited state vibrational coherences, which Song *et al.* demonstrated experimentally in a conjugated polymer film [170] in 2015.

In this Chapter we apply this analysis to both calculated and experimental 2D-ES spectra of the porphyrin monomer. We then employ it to discuss laser spectrum effects on coherent oscillations, where we find that under widely used excitation conditions vibrational and electronic coherences give rise to the same pattern of oscillatory features in the $(\tilde{\nu}_1, \tilde{\nu}_3)$ plane. The results are readily explained in terms of the Feynman diagrams, and the understanding of this result allows us to demonstrate how the laser spectrum can be used to unambiguously separate vibrational from electronic coherences in 2D-ES. The results were published in reference [171].

5.1 Ground and excited state vibrational coherences with 2D-ES

In this Section we apply the same analysis used in Section 4.3 to the full complex-valued 2D-ES spectra, in order to verify the predictions from Figure 2.9 regarding the frequency sign and the $(\tilde{\nu}_1, \tilde{\nu}_3)$ positions of oscillatory features. To this end, new 2D-ES measurements of the zinc-porphyrin monomer were performed aiming to acquire data of even higher quality. The datasets discussed in Chapter 4 were obtained between June and August of 2014, while the datasets we focus on in this Chapter were obtained between March and May of 2016, and the 2D-ES setup has been optimized in the meantime. Most of the measurements in this second set used *n*-pentane as a solvent, as its Raman active modes have significantly smaller cross-section than other solvents (toluene, acetone, dichloromethane, 2-methyltetrahydrofuran, methylcyclohexane) and therefore generates smaller oscillatory contributions in the 2D-ES data. Also aiming to minimise the coherent oscillations from the solvent, in this Chapter we make use of 200 μm pathlength cells, so that the concentration is about 5 times higher than in 1 mm cells, meaning that 5 time as many molecules are present in the same focal spot.

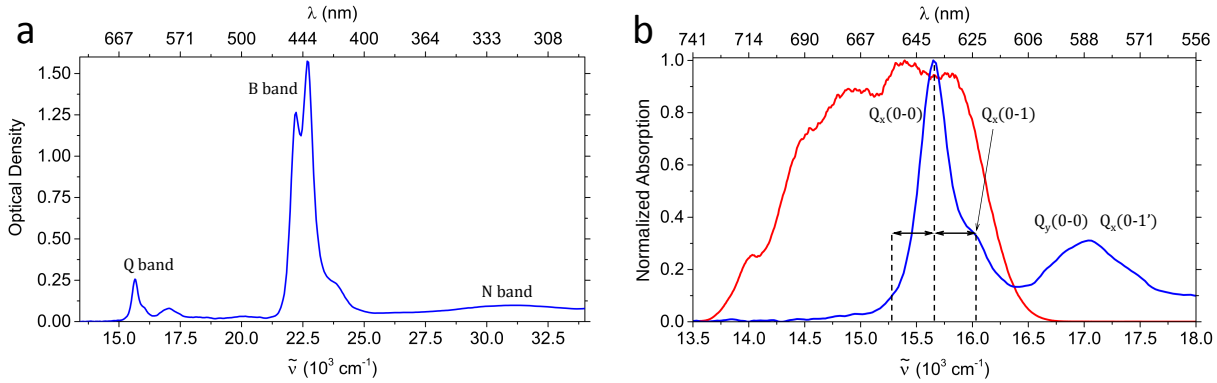

Figure 5.1: **(a)** Linear absorption spectrum of the monomer in *n*-pentane with 1% by volume of pyridine. **(b)** Linear absorption of the monomer normalized by the maximum value in the *Q* band (blue) and the normalized laser spectrum (red) used in the 2D-ES experiments described in this Section. Dashed lines mark the absorption and stimulated emission transition energies that can be present in pathways related to the 375 cm^{-1} vibrational mode.

In Figure 5.1a we show the linear absorption of the porphyrin monomer in *n*-pentane, while in Figure 5.1b we zoom in on the *Q* band and compare the normalized linear absorption with the normalized laser spectrum used in the experiments described in this Section. The laser spectrum is broader than the one used in the previous Chapter, with

significant amplitude even below $\tilde{\nu} = 14000$ cm^{-1} (714 nm), but covers the same region of the molecular absorption. The molecular absorption in n-pentane with 1% by volume of pyridine has the same qualitative features as in toluene (shown in Figure 4.2), but we observe a blue-shift of 100 cm^{-1} in the $Q_x(0-0)$ transition, with the vibronic signatures following this shift. Therefore, in this Chapter the $Q_x(0-0)$ transition – the gap between $|g_0\rangle$ and $|e_0\rangle$ – is at 15650 cm^{-1}, while the vibronic shoulder associated with the 375 cm^{-1} mode – gap between $|g_0\rangle$ and $|e_1\rangle$ – is at 16025 cm^{-1}. Finally, the stimulated emission from $|e_0\rangle$ to $|g_1\rangle$ is expected at 15275 cm^{-1}.

We performed 2D-ES experiments with population time steps of 5 fs in the range $30 \leq T \leq 1000$ fs, so the Nyquist limit for our wavenumber resolution is $\tilde{\nu}_2 \approx 3330$ cm^{-1} in the population time period. In Figures 5.2 and 5.3 we show the real and imaginary parts of the rephasing and of the non-rephasing spectra at $T = 70$ fs – maps at other populations times were qualitatively similar. All maps closely resemble the calculated results for a single inhomogeneously broadened electronic transition [66, 166], reinforcing that our experiment is recovering the imaginary parts correctly. We want to employ the same analysis from Section 4.3 for the complex-valued spectra.

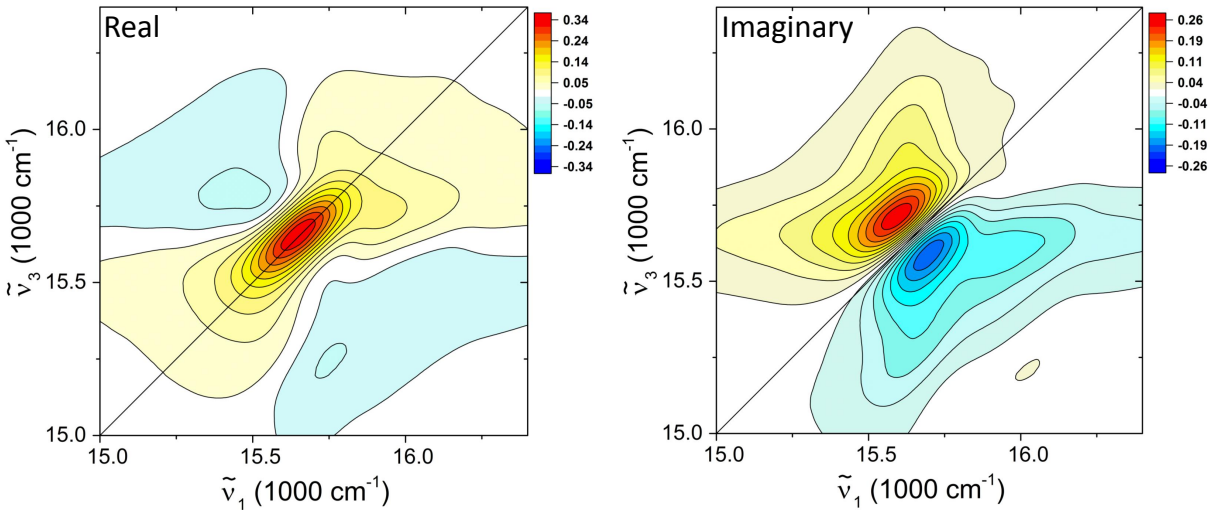

Figure 5.2: Real and imaginary rephasing maps for the porphyrin monomer at $T = 70$ fs.

Now we can proceed to use the 196 2D-ES spectra to build the complex-valued 3D matrix with all of them stacked, in order to assess the oscillation amplitude maps. Before that, it is desirable to check the quality of the data in the time domain, because the recovery of positive and negative frequencies relies on the phase-shift between real and imaginary parts of the signal being adequately measured. To check that, we will look at

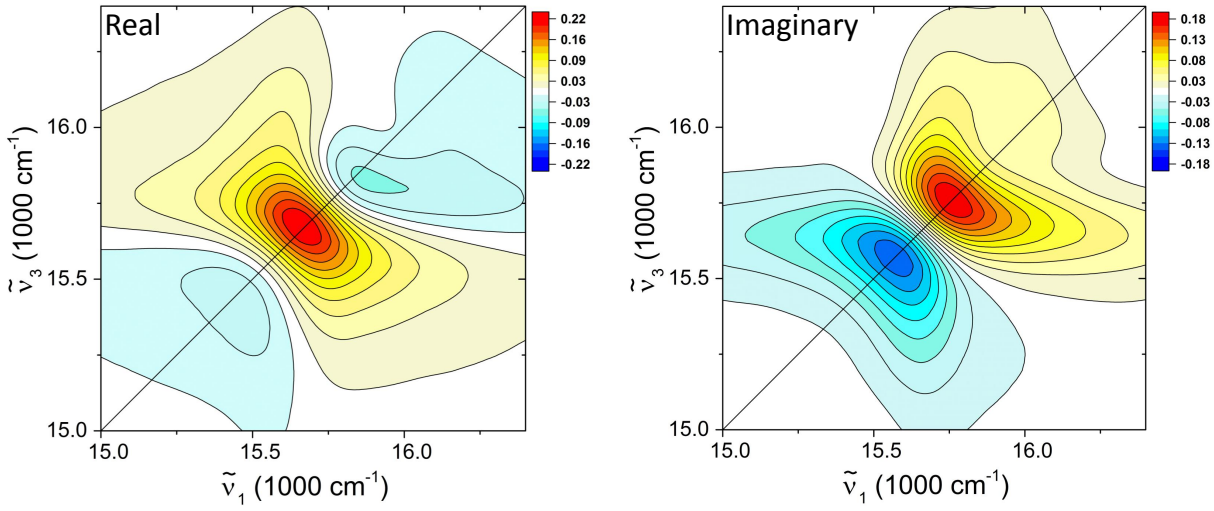

Figure 5.3: Real and imaginary non-rephasing maps for the porphyrin monomer at $T = 70$ fs.

points in the $(\tilde{\nu}_1, \tilde{\nu}_3)$ plane where strong oscillations of purely negative or purely positive frequency are expected due to vibrational coherences from the 375 cm^{-1} mode, and assess whether the oscillation presents the correct behavior.

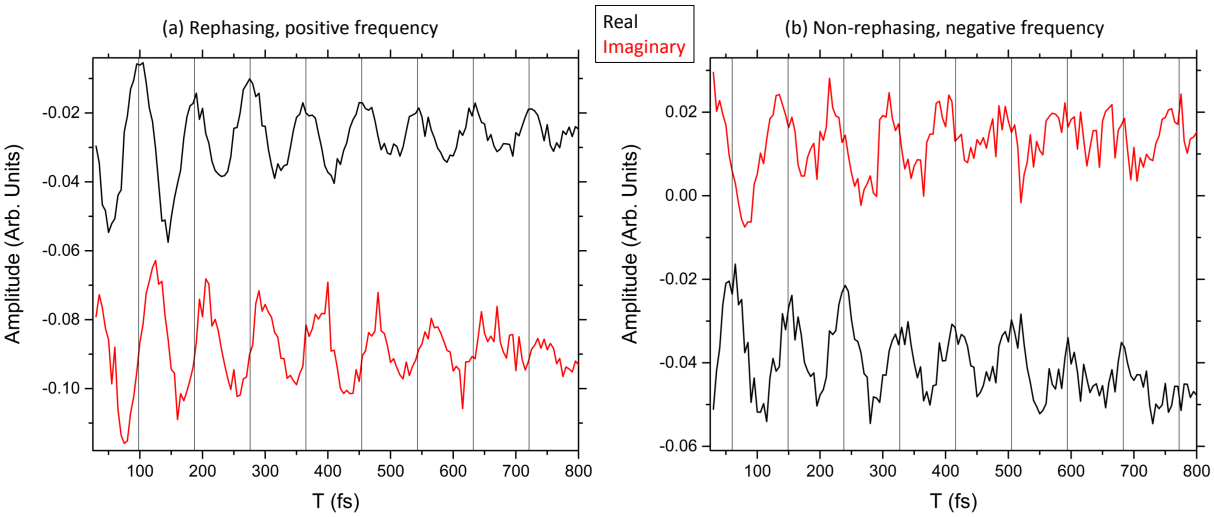

Figure 5.4: **(a)** Real (black) and imaginary (red) rephasing traces as a function of T for $\tilde{\nu}_1 = 15725$ cm^{-1} and $\tilde{\nu}_3 = 15295$ cm^{-1}. A factor of 0.05 was subtracted from the imaginary part to avoid overlap between the graphs. **(b)** Real (black) and imaginary (red) non-rephasing traces as a function of T for $\tilde{\nu}_1 = 15955$ cm^{-1} and $\tilde{\nu}_3 = 15918$ cm^{-1}, where only coherences of negative frequencies at 375 cm^{-1} are forecast. A factor of 0.035 was subtracted from the imaginary part to bring the traces closer together. The vertical lines are spaced by 89 fs and the first one is placed to coincide with the maximum of the real part of the signal.

In Figure 5.4a we show the real (black line) and imaginary (red line) rephasing traces as a function of T for $\tilde{\nu}_1 = 15725$ cm^{-1} and $\tilde{\nu}_3 = 15295$ cm^{-1}. At this point, which lies below the diagonal on our plots, the only coherences expected at 375 cm^{-1} have positive frequency, which corresponds to an oscillation like $\cos(\nu_0 T) + i \sin(\nu_0 T)$ in the

time domain, where $\nu_0 > 0$. In words, this means that both real and imaginary parts will have the same amplitude, but the maxima of the imaginary part will be delayed by $\frac{\pi}{2}$ compared to the real part, which is exactly what we observe in Figure 5.4a.

In Figure 5.4b we show non-rephasing traces for $\tilde{\nu}_1 = 15955$ cm^{-1} and $\tilde{\nu}_3 = 15918$ cm^{-1}, where only coherences of negative frequencies at 375 cm^{-1} are forecast. Negative frequencies consist of an oscillatory behavior like $\cos(\nu_0 T) - i \sin(\nu_0 T)$, implying that both real and imaginary parts will have the same oscillatory amplitude, but a phase-shift $\frac{\pi}{2}$ in the opposite direction to that observed in (a) is expected. Once again, the experimental results fully match the forecast.

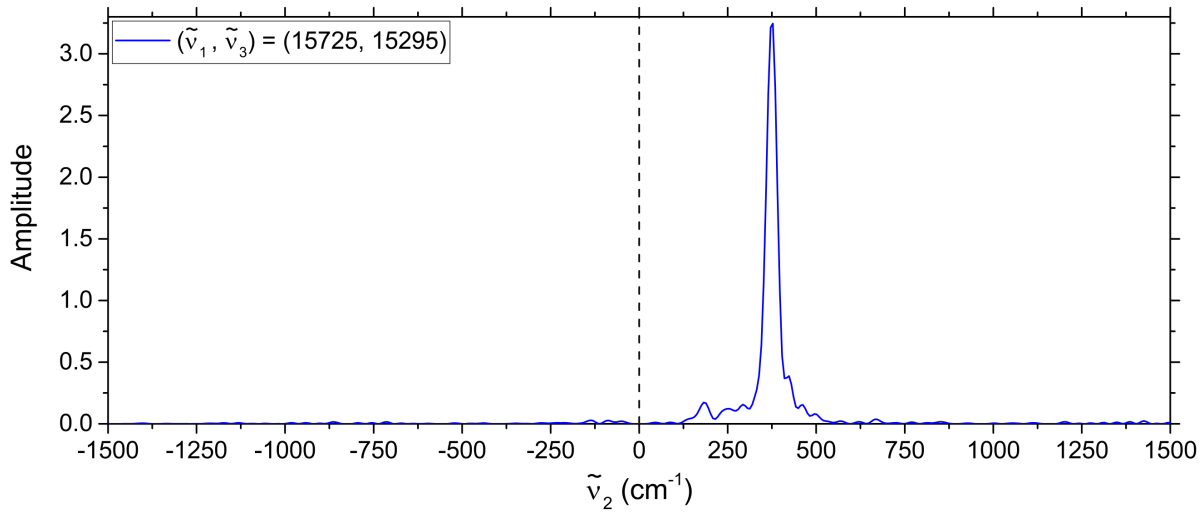

Figure 5.5: Power spectrum of the fit residuals of the time trace shown in Figure 5.4a. The signal is dominated by a peak at $\tilde{\nu}_2 = +375$ cm^{-1}, and no significant amplitude is found at negative frequencies.

However, $\frac{\pi}{2}$ phase shifts and oscillatory amplitudes are difficult to fully assess based on the oscillatory traces alone. In order to further check our experiment's ability to separate positive from negative frequencies we use the following procedure. First we generate the 3D matrix with all population times stacked together, perform the global fit and take the residuals from it, as in Section 4.3. We can then select $\tilde{\nu}_1 = 15725$ cm^{-1} and $\tilde{\nu}_3 = 15295$ cm^{-1} in the rephasing maps and plot the power spectrum of the Fourier transform, thus revealing which frequencies are observed in the waiting time response at those coordinates (which corresponds to the time domain trace from Figure 5.4a). This is shown in Figure 5.5, where we observe that a strong peak at $\tilde{\nu}_2 = +375$ cm^{-1} is present, with no significant amplitude observed at negative frequencies. A smaller peak at around $\tilde{\nu}_2 = +180$ cm^{-1} is also present. It is known from resonance Raman experiments [162]

that zinc-porphyrins have a vibrational mode at approximately 150 cm^{-1} coupled to the electronic structure, to which we assign this feature. However, only a handful of oscillation periods at this wavenumber are present within the 1 picosecond window of our measurement, so in order to fully resolve coherences from this mode longer scans are required. Because our objective is to study vibrational coherences in 2D-ES, not use 2D-ES to measure accurate Raman spectra of the zinc-porphyrin monomer, oscillatory features at this range are not considered further.

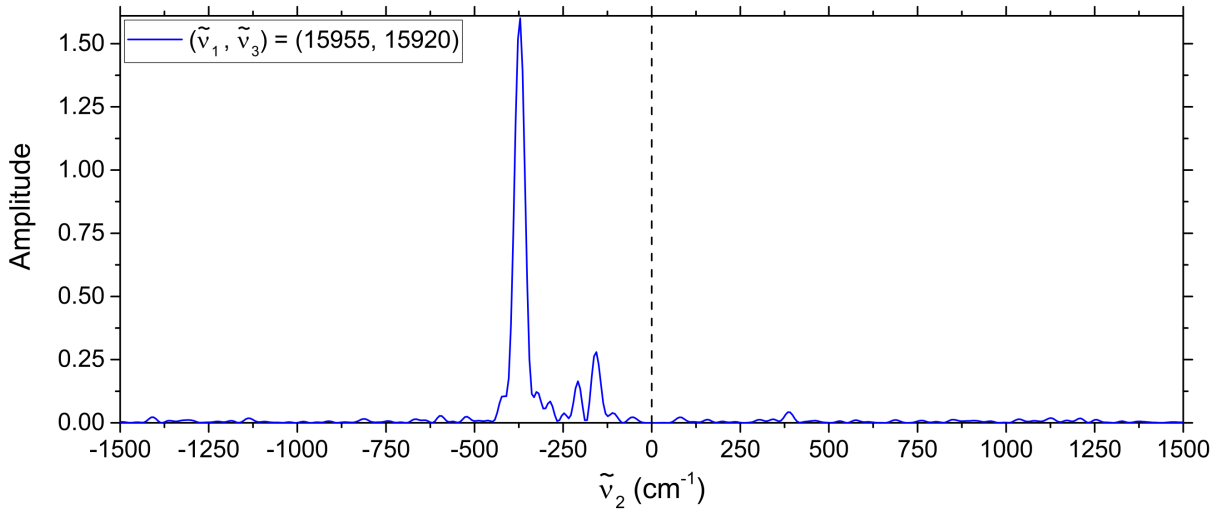

Figure 5.6: Power spectrum of fit residuals of the time trace shown in Figure 5.4b. The signal is dominated by a peak at $\tilde{\nu}_2 = -371$ cm^{-1}, and the small peak found at $\tilde{\nu}_2 = +384$ cm^{-1} has less than 3% of the highest amplitude observed. The small peak at $\tilde{\nu}_2 = +180$ cm^{-1} is related to a vibrational mode of the porphyrin molecule which also couples with Q_x. To resolve it well, a longer scan of T than 1 ps is required.

In Figure 5.6 we plot the power spectrum of the residuals of the non-rephasing trace from Figure 5.4b and verify that the coherent oscillation observed indeed corresponds to $\tilde{\nu}_2 = -375$ cm^{-1}. We note from Figure 2.9 that contrary to the rephasing case, for which plenty of the oscillatory peaks are located at low detection wavenumbers, and thus have fewer overlapping signals, the non-rephasing oscillations are strongest around the diagonal, where the largest non-oscillatory signals are also present. Therefore, the non-rephasing signal-to-noise of oscillatory positions as a function of T is generally worse than in the rephasing case. We thus attribute the presence of the small peak at $\tilde{\nu}_2 = +384$ cm^{-1} to inadequate separation between positive and negative frequencies from our experiment. Still, we emphasize that the peak at positive frequency in Figure 5.6 has less than 3% of the amplitude observed at the negative frequency, corresponding to a satisfactory discrimination between positive and negative frequencies.

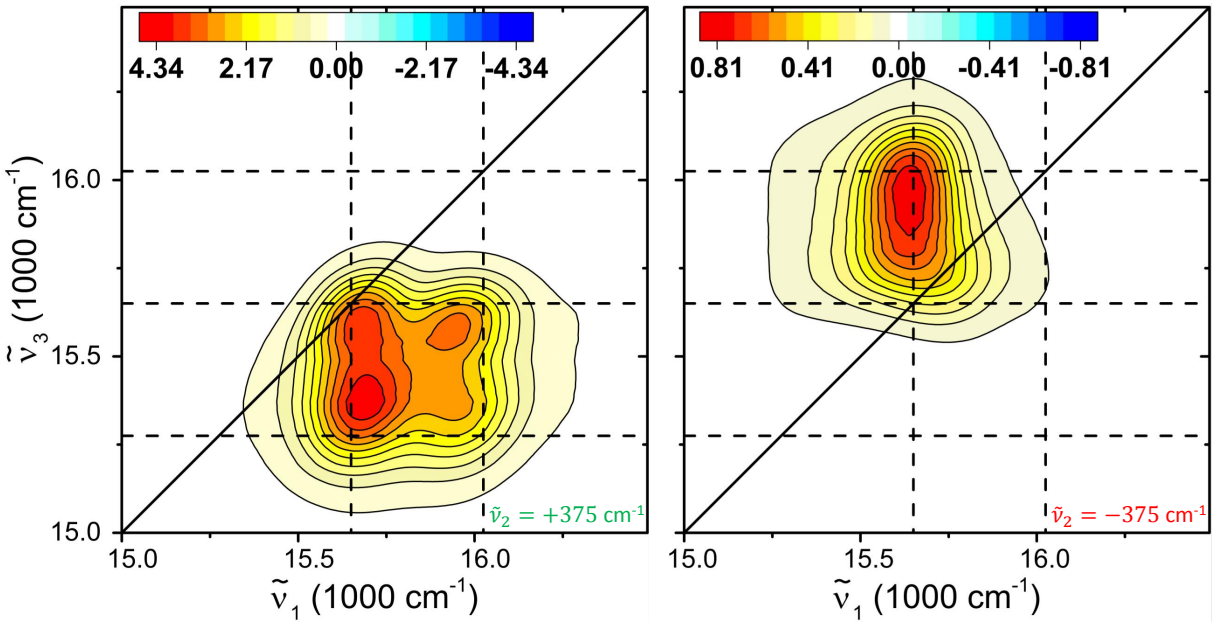

Figure 5.7: Rephasing oscillation amplitude maps showing the total oscillatory amplitude at $\tilde{\nu}_2 = +375$ cm^{-1} (left) and $\tilde{\nu}_2 = -375$ cm^{-1} (right) as a function of $(\tilde{\nu}_1, \tilde{\nu}_3)$. Lines mark the coordinates $\tilde{\nu}_{eg}$ and $\tilde{\nu}_{eg} \pm \tilde{\nu}_0$, with $\tilde{\nu}_{eg} = 15650$ cm^{-1} and $\tilde{\nu}_0 = 375$ cm^{-1}.

Finally we move on to display the full oscillatory amplitude at $\tilde{\nu}_2 = \pm 375$ cm^{-1} at all $(\tilde{\nu}_1, \tilde{\nu}_3)$ points. For that, we employ the procedure used in Section 4.3, that is, initially we perform a global fit of the now complex-valued 2D-ES rephasing and non-rephasing spectra, and then apply a Fourier transform to the residuals of the fit at each $(\tilde{\nu}_1, \tilde{\nu}_3)$ point. The fact that we now can separate positive from negative frequencies means that the red and green symbols from Figure 2.9 will be observed at their correspondingly signed frequencies, thus no longer overlapping.

In Figure 5.7 we show the rephasing oscillation maps at $\tilde{\nu}_2 = +375$ cm^{-1} (left) and $\tilde{\nu}_2 = -375$ cm^{-1} (right). In both we find good agreement with the prediction from Figure 2.9. At $\tilde{\nu}_2 = -375$ cm^{-1} we observe that the amplitude is elongated around the two points marked by the red squares in Figure 2.9. At $\tilde{\nu}_2 = +375$ cm^{-1} the oscillatory amplitude is distributed in four distinct peaks around the corners of a square with side 375 cm^{-1} with corners in the positions indicated in Figure 2.9.

The non-rephasing oscillation amplitude maps at $\tilde{\nu}_2 = \pm 375$ cm^{-1} are shown in Figure 5.8, and again good agreement with theory is found. At $\tilde{\nu}_2 = -375$ cm^{-1} we observe the amplitude in a square shape with two corners of the square corresponding to the diagonal, as expected from Figure 2.9. At $\tilde{\nu}_2 = +375$ cm^{-1} we again see amplitude elongated around the two peak positions forecast at $(\tilde{\nu}_1, \tilde{\nu}_3) = (15650, 15650)$ and $(\tilde{\nu}_1, \tilde{\nu}_3) = (15650, 15275)$.

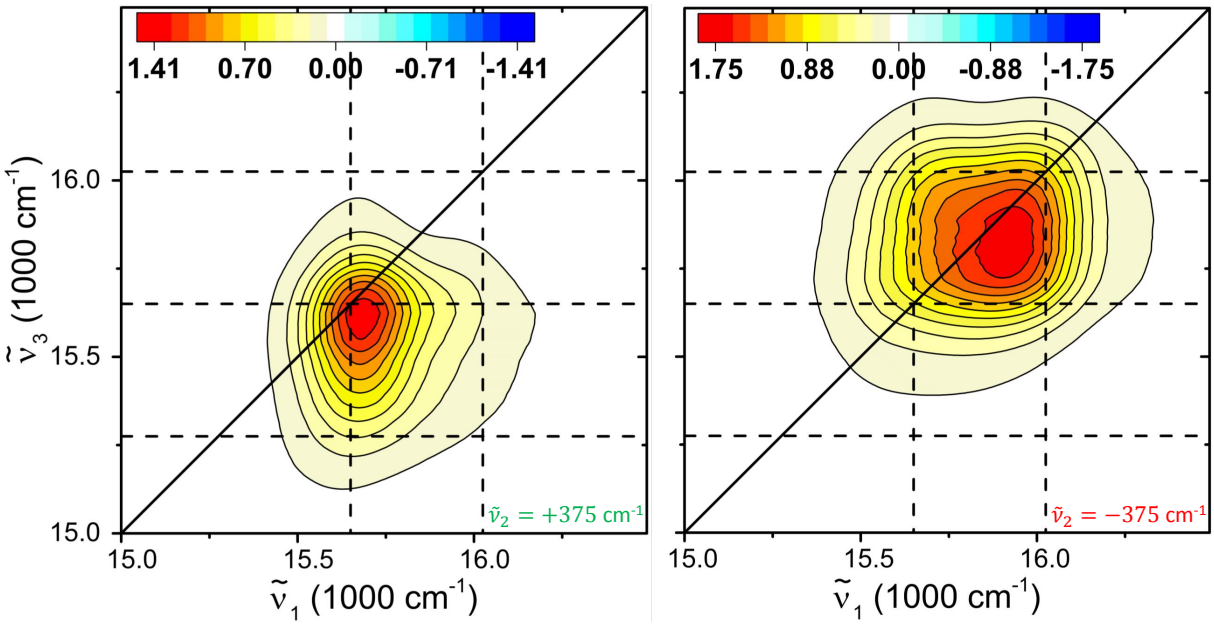

Figure 5.8: Non-rephasing oscillation amplitude maps showing the total oscillatory amplitude at $\tilde{\nu}_2 = +375$ cm^{-1} (left) and $\tilde{\nu}_2 = -375$ cm^{-1} (right) as a function of $(\tilde{\nu}_1, \tilde{\nu}_3)$. Lines mark the coordinates $\tilde{\nu}_{eg}$ and $\tilde{\nu}_{eg} \pm \tilde{\nu}_0$, with $\tilde{\nu}_{eg} = 15650$ cm^{-1} and $\tilde{\nu}_0 = 375$ cm^{-1}.

Although we are using all information available to isolate pathways, each of the maps shown in Figures 5.7 and 5.8 contains contributions of two (rephasing negative and non-rephasing positive) or six (rephasing positive and non-rephasing negative) double-sided Feynman diagrams, and the displacement between central positions of pathways in the $(\tilde{\nu}_1, \tilde{\nu}_3)$ plane corresponds to multiples of the vibrational mode wavenumber of 375 cm^{-1}. Because this value is comparable to the transition linewidth, there will still be significant overlap between neighbouring peaks, and therefore the considerations from Section 4.3 regarding interference also apply. We note however that Figures 5.7 and 5.8 resemble Figure 2.9 much more closely than what was observed in Section 4.3 (Figure 4.12), when only the real part of the 2D-ES maps was considered. The most striking difference observed in Figure 4.12 when compared to Figure 4.8 was the presence of clear minima in the amplitude for both rephasing and non-rephasing cases, whereas in Figures 5.7 and 5.8 no such features are seen. Before we discuss the reason behind this, we note that it is the same for rephasing and non-rephasing cases, with the only difference being the direction along which the phase varies. Thus, the discussion below will be exclusively focused on the non-rephasing case.

In order to understand the origin of the more pronounced interference when only the real part of the 2D-ES maps is used, we note that at $\tilde{\nu}_1 = \tilde{\nu}_3 = 15650$ cm^{-1} there are two

non-rephasing pathways with oscillatory frequency of opposite sign (and the same goes for rephasing – see Figure 4.8). From Equation 2.77, these diagrams' phases will have opposite sign compared to each other, and both remain constant along the anti-diagonal direction, varying most along the diagonal. Hence, at central position both start in phase, but while the phase of one of the diagrams increases towards $\frac{\pi}{2}$ in one direction of the $(\tilde{\nu}_1, \tilde{\nu}_3)$ plane, the phase of the other diagram decreases towards $-\frac{\pi}{2}$ along this same direction. Thus, if both diagrams have similar oscillatory amplitudes which are gradually going out of phase as distance from the central position increases, almost perfect cancellation will happen where they are completely out of phase. Because the phase changes along the diagonal both towards high and low wavenumbers, two interference minima are expected: one at higher and one at lower wavenumbers than the central position, exactly as experimentally observed in Figure 4.12b. For vibrational modes of higher wavenumbers, where no overlap is present, the expected result if only the real part of the signal is used is that this diagonal peak will present a sharper lineshape, stretched along the direction of constant phase. This has been observed by Senlik *et al.* in rephasing oscillation amplitude maps of monomeric chlorophyll a in solution, although the origin of the very different lineshape of this peak was not discussed [172].

We also emphasize that according to Equation 2.77 the phase of individual oscillatory pathways behaves as an arctangent, which implies that it asymptotically approaches $\pm\frac{\pi}{2}$. Therefore, exactly two interference minima are expected to result from the diagonal pathways of opposite frequency, as the phase difference between the two contributions gradually approaches π. On the other hand, oscillatory pathways that have all the same frequency sign will not interfere so strongly. To see that, we first note that if the two oscillatory pathways of the same frequency are centred at the same $(\tilde{\nu}_1, \tilde{\nu}_3)$ point, the phase of both is expected to vary exactly in the same way as a function of $(\tilde{\nu}_1, \tilde{\nu}_3)$, therefore not generating interference patterns. The other possibility is that of overlap between pathways which are each centered at a different $(\tilde{\nu}_1, \tilde{\nu}_3)$ coordinates. In this case, there is no obvious general rule for the phase and amplitude overlap, as it depends on their relative position and on their dephasing rate.

However, for clear interference minima or maxima to form, it is necessary that oscillatory signals of similar amplitude overlap with a phase shift of approximately zero or π, which is unlikely. The combination of phase and amplitude between different pathways

in the regions of overlap are expected to be strongly dependent on the system and the specific vibrational mode considered, which will determine the separation between neighboring contributions. What we observe for the 375 cm^{-1} mode of the porphyrin monomer in Figures 5.7 and 5.8 is that constructive interference in the region between the central positions obscures individual peaks. In Figure 5.8, non-rephasing oscillatory amplitude at $\tilde{\nu}_2 = -375$ cm^{-1} shows intense amplitude inside the square whose corners correspond to the pathways central position, while outside the square the amplitude decays strongly. A similar result is observed in Figure 5.7 for $\tilde{\nu}_2 = +375$ cm^{-1}, but rephasing lineshapes are sharper than non-rephasing ones, allowing individual peaks to be identified, although the interference features still cause their positions to shift from the corners of the square.

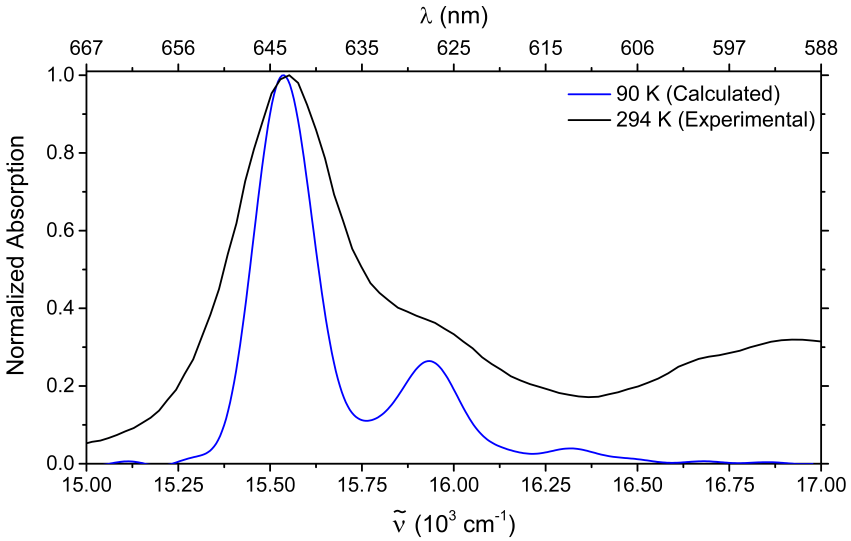

Figure 5.9: Calculated linear absorption of the porphyrin monomer (black line) in toluene using the same parameters from Section 4.3 apart from the temperature, which was set to 90 Kelvin. The blue line shows the experimental linear absorption in toluene and 1% of pyridine by volume for comparison.

It is thus interesting to have the results for a case in which there is no overlap between peaks. Although overlap for the features at 375 cm^{-1} is unavoidable in our measurements, we can assess this situation with the calculations we used in Section 4.3 and described in Appendix A. To do that, we use the same set of parameters employed before, but arbitrarily set the temperature to 90 Kelvin, which narrows the transition widths enough for the peaks associated with the 375 cm^{-1} mode to be fully separated. The calculated linear absorption in this case is shown in Figure 5.9, and we observe that the narrowing of the linewidth results in a sharper vibronic progression with well separated peaks. Therefore, we can calculate oscillation maps corresponding to the 375 cm^{-1} vibrational mode and

assess how their expected features when there is minimum overlap.

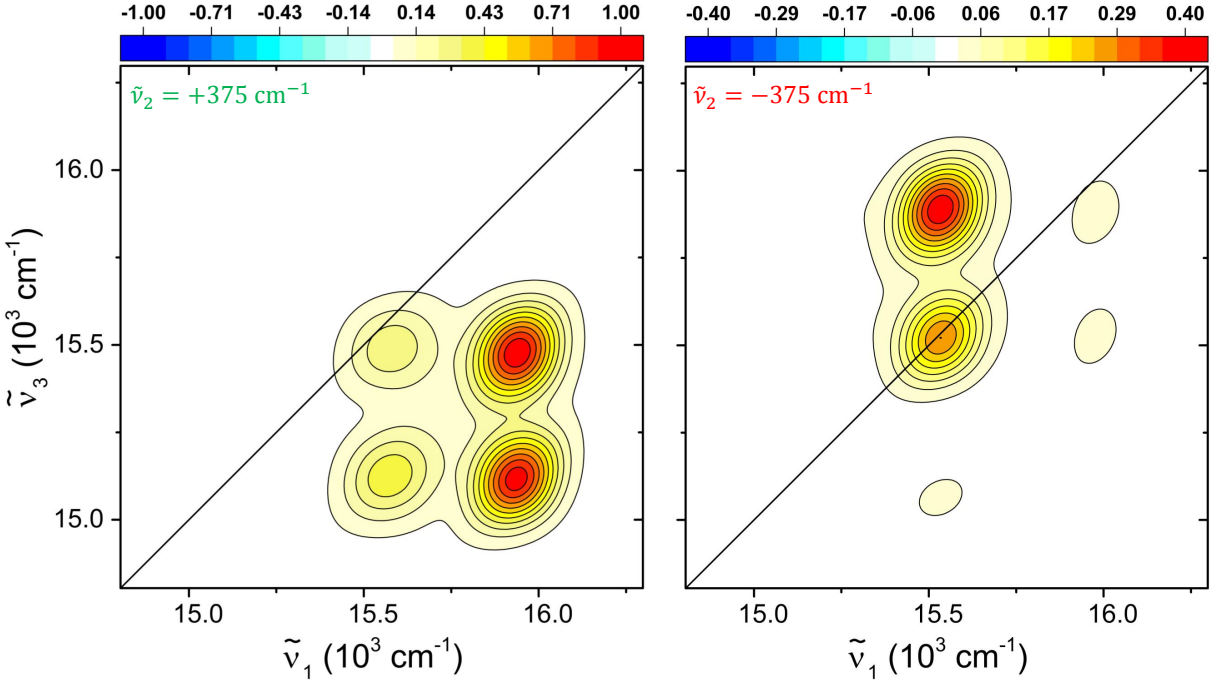

Figure 5.10: Calculated rephasing oscillation amplitude maps at 90 Kelvin showing the total oscillatory amplitude at $\tilde{\nu}_2 = +375$ cm^{-1} (left) and $\tilde{\nu}_2 = -375$ cm^{-1} (right) as a function of $(\tilde{\nu}_1, \tilde{\nu}_3)$. The color scale is such that the maximum of each map corresponds to the red layer, but the values displayed are normalized to the maximum value of the positive frequency map.

We have calculated the real and imaginary parts of the 2D-ES rephasing and non-rephasing signals at 90 K from 30 to 1000 fs in time steps of 10 fs and performed the same Fourier analysis described above; in Figure 5.10 we show the calculated rephasing oscillation amplitude maps at ± 375 cm^{-1}. At $\tilde{\nu}_2 = +375$ cm^{-1} we observe four peaks forming a square, and the two peaks at higher $\tilde{\nu}_1$ have larger amplitude – in accordance with the fact that there are two oscillatory pathways centered at those positions, compared to the single pathway centred at the positions at lower $\tilde{\nu}_1$. The amplitude observed at $\tilde{\nu}_2 = -375$ cm^{-1} also shows the expected two peaks, as well as small signals that are related to pathways involving higher levels of the vibrational ladder. We note that the peak at high $\tilde{\nu}_3$ is more intense, which agrees with the experimental map from Figure 5.7, where at negative frequency the maximum amplitude is closer to this peak's position.

The non-rephasing maps are shown in Figure 5.11 and present a similar situation, with four distinct peaks being observed at $\tilde{\nu}_2 = -375$ cm^{-1} in the forecast positions, with small amplitude also being present at higher values of $\tilde{\nu}_1$ corresponding to an initial excitation to $|e_2\rangle$, which is not observed in the experiment. Once again the positions in which two pathways are centered have more amplitude than those in which a single

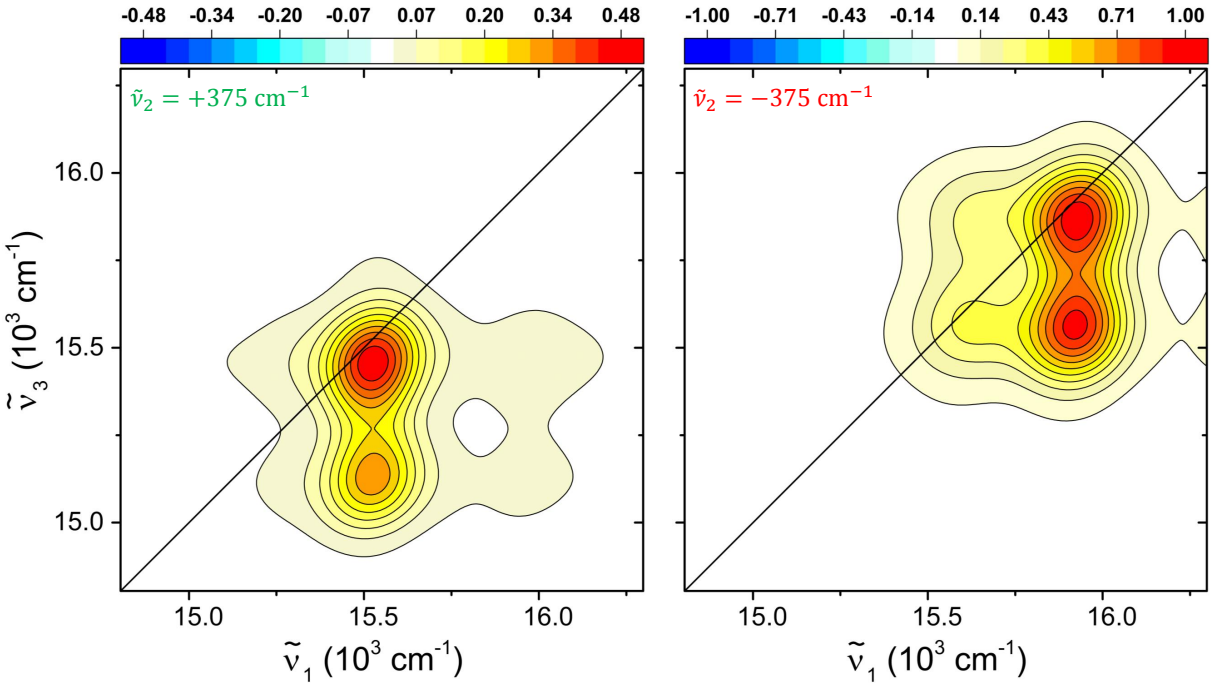

Figure 5.11: Calculated non-rephasing oscillation amplitude maps at 90 Kelvin showing the total oscillatory amplitude at $\tilde{\nu}_2 = +375\ \mathrm{cm}^{-1}$ (left) and $\tilde{\nu}_2 = -375\ \mathrm{cm}^{-1}$ (right) as a function of $(\tilde{\nu}_1, \tilde{\nu}_3)$. The color scale is such that the maximum of each map corresponds to the red layer, but the values displayed are normalized to the maximum value of the negative frequency map.

pathway is present. At $\tilde{\nu}_2 = +375\ \mathrm{cm}^{-1}$, apart from the small traces of amplitude at higher values of $\tilde{\nu}_1$, we observe that the amplitude is dominated by two peaks in the expected positions. This time it is the diagonal peak that shows higher amplitude, which is also in agreement with the experimental map (Figure 5.8). Thus, the calculations at 90 K show that the diagrammatic analysis summarized in Figure 4.8 predicts the most relevant coherence signals observed from vibrational coupling, and that separation between positive and negative frequencies avoid the most dramatic interference effects. The experimental results at room temperature agree with this forecast as well, in spite of significant overlap caused by the broad lineshapes.

Finally, it is interesting to note that the pathways with negative oscillatory frequencies in rephasing and positive frequencies in non-rephasing are all in the electronic excited state. Therefore, 2D-ES can in principle be used to assign vibrational coherences in the electronic excited state [170]. Porphyrins have a rather robust structure which does not change significantly between the ground and electronic excited state, so it is expected that ground and excited state vibrational coherences have the same frequency. Consequently, the oscillation maps are similar to Figure 4.8. For molecules that undergo structural changes in the excited state, the 2D-ES oscillation maps might deviate from those fore-

cast in Figure 4.8, with the pathways represented by squares potentially being shifted in frequency or undergoing a different dephasing rate than the pathways represented by triangles. In fact, the dephasing rates between coherences in the ground and electronic excited states can be expected to differ even for the zinc-porphyrin monomer, but such analysis was not performed yet. To our knowledge, there are no studies applying 2D-ES to recover such information, and our group plans to pursue this further with a more suitable sample which undergoes significant structural change in the excited state.

In summary, in this section we have added the imaginary part of the spectra to the analysis of coherent oscillations, which allowed us to further isolate coherence pathways. The experimental result for the porphyrin monomer matches the theoretical forecast very well, indicating that we are able to revolve positive from negative frequencies reliably with our 2D-ES setup. We also observed that interferences between neighboring pathways are less pronounced when positive and negative frequencies are separated, and showed why that is the case based on the theory used in Section 4.3. Last, we proposed that in samples which undergo significant structural change in the electronic excited state the vibrational coherence signatures from 2D-ES experiments can be used to investigate the dynamics of such changes.

5.2 Laser Spectrum Effects

Until this point, all theoretical considerations regarding the coherent oscillations in 2D-ES have ignored possible effects from the laser spectrum. We note however that the excitation spectrum used in the experiments reported above had significant amplitude at lower wavenumbers than the molecular absorption (see Figure 5.1b). This choice was based on our interest in benchmarking the vibrational coherences of the 375 cm^{-1}, and therefore bandwidth in the spectral region of the stimulated emission was important to capture pathways that emit at lower energies (see Figure 4.8). For the monomer it was also convenient not to have much amplitude beyond the vibronic shoulder corresponding to the 375 cm^{-1} mode in absorption, because the ESA pathways discussed in Section 4.2 are particularly prominent in that region, making the general interpretation of the 2D-ES results more complex. However, most samples of interest with absorption in the visible region typically have broad absorption bands that cannot be covered with the

laser spectrum as easily as the porphyrin monomer. Therefore, it is pertinent to ask how the coherence signatures are affected by the excitation laser spectrum. In the following we briefly review the studies which considered laser spectrum effects in 2D-ES, and then present our own results focusing on the effect of the spectrum on coherence pathways.

In their seminal work on 2D-ES, the Jonas group performed calculations of 2D-ES spectra of a two-level system including solvent interactions through a correlation function approach, and showed that finite pulse duration had the sole effect of filtering the 2D-ES lineshape across both $\tilde{\nu}_1$ and $\tilde{\nu}_3$ axes [146] for a single population time. Later theoretical work by the Pullerits group on an electronically coupled dimer model explored the extra signals which arise during pulse overlap, finding that for T larger than the pulse overlap, the only requirement for the laser spectrum is that is covers the absorption [173]. In another article, this same group described the effect of weakly-chirped pulses on 2D-ES spectra, observing that pulse-chirp causes mixing between real and imaginary contributions, and that positive and negative chirps generate different distortions, but still focusing on the lineshape of a single population time [174]. We note that all pulses used in this thesis are much closer to Fourier transform limit than those for which distortions were observed in that study (see Figure 4.3).

Caram *et al.* reported absorptive 2D-ES experiments on a cyanine dye with two different laser spectra, one with and the other without laser bandwidth in the stimulated emission spectral region, and observed the suppression of the peaks with emission wavenumber no longer covered by the laser as the sole effect [150]. Notwithstanding, that study did not include a systematic analysis of coherent oscillations due to vibrational coherences across the entire $(\tilde{\nu}_1, \tilde{\nu}_3)$ plane, so the effect of the laser spectrum on coherence pathways remained unexplored.

Theoretical work by Abramavicius *et al.* derived expressions using response function theory which included both pulse overlap and finite-bandwidth effects, using them to explore two-color 2D-ES pathways [175]. Experimentally, two-color experiments have been used to select specific coherence pathways using the different spectral composition between the first and second excitation pulses to ensure that the desired coherent superposition was prepared during T [172, 176].

Recently, Tempelaar *et al.* used experiments and theoretical modeling to specifically address the issue of finite bandwidth effects on coherent oscillations in 2D-ES spectra of

a cyanine dimer, where vibrational and electronic coupling are expected to coexist. They observed disagreements between experiment and calculations, which they attributed to the finite bandwidth of the laser spectrum. However, the agreement between experimental and calculated 2D-ES absorptive spectra even when the laser spectrum is included is poor, and not enough information was given on how the laser spectrum was incorporated and tested, which is significant because the 2D-ES results calculated including the pulse shape had a substantial signal amplitude in spectral regions where there is no laser intensity. Moreover, the experimental and calculated oscillation amplitude maps contain major discrepancies between each other, even when the laser spectrum is included, with strong peaks being present in the calculations but not in the experiment. The mix between vibrational and electronic coupling is intrinsically more complex than purely vibrational or purely electronic coupling, and therefore it is also unclear that the theoretical model used to describe the system was adequate in the first place, especially because no interpretation of the results in terms of Liouville-space pathways was presented. In spite of these issues, this paper highlights that a clear understanding of laser spectrum effects in coherent oscillations in 2D-ES is lacking.

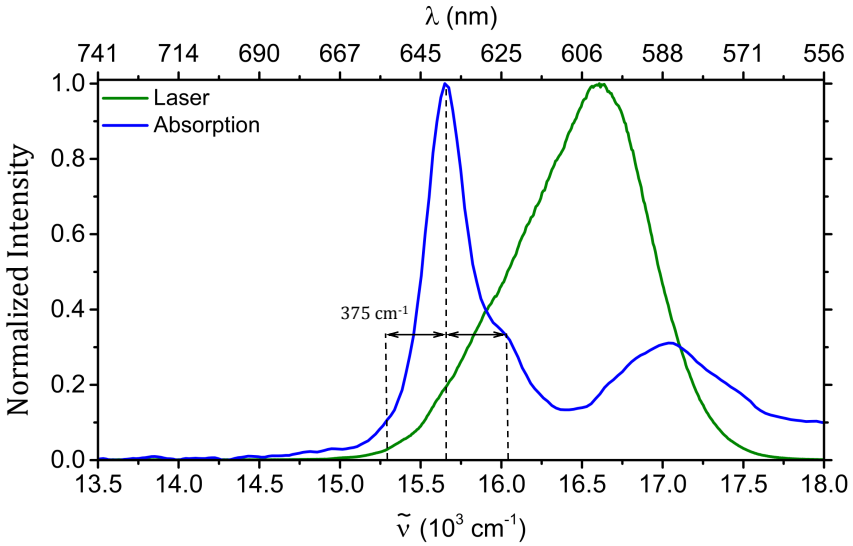

Figure 5.12: Normalized linear absorption of the porphyrin monomer in *n*-pentane with 1% of pyridine by volume (blue) and normalized laser intensity of the 2D-ES experiments described in this Section (green).

In this situation, a systematic study of the laser spectrum effects on the simplest case of vibrational coupling can bring important insights in the design and interpretation of 2D-ES experiments on coherences, especially because the laser spectrum used in 2D-ES experiments often does not have bandwidth on the red side of the absorption, as we had in

the previous sections (see Figures 4.3a and 5.1b). To that end, we have performed a similar set of 2D-ES measurements to that in Section 5.1, with the only difference being the laser spectrum used, which is shown by the green line in Figure 5.12. For completeness, Figure 5.13a shows the transient grating FROG trace on a fused silica window of the pulses (green line in Figure 5.12) used in the experiment described in this Section. The lowest absorption peak of the Q band remains fully covered by the laser, but there is negligible amplitude at the frequency corresponding to the energy gap between $|e_0\rangle$ and $|g_1\rangle$, which is red-shifted by 375 cm^{-1} from the main absorption (see Figures 2.4a and 5.12).

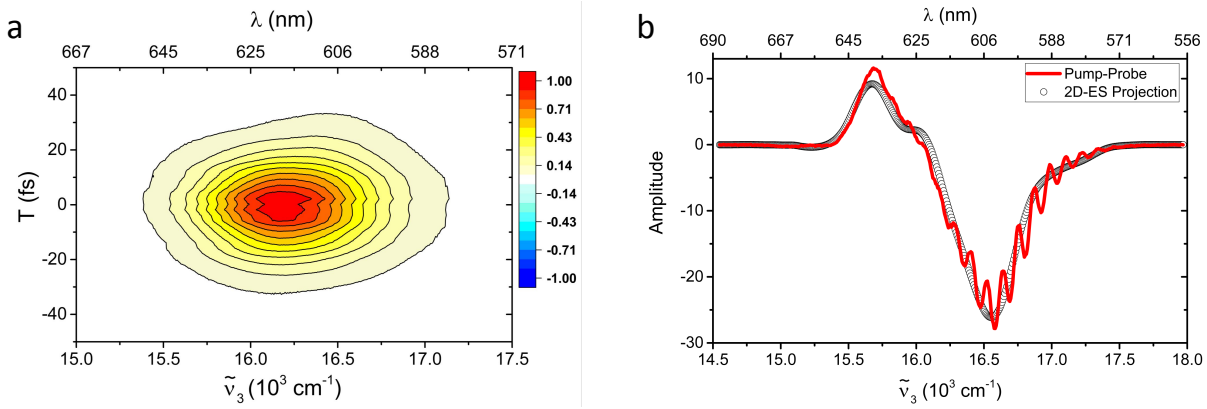

Figure 5.13: **(a)** Transient grating FROG trace of the pulses used for the 2D-ES experiments in this Section. **(b)** Projection of the real part of the 2D-ES spectrum at $T = 70$ fs (red line) and broadband transient absorption signal at the same population time (black circles). The oscillations are due to scattering.

In this experiment the laser also excites the absorption peak at $\tilde{\nu} \sim 17000$ cm^{-1}, so the resulting 2D-ES maps are more complex, but we can focus on the oscillatory features at 375 cm^{-1} following the procedure applied in Section 4.3. Before we proceed to analyze the coherent oscillations, we will present the basic 2D-ES results using this spectrum. As we have discussed in Section 4.2, significant excited state absorption (ESA) occurs from the Q band to the N band, as the energy gaps between the ground state and Q and between Q and the N band are similar [123]. The spectrum used in this section favors the ESA pathways more than that of Section 5.1, and the broad character of the N band implies that ESA contributions will be spread throughout the $(\tilde{\nu}_1, \tilde{\nu}_3)$ plane. Consequently, stronger cancellation between positive and negative contributions are expected to reduce the overall signal amplitude, which is observed in the broadband transient absorption measurement, which has a much smaller signal amplitude when compared to that of the previous sections (see Figure 4.4). In practice, the signal was so much smaller that the

200 μm pathlength cells were particularly important. The broadband transient absorption signal at $T = 70$ fs is shown in red in Figure 5.13b and the worse signal to noise level observed follows directly from the near perfect cancellation between positive and negative features across most of the spectrum.

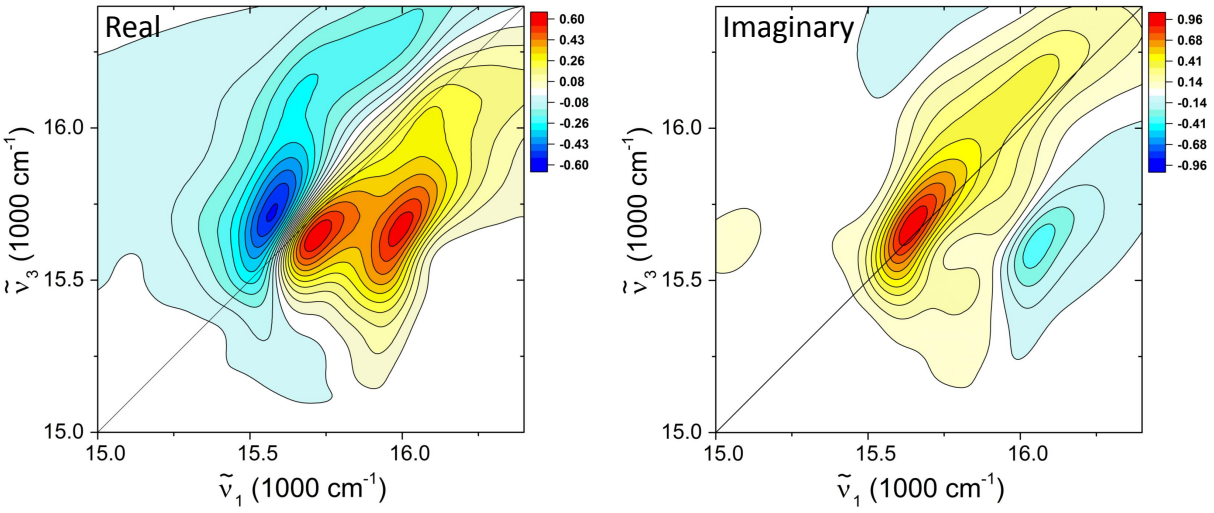

Figure 5.14: Real and imaginary rephasing maps for experiment 2 at $T = 70$ fs.

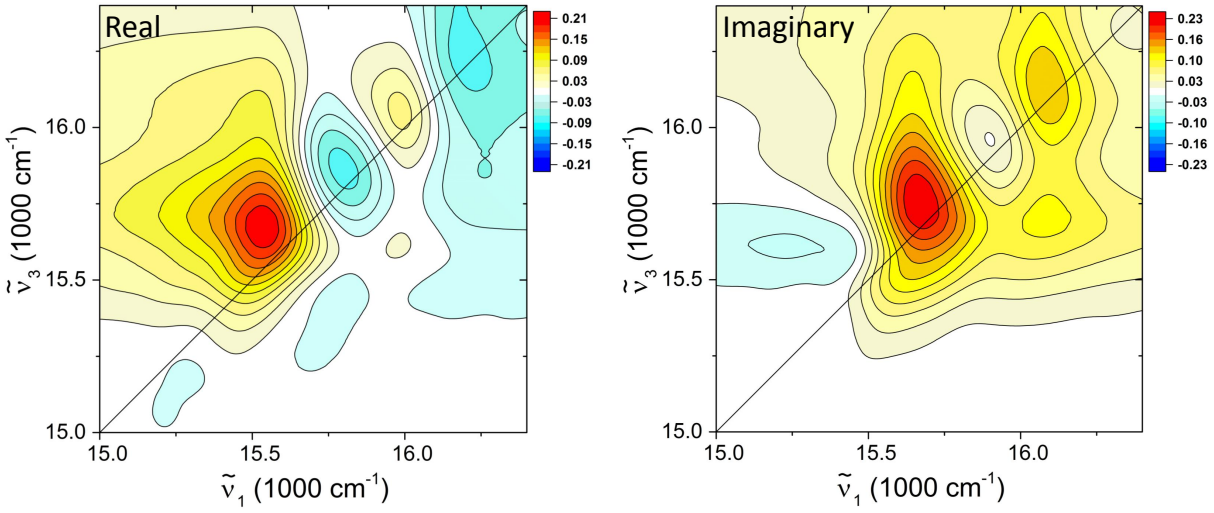

Figure 5.15: Real and imaginary non-rephasing maps for experiment 2 at $T = 70$ fs.

Due to the strong ESA features across most of the spectrum, the 2D-ES maps are also no longer easily comparable to simple models. The rephasing and non-rephasing maps at $T = 70$ fs are shown in Figures 5.14 and 5.15, and are now much more difficult to interpret. Nonetheless, the presence of the extra ESA pathways should not substantially affect the analysis of the oscillations in the region we are interested in. To understand why that is the case, it is necessary to note that any oscillatory ESA pathways will involve a coherence in the excited state during T, followed by an interaction leading to a higher

excited state (the N band, in our case). Because the N band is very broad, the amplitude of such a pathway will be spread over a broad range in the detection frequency, thus not generating any sharp feature with comparable amplitude to the other pathways.

The effect that ESA can have on the coherent oscillations we are concerned with relates to the relative amplitude between excited and ground state coherences. To that end, it is useful to consider that a certain number of monomer molecules inside the focal spot will generate a third-order signal. Out of these, a fraction will have gone through a pathway which is in the ground state during T, while the rest will have been in the electronic excited state during T. The arrival of the third laser pulse then splits this finite number of molecules that were in the excited state during T between the pathways R_1 and R_2 (from Figures 2.5 and 2.7 respectively) and ESA pathways. If the laser spectrum is more strongly resonant with the gap between the Q and the N band, this means that a larger fraction of the molecules that were in the excited state during T will go through the ESA pathways, meaning that a smaller fraction will go through the R_1 and R_2 pathways. For the reason discussed in the previous paragraph we expect that the coherent ESA pathways in our particular sample will not give rise to strong oscillatory signals, so the extra laser intensity at $\tilde{\nu} > 16300$ cm^{-1} is expected solely to reduce the amplitude of coherence pathways in the excited state when compared to the ground state ones (represented by squares in Figure 4.8).

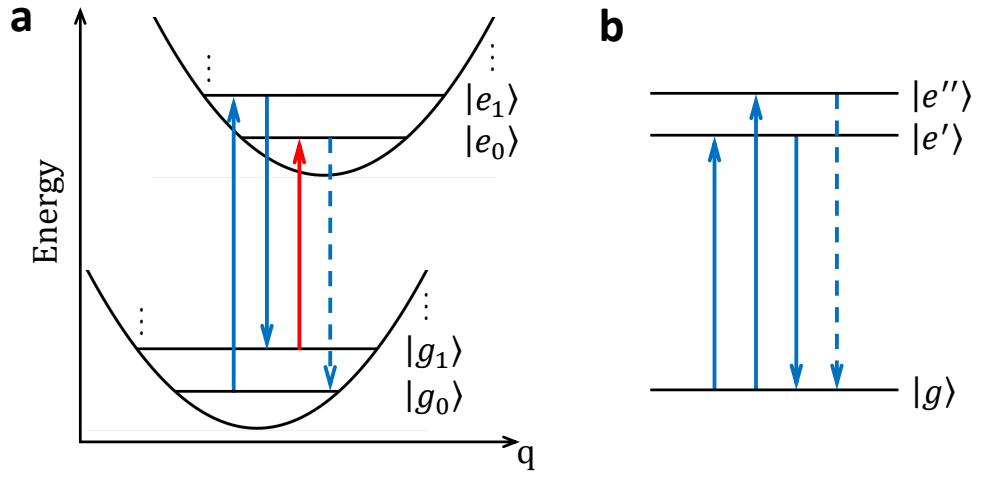

Figure 5.16: **(a)** Displaced harmonic oscillator energy level scheme plus an example of a four-wave mixing pathway with a $|g_1\rangle\langle g_0|$ coherence during T. Field-matter interactions are ordered in time from left to right, with the leftmost arrow defining $\tilde{\nu}_1$, and the signal emission (dashed line) defining $\tilde{\nu}_3$. The red arrow corresponds to an excitation from $|g_1\rangle$ to $|e_0\rangle$. **(b)** Example of an energy level scheme for which electronic coherences can be prepared by broadband laser excitation. The pathway shown includes a $|e''\rangle\langle e'|$ coherence during T.

However, the single most important effect expected from the shift in the laser spectrum from that of Figure 5.1b is related to the missing amplitude to cover the transition between $|e_0\rangle$ and $|g_1\rangle$, namely 15275 cm^{-1} for the monomer in n-pentane with 1% of pyridine. The fact that this frequency is not present in the laser spectrum automatically excludes the pathways for which $\tilde{\nu}_3 = 15275$ cm^{-1}, so they will not be detected in our experiment. Regarding the excitation axis, no effect can take place, because the lowest absorption peak in the Q band remains fully covered by the laser, and the initial excitation must happen at a frequency which the molecule absorbs.

Nonetheless, the four-wave mixing pathways that generate the 2D-ES signals include two field-matter interactions besides the initial excitation and the signal emission which define the $\tilde{\nu}_1$ and $\tilde{\nu}_3$ axes respectively, and those two intermediate field-matter interactions must also take place at a frequency contained in the laser spectrum. To our knowledge, the concept that a coherence signature might be missing because of such filtering in 2D-ES has only been briefly mentioned by Butkus *et al.*, but the coherences were not the main focus of that study and a systematic study of the implications was not presented [177].

To illustrate how the laser spectrum can filter out diagrams due to intermediate interactions, we consider a non-rephasing four-wave mixing pathway in Figure 5.16a which includes a $|g_1\rangle\langle g_0|$ ground state coherence. The excitation wavenumber is defined by the leftmost arrow and corresponds to an excitation from $|g_0\rangle\langle g_0|$ to $|e_1\rangle\langle g_0|$, which is $\tilde{\nu}_1 = 16025$ cm^{-1} in our case. The detection wavenumber is given by the dashed arrow and here it represents an emission from $|e_0\rangle\langle g_0|$ to $|g_0\rangle\langle g_0|$, meaning that $\tilde{\nu}_3 = 15650$ cm^{-1}. Therefore both excitation and detection wavenumbers for this pathway are covered by the laser spectrum (see Figure 5.12). However, there are two other field-matter interactions between excitation and emission which must also be within the laser spectrum for this pathway to be observed, and we note that the one represented by the red arrow in Figure 5.16a corresponds to an excitation from $|g_1\rangle\langle g_0|$ to $|e_0\rangle\langle g_0|$. In our case for the 375 cm^{-1} mode this is at 15275 cm^{-1}, where the laser intensity is negligible. Thus, this pathway cannot be observed in the set of experiments with the laser spectrum from Figure 5.12, and there is no particularly intuitive way to fully consider the suppressed pathways besides explicitly and systematically addressing the frequency of each interaction and whether it is present in the laser used.

Although analyzing all 32 double-sided Feynman diagrams considering the frequency

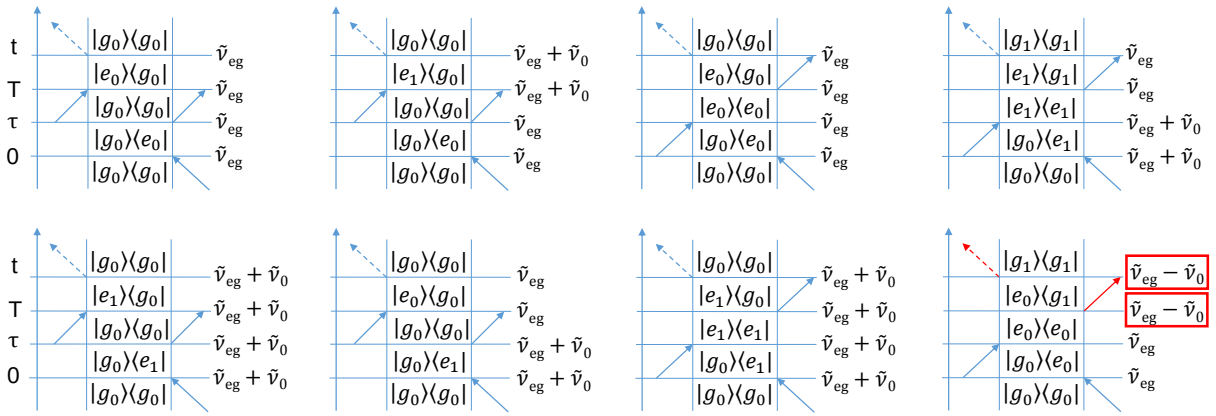

Figure 5.17: Rephasing population Liouville-space pathways for the displaced harmonic oscillator model. On the right hand side of each diagram the wavenumber of each interaction is explicitly shown and a red box encloses it in case it lies outside the spectral coverage of the laser from Figure 5.12. In this case, the arrow corresponding to that interaction is also displayed in red.

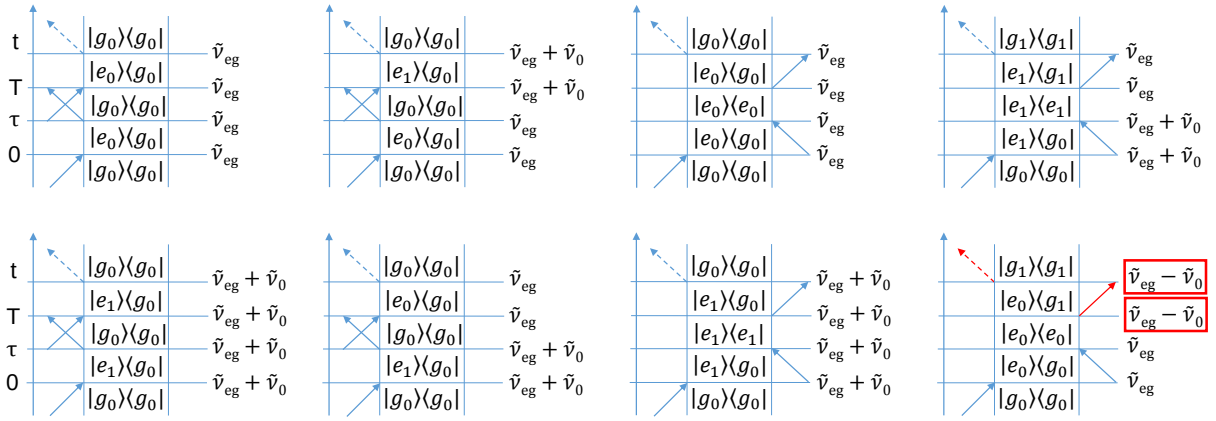

Figure 5.18: Non-rephasing population Liouville-space pathways for the displaced harmonic oscillator model. See caption of Figure 5.17 for details.

of each of the 128 transitions is not particularly convenient, it is certainly feasible, and here we present the pathways from Figures 2.5, 2.6, 2.7 and 2.8 once more, now including the frequency of each interaction. In Figures 5.17 and 5.18 we show all the rephasing and non-rephasing population pathways respectively. It is interesting to note that the requirement that the density matrix be in a population during T effectively forces the initial two field-matter interactions to happen at the same frequency, while the requirement that the signal emission takes the density matrix to a population implies that the third and fourth interactions also take place at the same frequency. That is easily observed in Figures 5.17 and 5.18, as either all interactions happen at a single frequency, or the pair of first and second interactions happen at a given frequency, while the pair of third and fourth interactions happen at another frequency. The transitions which are red-shifted from the

molecular absorption are enclosed in a red box and have the corresponding arrows drawn in red to facilitate visualization. One important result that follows from this analysis is that the only population diagrams which are filtered are those with their emission wavenumber not covered by the spectrum, as long as ESA is not considered. This is in full agreement with the conclusion that the laser spectrum acts as a filter on both excitation and emission axes, as reported in studies which focused on absorptive 2D-ES maps of systems where ESA was negligible [146, 150, 173].

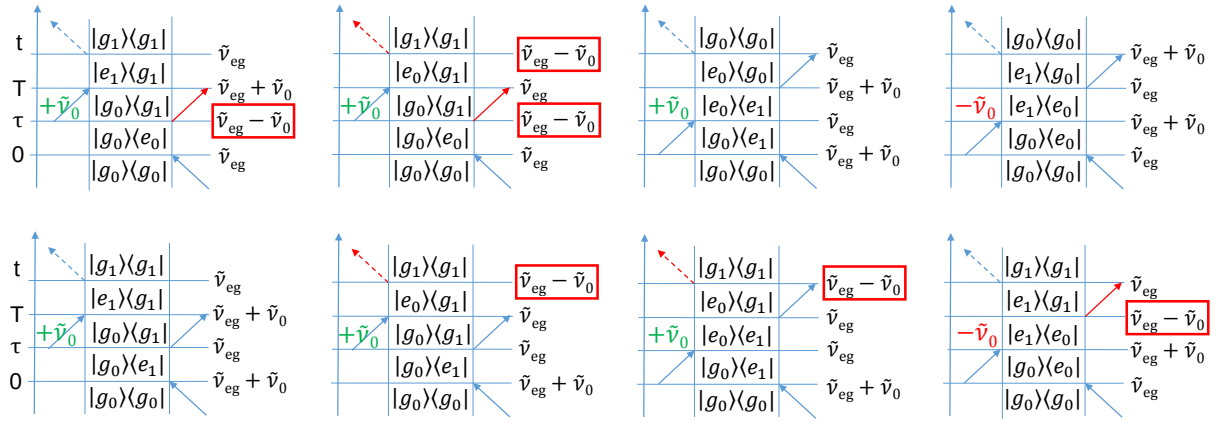

Figure 5.19: Rephasing oscillatory Liouville-space pathways for the displaced harmonic oscillator model. See caption of Figure 5.17 for details.

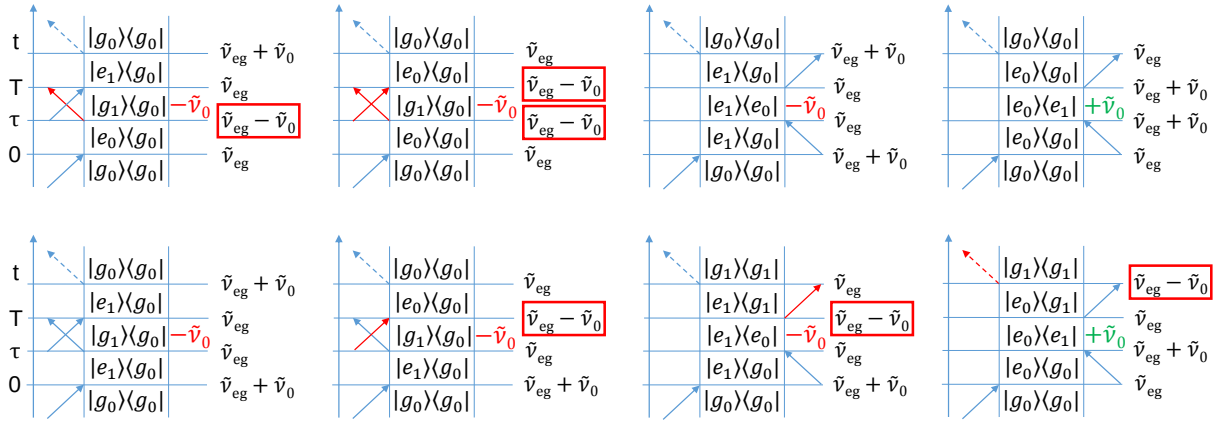

Figure 5.20: Non-rephasing oscillatory Liouville-space pathways for the displaced harmonic oscillator model. See caption of Figure 5.17 for details.

However, a very different picture arises when we consider the coherence pathways: in this case the requirement is that the density matrix is in a coherent superposition of states during T, which implies that the first and second field-matter interactions happen at frequencies different from each other. Therefore, a number of pathways arise which include multiple combinations of interactions at different frequencies, and some of the pathways with excitation and emission frequencies within the laser spectrum might be suppressed

due to an intermediate interaction requiring a frequency not present in the laser spectrum, as exemplified with the non-rephasing pathway in Figure 5.16a. In Figures 5.19 and 5.20 we show all the rephasing and non-rephasing coherence pathways respectively, once more highlighting the wavenumber of each interaction. As a consequence of the higher number of frequencies present in the coherence diagrams, we see that only 6 of the 16 pathways survive if the $\tilde{\nu}_{eg} - \tilde{\nu}_0$ wavenumber is not present in the laser spectrum.

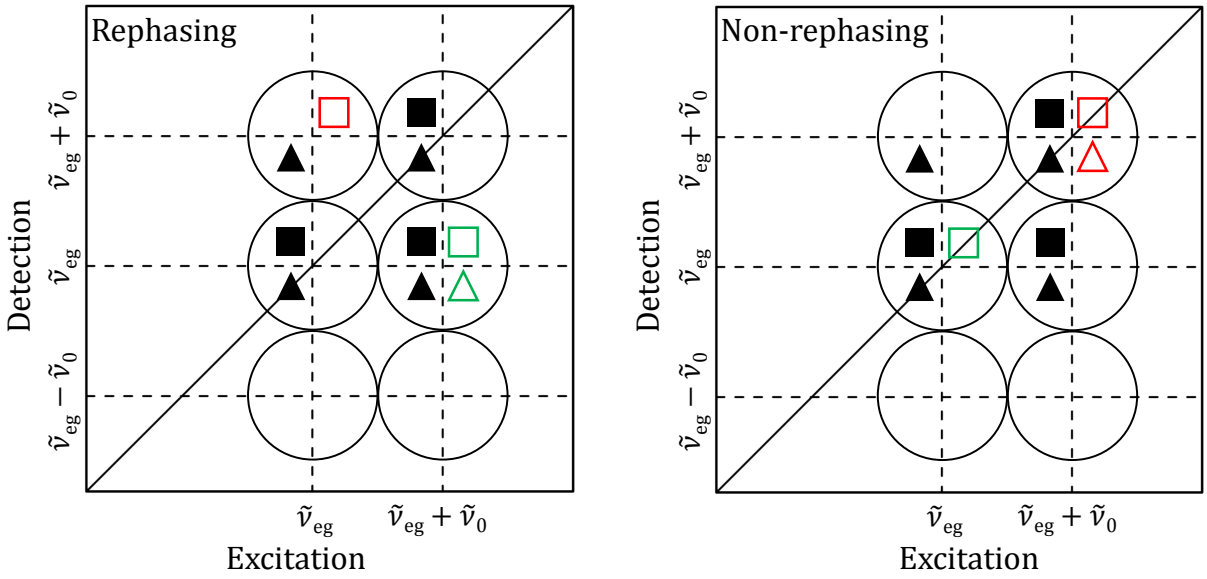

Figure 5.21: Scheme of Liouville-space pathways in rephasing (left) and non-rephasing (right) 2D maps if the frequency $\tilde{\nu}_{eg} - \tilde{\nu}_0$ is not present in the laser spectrum, corresponding to experiment 2. Green and red symbols represent positive and negative frequencies respectively. See caption of Figure 2.9 for details.

At this point, we are in position to draw a scheme with all pathways that are expected to contribute to our 2D-ES measurements when the laser spectrum does not cover the $\tilde{\nu}_{eg} - \tilde{\nu}_0$ energy gap, which is shown in Figure 5.21. In this Figure the population pathways are represented by solid black geometric figures, and one can see that the only difference between the initial forecast from Figure 2.9 is that the pathways with emission wavenumber no longer covered by the spectrum are suppressed, as discussed above. This result is not obvious in our data because of the strong ESA contributions present in the zinc-porphyrin monomer with the laser spectrum used in this Section, which cannot be conveniently taken into account in the diagrammatic analysis.

Nonetheless, the surprising result here concerns the coherence pathways, where the shift in the laser spectrum causes much more dramatic changes. The remaining oscillatory pathways in Figure 5.21 are off-diagonal for rephasing and diagonal for non-rephasing,

matching exactly the positions and frequency signs that would correspond to a purely electronic coherence (see Figure 2.12), with the main difference being that one of the positions has two diagrams, while the other has only one (in models for electronic coherence the same number of pathways in all positions is expected).

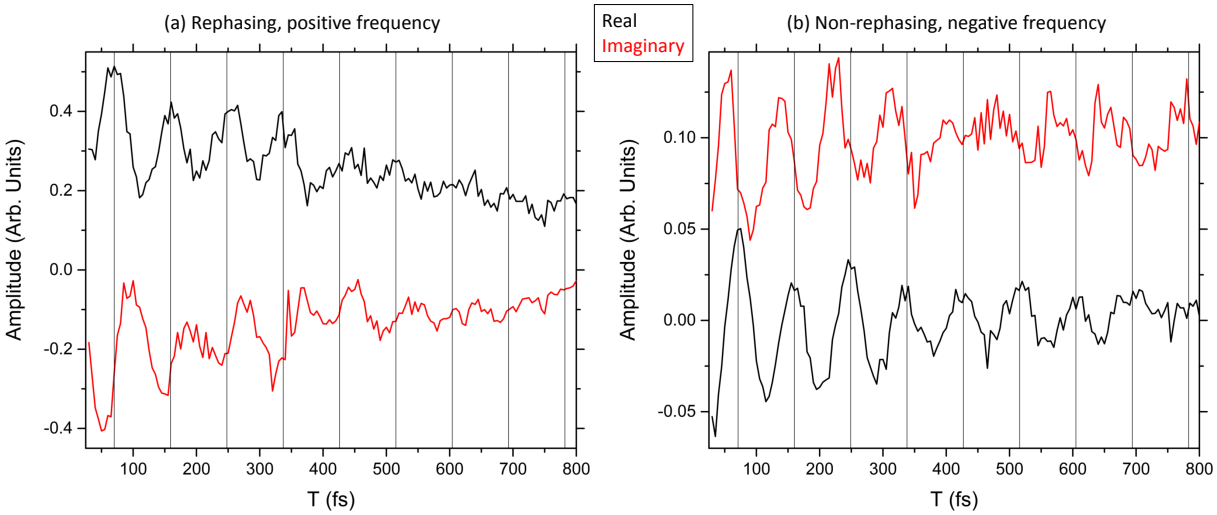

Figure 5.22: **(a)** Real and imaginary rephasing traces from experiment 2 as a function of T for $\tilde{\nu}_1 = 16025$ cm^{-1} and $\tilde{\nu}_3 = 15650$ cm^{-1}, corresponding to the expected central position of the double-sided Feynman diagrams with positive 375 cm^{-1} frequency. **(b)** Real and imaginary non-rephasing traces from experiment 2 as a function of T for $\tilde{\nu}_1 = \tilde{\nu}_3 = 16025$ cm^{-1}, corresponding to the expected central position of the double-sided Feynman diagrams with negative 375 cm^{-1} frequency.

This result can be easily rationalized through comparison between the energy level structure of a vibrationally coupled electronic transition (Figure 5.16a) to that of two electronic excited states of similar energy which share a common ground state, which is shown in Figure 5.16b. The main difference between these energy-level structures is the absence of a sub-level associated with the ground state in the latter case. Therefore, if a vibrationally coupled system is studied with a laser spectrum blue-shifted so that the energy gap between $|g_1\rangle$ and $|e_0\rangle$ is no longer probed, the two energy level structures become much more similar. The only difference which remains to be probed is the possibility of an initial excitation to $|e_1\rangle$ followed by a de-excitation to $|g_1\rangle$, thus generating a vibrational coherence in the ground state during T. These pathways are represented by the triangles in Figure 5.21 and overlap with coherences in the electronic excited state for both rephasing and non-rephasing.

In order to test if the forecast from Figure 5.21 is correct, our first step is to plot the real and imaginary rephasing and non-rephasing signal amplitude at points where

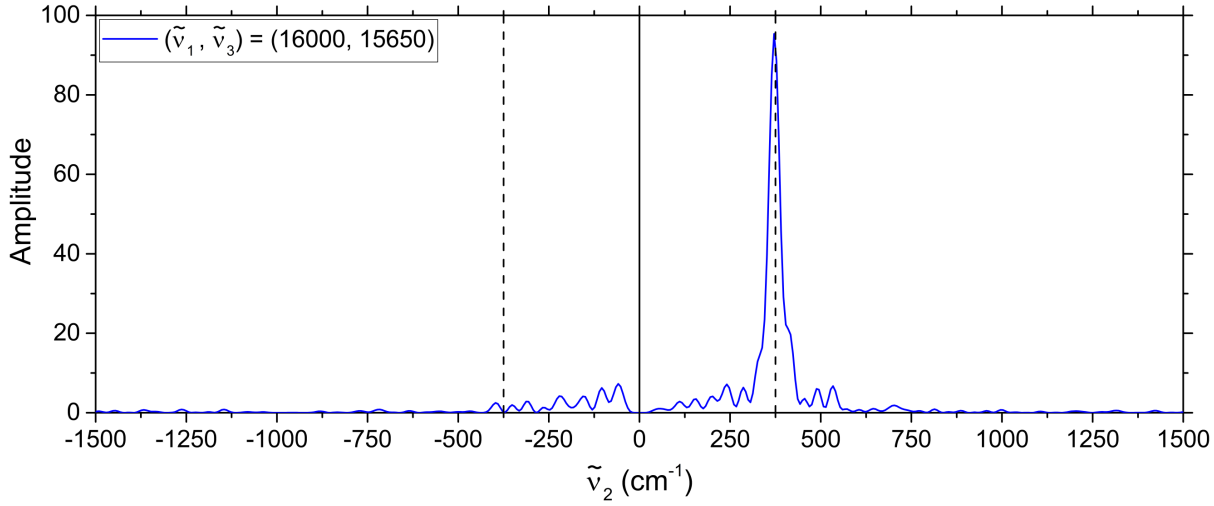

Figure 5.23: Power spectrum of the rephasing signal at $\tilde{\nu}_1 = 16025$ cm^{-1} and $\tilde{\nu}_3 = 15650$ cm^{-1}, confirming the oscillatory amplitude at $\tilde{\nu}_2 = +375$ cm^{-1}.

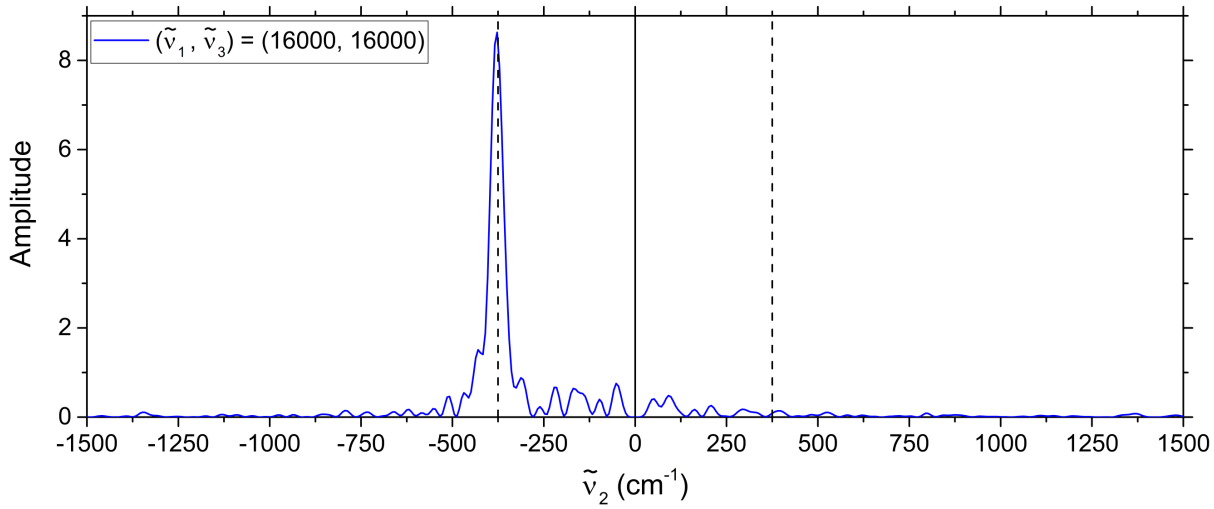

Figure 5.24: Power spectrum of the non-rephasing signal at $\tilde{\nu}_1 = \tilde{\nu}_3 = 16025$ cm^{-1}, confirming the oscillatory amplitude at $\tilde{\nu}_2 = -375$ cm^{-1}.

only positive or negative frequency oscillations are expected, which we do in Figure 5.22. The rephasing trace was chosen at $\tilde{\nu}_1 = 16025$ cm^{-1} and $\tilde{\nu}_3 = 15650$ cm^{-1}, which corresponds to the expected peak position at positive frequency, and the signal amplitude indeed shows oscillatory behaviour with the 89 fs period associated with the 375 cm^{-1} mode, with the real and imaginary parts oscillating with the same amplitude and phase-shift corresponding to a positive frequency (see Section 5.1). The corresponding power spectrum at this $(\tilde{\nu}_1, \tilde{\nu}_3)$ point is shown in Figure 5.23, and a strong oscillatory amplitude at $\tilde{\nu}_2 = +375$ cm^{-1} is found, with no corresponding amplitude at $\tilde{\nu}_2 = -375$ cm^{-1}.

Similarly, Figure 5.22 shows the non-rephasing trace at $\tilde{\nu}_1 = \tilde{\nu}_3 = 16025$ cm^{-1}, which is also the expected position for maximum amplitude at negative frequency for the 375 cm^{-1}

mode. Once more, we find that the real and imaginary parts have the same oscillatory amplitude and phase-shift corresponding to the expected negative frequency. That is confirmed by the power spectrum of the residuals of this trace, shown in Figure 5.24, where a peak at $\tilde{\nu}_2 = -375\text{cm}^{-1}$ is observed, with no corresponding amplitude at $\tilde{\nu}_2 = +375\ \text{cm}^{-1}$.

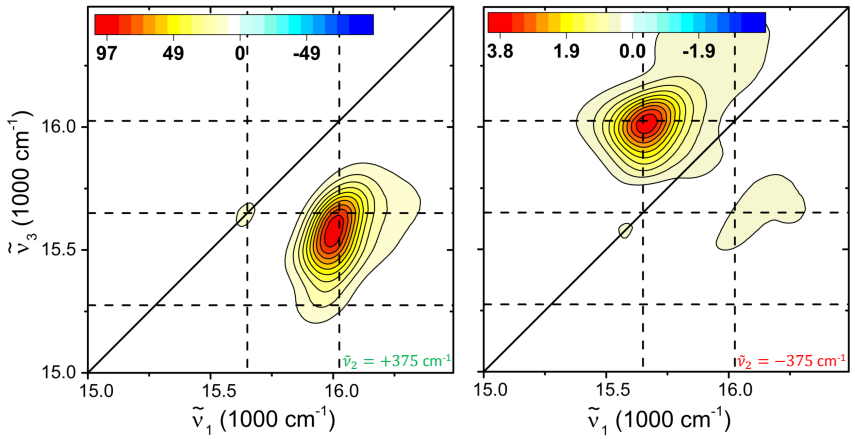

Figure 5.25: Rephasing oscillation amplitude maps at $\tilde{\nu}_2 = +375\ \text{cm}^{-1}$ (left) and at $\tilde{\nu}_2 = -375\ \text{cm}^{-1}$ (right).

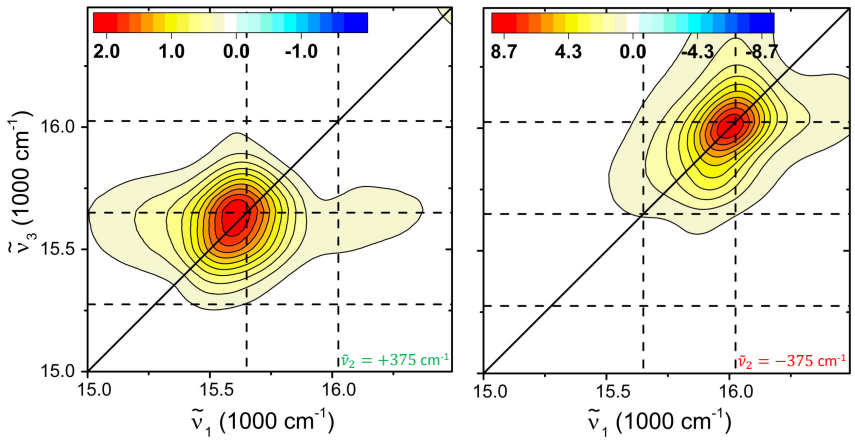

Figure 5.26: Non-rephasing oscillation amplitude maps at $\tilde{\nu}_2 = +375\ \text{cm}^{-1}$ (left) and at $\tilde{\nu}_2 = -375\ \text{cm}^{-1}$ (right).

In Figures 5.25 and 5.26 we show the rephasing and non-rephasing oscillation amplitude maps for $\tilde{\nu}_2 = \pm 375\ \text{cm}^{-1}$ respectively. Comparing these experimental results to the forecast from the double-sided Feynman diagrams in Figure 5.21 we find excellent agreement, with the oscillatory amplitude being observed with the expected frequency sign and around the forecast $(\tilde{\nu}_1, \tilde{\nu}_3)$ coordinates, thus confirming the importance of taking all field-matter interaction frequencies into account when addressing which coherence pathways will be detectable in a given 2D-ES experiment.

An important consequence of this result is that the distinction between purely electronic and vibrational coherences in 2D-ES requires that the laser spectrum be taken into account. For the relatively simple case of the porphyrin monomer, simple inspection of the double-sided Feynman diagrams and the frequency of each interaction sufficed to describe all qualitative features of the data. Furthermore, we also observe that the oscillatory amplitude at the positions where two pathways contribute is significantly larger than the ones where a single pathway contributes.

In the non-rephasing case, for instance, the oscillatory amplitude peak at $\tilde{\nu}_2 = -375$ cm^{-1} and $\tilde{\nu}_1 = \tilde{\nu}_3 = 16025$ cm^{-1} contains two pathways (one in the ground and one in the excited state), while the peak at $\tilde{\nu}_2 = +375$ cm^{-1} and $\tilde{\nu}_1 = \tilde{\nu}_3 = 15650$ cm^{-1} contains one excited state pathway. We observe that the amplitude of the latter peak is over a factor of 4 smaller than the former. That is consistent with the rephasing case, where the effect is even more pronounced, with the peak at $\tilde{\nu}_2 = -375$ cm^{-1} being a factor of approximately 25 times smaller than the peak at $\tilde{\nu}_2 = +375$ cm^{-1} in Figure 5.25.

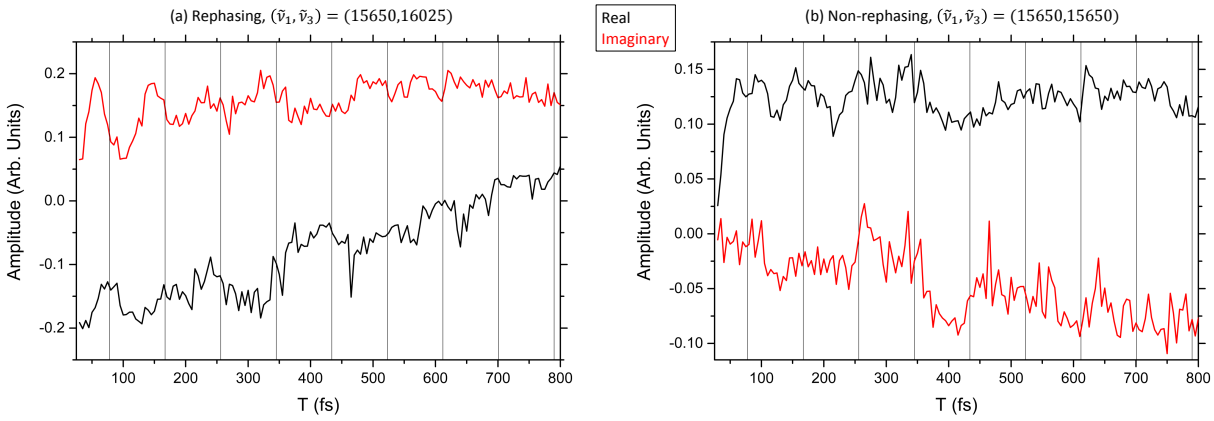

Figure 5.27: **(a)** Real (black) and imaginary (red) rephasing traces at $(\tilde{\nu}_1, \tilde{\nu}_3) = (15650, 16025)$. A factor of 0.13 was added to the real part to bring both traces closer together. **(b)** Real and imaginary non-rephasing traces at $(\tilde{\nu}_1, \tilde{\nu}_3) = (15650, 15650)$. A factor of 0.2 was subtracted from the imaginary part to avoid overlap with the real part.

Because all three oscillatory pathways include the same transition frequencies (see the non-suppressed pathways in Figure 5.21), the laser spectrum has the same effect on all three pathways, and the significantly larger amplitude at $\tilde{\nu}_1 = \tilde{\nu}_3 = 16025$ cm^{-1} can be attributed to the vibrational coherence in the ground state generating a larger signal. As discussed previously, we expect the strong resonance between the laser spectrum and the gap between the Q and N bands to reduce the amplitude of the excited state coherence pathways compared to the ground state ones, which is consistent with our

observations. We note that already in the experiment from Section 5.1 the maximum oscillatory amplitude observed on the maps which included only excited state pathways was significantly smaller than that observed in the maps which included both ground and excited state pathways. However, direct comparison between the results from this Section and those of Section 5.1 is not possible because of the significant overlap between neighboring pathways in Section 5.1.

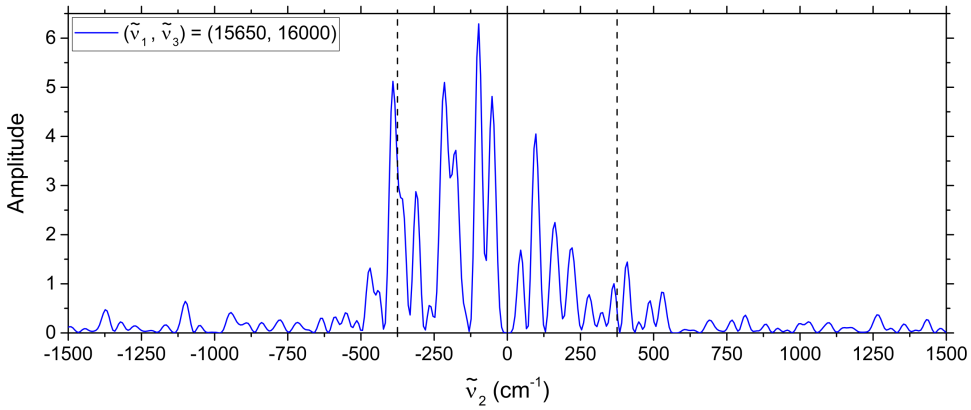

Figure 5.28: Power spectrum of the residuals of the rephasing signal at $(\tilde{\nu}_1, \tilde{\nu}_3) = (15650, 16025)$ shown in Figure 5.27a.

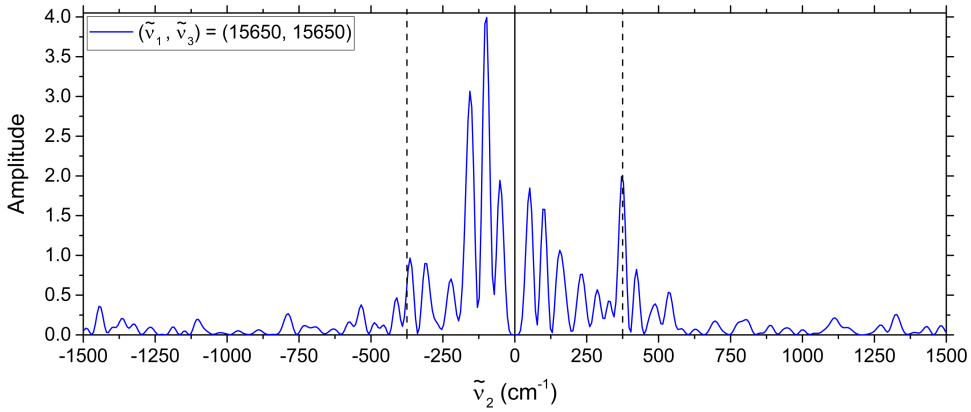

Figure 5.29: Power spectrum of the residuals of the non-rephasing signal at $(\tilde{\nu}_1, \tilde{\nu}_3) = (15650, 15650)$ shown in Figure 5.27b.

Still, the large disparity in oscillatory amplitude raises the question of whether the smaller amplitudes observed at rephasing $\tilde{\nu}_2 = -375$ cm^{-1} and non-rephasing $\tilde{\nu}_2 = +375$ cm^{-1} are more than noise. Normalized color maps can be very deceptive, as the signal to noise as a function of T and $\tilde{\nu}_2$ is hidden. In order to rigorously assess whether amplitude observed in an oscillation amplitude map indeed corresponds to a peak detected above noise it is essential to consider the data as a function of T or $\tilde{\nu}_2$. In Figure 5.27a we show the amplitude traces for real and imaginary parts of the rephasing signal

at $(\tilde{\nu}_1, \tilde{\nu}_3) = (15650, 16025)$. Although the signal to noise ratio is not very good, it is still possible to recognize oscillatory amplitude with period of approximately 89 fs and negative frequency, suggesting the amplitude peak observed in Figure 5.25 at $\tilde{\nu}_2 = -375$ cm^{-1} really corresponds to the vibrational coherence in the excited state.

The power spectrum of the residuals of the rephasing signal from Figure 5.27a is shown in Figure 5.28, where the effects of the worse signal to noise ratio can be seen in the form of many peaks at low frequencies. This worse signal to noise is partially due to the near perfect cancellation between positive and negative signals due to the high ESA in this spectral region. Scattering contributions in the broadband transient absorption become more important because of the small signal (see Figure 5.13b), and as they fluctuate for different values of T, the phasing procedure can find different local minima. Because the phasing compares the integral of the real part of the sum of rephasing and non-rephasing spectra, small shifts in the transient absorption signal due to these noise fluctuations at different values of T cause shifts in both $\tilde{\nu}_1$ and $\tilde{\nu}_3$ in the 2D-ES. This results in discontinuities in the signal amplitude of single $(\tilde{\nu}_1, \tilde{\nu}_3)$ points as a function of T, even if the 2D-ES maps for all T points show the same qualitative behavior.

In Figure 5.28 we observe a peak at $\tilde{\nu}_2 = -390$ cm^{-1} among the noise which corresponds to the amplitude seen in the oscillation amplitude map in Figure 5.25. The 15 cm^{-1} shift compared to the vibrational mode can be attributed to the overall higher noise levels in the data. In spite of the noise, the fact that the oscillatory amplitude at $\tilde{\nu}_2 = -375$ cm^{-1} forms a well defined peak in Figure 5.25 as a function of $(\tilde{\nu}_1, \tilde{\nu}_3)$ around the forecast coordinates, instead of being scattered around the excitation-detection plane, supports that we are observing a real signal.

A similar situation emerges for the non-rephasing signal at $\tilde{\nu}_1 = \tilde{\nu}_3 = 15650$ cm^{-1} shown in Figure 5.27b, where a weak oscillation of period of approximately 89 fs can be identified in the real part, not being as evident in the imaginary part. If an oscillation is present in the real part, but has zero amplitude in the imaginary part, this corresponds to an equal weight between positive and negative frequencies. In Figure 5.29 we show the power spectrum of the residuals of this trace, finding that indeed some amplitude is observed at $\tilde{\nu}_2 = -375$ cm^{-1}, although it is clearly outweighed by the amplitude at $\tilde{\nu}_2 = +375$ cm^{-1}, which is the expected one. As in the rephasing case from the previous paragraph, the amplitude around this point forms a clear peak as around the expected

position in the $(\tilde{\nu}_1, \tilde{\nu}_3)$ plane, which suggests that is is a real signal.

In summary, we have observed that in the two positions for which the coherence pathways expected are in the electronic excited state there is weak oscillatory amplitude at the expected frequencies. Although the amplitude is not unquestionably above noise in both cases, the behaviour of the amplitude as a function of $(\tilde{\nu}_1, \tilde{\nu}_3)$ strongly suggests that both of them correspond to real signatures, which were expected to be weak for this laser spectrum and sample, due to the strong excited state absorption. Importantly, we emphasize that our conclusion regarding the filtering effect of the laser spectrum does not rely on the observation or not of the vibrational coherences in the excited state, but rather on the suppression of the pathways with coherences in the ground state that have both excitation and detection wavenumbers where laser intensity is present.

The suppression of pathways due to the laser spectrum can be seen through comparison of the results from Figures 4.8 and 5.21. In the rephasing case, we see that at positive frequencies a ground state pathway is forecast at $\tilde{\nu}_1 = \tilde{\nu}_3 = \tilde{\nu}_{eg}$, and it is expected to be suppressed if the laser spectrum has zero intensity at $\tilde{\nu}_{eg} - \tilde{\nu}_0$. In our experiments, when the laser spectrum covered this wavenumber we detected all four peaks represented by the green symbols with amplitudes of the same order of magnitude (see Figure 5.7). However, when we shifted the spectrum to avoid that wavenumber, Figure 5.25 shows that at $\tilde{\nu}_2 = +375$ cm^{-1} a very strong amplitude is observed at $(\tilde{\nu}_1, \tilde{\nu}_3) = (\tilde{\nu}_{eg} + \tilde{\nu}_0, \tilde{\nu}_{eg})$, while no amplitude is observed at $\tilde{\nu}_1 = \tilde{\nu}_3 = \tilde{\nu}_{eg}$.

In the non-rephasing case this effect is even more dramatic, given that all ground state pathways have negative frequency and have excitation and emission wavenumber within the spectral range covered by the laser in both experiments. In Figure 5.8 we observe oscillatory intensity with the same order of magnitude at all four $(\tilde{\nu}_1, \tilde{\nu}_3)$ coordinates, where these pathways are expected. If the laser spectrum has no intensity at $\tilde{\nu}_{eg} - \tilde{\nu}_0$, the three pathways centred at the cross peak positions and the pathway centred at $\tilde{\nu}_1 = \tilde{\nu}_3 = \tilde{\nu}_{eg}$ are suppressed, so that the two pathways centred at $\tilde{\nu}_1 = \tilde{\nu}_3 = \tilde{\nu}_{eg} + \tilde{\nu}_0$ are the only ones that remain (see Figure 5.21). This is in complete agreement with the experimental results in Figure 5.26, where all amplitude observed is a single peak around the expected position. Thus the filtering of the laser spectrum in the intermediate interaction of four-wave mixing pathways is established as a general effect, and the difficulty of observing individual coherences in the electronic excited state follows from the ESA specific to the

zinc-porphyrin monomer and the laser spectrum used.

Furthermore, we note that the possibility of confusion between and electronic and vibrational coherence in our experiment where the laser did not include intensity at $\tilde{\nu}_{eg}-\tilde{\nu}_0$ could have been avoided exactly by addressing the disparity of amplitude between the two rephasing and non-rephasing oscillatory peaks. Because the oscillatory amplitude in the positions where two coherence pathways (one in the ground state) was substantially more intense than that found in the positions where only one coherence pathway is present, that is a strong indication of the vibrational nature of the coherence. That is because in the case of an electronic coherence, detailed in Figures 2.10, 2.11 and 2.12, the oscillatory pathways for each of rephasing and non-rephasing signals occur in the same number and are symmetric, thus are expected to generate oscillatory features of the same amplitude.

In summary, in this Section we investigated 2D-ES signatures of a vibrationally coupled system when the laser spectrum fails to have significant amplitude red-shifted to the main absorption. We confirmed results previously reported that non-oscillatory signals are merely filtered along both excitation and emission axes. On the other hand, for coherent oscillations we observed major effects on the positions where oscillatory amplitude is observed, with features within the excitation-emission window defined by the spectrum disappearing completely. The final result resembled that expected for a purely electronic coherence very closely. We proceeded to show that all observed features are promptly explained by considering the wavenumber of all field-matter interactions in the Liouville-space pathways discussed in Chapter 2. We also considered the effect of ESA on coherences in the electronic excited state, and discussed how oscillation amplitude maps alone can be deceptive in terms of data analysis, complementing them with power spectra at relevant $(\tilde{\nu}_1, \tilde{\nu}_3)$ coordinates, so that the signal-to-noise as a function of $\tilde{\nu}_2$ could be considered.

5.3 Benchmarking ground state coherences

So far this Chapter has described the signatures of vibrational coherences in 2D-ES for two different laser excitation spectra: that of Section 5.1 has significant amplitude from $\tilde{\nu}_{eg} - \tilde{\nu}_0$ to $\tilde{\nu}_{eg} + \tilde{\nu}_0$ for our sample, while that of Section 5.2 has no amplitude at $\tilde{\nu}_{eg} - \tilde{\nu}_0$, but still covered the region from $\tilde{\nu}_{eg}$ to $\tilde{\nu}_{eg} + \tilde{\nu}_0$. This comparison has proved insightful, but we note that there is yet another possibility that can be explored: the laser spectrum

can cover both $\tilde{\nu}_{eg} - \tilde{\nu}_0$ and $\tilde{\nu}_{eg}$, but not $\tilde{\nu}_{eg} + \tilde{\nu}_0$, which is the focus of this Section.

The first question to address is which double-sided Feynman diagrams will be observed with this spectrum, which can be done by analysing the diagrams and excluding all that contain a transition at $\tilde{\nu}_{eg} + \tilde{\nu}_0$. For the population diagrams the same conclusion as before is found: the pathways with both excitation and detection wavenumber inside the laser spectrum remain present, as can be seen in Figures 5.17 and 5.18. As for the coherence diagrams, inspection of Figures 5.19 and 5.20 shows that a single rephasing and a single non-rehasing pathway remain, both of them with coherences in the ground state (as vibrational coherences in excited state necessarily require an excitation to $|e_1\rangle$, at $\tilde{\nu}_{eg} + \tilde{\nu}_0$).

In Figure 5.30 we show a scheme showing the remaining pathways for rephasing and non-rephasing contributions. Regarding the population pathways, in both cases one ground state bleach and one stimulated emission pathway overlap in the diagonal, while a single stimulated emission pathway appears in the off-diagonal region at low emission wavenumbers. As for the coherence pathways, the non-rephasing one lies in the $\tilde{\nu}_1 = \tilde{\nu}_3 = \tilde{\nu}_{eg}$ diagonal, thus overlapping with the strongest non-oscillatory signals, while the rephasing one appears at the more convenient $(\tilde{\nu}_1, \tilde{\nu}_3) = (\tilde{\nu}_{eg}, \tilde{\nu}_{eg} - \tilde{\nu}_0)$ cross peak position, where it overlaps solely with a stimulated emission population pathway.

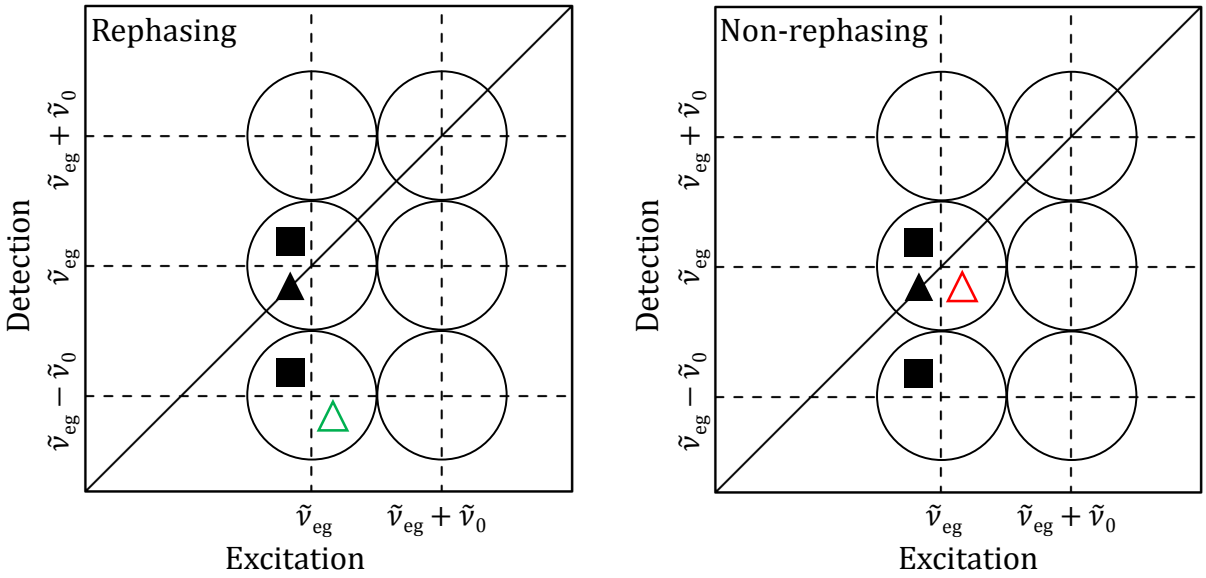

Figure 5.30: Scheme of double-sided Feynman diagrams in a rephasing (left) and non-rephasing (right) 2D maps if the laser spectrum has no amplitude at $\tilde{\nu}_{eg}+\tilde{\nu}_0$ (see Figure 4.8 for scheme with all diagrams independently of the laser spectrum). Green and red symbols represent positive and negative frequencies respectively.

This experiment can be useful to benchmark the coherences associated with sublevels in the ground state of a system. It is clear that in principle a spectrum such as that of Figure 5.1 is the most desirable, as it probes all energy gaps and therefore recovers more information. However such a spectrum is often unattainable in practice, and in such cases a combination of this 2D-ES experiment with the red-shifted spectrum with that of Section 5.2 would provide a complete and unambiguous picture of the coherences.

In order to demonstrate this experiment, we recall that in the linear absorption spectrum of the zinc-porphyrin monomer in n-pentane and 1% by volume of pyridine (Figure 5.1), the high energy peak in the Q band centered around $\tilde{\nu} = 17000$ cm^{-1} (588 nm) has been demonstrated to contain contributions both in the x and y polarizations in reference [160]. The y-polarized contribution has been assigned to the $Q_y(0-0)$ transition, while the contribution along x is assigned to vibronic peaks associated with the Q_x band, predicted at around $\tilde{\nu}_0 = 1340$ cm^{-1} $= 16990 - 15650$ cm^{-1}. Because the spectrum we used in the experiments of Section 5.1 has bandwidth well below 14000 cm^{-1} (1650 cm^{-1} below the main absorption), but only up to 16500 cm^{-1} (850 cm^{-1} higher than the main absorption), the data from that Section is already an example of an experiment where the spectrum does not cover the vibronic peak corresponding to the 1340 cm^{-1} mode, but does cover the energy gap corresponding to the $|g_1\rangle$ to $|e_0\rangle$ (for vibrational modes in the region defined by 850 cm^{-1} $< \tilde{\nu}_0 <$ 1650 cm^{-1}).

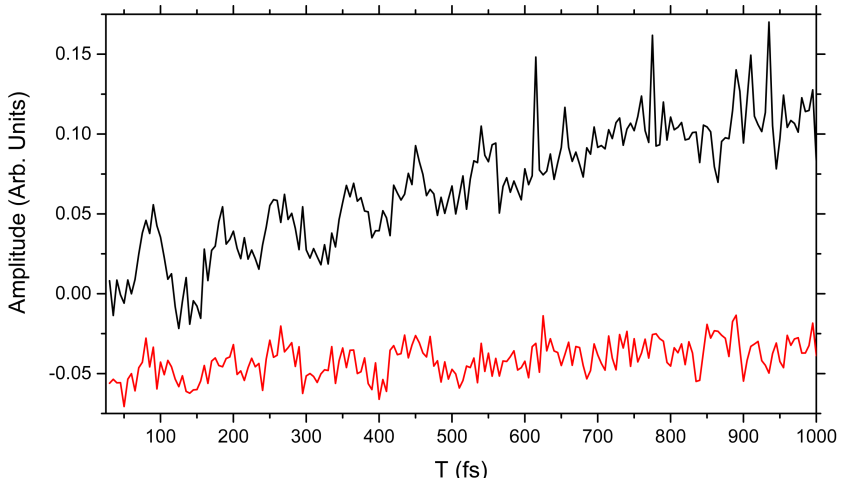

Figure 5.31: Non-rephasing real (black line) and imaginary (red line) signal at $\tilde{\nu}_1 = \tilde{\nu}_3 =$ 15650 cm^{-1} as a function of T. A factor of 0.25 was subtracted from the real part to bring the traces closer together.

We start by looking at the non-rephasing signal at $\tilde{\nu}_1 = \tilde{\nu}_3 = 15650$ cm^{-1}, the amplitude of which is displayed as a function of T in Figure 5.31. The dominant oscillatory

amplitude is observed at 375 cm^{-1}, and two pathways at this frequency are centered around this point, one of positive frequency corresponding to a coherence in the excited state, and one of negative frequency corresponding to a coherence in the ground state (see Figure 4.8). The presence of both positive and negative frequency amplitude at 375 cm^{-1} is manifested through the small amplitude of the imaginary part oscillation when compared to the real part, and it has already been discussed in Section 5.1 in Figure 5.8.

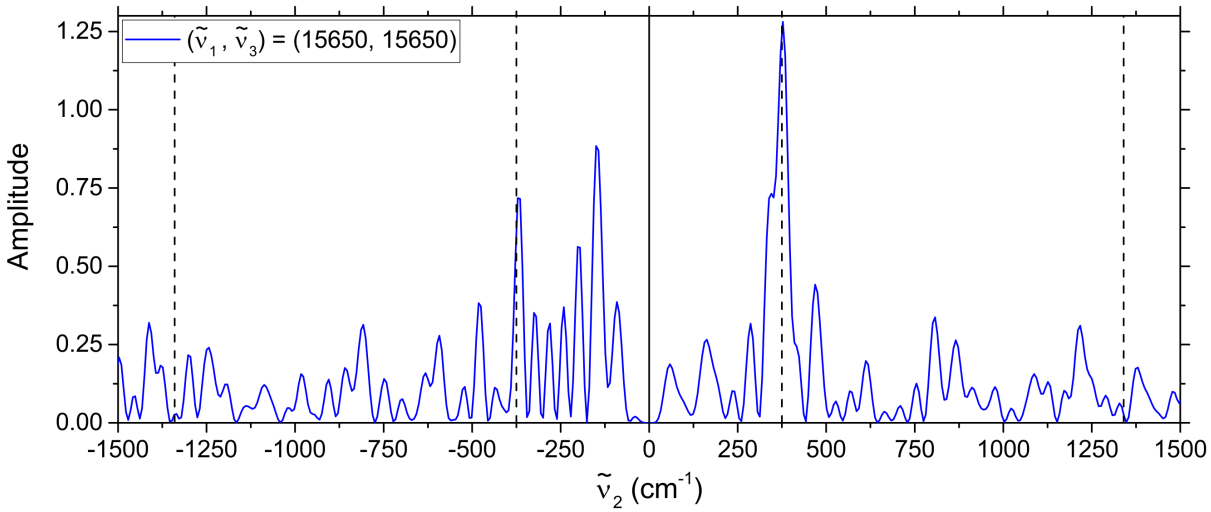

Figure 5.32: Power spectrum of the residuals of the non-rephasing signal at $\tilde{\nu}_1 = \tilde{\nu}_3 = 15650$ cm^{-1}. The dashed vertical lines mark $\tilde{\nu}_2 = \pm 375$ cm^{-1} and $\tilde{\nu}_2 = \pm 1340$ cm^{-1}.

Besides the amplitude at $\tilde{\nu}_2 = \pm 375$ cm^{-1}, it is unclear from the Figure 5.31 which other frequencies are present. To address that we show the power spectrum of the residuals of this signal in Figure 5.32, where we observe the amplitude at $\tilde{\nu}_2 = \pm 375$ cm^{-1} and $\tilde{\nu}_2 \approx -150$ cm^{-1}, as well as significant noise throughout the entire $\tilde{\nu}_2$ range with amplitude exceeding 0.15. We expect the observation of vibrational coherences to be generally challenging for the non-rephasing signal at $\tilde{\nu}_1 = \tilde{\nu}_3 = \tilde{\nu}_{eg}$, as not only are the oscillatory features on top of a strong non-oscillatory signal (see Figure 5.30), but also oscillatory amplitude of all ground state vibrational coherences overlap in this single point if more than one vibrational mode coupled to the electronic transition is present. Therefore, when an experiment with the red-shifted spectrum is performed the non-rephasing signal is always expected to be challenging, and in our case the data is not sufficiently good to permit clear interpretation.

The coherence pathway for the rephasing maps is more useful for two reasons: firstly, the non-oscillatory background is of smaller amplitude as it consists of a single stimulated emission pathway (see Figure 5.30). Secondly, because it is a cross-peak with emission

wavenumber $\tilde{\nu}_{eg} - \tilde{\nu}_0$, the only oscillatory frequencies present will be those of wavenumber around $\tilde{\nu}_0$, contrary to the non-rephasing case, where all coherent oscillations overlap in the diagonal. In our previous analysis of the 2D-ES data of this experiment in Section 5.1, we showed the real and imaginary parts of the rephasing spectra in Figure 5.2, but the $(\tilde{\nu}_1, \tilde{\nu}_3)$ scale was focused around the main signal, and the cross peak region associated with a vibrational coherence of $\tilde{\nu}_0 = 1340$ cm^{-1} – $(\tilde{\nu}_1, \tilde{\nu}_3) = (15650, 14310)$ – was not included. That was because no obvious amplitude was observed in this coordinate, which we show in Figure 5.33, where we display the full scale real and imaginary rephasing signals at $T = 125$ fs, with the $(\tilde{\nu}_1, \tilde{\nu}_3) = (15650, 14310)$ position marked by the dashed lines.

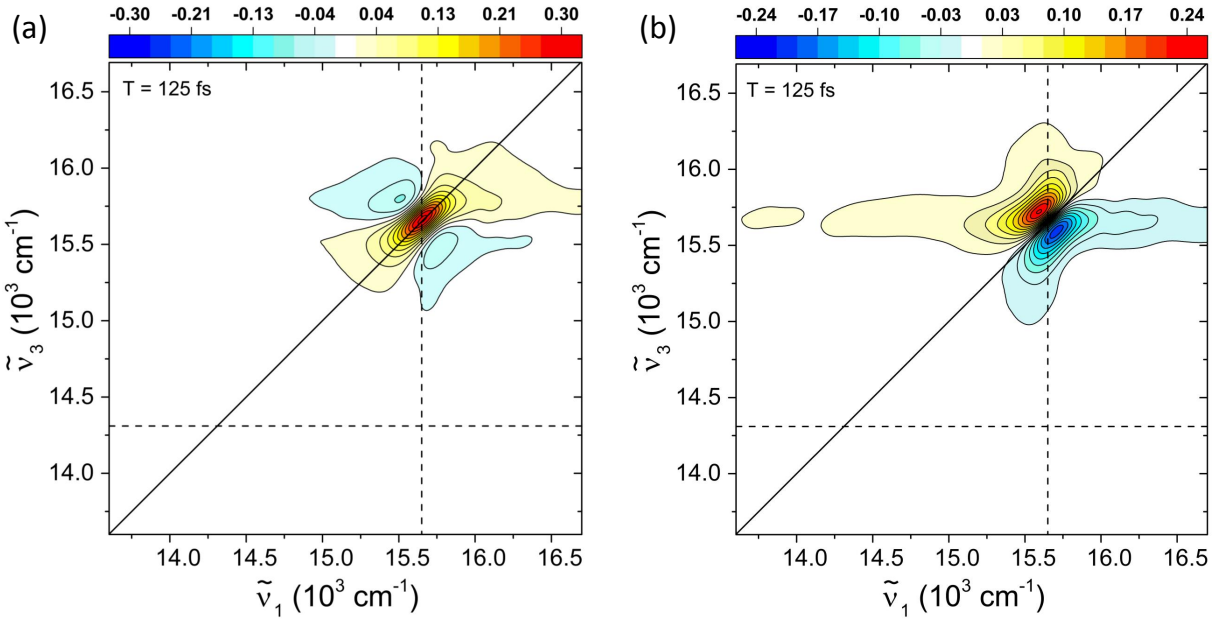

Figure 5.33: Rephasing real (a) and imaginary (b) signals with the laser spectrum from Section 5.1. The dashed lines mark the cross peak position where a positive frequency associated with the vibronic signal at 16990 cm^{-1} from the linear absorption would be expected.

Color maps can be deceptive and all that we can conclude from Figure 5.33 regarding the $(\tilde{\nu}_1, \tilde{\nu}_3) = (15650, 14310)$ coordinate is that any amplitude must lie between approximately -0.01 and 0.01, for both the real and imaginary parts (i.e., the white in the color scale). To investigate whether there is indeed no signal there, we look at the amplitude of this coordinate as a function of T (Figure 5.34). Here we indeed find persistent oscillatory amplitude with positive frequency and period of approximately 25 fs (1340 cm^{-1} corresponds to 24.89 fs), exactly as forecast. The maximum amplitude of the real part of the oscillation is roughly of 1.6×10^{-3}, which corresponds to only 0.47% of the maximum

rephasing real signal at $T = 70$fs (see Figure 5.2), thus falling in the white region of the color plot in Figures 5.2 and 5.33.

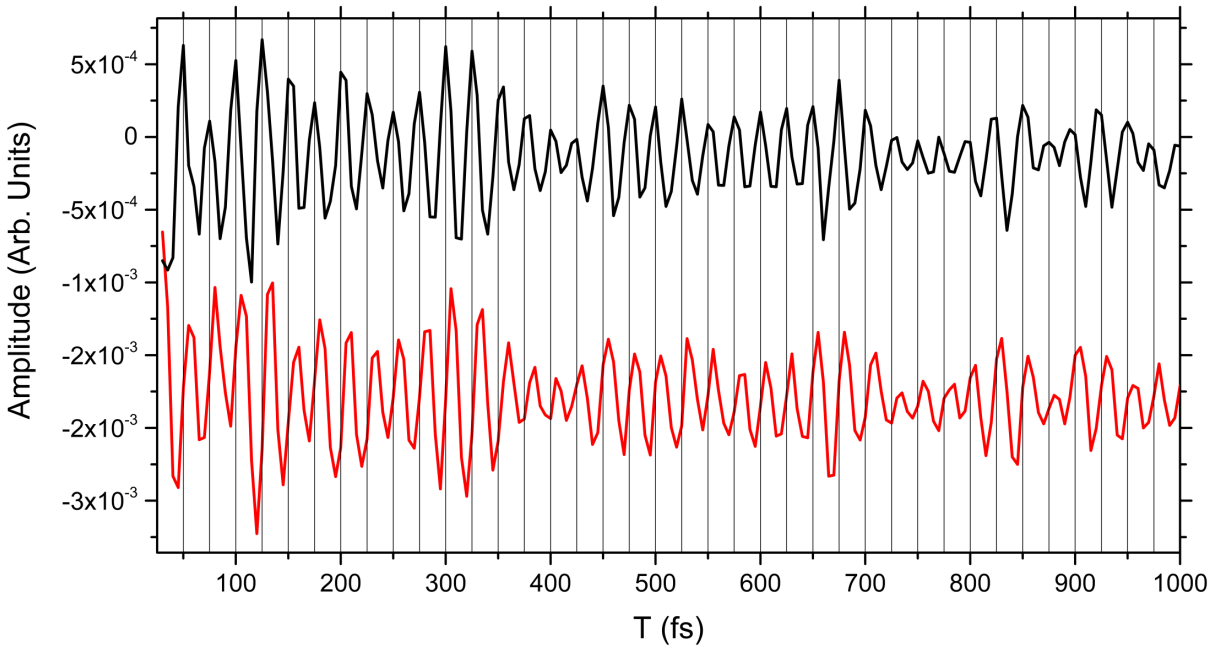

Figure 5.34: Real (black) and imaginary (red) rephasing amplitude at $\tilde{\nu}_1 = 15650$ cm^{-1} and $\tilde{\nu}_3 = 14310$ cm^{-1}. The amplitude scale is in arbitrary units, but the same as the corresponding real and imaginary maps in Figures 5.2 and 5.33.

The amplitude profile in Figure 5.34 is modulated, suggesting that other frequencies besides the 1340 cm^{-1} are present. To verify this, in Figure 5.35 we plot the power spectrum of the global fit residuals of the time trace from Figure 5.34. At negative values of $\tilde{\nu}_2$ negligible amplitude is found, while at positive frequencies a peak at $\tilde{\nu}_2 = +1340$ cm^{-1} dominates. The smaller peaks in the region defined by 800 cm^{-1} $< \tilde{\nu}_2 <$ 1300 cm^{-1} correspond to Raman modes of n-pentane [178], although in this experiment we do not recover them with quantitative precision, partially because of their small amplitude, the large number of overlapping modes and the fact that we scanned T only up to 1 picosecond.

Finally, in order to confirm that the oscillation at $\tilde{\nu}_2 = +1340$ cm^{-1} corresponds indeed to the pathway we described in the beginning of this Section, we check that this oscillatory amplitude forms a peak around $(\tilde{\nu}_1, \tilde{\nu}_3) = (15650, 14310)$. For that, in Figure 5.36 we plot the rephasing oscillation amplitude map at $\tilde{\nu}_2 = +1340$ cm^{-1} with 15150 cm^{-1} $\leq \tilde{\nu}_1 \leq$ 16250 cm^{-1} and 13700 cm^{-1} $\leq \tilde{\nu}_3 \leq$ 14800 cm^{-1}, where the amplitude is seen to form a peak around the correct position.

In summary, in this Section we have demonstrated that the laser spectrum can be used to perform a 2D-ES experiment that fully probes coherences between sublevels in

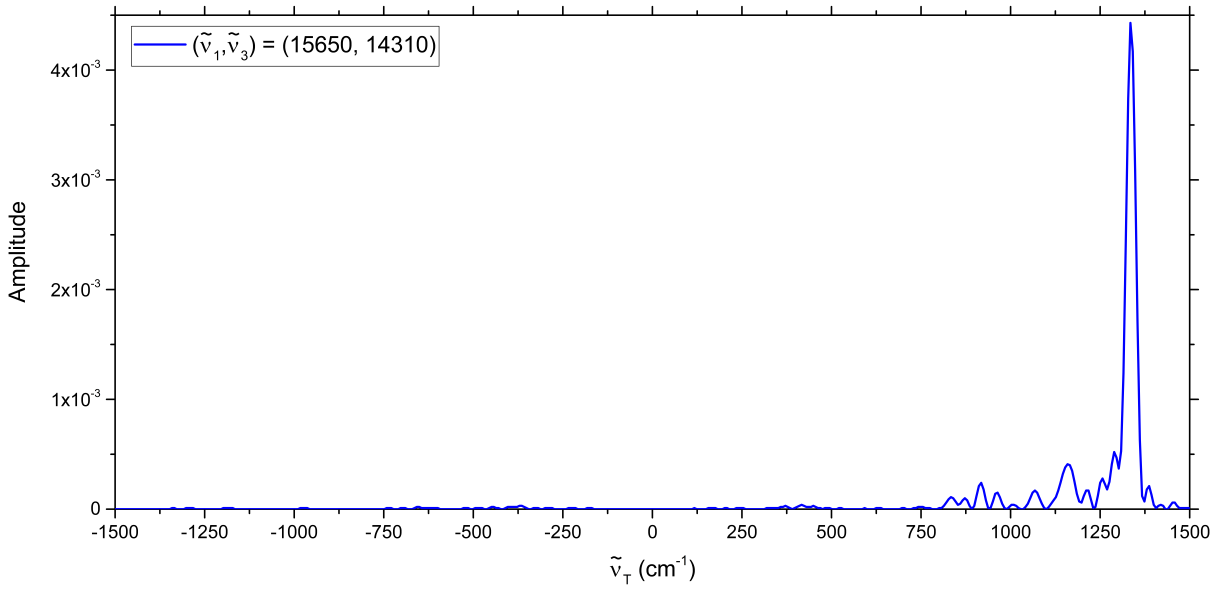

Figure 5.35: Power spectrum for $\tilde{\nu}_1 = 15650$ cm^{-1} and $\tilde{\nu}_3 = 14310$ cm^{-1}, where oscillatory amplitude at $\tilde{\nu}_T = +1340$ cm^{-1} was expected. The smaller peaks arise from Raman modes of n-pentane [178].

the ground state. We observed that recovering the non-rephasing signal with sufficient signal-to-noise to unravel all coherences can be difficult, but that the cross-peak nature of the coherences in rephasing maps isolates individual coherences in the excitation-emission plane. This experiment can be performed to complement regular 2D-ES experiments whenever ambiguity regarding the nature of observed coherent oscillations is found, as described in Section 5.2.

5.4 Summary

In conclusion, the results obtained in this Chapter deepen our understanding on how to detect and interpret coherent oscillations in 2D-ES measurements, highlighting the fact that for complex energy level structures, the laser spectrum plays a crucial and non trivial role regarding the oscillations detected. In Section 5.1 we have shown that under ideal conditions (very broad laser spectrum with abundant amplitude towards both high and low energies) the typically expected coherent signatures are observed. In Section 5.2 we blue-shifted the spectrum to cover more features at high energies, and we observed that the missing laser amplitude at low energies suppressed oscillatory features at excitation and emission wavenumbers within the new spectrum. The results resembled those expected for a purely electronic coherence. We have then shown how the different amplitude between

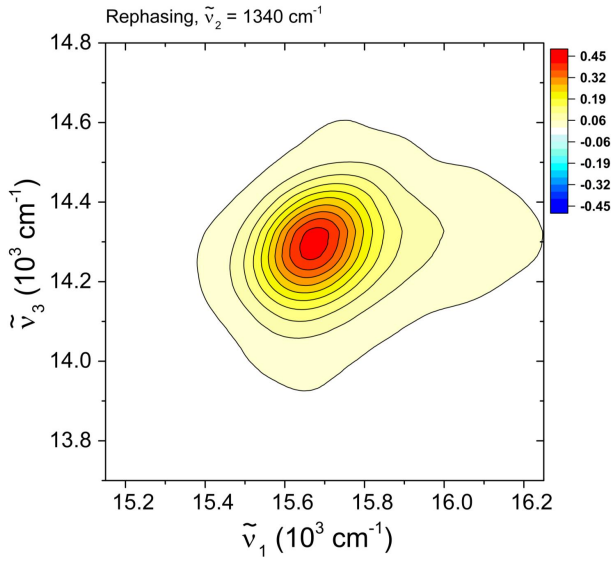

Figure 5.36: Rephasing oscillation amplitude map for $\tilde{\nu}_2 = +1340$ cm^{-1}, showing the cross peak around $\tilde{\nu}_1 = \tilde{\nu}_{eg} = 15650$ cm^{-1} and $\tilde{\nu}_3 = \tilde{\nu}_{eg} - \tilde{\nu}_0 = 14310$ cm^{-1}. The color scale amplitude has been multiplied by a factor of 10^3.

peaks can help assign them to a vibration in case a sufficiently broad spectrum cannot be obtained. In this process we have also shown how oscillation amplitude maps, although very useful, can give a false impression of good signal-to-noise as a function of T and $\tilde{\nu}_2$, thus implying that a rigorous analysis include multiple cuts of the 3D dataset. Finally, we have shown that by the same principle applied to address a blue-shifted spectrum, we can perform 2D-ES experiments with a very red-shifted spectrum which does not cover the higher levels of the vibronic progression of a molecule, and that the rephasing signals from this experiment allow the full benchmarking of coherences associated with the ground state. Therefore, if a very broad spectrum is unattainable, a combination of the red-shifted and the blue-shifted spectra, as shown in Sections 5.2 and 5.3, should allow complete unraveling of the coherences of a molecular system, a feature that can be particularly useful wherever both vibrational and electronic coupling are present, such as described in references [100, 101, 104].

Chapter 6

Conclusion

The material presented in the previous chapters does not exhaust the experiments performed during this PhD. Besides the studies of the conformation reaction of the butadiyne-linked zinc-porphyrin dimer mentioned in Chapter 1 and published in references [39, 40], a significant amount of data has not yet been fully analyzed and published. Below, some remaining open questions are briefly discussed, followed by a summary and concluding remarks.

6.1 Future work

Vibrational coherences in absorptive maps

All data analysis of the coherent oscillations in Chapters 4 and 5 has been performed on rephasing and non-rephasing maps, in order to maximally isolate individual Liouville-space pathways. However, 2D-ES spectrometers in the pump-probe or in the all collinear geometry are tailor-made for absorptive maps and do not easily recover rephasing and non-rephasing contributions (phase-cycling is required for that) [21].

Recently, a report focusing on showing phase variations of oscillations due to vibrational coherences in absorptive 2D-ES maps has been published [179]. In this study it was observed that the phase is a function of excitation and emission frequencies, but no explanation or modeling is presented, and it is concluded that the understanding of this issue is an important open problem. In view of the results presented in this thesis, it seems plausible that their observations correspond merely to the overall phase change we explained in Chapter 4, which has no strong obvious pattern due to the overlapping

presence or multiple rephasing and non-rephasing pathways in absorptive maps, which are excited in different ways according to the laser spectrum used.

The authors of that study were perhaps unaware of our interference results [123], and it remains true that we have not yet investigated the oscillatory features of our data when absorptive maps are used. Considering that absorptive maps are the sum of rephasing and non-rephasing, a quick look at Figure 2.9 shows that although there are many overlapping pathways, positive frequencies are found below the diagonal and negative frequencies are found above it. We can also apply this analysis to the blue-shifted spectrum, for which case Figure 5.21 predicts the results. Any 2D-ES setup that recovers absorptive maps can recover dispersive maps too, as both are connected through Kramers-Kronig relations [23, 107], so the analysis including negative frequencies is accessible in most experiments. Considering how well our data matched all other predictions, it is rather likely it will match this too, and the description can be valuable to the community; such an analysis is planned.

Vibrational coherences for intermediate spectra

The results from Chapter 5 have demonstrated the role of the second and third interactions of double-sided Feynman diagrams using two extreme cases: either full spectral coverage or zero amplitude at $\tilde{\nu}_{eg} - \tilde{\nu}_0$. In practice, it is often the case that some laser intensity is found at $\tilde{\nu}_{eg} - \tilde{\nu}_0$ in Figure 2.12, and the role of the laser spectrum in this case becomes much less intuitive. The data we have recorded with such intermediate spectra show results which are intermediate to both cases, but not in the sense that all missing peaks simultaneously become more important – one of the reasons being that some pathways have one transition at $\tilde{\nu}_{max} - \tilde{\nu}_0$, while some have two. Thus, if careful analysis of coherent oscillations is required in future work, further improving our simulations to include the laser spectrum would be of great help, and it can be tested against real data for the porphyrin monomer. Recently, Gellin and Domcke published an alternative way in which to compute 2D-ES spectra which takes the laser spectrum into account while requiring only one convolution integral instead of three, which can perhaps be incorporated in our simulations within the convenient Labview environment [180].

Coherences in porphyrin dimer

Experiments with fine scanning of T were also performed for a butadiyne-linked porphyrin dimer and coherent oscillations were observed at 375 cm^{-1}, 825 cm^{-1} (which was not present in the monomer data) and 1340 cm^{-1}. In this case the laser spectrum used was not broad enough to cover the main absorption $\pm$825 cm^{-1}, so the spectrum was tuned only to the high energy side. The electronic wavefunction is delocalized across the butadiyne bridge over the two porphyrin rings, so the presence of an oscillation not observed in the monomer merits careful analysis, as it could point to mixed electronic-vibrational coupling, in which case further insights about the delocalized electronic structure of this molecule can be obtained. Unfortunately in that data the strong presence of the 375 cm^{-1} mode around the diagonal causes ambiguity in this region regarding the presence or not of oscillations at 825 cm^{-1} and 1340 cm^{-1}.

Calculations by Peeks *et al.* predict a vibrational mode at around 825 cm^{-1} which includes displacements in the butadiyne bridge. However, many other modes are also expected, so reliability of such calculations for a large molecule is not clear [181]. Thus, future planning of experiments which are adequate to better address the interesting matter fully exploiting the capabilities of 2D-ES remains to be done. For now, it is clear that experiments with improved signal to noise and expanded spectral coverage would be desirable, and data analysis of the oscillations with global fitting tools can also be tested as a potentially more robust method [182]. Further, the experiment with the red-shifted spectrum described in Section 5.3 can be used to independently benchmark the ground state coherences can be used to reveal coherences associated with the ground state only, and low temperature studies might prove beneficial to reduce dephasing times.

Other open points

The theoretical insights that led us to understand the unexpected interference between pathways described in Chapter 4 were drawn from the work by Butkus *et al.* [78], which approached vibrational and electronic coupling starting from individual pathways. The equations from which we drew qualitative understanding of our data (equations 2.75, 2.76 and 2.77) are derived for a single Liouville-space pathway assuming a phenomenological dephasing that is equal among the three time intervals.

The 2D-ES experiment with the laser spectrum not covering the vibronic peak in the

linear absorption, designed and demonstrated in Section 5.3, can be used to recover the 2D-ES signal of a single rephasing coherence pathway, so that direct comparisons to the equations from Butkus *et al.* are possible. If agreement were found, this could be used to recover the phenomenological dephasing introduced to derive those equations. This opens the possibility of using the analytic expressions by Butkus *et al.* [78] to model vibrations in 2D-ES in a computationally efficient way by using analytic expressions, which can be useful if vibrational coherences are overlapped with fast dynamics.

So far two datasets in this configuration have been acquired for the porphyrin monomer, and an early assessment of the results showed vibrational modes at 375 cm^{-1}, 1340 cm^{-1} and two not previously described modes at 150 cm^{-1} and 1540 cm^{-1}. The mode at 150 cm^{-1} is present in all our data and had been overlooked due to the lower amplitude compared to the strong mode at 375 cm^{-1}, so it does not become apparent in traces in the time domain. The mode at 1540 cm^{-1} had never been within our spectral coverage before. All these results have been observed in the rephasing maps, where the coherences appear as cross-peaks. The non-rephasing maps have all coherences overlapping in the diagonal and are therefore much more difficult to unravel.

Finally, throughout all datasets Raman modes of the solvent are observed. Remarkably they have amplitude preferentially in the same regions where the solute modes do. This contradicts the more intuitive notion that non-resonant solvent modes be spread uniformly in 2D-ES maps. As of yet, we have no understanding as to why this is the case, but a substantial amount of data is available to further explore the issue.

6.2 Concluding remarks

In this Thesis we presented an in-depth discussion of vibrational coherences in 2D-ES. We started discussing the basics of semi-classical perturbative theory as a framework to interpret non-linear optical experiments. We placed the focus specifically in developing the Liouville-space pathway diagrammatic analysis, which is a convenient way to help interpret 2D-ES experiments, and presented it making didactic connections to the equations, phase matching and the rotating wave approximation [27]. We proceeded to discuss the Liouville-space pathways for vibrationally coupled systems, and then the limitations that the assumption of infinitely sharp transitions inflicts on the results [78].

We then presented a description of the 2D-ES spectrometer built in our group between 2013 and 2014. We discussed the experimental design, which has four beams incident on the sample in the boxcar geometry, is intrinsically phase stable [142] and is solely based on conventional optics (as opposed to the use of diffractive optics elements, for example) [140]. Our main contribution to previous developments was the introduction of two choppers, which brought significant advantages, including the possibility of shot to shot data acquisition, the ability to measure the broadband transient absorption signal quasi simultaneously with the 2D-ES signal, and better removal of scattering contributions [131]. We described these points, the phase stability and the movement of the delay stages in detail. And finally we discussed the data processing required to convert the raw heterodyne-detected data to the complex-valued 2D-ES absorptive, rephasing and non-rephasing maps.

The remainder of the thesis was then concerned with investigating vibrational coherence signatures in 2D-ES. All experiments described were performed on a zinc-porphyrin monomer which has its first excited state strongly coupled to a vibrational mode at 375 cm^{-1}, with a linear absorption spectrum that is very convenient for our NOPA, allowing us to have laser intensity towards both the high and the low energy sides of the main electronic transition well in excess of the 375 cm^{-1} vibrational quantum. In Chapter 4 we reported 2D-ES experiments in this sample, and initially presented basic results such as spectral diffusion, Stokes-shift and excited state absorption. We then discussed the challenges of performing data analysis on coherent oscillations in 2D-ES measurements, gradually developing oscillation amplitude and phase maps, which consist of a general method to address oscillatory behavior across the entire excitation-emission plane.

Applying this method we build a picture of all oscillatory features at 375 cm^{-1} in the real part of rephasing and non-rephasing maps, which revealed interference between different oscillatory Liouville-space pathways. This phenomenon was qualitatively explained with the theory from Butkus *et al.* [78] and modeled with calculations based on standard third-order response function theory [123]; the implications were discussed.

In Chapter 5 we further refined our studies by performing new experiments, with finer scanning of T and better signal to noise. We also developed the analysis by using the complex-valued 2D-ES maps, which enable the recovery of the frequency sign of any oscillation during T, further discriminating Feynman diagrams. As a result, we observed

that the interference effect became substantially less pronounced, which we were once again able to explain through careful analysis of the work by Butkus *et al.*.

We proceeded to note that the laser spectrum used up to that point compares to the molecular absorption in a way that is not usually attainable for most systems of interest which absorb in the visible spectral range. We then performed the same experiment and analysis with a spectrum that more closely resembles typical experimental conditions and found that coherent oscillations within the excitation-emission spectral range disappear completely. Further, the remaining signatures match exactly those expected for pure electronic coherences. We showed that the rather counterintuitive results can be properly understood considering whether all field-matter interactions in the contributing Liouville-space pathways lie within the laser spectrum, demonstrating that the unexpectedly missing pathways had either the second or third (or both) field-matter interaction that did not satisfy this condition. Finally, we extended this understanding of the role of the laser spectrum to propose and demonstrate a 2D-ES experiment that can be used to benchmark coherences associated with the ground state only. Hence, this new experiment complements the previous experiment, in which the coherence signatures were ambiguous, allowing clear determination of the nature of coherences using only 2D-ES.

In summary, our results show that 2D-ES can indeed be used to thoroughly study coherent couplings as envisioned in its early days. However, the previously unreported phenomena that arose from our study of vibrational coherences show that 2D-ES can only reach its full potential through sophisticated data analysis that meticulously and rigorously considers the many details involved in third-order signals. Further, very high quality data is required for complex systems. In this sense, 2D-ES is not very different to other advanced spectroscopic techniques such as X-ray crystallography or NMR: while the basic concepts are reasonably simple, very intricate technical knowledge of both experiment and theory is required to make the most use of it.

Appendix A

Calculations of 2D-ES Spectra

Here we describe the calculation of 2D-ES spectra used in section 4.3. The procedure employed to calculate the 2D spectra is similar to that reported in references [77,132,150], being based on third-order perturbation theory and a spectral density described by a Brownian oscillator model [183]. If we assume the rotating wave approximation then the response function is reduced to eight different terms: $R_n, n \in \{1,2,3,4\}$ and their complex conjugates. If the excitation pulses are treated as Dirac delta functions, as used in our calculations, then the third order nonlinear polarization is just proportional to the sum of all eight response functions, which we need to model. As a first approximation it is reasonable to model the porphyrin chromophore as an electronic two-level system, with the coupled vibration modelled with a spectral density $C(\omega)$. Given a known temperature independent spectral density, by means of the cumulant expansion [23] one can obtain the line shape functions as:

$$g(t) = \frac{1}{2\pi}\int_{-\infty}^{\infty} \mathrm{d}\omega \left(1-\cos\left(\omega t\right)\right) \coth\left(\frac{\beta\hbar\omega}{2}\right)\frac{C(\omega)}{\omega^2} + \frac{i}{2\pi}\int_{-\infty}^{\infty} \mathrm{d}\omega \left(\sin\left(\omega t\right)-\omega t\right)\frac{c(\omega)}{\omega^2}, \tag{A.1}$$

where $\beta = {}^{1}\!/_{k_B T}$. If the line shape function is known, the linear absorption can be calculated as:

$$\sigma_{ABS} = |\mu_{eg}|^2 \mathrm{Re}\left[\int_{-\infty}^{\infty} \mathrm{d}t \mathrm{e}^{i\omega_{eg}t - g(t)}\right], \tag{A.2}$$

where μ_{eg} and ω_{eg} are respectively the transition dipole moment and frequency of the ground to first electronic state transition. Finally, the third order response functions can

be calculated as:

$$R_1 = \mathrm{e}^{-i\omega_{eg}\tau - i\omega_{eg}t}\mathrm{e}^{-g(\tau)-g^*(T)-g^*(t)+g(\tau+T)+g^*(T+t)-g(\tau+T+t)} \tag{A.3}$$

$$R_2 = \mathrm{e}^{i\omega_{eg}\tau - i\omega_{eg}t}\mathrm{e}^{-g^*(\tau)+g(T)-g^*(t)-g^*(\tau+T)-g(T+t)+g^*(\tau+T+t)} \tag{A.4}$$

$$R_3 = \mathrm{e}^{i\omega_{eg}\tau - i\omega_{eg}t}\mathrm{e}^{-g^*(\tau)+g^*(T)-g(t)-g^*(\tau+T)-g^*(T+t)+g^*(\tau+T+t)} \tag{A.5}$$

$$R_4 = \mathrm{e}^{-i\omega_{eg}\tau - i\omega_{eg}t}\mathrm{e}^{-g(\tau)-g(T)-g(t)+g(\tau+T)+g(T+t)-g(\tau+T+t)}. \tag{A.6}$$

The third-order nonlinear response function in the time domain is given by $S^{(3)}(\tau, T, t) = R_1 + R_2 + R_3 + R_4$, and it can be converted to the usual 2D-ES maps by performing Fourier transforms on the coherence and detection times:

$$S^{(3)}(\omega_\tau, T, \omega_t) = \int_{-\infty}^{\infty} \mathrm{d}\tau \int_{-\infty}^{\infty} \mathrm{d}t S^{(3)}(\tau, T, t)\mathrm{e}^{i\omega_\tau \tau}\mathrm{e}^{i\omega_t t}. \tag{A.7}$$

Having this equations, we can approach the modelling problem systematically by first finding a spectral density $C(\omega)$ that adequately describes the linear absorption of our real sample and then calculate the third-order nonlinear response function. Our treatment of the spectral density is based on a Brownian oscillator model which allows us to account for intramolecular vibrations coupled to the electronic transition (underdamped oscillator) as well as bath fluctuations (overdamped oscillators) [77, 150]. This approach accounts for the Stokes-shift and satisfies the fluctuation-dissipation theorem. To properly model the porphyrin monomer data we needed to include three overdamped Brownian oscillators:

$$C_0(\omega) = \sum_{i=1}^{3} 2\lambda_i \frac{\omega\Lambda_i}{\omega^2 + \Lambda_i^2}, \tag{A.8}$$

where λ is the coupling strength (sometimes also referred to as the reorganization energy), Λ is the inverse of the fluctuation correlation time and the sum is over the three different oscillators we used. The underdamped oscillator used to model the intramolecular vibration has spectral density given by:

$$C_u(\omega) = \frac{2\sqrt{2}\lambda\omega\omega_0^2\gamma}{(\omega^2 - \omega_0^2)^2 + 2\gamma^2\omega^2}, \tag{A.9}$$

where γ is the damping constant and ω_0 is the oscillator frequency. The parameters used in order to match the linear absorption of the electronic transition we are studying are listed

in tables A.1 and A.2. The resulting linear absorption from this model is compared to the sample's linear absorption in figure A.1 (a). The quality of the match is adequate up to 16000 cm^{-1}, after which it breaks down as there is some overlap with the Q_y band centred at 17000 cm^{-1}. Although the laser spectrum used for the 2D-ES measurements did have significant amplitude up to 16500 cm^{-1} the calculated linear absorption is still adequately describing the main electronic transition and the first peak of the vibronic progression due to the 375 cm^{-1} mode, and all predicted peaks in the schematic 2D-ES maps have both excitation and detection wavenumbers smaller than 16000 cm^{-1}. Therefore we expect this model to suffice to describe the spectral regions we are interested in.

ω_0 (cm^{-1})	λ (cm^{-1})	γ (cm^{-1})
380	275	9

Table A.1: Parameters used for the underdamped oscillator.

	λ (cm^{-1})	Λ (cm^{-1})
Mode 1	21	83
Mode 2	19	8.3
Mode 3	16	0.33

Table A.2: Parameters used for the overdamped oscillators.

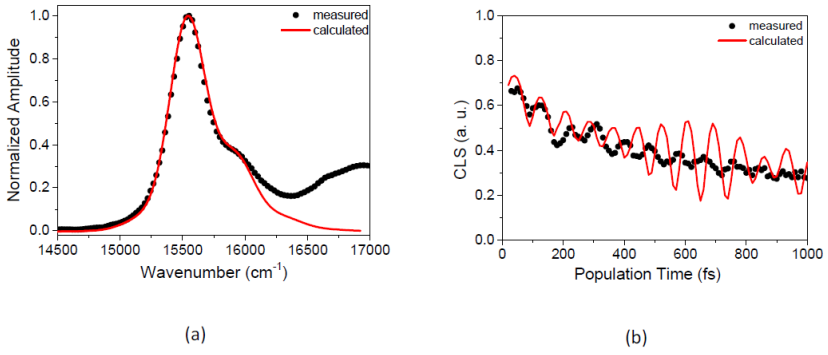

Figure A.1: **(a)** Calculated (red) and experimental (black) linear absorption spectra for the zinc-porphyrin monomer. **(b)** Comparison between the center line slope (CLS) between measured (black) and calculated (red) data.

The calculated absorptive 2D-ES maps using this model at early population times (30 to 80fs) are shown in figure A.2 and the corresponding experimental spectra are shown in figure A.3. The very good match between simulation and experiment is apparent, especially for times longer than 40 fs, when pulse overlap effects are absent. To estimate whether the overdamped Brownian oscillators used are indeed giving a fair account of

the system-bath relaxation mechanisms we have plotted the center line slope for both experimental and simulated data in figure A.1 (b). The center line slope (CLS) is a quantity used to describe the shape of peaks in 2D maps and it is often used to study phenomena such as spectral diffusion [33]. To compute the CLS one considers cuts of the 2D maps parallel to the excitation axis. For each such cut, the 2D signal will have a maximum, and a curve is drawn in the 2D map that passes through all of those maxima. This curve is then fitted to a line, the inverse slope of which is called the CLS. Therefore a peak completely elongated along the diagonal will have CLS of 1, whereas a completely round peak will have a CLS of 0 [184].

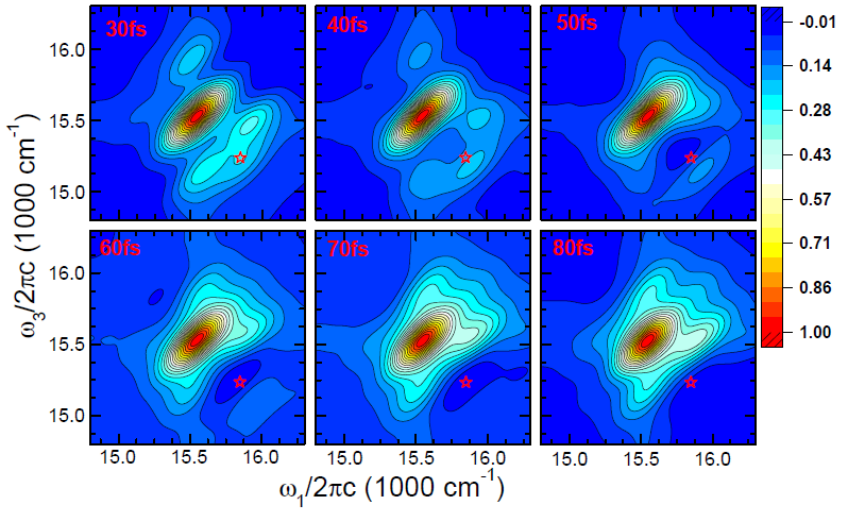

Figure A.2: Simulated absorptive 2D-ES maps from 30 to 80 fs for the two-level electronic system model coupled with the spectral density described in this section. The red star marks the position of peak F from figure 4.5a.

By applying this algorithm to both our calculated and experimental 2D-ES maps we obtained the results shown in figure A.1 (b), where the good agreement between the relaxation time scales can be seen. The oscillations present in both CLS traces are due to the 380cm^{-1} mode and they cannot be fully reproduced by this calculations, which we attribute to numerical artefacts that arise from the multiple Fourier transforms involved in the calculations. It is nonetheless interesting to note that the spectral diffusion of the porphyrin chromophore is captured by this model.

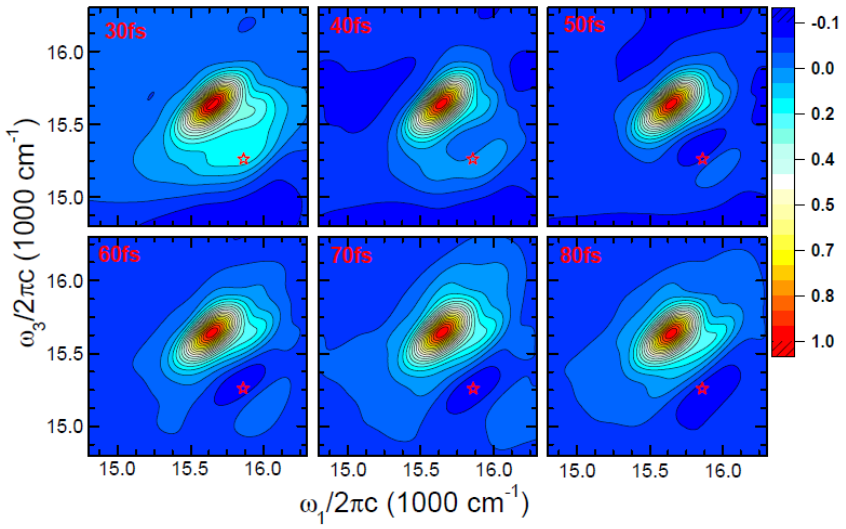

Figure A.3: Experimental absorptive 2D-ES maps from 30 to 80 fs for the two-level electronic system model coupled with the spectral density described in this section. The red star marks the position of peak F from figure 4.5a.

Bibliography

[1] Ahmed H. Zewail. Laser femtochemistry. *Science*, 242(4886):1645–1653, 1988.

[2] Ahmed H. Zewail. Femtochemistry: atomic-scale dynamics of the chemical bond. *The Journal of Physical Chemistry A*, 104(24):5660–5694, 2000.

[3] Ferenc Krausz and Misha Ivanov. Attosecond physics. *Reviews of Modern Physics*, 81:163–234, 2009.

[4] Michael Chini, Kun Zhao, and Zenghu Chang. The generation, characterization and applications of broadband isolated attosecond pulses. *Nature Photonics*, 8:178–186, 2014.

[5] Rienk van Grondelle, Jan P. Dekker, Tomas Gillbro, and Villy Sundstrom. Energy transfer and trapping in photosynthesis. *Biochimica et Biophysica Acta (BBA) - Bioenergetics*, 1187(1):1–65, 1994.

[6] Villy Sundström, Tnu Pullerits, and Rienk van Grondelle. Photosynthetic light-harvesting: reconciling dynamics and structure of purple bacterial lh2 reveals function of photosynthetic unit. *The Journal of Physical Chemistry B*, 103(13):2327–2346, 1999.

[7] David M. Jonas, Stephen E. Bradforth, Sean A. Passino, and Graham R. Fleming. Femtosecond wavepacket spectroscopy: Influence of temperature, wavelength, and pulse duration. *The Journal of Physical Chemistry*, 99(9):2594–2608, 1995.

[8] W P de Boeij, M S Pshenichnikov, and D A Wiersma. Ultrafast solvation dynamics explored by femtosecond photon echo spectroscopies. *Annual Review of Physical Chemistry*, 49:99–123, 1998.

[9] Ismael A. Heisler and Stephen R. Meech. Low-frequency modes of aqueous alkali halide solutions: Glimpsing the hydrogen bonding vibration. *Science*, 327(5967):857–860, 2010.

[10] C. J. Fecko, J. D. Eaves, J. J. Loparo, A. Tokmakoff, and P. L. Geissler. Ultrafast hydrogen-bond dynamics in the infrared spectroscopy of water. *Science*, 301(5640):1698–1702, 2003.

[11] Johannes Knorr, Pandian Sokkar, Sebastian Schott, Paolo Costa, Walter Thiel, Wolfram Sander, Elsa Sanchez-Garcia, and Patrick Nuernberger. Competitive solvent-molecule interactions govern primary processes of diphenylcarbene in solvent mixtures. *Nature Communications*, 7:3238–3239, 2016.

[12] Jamie Conyard, Kiri Addison, Ismael a. Heisler, Arjen Cnossen, Wesley R. Browne, Ben L. Feringa, and Stephen R. Meech. Ultrafast dynamics in the power stroke of a molecular rotary motor. *Nature Chemistry*, 4(7):547–551, 2012.

[13] Roger F. Loring, Yi Jing Yan, and Shaul Mukamel. Timeresolved fluorescence and holeburning line shapes of solvated molecules: Longitudinal dielectric relaxation and vibrational dynamics. *The Journal of Chemical Physics*, 87(10):5840–5857, 1987.

[14] Jonas D. M. Two-dimensional femtosecond spectroscopy. *Annual Review of Physical Chemistry*, 54:425, 2003.

[15] N. S. Ginsberg, Y. C. Cheng, and Graham R. Fleming. Two-dimensional electronic spectroscopy of molecular aggregates. *Accounts of Chemical Research*, 42:1352–1363, 2009.

[16] W. P. Aue, E. Bartholdi, and R. R. Ernst. Two-dimensional spectroscopy. application to nuclear magnetic resonance. *Journal of Chemical Physics*, 64(2229), 1976.

[17] R. R. Ernst, G. Bodenhausen, and A. Wokaun. *Principles of Nuclear Magnetic Resonance in One and Two Dimensions*. Oxford University Press, Oxford, 1987.

[18] J. D. Hybl, A. W. Albrecht, S. M. Gallagher Faeder, and D. M. Jonas. Two-dimensional electronic spectroscopy. *Chemical Physics Letters*, 297:307, 1998.

[19] P. Hamm, M. H. Lim, and R. M. Hochstrasser. Structure of the amide i band of peptides measured by femtosecond nonlinear-infrared spectroscopy. *Journal of Physical Chemistry B*, 102:6123, 1998.

[20] Yung Sam Kim and Robin M. Hochstrasser. Applications of 2d ir spectroscopy to peptides, proteins, and hydrogen-bond dynamics. *The Journal of Physical Chemistry B*, 113(24):8231–8251, 2009.

[21] Franklin D. Fuller and Jennifer P. Ogilvie. Experimental implementations of two-dimensional fourier transform electronic spectroscopy. *Annual Review of Physical Chemistry*, 66:667–690, 2015.

[22] Andrei Tokmakoff. Two-dimensional line shapes derived from coherent third-order nonlinear spectroscopy. *The Journal of Physical Chemistry A*, 104(18):4247–4255, may 2000.

[23] Shaul Mukamel. *Principles of Nonlinear Optical Spectroscopy*. Oxford University Press, New York, Oxford, 1999.

[24] J. D. Hybl, Y. Christophe, and D. M. Jonas. Peak shapes in femtosecond 2d correlation spectroscopy. *Chemical Physics*, 266:295, 2001.

[25] J. P. Ogilvie and K. J. Kubarich. Multidimensional electronic and vibrational spectroscopy: An ultrafast probe of molecular relaxation and reaction dynamics. *Advances in Atomic, Molecular, and Optical Physics*, 57, 2009.

[26] Alexandra Nemeth. *Exploring the potential of two-dimensional electronic spectroscopy*. PhD thesis, University of Vienna, 2010.

[27] Peter Hamm and Martin Zanni. *Concepts and Methods of 2D Infrared Spectroscopy*. Cambridge University Press, Cambridge, New York, Melbourne, Madrid, Cape Town, Singapore, São Paulo, Delhi, Mexico City, 2011.

[28] K. Okumura, A. Tokmakoff, and Y. Tanimura. Two-dimensional line-shape analysis of photon-echo signal. *J. Chem. Phys.*, 111:492, 1999.

[29] Roberta Moca, Stephen R. Meech, and Ismael A. Heisler. Two-dimensional electronic spectroscopy of chlorophyll a: Solvent dependent spectral evolution. *Journal of Physical Chemistry B*, 119(27):8623–8630, 2015.

[30] R. Kubo. A stochastic theory of line-shape and relaxation. In D. Ter Haar, editor, *Fluctuation, Relaxation and Resonance in Magnetic Systems*, pages 23–68. Oliver and Boyd, Edinburgh, 1962.

[31] Igor Stiopkin, Tobias Brixner, Mino Yang, and Graham R. Fleming. Heterogeneous exciton dynamics revealed by two-dimensional optical spectroscopy. *Journal of Physical Chemistry B*, 110(40):20032–20037, 2006.

[32] Kym L Wells, Zhengyang Zhang, Jérémy R Rouxel, and Howe-Siang Tan. Measuring the spectral diffusion of chlorophyll a using two-dimensional electronic spectroscopy. *The Journal of Physical Chemistry B*, 117(8):2294–9, 2013.

[33] František Šanda, Václav Perlík, Craig N. Lincoln, and Jürgen Hauer. Center line slope analysis in two-dimensional electronic spectroscopy. *The Journal of Physical Chemistry A*, 119(44):10893–10909, 2015.

[34] Kyungwon Kwak, Junrong Zheng, Hu Cang, and M D Fayer. Ultrafast two-dimensional infrared vibrational echo chemical exchange experiments and theory. *The Journal of Physical Chemistry B*, 110(40):19998–20013, 2006.

[35] Jessica M Anna, Carlos R Baiz, Matthew R Ross, Robert Mccanne, and Kevin J Kubarych. Ultrafast equilibrium and non-equilibrium chemical reaction dynamics probed with multidimensional infrared spectroscopy. *International Reviews in Physical Chemistry*, 31(3):367–419, 2012.

[36] Jessica M. Anna, Matthew R. Ross, and Kevin J. Kubarych. Dissecting enthalpic and entropie barriers to ultrafast equilibrium isomerization of a flexible molecule using 2dir chemical exchange spectroscopy. *Journal of Physical Chemistry A*, 113(24):6544–6547, 2009.

[37] Jessica M. Anna and Kevin J. Kubarych. Watching solvent friction impede ultrafast barrier crossings: A direct test of kramers theory. *Journal of Chemical Physics*, 133(17), 2010.

[38] Mikael U. Winters, Joakim Kärnbratt, Mattias Eng, Craig J. Wilson, Harry L. Anderson, and Bo Albinsson. Photophysics of a butadiyne-linked porphyrin dimer:

influence of conformational flexibility in the ground and first singlet excited state. *The Journal of Physical Chemistry C*, 111(19):7192–7199, 2007.

[39] Franco V. A. Camargo, Harry L. Anderson, Stephen R. Meech, and Ismael A. Heisler. Time-resolved twisting dynamics in a porphyrin dimer characterized by two-dimensional electronic spectroscopy. *Journal of Physical Chemistry B*, 119(46):14660–14667, 2015.

[40] Franco V. A. Camargo, Christopher R. Hall, Harry L. Anderson, Stephen R. Meech, and Ismael A. Heisler. Time resolved structural dynamics of butadiyne-linked porphyrin dimers. *Structural Dynamics*, 3(2), 2016.

[41] Martin Kullmann, Stefan Ruetzel, Johannes Buback, Patrick Nuernberger, and Tobias Brixner. Reaction dynamics of a molecular switch unveiled by coherent two-dimensional electronic spectroscopy. *Journal of the American Chemical Society*, 133(33):13074–80, aug 2011.

[42] Oliver Bixner, Vladimír Lukeš, Tomáš Mančal, Jürgen Hauer, Franz Milota, Michael Fischer, Igor Pugliesi, Maximilian Bradler, Walther Schmid, Eberhard Riedle, Harald F Kauffmann, and Niklas Christensson. Ultrafast photo-induced charge transfer unveiled by two-dimensional electronic spectroscopy. *The Journal of Chemical Physics*, 136(20):204503, 2012.

[43] Stefan Ruetzel, Martin Kullmann, Johannes Buback, Patrick Nuernberger, and Tobias Brixner. Tracing the steps of photoinduced chemical reactions in organic molecules by coherent two-dimensional electronic spectroscopy using triggered exchange. *Physical Review Letters*, 110(14):148305, April 2013.

[44] Stefan Ruetzel, Meike Diekmann, Patrick Nuernberger, Christof Walter, Bernd Engels, and Tobias Brixner. Multidimensional spectroscopy of photoreactivity. *Proceedings of the National Academy of Sciences of the United States of America*, 111(13):4764–9, 2014.

[45] Patrick Nuernberger, Stefan Ruetzel, and Tobias Brixner. Multidimensional electronic spectroscopy of photochemical reactions. *Angewandte Chemie - International Edition*, 54(39):11368–11386, 2015.

[46] T. Brixner, J. Stenger, H. M. Vaswani, M. Cho, R. E. Blankenship, and G. R. Fleming. Two-dimensional spectroscopy of electronic couplings in photosynthesis. *Nature*, 434:625, 2005.

[47] Donatas Zigmantas, Elizabeth L Read, Tomáš Mančal, Tobias Brixner, Alastair T. Gardiner, Richard J. Cogdell, and Graham R. Fleming. Two-dimensional electronic spectroscopy of the b800-b820 light-harvesting complex. *Proceedings of the National Academy of Sciences of the United States of America*, 103(34):12672–7, 2006.

[48] Gabriela S. Schlau-Cohen, Tessa R. Calhoun, Naomi S. Ginsberg, Elizabeth L. Read, Matteo Ballottari, Roberto Bassi, Rienk van Grondelle, and Graham R. Fleming. Pathways of energy flow in lhcii from two-dimensional electronic spectroscopy. *Journal of Physical Chemistry B*, 113(46):15352–15363, 2009.

[49] J. Dostál, T. Mančal, R. Augulis, F. Vácha, J. Pšenčík, and D. Zigmantas. Two-dimensional spectroscopy reveals ultrafast energy diffusion in chlorosomes. *Journal of the American Chemical Society*, 134:11611–11617, 2012.

[50] Evgeny E. Ostroumov, Rachel M. Mulvaney, Richard J. Cogdell, and Gregory D. Scholes. Broadband 2d electronic spectroscopy reveals a carotenoid dark state in purple bacteria. *Science*, 340(6128):52–56, 2013.

[51] Evgeny E Ostroumov, Rachel M Mulvaney, Jessica M Anna, Richard J Cogdell, and Gregory D Scholes. Energy transfer pathways in light-harvesting complexes of purple bacteria as revealed by global kinetic analysis of two-dimensional transient spectra. *The Journal of Physical Chemistry B*, 117(38):11349–62, 2013.

[52] Erling Thyrhaug, Karel Žídek, Jakub Dostál, David Bína, and Donatas Zigmantas. Exciton structure and energy transfer in the fenna-matthews-olson complex. *The Journal of Physical Chemistry Letters*, 7(9):1653–1660, 2016.

[53] Hong-Guang Duan, Amy L Stevens, Peter Nalbach, Michael Thorwart, Valentyn I. Prokhorenko, and R. J. Dwayne Miller. Two-dimensional electronic spectroscopy of light-harvesting complex ii at ambient temperature: A joint experimental and theoretical study. *The Journal of Physical Chemistry B*, 119(36):12017–12027, 2015.

[54] Alexandra Nemeth, Franz Milota, Jaroslaw Sperling, Darius Abramavicius, Shaul Mukamel, and Harald F. Kauffmann. Tracing exciton dynamics in molecular nanotubes with 2d electronic spectroscopy. *Chemical Physics Letters*, 469(130), 2009.

[55] Franz Milota, Jaroslaw Sperling, Alexandra Nemeth, Tomáš Mančal, and Harald F. Kauffmann. Two-dimensional electronic spectroscopy of molecular excitons. *Accounts of Chemical Research*, 42(9, SI):1364–1374, 2009.

[56] Federico Koch, Andreas Steinbacher, Cristina Consani, André Zitzler-Kunkel, Matthias Stolte, Frank Würthner, and Tobias Brixner. The role of the dipolar neighborhood on the relaxation dynamics of multichromophoric merocyanines. *Phys. Chem. Chem. Phys.*, pages 19820–19831, 2016.

[57] C. N. Borca, T. H. Zhang, X. Q. Li, and S. T. Cundiff. Optical two-dimensional fourier transform spectroscopy of semiconductors. *Chemical Physics Letters*, 416:311, 2005.

[58] Katherine W. Stone, Kenan Gundogdu, Daniel B. Turner, Xiaoqin Li, Steven T. Cundiff, and Keith A. Nelson. Two-quantum 2d ft electronic spectroscopy of biexcitons in gaas quantum wells. *Science*, 324(5931):1169–73, may 2009.

[59] Gaël Nardin, Galan Moody, Rohan Singh, Travis M. Autry, Hebin Li, François Morier-Genoud, and Steven T. Cundiff. Coherent excitonic coupling in an asymmetric double ingaas quantum well arises from many-body effects. *Physical Review Letters*, 112(4):046402, 2014.

[60] G. Moody, I. A. Akimov, H. Li, R. Singh, D. R. Yakovlev, G. Karczewski, M. Wiater, T. Wojtowicz, M. Bayer, and S. T. Cundiff. Coherent coupling of excitons and trions in a photoexcited cdte/cdmgte quantum well. *Physical Review Letters*, 112(9):097401, 2014.

[61] Christoph Lambert, Federico Koch, Sebastian F. Völker, Alexander Schmiedel, Marco Holzapfel, Alexander Humeniuk, Merle I S Röhr, Roland Mitric, and Tobias Brixner. Energy transfer between squaraine polymer sections: From helix to zigzag and all the way back. *Journal of the American Chemical Society*, 137(24):7851–7861, 2015.

[62] Tatjana Stoll, Enrico Sgrò, Jeremy W. Jarrett, Julien Réhault, Aurelio Oriana, Luca Sala, Federico Branchi, Giulio Cerullo, and Kenneth L. Knappenberger. Superatom state-resolved dynamics of the au25(sc8h9)18- cluster from two-dimensional electronic spectroscopy. *Journal of the American Chemical Society*, 138(6):1788–1791, 2016.

[63] Alexandra Nemeth, Franz Milota, Tomáš Mančal, Vladimír Lukeš, Jürgen Hauer, Harald F. Kauffmann, and Jaroslaw Sperling. Vibrational wave packet induced oscillations in two-dimensional electronic spectra. i. experiments. *The Journal of Chemical Physics*, 132(18):184514, 2010.

[64] Tomáš Mančal, Alexandra Nemeth, Franz Milota, Vladimiír Lukeš, Harald F. Kauffmann, and Jaroslaw Sperling. Vibrational wave packet induced oscillations in two-dimensional electronic spectra. ii. theory. *The Journal of Chemical Physics*, 132(18):184515, 2010.

[65] Minhaeng Cho. *Two-Dimensional Optical Spectroscopy*. CRC Press, Boca Raton, London, 2009.

[66] Leonas Valkunas, Darius Abramavicius, and Tomáš Mančal. *Molecular Excitation Dynamics and Relaxation*. Wiley-VCH, Weinheim, 2013.

[67] Jonathan O. Tollerud, Steven T. Cundiff, and Jeffrey A. Davis. Revealing and characterizing dark excitons through coherent multidimensional spectroscopy. *Physical Review Letters*, 117(9):097401, 2016.

[68] G. S. Engel, T. R. Calhoun, E. L. Read, T. K. Ahn, T. Mančal, Y. C. Cheng, R. E. Blankenship, and G. R. Fleming. Evidence for wavelike energy transfer through quantum coherence in photosynthetic systems. *Nature*, 446:782, 2007.

[69] Hohjai Lee, Yuan-Chung Cheng, and Graham R. Fleming. Coherence dynamics in photosynthesis: Protein protection of excitonic coherence. *Science*, 316(5830):1462–1465, 2007.

[70] Elisabetta Collini and Gregory D Scholes. Coherent intrachain energy migration in a conjugated polymer at room temperature. *Science*, 323(5912):369–73, jan 2009.

[71] Elisabetta Collini, Cathy Y Wong, Krystyna E Wilk, Paul M G Curmi, Paul Brumer, and Gregory D Scholes. Coherently wired light-harvesting in photosynthetic marine algae at ambient temperature. *Nature*, 463(7281):644–647, 2010.

[72] Gitt Panitchayangkoon, Dugan Hayes, Kelly A. Fransted, Justin R. Caram, Elad Harel, Jianzhong Wen, Robert E. Blankenship, and Gregory S. Engel. Long-lived quantum coherence in photosynthetic complexes at physiological temperature. *Proceedings of the National Academy of Sciences of the United States of America*, 107(29):12766–12770, 2010.

[73] Tessa R Calhoun, Naomi S Ginsberg, Gabriela S Schlau-Cohen, Yuan-Chung Cheng, Matteo Ballottari, Roberto Bassi, and Graham R Fleming. Quantum coherence enabled determination of the energy landscape in light-harvesting complex ii. *The Journal of Physical Chemistry B*, 113(51):16291–5, 2009.

[74] Dugan Hayes, Jianzhong Wen, Gitt Panitchayangkoon, Robert E. Blankenship, and Gregory S. Engel. Robustness of electronic coherence in the fennamatthewsolson complex to vibronic and structural modifications. *Faraday Discussions*, 150:459, 2011.

[75] Justin R. Caram and Gregory S. Engel. Extracting dynamics of excitonic coherences in congested spectra of photosynthetic light harvesting antenna complexes. *Faraday Discussions*, 153:93, 2011.

[76] G H Richards, K E Wilk, P M G Curmi, H M Quiney, and J a Davis. Excited state coherent dynamics in light-harvesting complexes from photosynthetic marine algae. *Journal of Physics B: Atomic, Molecular and Optical Physics*, 45:154015, 2012.

[77] N. Christensson, F. Milota, J. Hauer, J. Sperling, O. Bixner, A. Nemeth, and H. F. Kauffmann. High frequency vibrational modulations in two-dimensional electronic spectra and their resemblance to electronic coherence signatures. *Journal of Physical Chemistry B*, 115:5383–5391, 2011.

[78] Vytautas Butkus, Donatas Zigmantas, Leonas Valkunas, and Darius Abramavicius. Vibrational vs. electronic coherences in 2d spectrum of molecular systems. *Chemical Physics Letters*, 545:40 – 43, 2012.

[79] Vytautas Butkus, Leonas Valkunas, and Darius Abramavicius. Molecular vibrations-induced quantum beats in two-dimensional electronic spectroscopy. *The Journal of Chemical Physics*, 137(4):044513, 2012.

[80] Daniel B. Turner, Krystyna E. Wilk, Paul M. G. Curmi, and Gregory D. Scholes. Comparison of electronic and vibrational coherence measured by two-dimensional electronic spectroscopy. *Journal of Physical Chemistry Letters*, 2(15):1904–1911, 2011.

[81] Gitt Panitchayangkoon, Dmitri V. Voronine, Darius Abramavicius, Justin R. Caram, Nicholas H. C. Lewis, Shaul Mukamel, and Gregory S. Engel. Direct evidence of quantum transport in photosynthetic light-harvesting complexes. *Proceedings of the National Academy of Sciences of the United States of America*, 108(52):20908–20912, 2011.

[82] A. V. Pisliakov, T. Mančal, and G. R. Fleming. Two-dimensional optical three-pulse photon echo spectroscopy. ii: Signatures of coherent electronic motion and exciton population transfer in dimer two-dimensional spectra. *Journal of Chemical Physics*, 124:234505, 2006.

[83] Václav Perlík, Craig Lincoln, František Šanda, and Jürgen Hauer. Distinguishing electronic and vibronic coherence in 2d spectra by their temperature dependence. *The Journal of Physical Chemistry Letters*, 5(3):404–407, 2014.

[84] Rayomond Dinshaw. Spectroscopic investigations of the photophysics of cryptophyte light-harvesting. Master's thesis, University of Toronto, 2012.

[85] Yuan-Chung Cheng and Graham R. Fleming. Coherence quantum beats in two-dimensional electronic spectroscopy. *Journal of Physical Chemistry A*, 112(18):4254–4260, 2008.

[86] Tomáš Mančal, Niklas Christensson, Vladimír Lukeš, Franz Milota, Oliver Bixner, Harald F. Kauffmann, and Jürgen Hauer. System-dependent signatures of electronic and vibrational coherences in electronic two-dimensional spectra. *Journal of Physical Chemistry Letters*, 3(11):1497–1502, 2012.

[87] Kelly A. Fransted, Justin R. Caram, Dugan Hayes, and Gregory S. Engel. Two-dimensional electronic spectroscopy of bacteriochlorophyll a in solution: Elucidating the coherence dynamics of the fenna-matthews-olson complex using its chromophore as a control. *Journal of Chemical Physics*, 137(12), 2012.

[88] Dugan Hayes, Graham B. Griffin, and Gregory S. Engel. Engineering coherence among excited states in synthetic heterodimer systems. *Science*, 340(6139):1431–1434, 2013.

[89] Alexei Halpin, Philip J. M. Johnson, and R. J. Dwayne Miller. Comment on "engineering coherence among excited states in synthetic heterodimer systems". *Science*, 344(6188):1099–1099, 2014.

[90] Akihito Ishizaki and Graham R. Fleming. Theoretical examination of quantum coherence in a photosynthetic system at physiological temperature. *Proceedings of the National Academy of Sciences of the United States of America*, 106(41):17255–17260, 2009.

[91] A. W. Chin, S. F. Huelga, and M. B. Plenio. Coherence and decoherence in biological systems: principles of noise-assisted transport and the origin of long-lived coherences. *Philosophical Transactions of the Royal Society A: Mathematical, Physical and Engineering Sciences*, 370(1972):3638–3657, 2012.

[92] Avinash Kolli, Edward J. O'Reilly, Gregory D. Scholes, and Alexandra Olaya-Castro. The fundamental role of quantized vibrations in coherent light harvesting by cryptophyte algae. *Journal of Chemical Physics*, 137(17), 2012.

[93] Konstantin E Dorfman, Dmitri V Voronine, Shaul Mukamel, and Marlan O Scully. Photosynthetic reaction center as a quantum heat engine. *Proceedings of the National Academy of Sciences of the United States of America*, 110(8):2746–2751, 2012.

[94] Edward J O'Reilly and Alexandra Olaya-Castro. Non-classicality of the molecular vibrations assisting exciton energy transfer at room temperature. *Nature Communications*, 5:3012, 2014.

[95] Sergey Polyutov, Oliver Kühn, and Tõnu Pullerits. Exciton-vibrational coupling in molecular aggregates: Electronic versus vibronic dimer. *Chemical Physics*, 394(1):21–28, 2012.

[96] Leah Z Sharp and Dassia Egorova. Towards microscopic assignment of oscillative signatures in two-dimensional electronic photon-echo signals of vibronic oligomers: a vibronic dimer model. *The Journal of Chemical Physics*, 139(14):144304, 2013.

[97] Vytautas Butkus, Donatas Zigmantas, Darius Abramavicius, and Leonas Valkunas. Distinctive character of electronic and vibrational coherences in disordered molecular aggregates. *Chemical Physics Letters*, 587:93 – 98, 2013.

[98] Dassia Egorova. Oscillations in two-dimensional photon-echo signals of excitonic and vibronic systems: Stick-spectrum analysis and its computational verification. *Journal of Chemical Physics*, 140(3):0–12, 2014.

[99] Vytautas Butkus, Leonas Valkunas, and Darius Abramavicius. Vibronic phenomena and excitonvibrational interference in two-dimensional spectra of molecular aggregates. *The Journal of Chemical Physics*, 140(3):034306, 2014.

[100] Vivek Tiwari, William K. Peters, and David M. Jonas. Electronic resonance with anticorrelated pigment vibrations drives photosynthetic energy transfer outside the adiabatic framework. *Proceedings of the National Academy of Sciences*, 110(4):1203–1208, 2013.

[101] Alexei Halpin, Philip J. M. Johnson, Roel Tempelaar, R. Scott Murphy, Jasper Knoester, Thomas L. C. Jansen, and R. J. Dwayne Miller. Two-dimensional spectroscopy of a molecular dimer unveils the effects of vibronic coupling on exciton coherences. *Nature Chemistry*, 6(3):196–201, 2014.

[102] Hong Guang Duan, Peter Nalbach, Valentyn I. Prokhorenko, Shaul Mukamel, and Michael Thorwart. On the origin of oscillations in two-dimensional spectra of excitonically-coupled molecular systems. *New Journal of Physics*, 17(7):1–12, 2015.

[103] Franz Milota, Valentyn I. Prokhorenko, Tomáš Mančal, Hans von Berlepsch, Oliver Bixner, Harald F. Kauffmann, and Jürgen Hauer. Vibronic and vibrational co-

herences in two-dimensional electronic spectra of supramolecular j-aggregates. *The Journal of Physical Chemistry A*, 117(29):6007–6014, 2013.

[104] James Lim, David Paleček, Felipe Caycedo-Soler, Craig N. Lincoln, Javier Prior, Hans von Berlepsch, Susana F. Huelga, Martin B. Plenio, Donatas Zigmantas, and Jürgen Hauer. Vibronic origin of long-lived coherence in an artificial molecular light harvester. *Nature Communications*, 6, July 2015.

[105] Claude Cohen-Tannoudji, Bernard Diu, and Franck Laloë. *Quantum Mechanics*, volume 1. John Wiley & Sons, New York, 1977.

[106] Jun John Sakurai. *Modern Quantum Mechanics*. Addison-Wesley, Reading MA, 1994.

[107] John David Jackson. *Classical Electrodynamics*. John Wiley & Sons, New York, 3 edition, 1998.

[108] R. Kubo. *Statistical Mechanics: An Advanced Course with Problems and Solutions*. North Holland, Amsterdam, 2 edition, 1998.

[109] Karl Blum. *Density Matrix Theory and Applications*. Springer, New York, London, 3 edition, 2011.

[110] Robert W. Boyd. *Nonlinear Optics*. Academic Press, New York, 3 edition, 2008.

[111] Eugene Hecht. *Optics*. Springer, Reading MA, 4 edition, 2001.

[112] Jean-Claude Diels and Wolfganf Rudolph. *Ultrashort Laser Pulse Phenomena: Fundamentals, Techniques, and Applications on a Femtosecond Timescale*. Academic Press, San Diego, London, 2 edition, 2006.

[113] David L. Andrews. Physicality of the photon. *Journal of Physical Chemistry Letters*, 4(22):3878–3884, 2013.

[114] Nicolaas Bloembergen. *Nonlinear Optics*. World Scientific Publishing Company, Singapore, London, 4 edition, 1996.

[115] Yuen-Ron Shen. *The Principles of Nonlinear Optics*. Wiley-Interscience, New York, Chichester, 1 edition, 1984.

[116] Gabriela S. Schlau-Cohen, Akihito Ishizaki, and Graham R. Fleming. Two-dimensional electronic spectroscopy and photosynthesis: Fundamentals and applications to photosynthetic light-harvesting. *Chemical Physics*, 386(1-3):1–22, 2011.

[117] Minhaeng Cho. Coherent two-dimensional optical spectroscopy. *Chemical Reviews*, 108(4):1331–1418, 2008.

[118] M. Kasha, H. R. Rawls, and M. A. El-Bayoumi. The exciton model in molecular spectroscopy. *Pure and Applied Chemistry*, 11:371 – 392, 1965.

[119] Aurélia Chenu and Gregory D. Scholes. Coherence in energy transfer and photosynthesis. *Annual Review of Physical Chemistry*, 66(August):69–96, 2015.

[120] Elsa Cassette, Ryan D. Pensack, Benoît Mahler, and Gregory D. Scholes. Room-temperature exciton coherence and dephasing in two-dimensional nanostructures. *Nature Communications*, 6:6086, 2015.

[121] M. Khalil, N. Demirdöven, and A. Tokmakoff. Coherent 2d ir spectroscopy: molecular structure and dynamics in solution. *Journal of Physical Chemistry A*, 107:5258, 2003.

[122] M. Khalil, N. Demirdöven, and A. Tokmakoff. Obtaining absorptive line shapes in two-dimensional infrared vibrational correlation spectra. *Physical Review Letters*, 90:047401, 2003.

[123] Franco V. A. Camargo, Harry L. Anderson, Stephen R. Meech, and Ismael A. Heisler. Full characterization of vibrational coherence in a porphyrin chromophore by two-dimensional electronic spectroscopy. *The Journal of Physical Chemistry A*, 119:95–101, 2015.

[124] N. Krebs, I. Pugliesi, J. Hauer, and E. Riedle. Two-dimensional fourier transform spectroscopy in the ultraviolet with sub-20 fs pump pulses and 250720 nm supercontinuum probe. *New Journal of Physics*, 15(8):085016, 2013.

[125] Cristina Consani, Gerald Auböck, Frank van Mourik, and Majed Chergui. Ultrafast tryptophan-to-heme electron transfer in myoglobins revealed by uv 2d spectroscopy. *Science*, 339(6127):1586–1589, 2013.

[126] Valentyn I. Prokhorenko, Alessandra Picchiotti, Samansa Maneshi, and R. J. Dwayne Miller. Broadband electronic two-dimensional spectroscopy in the deep uv. In Kaoru Yamanouchi, Steven Cundiff, Regina de Vivie-Riedle, Makoto Kuwata-Gonokami, and Louis DiMauro, editors, *Ultrafast Phenomena XIX: Proceedings of the 19th International Conference, Okinawa Convention Center, Okinawa, Japan, July 7-11, 2014*, pages 432–435. Springer International Publishing, Cham, 2015.

[127] W Kuehn, K Reimann, M Woerner, T Elsaesser, and R Hey. Two-dimensional terahertz correlation spectra of electronic excitations in semiconductor quantum wells. *The Journal of Physical Chemistry B*, 115(18):5448–55, 2011.

[128] W. Kuehn, K. Reimann, M. Woerner, T. Elsaesser, R. Hey, and U. Schade. Strong correlation of electronic and lattice excitations in gaas/algaas semiconductor quantum wells revealed by two-dimensional terahertz spectroscopy. *Physical Review Letters*, 107(6):2–6, 2011.

[129] Janne Savolainen, Saima Ahmed, and Peter Hamm. Two-dimensional raman-thz spectroscopy of water. *Proceedings of the National Academy of Sciences*, 110(51):20402, 2013.

[130] Carmine Somma, Giulia Folpini, Klaus Reimann, Michael Woerner, and Thomas Elsaesser. Two-phonon quantum coherences in indium antimonide studied by non-linear two-dimensional terahertz spectroscopy. *Physical Review Letters*, 116(17):1–6, 2016.

[131] Ismael A. Heisler, Roberta Moca, Franco V. A. Camargo, and Stephen R. Meech. Two-dimensional electronic spectroscopy based on conventional optics and fast dual chopper data acquisition. *Review of Scientific Instruments*, 85:063103, 2014.

[132] T. Brixner, T. Mančal, I. V. Stiopkin, and G. R. Fleming. Phase-stabilized two-dimensional electronic spectroscopy. *Journal of Chemical Physics*, 121:4221, 2004.

[133] T. Zhang, C. N. Borca, X. Li, and S. T. Cundiff. Optical two-dimensional fourier transform spectroscopy with active interferometric stabilization. *Optics Express*, 13:7432–7441, 2005.

[134] Sang-Hee Shim and Martin T. Zanni. How to turn your pump-probe instrument into a multidimensional spectrometer: 2d ir and vis spectroscopies via pulse shaping. *Physical Chemistry Chemical Physics*, 11(5):748–761, 2009.

[135] Ramunas Augulis and Donatas Zigmantas. Two-dimensional electronic spectroscopy with double modulation lock-in detection: enhancement of sensitivity and noise resistance. *Optics Express*, 19(14):13126–13133, 2011.

[136] Julien Réhault, Margherita Maiuri, Aurelio Oriana, and Giulio Cerullo. Two-dimensional electronic spectroscopy with birefringent wedges. *Review of Scientific Instruments*, 85(12), 2014.

[137] Patrick E. Tekavec, Jeffrey A. Myers, Kristin L. M. Lewis, and Jennifer P. Ogilvie. Two-dimensional electronic spectroscopy with a continuum probe. *Optics Letters*, 34(9):1390–1392, 2009.

[138] Howe Siang Tan. Theory and phase-cycling scheme selection principles of collinear phase coherent multi-dimensional optical spectroscopy. *Journal of Chemical Physics*, 129(12), 2008.

[139] Erik M. Grumstrup, Sang-Hee Shim, Matthew A. Montgomery, Niels H. Damrauer, and Martin T. Zanni. Facile collection of two-dimensional electronic spectra using femtosecond pulse-shaping technology. *Optics Express*, 15(25):16681–16689, 2007.

[140] Ulrike Selig, Florian Langhojer, Frank Dimler, Tatjana Loehrig, Christoph Schwarz, Bjoern Gieseking, and Tobias Brixner. Inherently phase-stable coherent two-dimensional spectroscopy using only conventional optics. *Optics Letters*, 33(23):2851–2853, 2008.

[141] U. Megerle, I. Pugliesi, C. Schriever, C. F. Sailer, and E. Riedle. Sub-50 fs broadband absorption spectroscopy with tunable excitation: putting the analysis of ultrafast molecular dynamics on solid ground. *Applied Physics B - Lasers and Optics*, 96(2-3):215–231, 2009.

[142] M. L. Cowan, J. P. Ogilvie, and R. J. D. Miller. Two-dimensional spectroscopy using diffractive optics based phased-locked photon echoes. *Chemical Physics Letters*, 386(1-3):184–189, 2004.

[143] Wei Xiong, David B. Strasfeld, Sang-Hee Shim, and Martin T. Zanni. Automated 2d ir spectrometer mitigates the influence of high optical densities. *Vibrational Spectroscopy*, 50(1):136–142, 2009.

[144] E. Vogel, A. Gbureck, and W. Kiefer. Vibrational spectroscopic studies on the dyes cresyl violet and coumarin 152. *Journal of Molecular Structure*, 550(SI):177–190, 2000.

[145] Ulrike Seelig. *Methods of nonlinear femtosecond spectroscopy in the visible and ultraviolet regime and their application to coupled multichromophore systems.* PhD thesis, University of Würzburg, 2012.

[146] S. M. G. Faeder and D. M. Jonas. Two-dimensional electronic correlation and relaxation spectra: Theory and model calculations. *Journal of Physical Chemistry A*, 103(49):10489–10505, 1999.

[147] G. R. Fleming and M. H. Cho. Chromophore-solvent dynamics. *Annual Review of Physical Chemistry*, 47:109–134, 1996.

[148] W. P. de Boeij, M. S. Pshenichnikov, and D. A. Wiersma. Ultrafast solvation dynamics explored by femtosecond photon echo spectroscopies. *Annual Review of Physical Chemistry*, 49:99–123, 1998.

[149] Yuan-Chung Cheng and Graham R. Fleming. Dynamics of light harvesting in photosynthesis. *Annual Review of Physical Chemistry*, 60:241–262, 2009.

[150] J. R. Caram, A. F. Fidler, and G. S. Engel. Excited and ground state vibrational dynamics revealed by two-dimensional electronic spectroscopy. *The Journal of Chemical Physics*, 137:024507, 2012.

[151] I. Hwang, U. Seelig, S. S. Y. Chen, P. E. Shaw, T. Brixner, P. L. Burn, and G. D. Scholes. Photophysics of delocalized excitons in carbazole dendrimers. *Journal of Physical Chemistry A*, 117:6270–6278, 2013.

[152] Tõnu Pullerits, Donatas Zigmantas, and Villy Sundström. Beatings in electronic 2d spectroscopy suggest another role of vibrations in photosynthetic light harvesting. *Proceedings of the National Academy of Sciences*, 110(4):1148–1149, 2013.

[153] A. Chenu, N. Christensson, H. F. Kauffmann, and T. Mancal. Enhancement of vibronic and ground-state vibrational coherences in 2d spectra of photosynthetic complexes. *Scientific Reports*, 3:2029, 2013.

[154] Kelly A. Fransted, Justin R. Caram, Dugan Hayes, and Gregory S. Engel. Two-dimensional electronic spectroscopy of bacteriochlorophyll a in solution: Elucidating the coherence dynamics of the fenna-matthews-olson complex using its chromophore as a control. *The Journal of Chemical Physics*, 137(12):125101, 2012.

[155] Dominik Koszelewski, Agnieszka Nowak-Krol, Mikhail Drobizhev, Craig J. Wilson, Joy E. Haley, Thomas M. Cooper, Jerzy Romiszewski, Ewa Gorecka, Harry L. Anderson, Aleksander Rebane, and Daniel T. Gryko. Synthesis and linear and non-linear optical properties of low-melting π-extended porphyrins. *Journal of Materials Chemistry C*, 1:2044–2053, 2013.

[156] Martin Gouterman. Spectra of porphyrins. *Journal of Molecular Spectroscopy*, 6(1):138–163, 1961.

[157] Harry L. Anderson. Conjugated porphyrin ladders. *Inorganic Chemistry*, 33(5):972–981, 1994.

[158] D. Beljonne, G. E. O'Keefe, P. J. Hamer, R. H. Friend, H. L. Anderson, and Brédas. Investigation of the linear and nonlinear optical response of edge-linked conjugated zinc porphyrin oligomers by optical spectroscopy and configuration interaction techniques. *The Journal of Chemical Physics*, 106(23):9439–9460, 1997.

[159] Harry L. Anderson. Supramolecular orientation of conjugated porphyrin oligomers in stretched polymers. *Advanced Materials*, 6(11):834–836, 1994.

[160] Mikhail Drobizhev, Yuriy Stepanenko, Yuliya Dzenis, Aliaksandr Karotki, Aleksander Rebane, Peter N. Taylor, and Harry L. Anderson. Extremely strong near-ir two-photon absorption in conjugated porphyrin dimers: quantitative description with three-essential-states model. *The Journal of Physical Chemistry B*, 109(15):7223–7236, 2005.

[161] Claudia E. Tait, Patrik Neuhaus, Harry L. Anderson, and Christiane R. Timmel. Triplet state delocalization in a conjugated porphyrin dimer probed by transient

electron paramagnetic resonance techniques. *Journal of the American Chemical Society*, 137(20):66706679, 2015.

[162] Michael Atamian, Robert J. Donohoe, Jonathan S. Lindsey, and David F. Bocian. Resonance raman spectra and normal-coordinate analysis of reduced porphyrins. 1. zinc(ii) tetraphenylporphyrin anion. *The Journal of Physical Chemistry*, 93(6):2236–2243, 1989.

[163] Baxter Abraham, Jesus Nieto-Pescador, and Lars Gundlach. Ultrafast relaxation dynamics of photoexcited zinc-porphyrin: Electronic-vibrational coupling. *The Journal of Physical Chemistry Letters*, pages 3151–3156, 2016.

[164] E. W. Castner and M. Maroncelli. Solvent dynamics derived from optical kerr effect, dielectric dispersion, and time-resolved stokes shift measurements: An empirical comparison. *Journal of Molecular Liquids*, 77(1-3):1–36, 1998.

[165] Elad Harel and Gregory S Engel. Quantum coherence spectroscopy reveals complex dynamics in bacterial light- harvesting complex 2 (lh2). *Proceedings of the National Academy of Sciences*, 109(3):706–711, 2011.

[166] Vytautas Butkus, Darius Abramavicius, A. Gelzinis, and Leonas Valkunas. Two-dimensional optical spectroscopy of molecular aggregates. *Lithuanian Journal of Physics*, 50(3):267 – 303, 2010.

[167] Joachim Seibt and Tõnu Pullerits. Beating signals in 2d spectroscopy: Electronic or nuclear coherences? application to a quantum dot model system. *The Journal of Physical Chemistry C*, 117(36):18728–18737, 2013.

[168] Daniel B. Turner, Rayomond Dinshaw, Kyung-Koo Lee, Michael S. Belsley, Krystyna E. Wilk, Paul M. G. Curmi, and Gregory D. Scholes. Quantitative investigations of quantum coherence for a light-harvesting protein at conditions simulating photosynthesis. *Physical Chemistry Chemical Physics*, 14:4857–4874, 2012.

[169] Valentyn I. Prokhorenko. Global analysis of multi-dimensional experimental data. *EPA Newsletter*, pages 21–23, 2012.

[170] Y. Song, C. Hellmann, N. Stingelin, and G. D. Scholes. The separation of vibrational coherence from ground- and excited-electronic states in p3ht film. *The Journal of Chemical Physics*, 142(21):–, 2015.

[171] Franco V A Camargo, Lena Grimmelsmann, Harry L. Anderson, Stephen R. Meech, and Ismael A. Heisler. Resolving vibrational from electronic coherences in two-dimensional electronic spectroscopy: The role of the laser spectrum. *Physical Review Letters*, 118(17), 2017.

[172] S. Seckin Senlik, Veronica R. Policht, and Jennifer P. Ogilvie. Two-color nonlinear spectroscopy for the rapid acquisition of coherent dynamics. *Journal of Physical Chemistry Letters*, 6(13):2413–2420, 2015.

[173] Par Kjellberg, Ben Bruggemann, and Tonu Pullerits. Two-dimensional electronic spectroscopy of an excitonically coupled dimer. *Physical Review B*, 74(2), 2006.

[174] Niklas Christensson, Yuri Avlasevich, Arkady Yartsev, Klaus Müllen, Torbjörn Pascher, and Tõnu Pullerits. Weakly chirped pulses in frequency resolved coherent spectroscopy. *Journal of Chemical Physics*, 132(17), 2010.

[175] D. Abramavicius, V. Butkus, J. Bujokas, and L. Valkunas. Manipulation of two-dimensional spectra of excitonically coupled molecules by narrow-bandwidth laser pulses. *Chemical Physics*, 372(1-3):22–32, 2010.

[176] Jonathan O. Tollerud, Christopher R. Hall, and Jeffrey A. Davis. Isolating quantum coherence using coherent multi-dimensional spectroscopy with spectrally shaped pulses. *Optics Express*, 22(6):6719–33, 2014.

[177] Vytautas Butkus, Andrius Gelzinis, Ramunas Augulis, Andrew Gall, Claudia Büchel, Bruno Robert, Donatas Zigmantas, Leonas Valkunas, and Darius Abramavicius. Coherence and population dynamics of chlorophyll excitations in fcp complex: Two-dimensional spectroscopy study. *The Journal of Chemical Physics*, 142(21), 2015.

[178] C Dale Keefe and Scott Jaspers-Fayer. Infrared optical properties and raman spectra of *n*-pentane and n-pentane-d12. *Vibrational Spectroscopy*, 57(1):72–80, 2011.

[179] Ki Hee Song, Munui Gu, Min Seok Kim, Hyeok Jun Kwon, Hanju Rhee, Hogyu Han, and Minhaeng Cho. Quantum beats and phase shifts in two-dimensional electronic spectra of zinc naphthalocyanine monomer and aggregate. *Journal of Physical Chemistry Letters*, 6(21):4314–4318, 2015.

[180] Maxim F. Gelin and Wolfgang Domcke. Alternative view of two-dimensional spectroscopy. *Journal of Chemical Physics*, 144(19):0–9, 2016.

[181] Martin D. Peeks, Patrik Neuhaus, and Harry L. Anderson. Experimental and computational evaluation of the barrier to torsional rotation in a butadiyne-linked porphyrin dimer. *Physical Chemistry Chemical Physics*, 18:5264–5274, 2016.

[182] Andrea Volpato, Luca Bolzonello, Elena Meneghin, and Elisabetta Collini. Global analysis of coherence and population dynamics in 2d electronic spectroscopy. *Optics Express*, 24(21):24773–24785, 2016.

[183] Wim P. de Boeij, Maxim S. Pshenichnikov, and Douwe A. Wiersma. Systembath correlation function probed by conventional and time-gated stimulated photon echo. *The Journal of Physical Chemistry*, 100(29):11806–11823, 1996.

[184] Kyungwon Kwak, Sungnam Park, Ilya J. Finkelstein, and M. D. Fayer. Frequency-frequency correlation functions and apodization in two-dimensional infrared vibrational echo spectroscopy: A new approach. *The Journal of Chemical Physics*, 127(12):–, 2007.